Conformational Landscape, Internal Dynamics, and Non-Covalent Interactions of Flexible Molecular Systems by Rotational Spectroscopy and Quantum Chemistry Calculations

by

Weslley Guilherme Dias de Paiva Silva

A thesis submitted to the Faculty of Graduate Studies of the University of Manitoba in partial fulfillment of the requirements of the degree of

Doctor of Philosophy

Department of Chemistry

University of Manitoba

Winnipeg, Canada

Abstract

Non-covalent interactions govern the three-dimensional structures of molecules and are thus central to their function, reactivity, and spectroscopic fingerprints, but despite this pivotal role, remain undercharacterized. Rotational spectroscopy is an ideal tool to study the structure, conformational flexibility and internal dynamics of molecules and molecular clusters under collision-free and isolated conditions. In this thesis, rotational spectroscopy (6–24 GHz) and quantum chemistry calculations were used to study the effects ruling the geometric preferences of selected molecular systems (monomers and water complexes) with a wide range of applicability from biological to astrophysical interest. The studied monomers are 3-mercaptopropionic acid ($HO(C{=}O)CH_2CH_2SH$, MPA), methyl 3-mercaptopropionate ($CH_3O(C{=}O)CH_2CH_2SH$, MP) and *N*-allylmethylamine ($CH_2CHCH_2NHCH_3$, AMA) which are models for elucidating intramolecular interactions involving thiols and amines. Regarding the molecular aggregates, water complexes of AMA and non-aromatic, trimethylene sulfide (c-C_3H_6S) and oxide (c-C_3H_6O), and aromatic (C_4H_4S, thiophene) heterocycles, which are prototypes of the intermolecular interactions occurring in the first steps of water solvation, were investigated. In particular, the focus of this research is to provide accurate and detailed experimental data on the nature of non-covalent interactions involving oxygen, nitrogen, and sulfur and to characterize their influence on the stabilization of the studied molecules. The experimental measurements for these systems validated the computational methods employed in terms of both relative energies and molecular structures. To understand the underlying complex effects that drive their unusual conformational preferences, quantum theory of atoms in molecules, non-covalent interaction, natural bond orbital and an energy decomposition analysis scheme were employed. Collectively, general observations could

be made including drastic changes in the conformational equilibria in moving from interactions involving O and N to those with S and that the inclusion of water disrupts the conformational distribution further. Although weaker than classical hydrogen bonds (HBs), non-classical sulfur HBs and secondary contacts (e.g. involving C–H groups) which are longer-range and more dispersive in nature were proven to play a crucial role in the stabilization of both monomers and molecular aggregates. The results presented in this thesis lay groundwork for the improvement of chemical modelling tools and deepen our understanding of non-covalent interactions that are ubiquitous in many fields of science including molecular recognition, self-assembly and supramolecular chemistry.

Acknowledgements

I would like to express my sincere gratitude to everyone who somehow contributed to the development of this work, especially to:

My Ph.D. advisor Professor Jennifer van Wijngaarden for her guidance, patience, and support over the last four years. I have learned many different aspects of science with her that includes not only chemistry, but also how to improve science communication and to deal with different situations in academia. These are skills that I will carry with me for the rest of my life and that I am grateful to have acquired them in the van Wijngaarden research group.

My advisory and evaluation committee members Professors Georg Schreckenbach, Jacob Burgess, Mazdak Khajehpour and Maria Sanz (King's College London) for their great support and assistance throughout my Ph.D. program and for their valuable contributions to this thesis.

My former professors and good friends Matheus Freitas, Claudio Tormena and Roberto Rittner. Their advice was essential for the early stages of my career as a scientist. Thanks for introducing me to the research world!

My research collaborators Luca Evangelisti from the University of Bologna and Tamanna Poonia (also a friend from the van Wijngaarden research group).

All workers from the Department of Chemistry of the University of Manitoba for being very kind in helping me to solve several issues I had during my program.

Ali Kerrache and Grigory Shamov from the GREX supercomputer from the University of Manitoba for their supporting in solving technical issues related to quantum mechanical calculations.

The current and past members of the van Wijngaarden research group who I had the opportunity to learn with and to discuss good science to: Wenhao Sun, Tamanna Poonia, Carolyn Gregory, Joseph Stitsky, Paul Sogeke, Gabrielle Daudet, Katrina Bergmann and Sem Perez.

My old undergraduate (Casa Lar and friends), Master's (Unicamp, in special to my friends Lucas and Renan for being always supportive and present daily in my life) and Science Without Borders friends for their support and friendship over many years.

My friends that I made in Canada who were very important during this journey, especially to Ewan McRae, Görkem Bakir, Jorge Dourado, Simarpreet Singh, Kleiton Souza and Cheryl Debets. Thanks to all of you!

My family and loved ones in Brazil who even being thousands of miles away have always showed their unconditional love and support for me. Special thanks to my mother Ana Paula Dias de Paiva, brother Felipe Lua Dias de Paiva and girlfriend Aliny Reis. I love all of you.

Finally, I am also thankful for the financial support provided by the Faculty of Graduate Studies from the University of Manitoba through the University of Manitoba Graduate Fellowship (UMGF) and GETS program.

Dedication

To my parents Ana Paula Dias de Paiva and Geová Paiva da Silva (*in memoriam*).

Table of Contents

List of Figures

List of Tables

List of Abbreviations

AIMALL	Atoms In Molecules All Program
AMA	*N*-Allylmethylamine
aug-cc-pVTZ	Augmented Correlation-Consistent Polarized Valence Triple Zeta Basis Set
AWG	Arbitrary Waveform Generator
B2PLYP	Grimme's Becke, 2-parameter, Perturbative, Lee–Yang–Parr Double-Hybrid Functional
B3LYP-D3BJ	Becke, 3-Parameter, Lee–Yang–Parr
BCP	Bond Critical Point
BF-FTMW	Balle-Flygare Fourier Transform Microwave
BP	Bond Path
BSSE	Basis Set Superposition Error
CAM	Combined Axis Method
CP-FTMW	Chirped-Pulse Fourier Transform Microwave
CREST	Conformer-Rotamer Ensemble Sampling Tool
D3(BJ)	Dispersion Correction with Becke-Johnson Damping
def2-TZVP	Karlsruhe Triple Zeta Valence Polarization Basis Set
DFT	Density Functional Theory
DMA	Dimethylamine
DNA	Deoxyribonucleic Acid
EDA	Energy Decomposition Analysis
FF	Force Field
FID	Free Induction Decay
FTIR	Fourier Transform Infrared
FTMW	Fourier Transform Microwave
FWHM	Full Width at Half Maximum
GFN2-xTB	Geometry, Frequency, Non-covalent, 2, Extended Tight Binding
HB	Hydrogen Bond
IHB	Intramolecular Hydrogen Bonding

iMTD-GC	Iterative Metadynamic Sampling and Genetic Crossover
IR	Infrared
ISM	Interstellar Medium
IUPAC	International Union of Pure and Applied Chemistry
KRA	Kraitchman Program
LP	Lone Pair
MA	Methylamine
MM	Molecular Mechanics
MMFF94	Merck Molecular Force Field 94
MP	Methyl 3-Mercaptopropionate
MP2	Second Order Møller-Plesset Perturbation Theory
MPA	3-Mercaptopropionic Acid
NBO	Natural Bond Orbital
NCI	Non-Covalent Interaction
NCIPLOT	Non-Covalent Interaction Plotting Program
NMR	Nuclear Magnetic Resonance
PES	Potential Energy Surface
PGOPHER	Program for Rotational, Vibrational and Electronic Spectra
QTAIM	Quantum Theory of Atoms in Molecules
RCP	Ring Critical Point
SAPT	Symmetry-Adapted Perturbation Theory
TMA	Trimethylamine
TMC-1	Taurus Molecular Cloud
TMO	Trimethylene Oxide
TMS	Trimethylene Sulfide
TS	Transition State
UV-Vis	Ultraviolet-Visible
VDD	Voronoi Deformation Density
XIAM	Holger Hartwig's Internal Axis Method Program
XTB	Extended Tight Binding
ZPE	Zero-Point Energy

Contribution of Authors

Chapter 4: Sulfur as a Hydrogen Bonding Donor in the Gas Phase: Rotational Spectroscopic and Computational Study of 3-Mercaptopropionic Acid

i) Weslley G. D. P. Silva: Conceptualization, Formal analysis, Investigation, Writing – Original Draft, Review and Editing.
ii) Jennifer van Wijngaarden: Funding acquisition, Resources, Supervision, Writing – Review and Editing.

Chapter 5: Internal Motions and Sulfur Hydrogen Bonding in Methyl 3-Mercaptopropionate

iii) Weslley G. D. P. Silva: Conceptualization, Formal analysis, Investigation, Writing - Original Draft, Review and Editing.
i) Luca Evangelisti: Formal analysis, Writing - Review and Editing.
iv) Jennifer van Wijngaarden: Funding acquisition, Resources, Supervision, Writing - Review and Editing.

Chapter 6: Hydrogen Bonding Networks and Cooperativity Effects in the Aqueous Solvation of Trimethylene Oxide and Sulfide Rings by Microwave Spectroscopy and Computational Chemistry

v) Weslley G. D. P. Silva: Conceptualization, Formal analysis, Investigation, Writing - Original Draft, Review and Editing.
vi) Jennifer van Wijngaarden: Funding acquisition, Resources, Supervision, Writing - Original Draft, Review and Editing.

Chapter 7: Characterization of Large Amplitude Motions and Hydrogen Bonding Interactions in the Thiophene–Water Complex by Rotational Spectroscopy

i) Weslley G. D. P. Silva: Conceptualization, Formal analysis, Investigation, Writing - Original Draft, Review and Editing.
ii) Jennifer van Wijngaarden: Funding acquisition, Resources, Supervision, Writing - Original Draft, Review and Editing.

Chapter 8: Targeting the Rich Conformational Landscape of *N*-allylmethylamine Using Rotational Spectroscopy and Quantum Mechanical Calculations

i) Weslley G. D. P. Silva: Conceptualization, Formal Analysis, Investigation, Writing – Original Draft, Review and Editing.
ii) Tamanna Poonia: Formal Analysis, Investigation, Writing - Original Draft, Review and Editing.
iii) Jennifer van Wijngaarden: Conceptualization, Funding acquisition, Resources, Supervision, Writing - Review and Editing.

Chapter 9: Exploring the Non-Covalent Interactions Behind the Formation of Amine–Water Complexes: The Case of the *N*-allylmethylamine Monohydrate

i) Weslley G. D. P. Silva: Conceptualization, Formal Analysis, Investigation, Writing - Original Draft, Review and Editing.
ii) Tamanna Poonia: Formal Analysis, Investigation, Writing – Original Draft, Review and Editing.
iii) Jennifer van Wijngaarden: Funding acquisition, Resources, Supervision, Writing - Review and Editing.

Chapter 1. Introduction

1.1 Conformational Analysis

In the same way that human beings can respond to different biological and environmental stresses, molecules can vary in shape and function depending on their chemical surroundings. These different spatial arrangements adopted by a molecule, which arise due to rotations about its individual single bond(s), are known as conformational isomers or simply conformers.[1] When a molecule exhibits conformational isomerism, it is common to observe that one geometry may be preferred over another usually because of interactions, either attractive or repulsive, that occur between the different fragments of the molecule or with the external medium (e.g. solvent molecules) and these interactions are responsible for the conformer stabilities.[2] Interactions occurring within the same molecule and in between two distinct binding partners are generally referred as intramolecular and intermolecular interactions, respectively. The detailed study of determining the conformers of a molecular system, their energies and the steric and/or electronic effects governing their stabilities is known as conformational analysis.

The study of conformational analysis began in the middle of the 20th century with the pioneering works of Barton and Hassel whose contributions to the development of the concept of conformation and its application in chemistry were recognized in 1969 as a shared Nobel Prize award.[3] In particular, in 1950 in a publication entitled "The conformation of the steroid nucleus",[4] using previous concepts from electron diffraction studies on cyclohexane derivatives reported by Hassel,[5,6] Barton showed that biologically active steroid molecules adopt a preferred conformation and that the chemical and physical properties of these molecules could be interpreted as a result of

the favoured geometry. It thus became clear that the geometries of molecules have a great impact on their configuration, reactivity and spectroscopic behaviour and the knowledge of molecular structures is fundamental to many fields of science including spectroscopy, materials design, organic synthesis and biochemistry.[2,7–9]

Practically, insights on the geometries of molecules can be obtained using a variety of spectroscopic techniques including rotational, infrared, Raman, ultraviolet-visible (UV-vis) and nuclear magnetic resonance (NMR) spectroscopy.[2,10] Whether the measured spectroscopic parameters (e.g. frequencies) are characteristic of each individual conformer or represent averages over all possible geometries of a molecule will depend on the timescale of the technique in comparison to that related to the conformational change which is usually dictated by the energy barriers of interconversion.[2] Among the different spectroscopic methods used for conformational analysis purposes, microwave or rotational spectroscopy has proven to be a powerful technique to determine accurate molecular structures in the gas phase as it offers a direct structural connection through the rotational moments of inertia.[9] As each conformer has a unique geometry, each will have its own fingerprints in the rotational spectrum. Although rotational spectroscopy has traditionally been focused on the study of small molecules, since the development of the microwave broadband spectroscopy by Pate and co-workers in 2008,[11] the number of complex systems investigated by rotational spectroscopy has increased drastically. Examples include the rich conformational landscapes of monomers, such as citronellal[12] and perillyl alcohol[13], and molecular complexes, such as the limonene monohydrate[14] and the tetrahydro-2-furoic acid dimer.[15] In particular, in the citronellal study,[12] spectral features related to the rotational energies of a surprising 15 individual conformers were observed.

In addition to advanced experimental methods, with the recent developments in hardware and computational capabilities, quantum mechanical calculations have become crucial to guide the assignments of complex molecular spectra in order to unveil the effects responsible for the observed conformational preferences. Thus, an interplay between experiment and theory is key to the success of conformational analysis studies. Even for the very simple case of ethane, for example, there has been some controversy in the literature of the reasons behind the larger stability of its *staggered* over the *eclipsed* form (Figure 1.1). While classical explanations attributed the lower energy of the *staggered* form to the presence of steric repulsion between the electrons of the C–H bonds in the *eclipsed* configuration, it has also been suggested that rotation-induced weakening of the central C–C bond and favourable orbital interactions $\sigma_{C-H} \rightarrow \sigma^*_{C-H}$ between the C–H orbitals in the *staggered* form, also known as hyperconjugation, contribute to the relative energy ordering.[16]

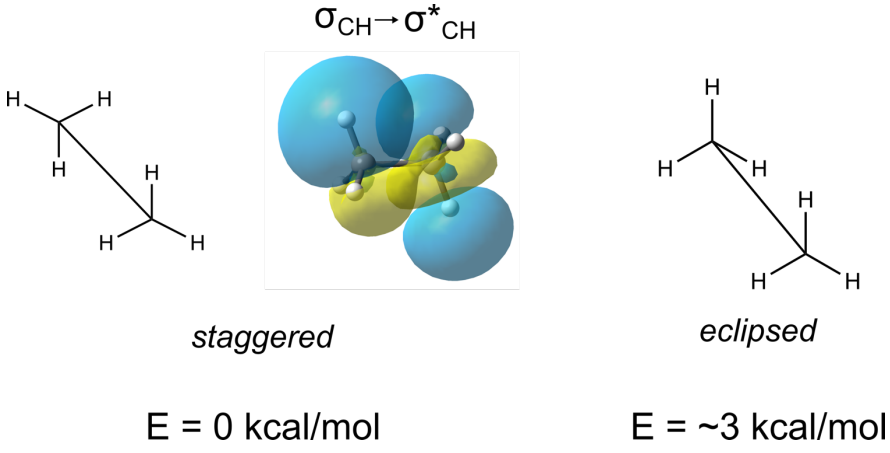

Figure 1.1 *Staggered* and *eclipsed* conformations of ethane. The orbital interaction $\sigma_{CH} \rightarrow \sigma^*_{CH}$ that stabilizes the staggered form is highlighted.

As for ethane, a variety of stabilizing and destabilizing effects (and combination of those) rule the stability of many molecular systems. In the next section, a brief introduction to some effects that stabilize molecules, namely non-covalent interactions, will be provided. It is worth noting that non-covalent interactions comprise a range of intra- and intermolecular forces with a diversity of strength and characteristics, but only those relevant for the understanding of this thesis will be presented.

1.2 Non-Covalent Interactions

Stabilizing non-covalent interactions comprise a collection of phenomena that attract molecules or ions toward one another.[10] As stated by its very name, it excludes the strong covalent bonds that hold the atoms within a molecule together. Non-covalent forces are ubiquitous in nature and include, for example, the chemical interactions between a protein and a drug, a catalyst and a substrate, the Coulombic attraction between ions of opposite charges and the very small forces forming weakly bound complexes with noble gases.[7,9,10] This class of interactions include a wide range of contacts with distinct structural and energetic parameters and spans from the relatively strong classical hydrogen bonds to non-classical weak interactions such as the halogen,[17] chalcogen,[18] pnictogen[19,20] and tetrel bond,[20] among others. These latter interactions were experimentally proven to drive the geometries of many chemical systems and are now recognized by the International Union of Pure and Applied Chemistry (IUPAC).

1.2.1 Classical Hydrogen Bond

Hydrogen bonding (HB) is one of the most important attractive interactions responsible for the three-dimensional structures of molecules.[8,21,22] After the introduction of the HB concept in 1920 as the "hydrogen nucleus held between two atoms",[22] many research studies have focused on unveiling the structures of molecules which could be explained by the presence of HB interactions. Approximately thirty years later, during the early developments of crystallography in the 1950s, the double helix DNA structure[23] as well as the α-helix[24] and β-sheet[25] structures of proteins were shown to be due to HB interactions and this remarkable finding constituted a significant milestone at the time.[21] Since then, HB concepts were applied to several fields of science including molecular recognition, catalysis, self-assembly and supramolecular chemistry.[8,21]

A HB interaction is represented as X–H···Y in which X and Y are usually electronegative atoms defined as the HB donor and HB acceptor, respectively. The HB may be viewed as a donor–acceptor orbital interaction where a lone pair of electrons from the atom Y is donated into the antibonding σ* X–H orbital. As the strength of a HB will depend on the intrinsic abilities of the donor and acceptor orbitals, it is generally recognized that the larger the electronegativity of the X and Y atoms, the stronger the HB will be and thus, the HB distance (H···Y) is smaller. When comparing the O–H···N and N–H···N HBs, for example, as O (3.5) is more electronegative than N (3.0), the antibonding σ* O–H orbital has a larger coefficient on the electropositive H atom increasing the orbital interaction with the electron donor N. In the same way, as O is more electronegative, the H atom of the O–H bond will be more positively charged which also increases the dipole–dipole interaction with the N atom. These two reasons explain why the O–H···N

interaction is stronger than N–H···N. It is important to note, however, that the strength of a HB does not solely rely on electronegativities but also depend on orbital overlap, directionality and the energy of the donor and acceptor orbitals.

Although the classical picture of a HB involves highly electronegative atoms such as F, O, and N, it soon became clear that X and Y do not always have to be electronegative atoms as long as attractive interactions could be established in between the H and the Y atom ($^{\delta-}$X–H$^{\delta+\cdots}$Y$^{\delta-}$).[21] Thus, there are many other important non-classical HBs such as those involving less electronegative atoms as the chalcogens S and Se, the so-called sulfur centered HBs (SCHBs), and non-typical groups such as aliphatic donors (C–H···Y) and π-acceptors (X–H···π).[10,21] Although these non-classical interactions may be weaker in strength, they have been shown to be key to the stabilization of many systems.[10,21,26] Below, a brief description of the non-classical interactions observed in this thesis is provided.

1.2.2 Non-Classical Hydrogen Bonds

While HBs formed with O (3.5) and N (3.0) have been more widely studied, weaker contacts, such as sulfur HBs, have been dismissed as weak and dispersive in nature due to the lower electronegativity of S (2.6).[10,27–29] However, S has been shown to form a variety of HBs acting as both acceptor (as O–H···S, N–H···S) and donor (as S–H···O, S–H···S, S–H···π) and these HBs can be as strong as conventional HBs.[9,10] Examples include the amide N–H···S HB found in cysteine and methionine containing peptides which was shown to be as strong as the interaction formed with its O counterpart and also the C–H···S interaction recently proved to have a binding energy comparable to that found for O–H···S and slightly smaller than that of O–H···O.[27,29,30] In

fact, this type of interaction is ubiquitous in biological environments,[27] but when it comes to the analysis and identification of sulfur HBs in protein and crystal structure databases, many structural searches result in incorrect and/or incomplete interpretations.[29] This is because the codes are parameterized using geometric information from traditional HBs such as those formed with O and N (e.g. HB distances up to 2.4 Å) and sulfur interactions have unique geometric parameters such as distances as long as 2.8 Å. The tendency to overlook the importance of these interactions in biology can quite simply be a consequence of outdated criteria in the prediction and detection tools for describing non-conventional HBs.

It is therefore of great interest to study interactions involving sulfur containing compounds in isolation so that a deeper knowledge about their geometric characteristics, nature and strength could be achieved to overcome the lack of experimental data. Although significant progress on classical HBs has been achieved through crystallography, in the last decade, most advancements in the description of sulfur HBs were achieved using gas phase techniques such as IR-UV double resonance and rotational spectroscopy.[10,27] These techniques have the advantage of working in a collision-free environment in isolation of solvent and crystal packing effects. As recently reviewed by Biswal,[31] many more systems still need to be studied in order to better understand the many facets of sulfur HBs.

Apart from interactions involving less electronegative atoms such as S and Se, non-covalent interactions of the type C–H···Y and X–H···π have also proven important.[21] The C–H bond acts as a HB donor and this group can be activated by other atoms or groups bound to it to promote ionization or partial ionization of the H atom making it susceptible to interact with other HB acceptors. Although weaker, the C–H···O interaction, for example, has been shown to contribute to the stabilization of molecular complexes formed with cyclic structures and many other

systems.[21,32] On the other hand, π-bonds are electron rich and can replace the electronegative atoms F, O and N as HB acceptors. A typical example is the complex between benzene and water formed by a O–H···π HB.[33]

1.3 Outline

In this thesis, the conformational landscape of prototypical monomers and molecular aggregates (water complexes) are investigated using rotational spectroscopy in the microwave region aided by quantum chemistry calculations. The focus of the work presented here is to elucidate the system's most stable geometries as well as the stereoelectronic effects governing their conformational preferences at the molecular level. Insights on molecular geometries, internal dynamics, microsolvation (for the water complexes), and on the parameters associated with the non-covalent interactions are of particular interest.

A description of rotational spectroscopy and the two microwave spectrometers used to collect the spectra reported in the thesis is provided in Chapter 2. In Chapter 3, an introduction to the computational methods used, that are essential to predict the molecule's geometries and relative energies to guide the spectral assignments and investigate the stereoelectronic effects behind the stability of the observed conformers, is given.

Next, Chapter 4 (mercaptopropionic acid, MPA) and Chapter 5 (methyl 3-mercaptopropionate, MP) report on the study of two model sulfur containing compounds featuring an intramolecular S–H···O=C HB which is a biologically relevant interaction that has not been studied in detail before. In Chapter 4 and Chapter 5, the sulfur HB is shown to be dominant in stabilizing the global minimum geometry of MPA and MP as confirmed by the spectral

assignments. With experimental information from the singly substituted ^{13}C and ^{34}S minor isotopic species of MP (Chapter 5), the geometric parameters associated with the sulfur HB were derived providing experimental evidence for the HB distance and angle. Those are then compared with literature data available for its oxygen counterpart and discussed in detail.

While one way to study interactions is to evaluate their presence in monomer structures as done in Chapter 4 and Chapter 5, another important alternative is to study the nature, strength, and geometric parameters of HBs in molecular aggregates. The advantage is that the interaction energy between the monomers that form the complexes can be decomposed computationally into four physically meaningful components (electrostatic, dispersion, induction, and exchange-repulsion) revealing the nature of the interaction. It is usually of interest to compare the binding characteristics in series of analogous clusters to determine the influence of different groups in the interaction energies (e.g. effect of O to S chalcogen substitution). In this sense, in the remaining chapters, the attention of the thesis is turned to the investigation of weakly bound complexes, in particular water clusters.

In Chapter 6, the microsolvation of the four-membered rings trimethylene oxide (TMO) and sulfide (TMS) with one and two water molecules is reported. A strong preference for water to bind primarily to the heteroatoms S and O is revealed, but also secondary contacts are observed and discussed to be important for the stabilization of the systems, especially for the dihydrates. Additionally, the influence of water in the ring structures is analyzed as these rings are flexible and undergo large amplitude motions which can result in different binding characteristics with a partner molecule.

Following this, in Chapter 7, the thiophene–water complex is investigated to evaluate the large amplitude motions and the preferred binding sites of water in an aromatic ring that contains

both the S atom and the π-electron cloud. The thiophene–water complex is shown to be very dynamic with its ground state structure being highly averaged over a barrierless rocking motion of water which interconverts two equivalent forms of the global minimum geometry. To provide insights on the position of the water subunit within the complex, observation of transitions corresponding to the singly substituted ^{18}O minor isotopologues were crucial. With an understanding of the large amplitude motions and molecular structure, the non-covalent interactions stabilizing the complex were analyzed and while the absence of the π-electrons favours interactions directly with S, as in TMS–w (Chapter 6), in thiophene–water, the water molecule prefers to bind first to the aromatic ring via an O–H···π HB, with the S···H–O contact playing a secondary role. This result is surprisingly different to what has been previously reported for the oxygen and nitrogen counterparts of thiophene. The reasons behind the differences in the molecular geometries of these complexes are discussed in detail in Chapter 7.

Chapter 8 and Chapter 9 report on the conformational study of an amine containing compound, *N*-allylmethylamine (AMA), and its monohydrated complex, respectively. The interaction between AMA and water is essential to model the role of the N atom of amines as a HB donor. However, as the monomer had not been studied before, it was essential to first understand its rotational fingerprints (Chapter 8) prior to investigating its water complex. The AMA monomer showed a surprisingly rich conformational landscape featuring four geometries experimentally which are stabilized by a subtle balance of attractive and repulsive forces. Upon introduction of a water molecule (Chapter 9), the complexes are shown to be stabilized by both N···H–O and C–H···O HBs. This work also allowed the evaluation of the effect of water in the conformational landscape of AMA in that water was shown to alter the equilibrium of AMA to some extent with the effects being more pronounced for the higher energy conformations. Finally,

Chapter 10 provides summary of the key findings of the thesis, the impact of the results presented and how this research could be further extended.

1.4 References

(1) Eliel, Ernest L.; Wilen, S. H. *Stereochemistry of Organic Compounds*; John Wiley & Sons: New York, 1994.

(2) Tormena, C. F. Conformational Analysis of Small Molecules: NMR and Quantum Mechanics Calculations. *Prog. Nucl. Magn. Reson. Spectrosc.* **2016**, *96*, 73–88.

(3) *The Nobel Prize Home Page*: https://www.nobelprize.org/prizes/chemistry/1969/summary/ (accessed on May 20, 2021).

(4) Barton, D. H. The Conformation of the Steroid Nucleus. *Experientia* **1994**, *50* (4), 390–394.

(5) Hassel, O.; Viervoll, H.; Sillén, L. G.; Linnasalmi, A.; Laukkanen, P. Electron Diffraction Investigations of Molecular Structures. II. Results Obtained by the Rotating Sector Method. *Acta Chem. Scand.* **1947**, *1*, 149–168.

(6) Hassel, O.; Ottar, B.; Roald, B.; Linnasalmi, A.; Laukkanen, P. The Structure of Molecules Containing Cyclohexane or Pyranose Rings. *Acta Chem. Scand.* **1947**, *1*, 929–943.

(7) Johnson, E. R.; Keinan, S.; Mori-Sánchez, P.; Contreras-García, J.; Cohen, A. J.; Yang, W. Revealing Noncovalent Interactions. *J. Am. Chem. Soc.* **2010**, *132* (18), 6498–6506.

(8) Grabowski, S. J. What Is the Covalency of Hydrogen Bonding? *Chem. Rev.* **2011**, *111* (4), 2597–2625.

(9) Juanes, M.; Saragi, R. T.; Caminati, W.; Lesarri, A. The Hydrogen Bond and Beyond: Perspectives for Rotational Investigations of Non-Covalent Interactions. *Chem. – A Eur. J.*

2019, *25* (49), 11402–11411.

(10) Scheiner, S. *Noncovalent Forces*, 1st ed.; Scheiner, S., Ed.; Springer International Publishing: Switzerland, 2015.

(11) Brown, G. G.; Dian, B. C.; Douglass, K. O.; Geyer, S. M.; Shipman, S. T.; Pate, B. H. A Broadband Fourier Transform Microwave Spectrometer Based on Chirped Pulse Excitation. *Rev. Sci. Instrum.* **2008**, *79* (5), 053103.

(12) Domingos, S. R.; Pérez, C.; Medcraft, C.; Pinacho, P.; Schnell, M. Flexibility Unleashed in Acyclic Monoterpenes: Conformational Space of Citronellal Revealed by Broadband Rotational Spectroscopy. *Phys. Chem. Chem. Phys.* **2016**, *18* (25), 16682–16689.

(13) Xie, F.; Seifert, N. A.; Heger, M.; Thomas, J.; Jäger, W.; Xu, Y. The Rich Conformational Landscape of Perillyl Alcohol Revealed by Broadband Rotational Spectroscopy and Theoretical Modelling. *Phys. Chem. Chem. Phys.* **2019**, *21* (28), 15408–15416.

(14) Murugachandran, S. I.; Tang, J.; Peña, I.; Loru, D.; Sanz, M. E. New Insights into Secondary Organic Aerosol Formation: Water Binding to Limonene. *J. Phys. Chem. Lett.* **2021**, *12* (3), 1081–1086.

(15) Xie, F.; Seifert, N. A.; Jäger, W.; Xu, Y. Conformational Panorama and Chirality Controlled Structure–Energy Relationship in a Chiral Carboxylic Acid Dimer. *Angew. Chemie Int. Ed.* **2020**, *59* (36), 15703–15710.

(16) Alabugin, I. V. *Stereoelectronic Effects: A Bridge between Structure and Reactivity*; John Wiley & Sons, Ltd: Chichester, 2016.

(17) Cavallo, G.; Metrangolo, P.; Milani, R.; Pilati, T.; Priimagi, A.; Resnati, G.; Terraneo, G. The Halogen Bond. *Chem. Rev.* **2016**, *116* (4), 2478–2601.

(18) Vogel, L.; Wonner, P.; Huber, S. M. Chalcogen Bonding: An Overview. *Angew. Chemie*

Int. Ed. **2018**.

(19) Scheiner, S.; Lu, J. Halogen, Chalcogen, and Pnicogen Bonding Involving Hypervalent Atoms. *Chem. - A Eur. J.* **2018**, *24* (32), 8167–8177.

(20) Grabowski, S. J. Pnicogen and Tetrel Bonds—Tetrahedral Lewis Acid Centres. *Struct. Chem.* **2019**, *30* (4), 1141–1152.

(21) Karas, L. J.; Wu, C.; Das, R.; Wu, J. I. Hydrogen Bond Design Principles. *WIREs Comput. Mol. Sci.* **2020**, *10* (6), 1–15.

(22) Latimer, W. M.; Rodebush, W. H. Polarity and Ionization From the Standpoint of the Lewis Theory of Valence. *J. Am. Chem. Soc.* **1920**, *42* (7), 1419–1433.

(23) Watson, J. D.; Crick, F. H. C. Molecular Structure of Nucleic Acids: A Structure for Deoxyribose Nucleic Acid. *Nature* **1953**, *171* (4356), 737–738.

(24) Pauling, L.; Corey, R. B.; Branson, H. R. The Structure of Proteins: Two Hydrogen-Bonded Helical Configurations of the Polypeptide Chain. *Proc. Natl. Acad. Sci.* **1951**, *37* (4), 205–211.

(25) Pauling, L.; Corey, R. B. The Pleated Sheet, A New Layer Configuration of Polypeptide Chains. *Proc. Natl. Acad. Sci.* **1951**, *37* (5), 251–256.

(26) Zhou, P.; Tian, F.; Lv, F.; Shang, Z. Geometric Characteristics of Hydrogen Bonds Involving Sulfur Atoms in Proteins. *Proteins Struct. Funct. Bioinforma.* **2009**, *76* (1), 151–163.

(27) Chand, A.; Sahoo, D. K.; Rana, A.; Jena, S.; Biswal, H. S. The Prodigious Hydrogen Bonds with Sulfur and Selenium in Molecular Assemblies, Structural Biology, and Functional Materials. *Acc. Chem. Res.* **2020**, *53* (8), 1580–1592.

(28) Juanes, M.; Lesarri, A.; Pinacho, R.; Charro, E.; Rubio, J. E.; Enríquez, L.; Jaraíz, M. Sulfur

Hydrogen Bonding in Isolated Monohydrates: Furfuryl Mercaptan versus Furfuryl Alcohol. *Chem. - A Eur. J.* **2018**, *24* (25), 6564–6571.

(29) van Bergen, L. A. H.; Alonso, M.; Palló, A.; Nilsson, L.; De Proft, F.; Messens, J. Revisiting Sulfur H-Bonds in Proteins: The Example of Peroxiredoxin AhpE. *Sci. Rep.* **2016**, *6* (1), 30369.

(30) Rao Mundlapati, V.; Ghosh, S.; Bhattacherjee, A.; Tiwari, P.; Biswal, H. S.; Mundlapati, V. R.; Ghosh, S.; Bhattacherjee, A.; Tiwari, P.; Biswal, H. S. Critical Assessment of the Strength of Hydrogen Bonds between the Sulfur Atom of Methionine/Cysteine and Backbone Amides in Proteins. *J. Phys. Chem. Lett.* **2015**, *6* (8), 1385–1389.

(31) Biswal H. S., Hydrogen Bonds Involving Sulfur: New Insights from ab Initio Calculations and Gas Phase Laser Spectroscopy, In *Noncovalent Forces*, *Challenges and Advances in Computational Chemistry and Physics*, 1st ed.; Springer International: Switzerland, 2015, 2, pp. 15–45.

(32) Wang, J.; Spada, L.; Chen, J.; Gao, S.; Alessandrini, S.; Feng, G.; Puzzarini, C.; Gou, Q.; Grabow, J.; Barone, V. The Unexplored World of Cycloalkene–Water Complexes: Primary and Assisting Interactions Unraveled by Experimental and Computational Spectroscopy. *Angew. Chemie Int. Ed.* **2019**, *58* (39), 13935–13941.

(33) Li, S.; Cooper, V. R.; Thonhauser, T.; Puzder, A.; Langreth, D. C. A Density Functional Theory Study of the Benzene−Water Complex. *J. Phys. Chem. A* **2008**, *112* (38), 9031–9036.

Chapter 2. Microwave Rotational Spectroscopy

Microwave spectroscopy measures the rotational transitions of gaseous molecules in the cm-wave region of the electromagnetic spectrum.[1,2] The main selection rule for microwave spectroscopy is that only species that have a permanent electric dipole moment exhibit a microwave (or pure rotational) spectrum. When the molecular spectrum is recorded, a collection of lines, corresponding to transition frequencies associated with energy differences between rotational energy levels, are observed. By analyzing the rotational fingerprints in detail, accurate spectroscopic parameters such as rotational and centrifugal distortion constants can be determined whose interpretation leads to key insights about the studied molecular systems. Since rotational constants are inversely proportional to the molecular moments of inertia, microwave spectroscopy is a powerful technique to determine experimental molecular structures and to identify the different conformers of flexible molecules and molecular aggregates in the gas phase. Occasionally, observed spectral transitions exhibit splitting patterns as a consequence of intrinsic molecular dynamics or interactions within the molecules. Analysis of these patterns leads to additional detailed information about energy barriers to internal motions and the local environment surrounding a quadrupolar nucleus ($I > 1/2$, for example), respectively. Laboratory rotational spectroscopic studies are also important to assist in the discovery of molecules in interstellar space since they are often identified by their rotational patterns in the cm or mm-wave spectrum collected from different astronomical sources.

Although the microwave radiation corresponds to a frequency range in between 3–300 GHz, in this thesis, the rotational spectra of the studied molecular systems were investigated from 4–26 GHz which is the frequency range in which the two custom-built Fourier transform

microwave (FTMW) spectrometers available at the University of Manitoba operate. In this Chapter 2, theoretical descriptions of rotational spectroscopy and the microwave instrumentation, necessary for understanding of the data presented in this thesis, is provided.

2.1 Principles of Rotational Spectroscopy

This following section was written based on three textbooks[3–5] on molecular and rotational spectroscopy. The reader interested in more detailed information can refer to these references.

2.1.1 Rigid Rotor Approximation

The theoretical principles of many molecular spectroscopic techniques arise from obtaining the quantized energy levels of the molecular system by solving the time-independent Schrödinger equation from quantum mechanics,

$$\hat{H}\Psi = E\Psi, \tag{2-1}$$

in which $\hat{H}$ is the Hamiltonian operator, Ψ is the eigenfunction and E is the corresponding energy eigenvalue of the quantum system. For the rotation of molecules in their electronic and vibrational ground states, the operator in Equation (2-1) is known as the rotational Hamiltonian operator. Considering the simple case for the rotation of a rigid linear molecule, in which the bond lengths interconnecting the atoms are considered fixed and internal vibrations are excluded, the rotational Hamiltonian operator can be expressed using the rigid rotor approximation model from classical mechanics as

$$\widehat{H} = \frac{1}{2} I_a \omega_a^2 + \frac{1}{2} I_b \omega_b^2 + \frac{1}{2} I_c \omega_c^2$$

$$\widehat{H} = \frac{\hat{J}_a^2}{2I_a} + \frac{\hat{J}_b^2}{2I_b} + \frac{\hat{J}_c^2}{2I_c}$$

$$\widehat{H} = \frac{\hat{J}^2}{2I} \tag{2-2}$$

In equation (2-2), $\hat{J}$ is the total rotational angular momentum operator defined by the sum of its components $\hat{J}_a + \hat{J}_b + \hat{J}_c = I_a\omega_a + I_b\omega_b + I_c\omega_c$ and I is the moment of inertia tensor. I_a, I_b and I_c and ω_a, ω_b and ω_c are the moments of inertia and angular velocity components, respectively, associated with the three mutually perpendicular axes (known as a, b and c) composing the principal inertial axis system located at the center of mass of the rotating body. The moment of inertia associated with each rotating axis (I_a, I_b or I_c) can be further described as $\sum_i m_i r_i$, in which m_i is the atomic mass and r_i is the internuclear distance between an atom i from that specific rotating axis. In a molecule, the classification of the axes in the principal axis system follows a labeling scheme to satisfy the $I_a \leq I_b \leq I_c$ relationship. This means that the a-axis, with the smallest moment of inertia I_a, will always be closer to the heaviest atoms of the molecular system. Based on symmetry and on the components of the moment of inertia, molecules are classified into four different categories:

1. Linear molecules ($I_a = 0,\ I_b = I_c$) such as HCN.
2. Spherical tops ($I_a = I_b = I_c$) such as SF_6.
3. Symmetric tops ($I_a < I_b = I_c$ for a prolate top such as CH_3Cl and $I_a = I_b < I_c$ for an oblate top such as BF_3).

4. Asymmetric tops ($I_a < I_b < I_c$) such as H_2O. Asymmetric top molecules can also be classified as near prolate and near oblate if $I_a < I_b \approx I_c$ and $I_a \approx I_b < I_c$, respectively.

All molecular systems studied in this thesis are asymmetric top rotors where the three principal moments of inertia are different and non-zero. With the classification of molecules introduced, we can now look at the possible solutions of the Schrödinger equation (2-1) for each case which will lead to insights on their rotational energy levels.

2.1.2 The Simplest Case: The Rigid Diatomic Molecule

Starting with the simple case of a rigid linear molecule, in which $I_a = 0$ and $I_b = I_c$, by including the rotational Hamiltonian operator from equation (2-2) into the Schrödinger equation (2-1), the energy eigenvalue of the rotational energy levels, represented by its term value $F(J)$ can be obtained as

$$F(J) = \frac{h^2}{8\pi^2 I_b} J(J+1) = BJ(J+1) \tag{2-3}$$

in which h is Planck's constant, I_b is the moment of inertia along the *b*-axis defined above, J is the rotational quantum number, which can assume any positive integer value starting from zero and is used to label the different rotational energy levels, and $B = (\frac{h^2}{8\pi^2 I_b})$ is known as the rotational constant (in Joules) associated with the principal *b*-axis. Note that since in a linear molecule I_b and I_c are equal, only one unique rotational constant is needed to describe the molecular energy levels. By convention, the representations following those of the principal *b*-axis are used. In

spectroscopy, rotational constants are usually reported in units of frequency (in MHz) for simplicity, following the equation:

$$B(\text{MHz}) = \frac{B(\text{Joules})}{h} = \frac{h}{8\pi^2 I_b} \times 10^{-6} \tag{2-4}$$

From equation (2-4), the inversely proportional relationship between the rotational constant and the moment of inertia is mathematically shown which indicates that the rotational energy levels and consequently the rotational transition frequencies (introduced in detail below) are sensitive to the molecular geometry. This means that each molecular species (molecules, isotopes, conformers), which has distinct moments of inertia, will have a unique rotational fingerprint. When a rotational spectrum is recorded, the observed frequency (or line position) for a given transition is a result of the energy difference between a lower (represented by the quantum number *J*' or simply *J*) and an upper (represented by the quantum number *J*' or *J*+1) energy level which follows the $\Delta J = \pm 1$ selection rule. The transition frequency (ν) is given by:

$$\nu_{J' \rightarrow J''} = F(J') - F(J'') = 2B(J+1) \tag{2-5}$$

For the rigid linear molecule, equation (2-5) shows that the first transition (written as emission here) with *J*'→*J*'' = 1→0 occurs at 2B and the subsequent transitions are spaced out by multiples of 2B. The transitions 2→1 and 3→2, for example, will have frequencies corresponding to 4B and 6B, respectively. Since the transition frequencies can be measured experimentally and the *J* quantum numbers are known, the rotational constant B can be determined which is related to the molecular geometry through the moment of inertia as shown in equation (2-4). The intensity of the rotational transitions—for any molecular system not only for rigid linear molecules—is proportional to both the magnitude of the electric dipole moment components, and to the population of the rotational energy levels. This principle is also valid for the study of molecules containing several conformers in which the dominant species in the spectrum often resembles the

pattern of the most populated conformer or those possessing the largest dipole moment components along any of the three principal inertial axes (*a*, *b* and *c*).

2.1.3 Symmetric and Asymmetric Top Molecules

While in a linear molecule such as the rigid diatomic rotor (2.1.2), there is only one unique (non-zero) moment of inertia related to the angular momentum and energy for rotation about the *b*-axis (by convention), in a symmetric top, two terms are needed in the Hamiltonian operator: I_a and I_b (prolate) or I_b and I_c (oblate). The solutions to the Schrödinger equation are a set of functions that depend on the total rotational angular momentum (quantum number *J*) and its projection (quantum *K*) onto the highest symmetry axis. To simplify the notation, it is common to provide a subscript on *K* to distinguish whether the top is prolate (K_a) or oblate (K_c) in the term value equations that define the energy levels of symmetric top molecules:

$$F(J,K) = BJ(J+1) + (A-B){K_a}^2 \quad \text{prolate} \tag{2-6}$$

$$F(J,K) = BJ(J+1) + (C-B){K_c}^2 \quad \text{oblate} \tag{2-7}$$

The new quantum number *K* may take values $K = 0, 1, 2, \ldots, J$. Since *K* cannot be greater than *J*, all levels with $K > 0$ are two-fold degenerate which can be interpreted as a consequence of the energy associated with a clockwise and a counter-clockwise rotation about an axis being the same. For $K = 0$, there is no *K*-degeneracy since there is no angular momentum about the *a*- or *c*-axis. In order for rotational transitions to be allowed in a symmetric rotor, in addition to the presence of a permanent dipole moment and $\Delta J = \pm 1$, the $\Delta K = 0$ selection rule must be satisfied. It is interesting to note that as $A \geq B \geq C$ (since $I_a \leq I_b \leq I_c$) by definition, the energy levels with

a specific J rotational quantum number will increase in energy with an increase in the K values in a prolate top (2-6), while they will decrease in energy in an oblate top molecule (2-7). The transition frequency expression for a symmetric top molecule is similar to the rigid linear rotor case as

$$\nu_{J',K\rightarrow J'',K} = F(J',K) - F(J'',K) = 2B(J+1). \quad (2\text{-}8)$$

As there are no exact solutions to describe the rotational energy levels of asymmetric tops ($I_a \neq I_b \neq I_c$), the analysis of their rotational spectra is based on solutions obtained for the prolate and oblate symmetric top limits. The rotational energy level diagram for an asymmetric top molecule is shown in Figure 2.1. The energy states are identified using the J rotational quantum number followed by the two labels K_a and K_c from the prolate and oblate limits, respectively, so that each level is identified as J_{KaKc}.

The selection rule $\Delta J = 0, \pm 1$ is valid for an asymmetric molecule, but since there are now three non-equivalent rotation axes (a, b and c) along which three components of the dipole moment exist (μ_a, μ_b and μ_c), transitions corresponding to each of these axes, known as a-, b- and c-type transitions, follow additional selection rules associated with the K_a and K_c labels:

1. a-type transitions ($\mu_a \neq 0$): $\Delta K_a = 0$ ($\pm 2, \pm 4, \ldots$) and $\Delta K_c = \pm 1$ ($\pm 3, \pm 5, \ldots$).
2. b-type transitions ($\mu_b \neq 0$): $\Delta K_a = \pm 1$ ($\pm 3, \pm 5, \ldots$) and $\Delta K_c = \pm 1$ ($\pm 3, \pm 5, \ldots$).
3. c-type transitions ($\mu_c \neq 0$): $\Delta K_a = \pm 1$ ($\pm 3, \pm 5, \ldots$) and $\Delta K_c = 0$ ($\pm 2, \pm 4, \ldots$).

Examples of a- ($J'_{Ka'Kc'} \rightarrow J''_{Ka''Kc''} = 1_{01} \rightarrow 0_{00}$), b- ($1_{11} \rightarrow 0_{00}$) and c-type ($1_{10} \rightarrow 0_{00}$) transitions are provided in Figure 2.1. The transitions can be identified by the red, blue and green arrows, respectively, in the center of the energy level diagram.

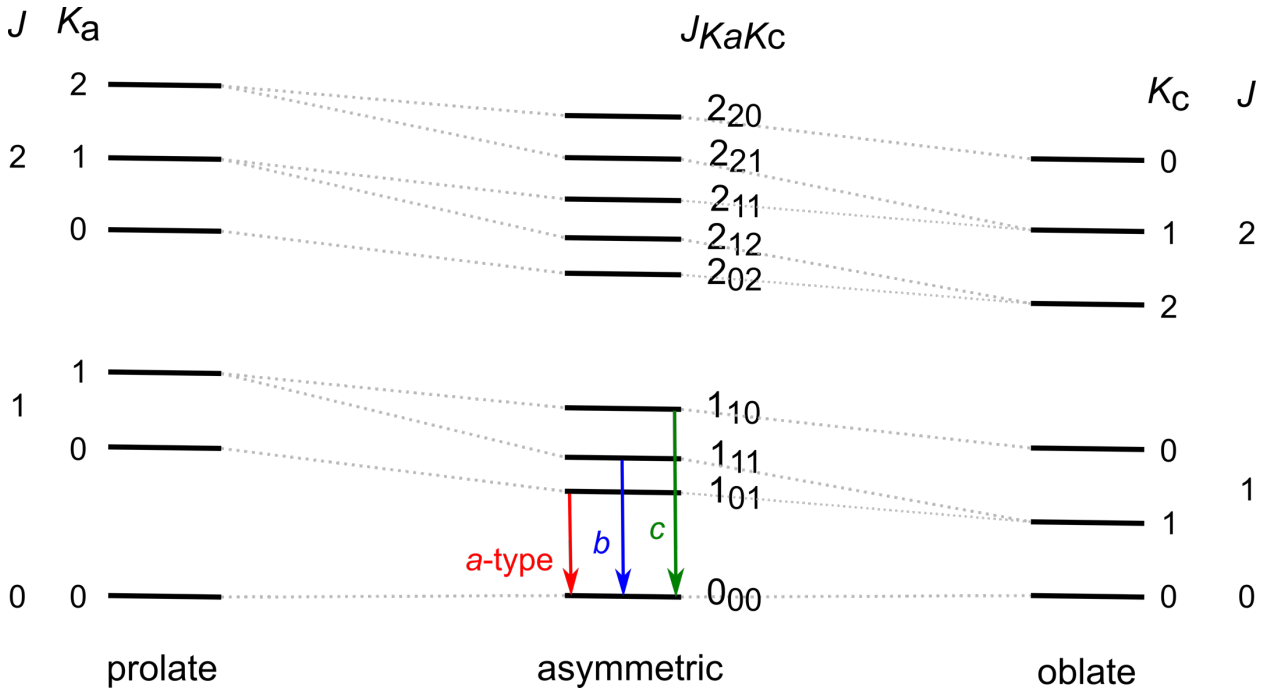

Figure 2.1 Energy level diagram for an asymmetric top (center) originated by combining solutions for the prolate (left) and oblate (right) top limits. A sample of *a*-, *b*- and *c*-type rotational transitions (shown as emission) between the energy levels with $J'= 1$ and $J''= 0$ are depicted in red, blue and green, respectively. The energy level spacings are not to scale in this representation.

It is important to highlight that asymmetric top molecules do not always display the three types of transitions in the rotational spectrum since for some molecules, the dipole component along a specific axis may be zero, or close to zero. As long as one of the three dipole components is non-zero, the molecule can have a rotational spectrum. Also, the stronger the dipole component along a given axis, the more likely that transitions related to that rotational axis will dominate the rotational spectrum.

2.1.4 Centrifugal Distortion

While the rigid rotor model is a good approximation to describe rigid molecules and, in particular, energy levels with low *J* rotational quantum numbers, in reality, molecules are not rigid bodies. When a diatomic molecule rotates, for example, distortions in the internuclear atomic distances occur as a consequence of centrifugal forces. Centrifugal distortion becomes more evident at higher energy levels in which the atomic distances increase as the speed of rotation increases. This results in a decrease in the energy difference between the rotational states as *J* increases. As a result, correction terms need to be included in the rotational energy level equations to account for distortion effects. For a diatomic molecule, for example, equation (2-3) becomes

$$F(J) = BJ(J+1) - DJ^2(J+1)^2 \tag{2-9}$$

in which *D* is known as the centrifugal distortion constant which is related to the vibrational frequency ω within the harmonic oscillator approximation:

$$D = \frac{4B^3}{\omega^2} \tag{2-10}$$

Accordingly, the expression for the frequency (ν) of a given transition is

$$\nu_{J+1\rightarrow J} = F(J') - F(J'') = 2B(J+1) - 4\mathrm{D}(\mathrm{J}+1)^3 \tag{2-11}$$

The distortion constant *D* is always positive for a diatomic molecule and, considering equation (2-9), the term value *F*(*J*) decreases with any non-zero value of *D* which results in the decrease of the energy gap between high *J* rotational energy levels. Consequently, the transition frequency also decreases by increasing *J* as given by the expression in equation (2-11). For non-diatomic molecules, such as the asymmetric top molecules studied in this thesis, additional centrifugal distortion constants are needed to account for all bond and angular distortions. Generally, five quartic centrifugal distortion constants (D_J, D_{JK}, D_K, d_1 and d_2) for example from

one sample Hamiltonian,[6] are sufficient to describe distortions in the systems studied in the frequency range used in this work. If needed, higher order terms such as sextic or octic distortion constants can be included and those are usually necessary in studies in higher frequency regions of the electromagnetic spectrum where transitions with higher *J* quantum numbers are observed.

2.2 Perturbations in the Rotational Spectrum

Spectral rotational transitions often show splitting patterns, also known as fine structure, as a consequence of large amplitude internal motions associated with the interconversion between equivalent configurations of the molecule. Typical examples of large amplitude motions include the inversion umbrella motion in ammonia (NH_3)[7] and internal rotations of the methyl group in many organic molecules. These motions lead to splittings of the rotational energy levels and consequently, fine structure related to quantum mechanical tunneling is observed in the rotational spectrum. Generally, the smaller the size of the spectral splitting, the higher is the energy barrier to the corresponding internal motion. By employing the use of appropriate effective Hamiltonians, the spectral splittings can be analyzed and important parameters related to the internal motion can be derived such as energy barriers for interconversion.[2] In this thesis, tunneling splittings associated with methyl internal rotation, torsion of the thiol (SH) group and internal dynamics of water (among others) have been observed and will be discussed in detail in the specific chapters. Apart from fine structure, rotational transitions may also show hyperfine splittings as a result of magnetic or electric interactions. A typical example is the nuclear quadrupole hyperfine structure which is observed for molecules containing a quadrupolar nucleus such as *N*-allylmethylamine

(Chapter 8) that contains a ^{14}N nucleus. In the next section, a brief description on nuclear quadrupole hyperfine splittings is provided.

2.3 Nuclear Quadrupole Hyperfine Splitting

The presence of an atom with a nuclear spin higher than ½ in a molecule leads to a characteristic splitting in the molecular rotational spectrum, known as nuclear quadrupole hyperfine structure. For the systems of this thesis, hyperfine splittings were observed in the spectrum of molecules containing nitrogen as mentioned above. This is because the most naturally abundant nitrogen isotope is the ^{14}N nucleus with a nuclear spin $I = 1$ giving rise to a non-spherical distribution of the nuclear charge which interacts with the electric field gradient generated by the surrounding electrons at the site of the nucleus. The nuclear spin angular momentum of the ^{14}N nucleus couples with the rotational angular momentum resulting in the splitting of the rotational energy levels. To describe the energy states for molecules containing a quadrupolar nucleus, an additional quantum number F is necessary. For a molecule with one quadrupolar nucleus, such as the compounds studied here, the quantum number F can adopt values of $J + I$, $J + I - 1$, $J + I - 2$, ... , $| J - I |$. The selection rules for hyperfine transitions are $\Delta F = 0, \pm 1$. The $J_{KaKc} = 2_{02}$ energy level of an asymmetric molecule, for example, containing a quadrupolar ^{14}N nucleus will split into three energy levels with F quantum numbers of 1, 2 and 3. Thus, the energy levels are now labeled as J_{KaKc} F.

2.4 Fourier Transform Microwave (FTMW) Spectroscopy Instrumentation

Once a theoretical description of the rotational energy levels and selection rules for dipole-allowed rotational transitions is introduced, it is now time to understand how the rotational spectrum is collected in the laboratory. Two custom-built Fourier transform microwave (FTMW) spectrometers, available at the University of Manitoba in the van Wijngaarden research group, were used to record the pure rotational spectra presented in this thesis. The instruments are the narrowband cavity-based Balle-Flygare (BF) type FTMW and the broadband chirped-pulse (CP) FTMW spectrometer, both of which have been described in detail previously.[8,9] Both instruments have some overlap in the underlying operational principle, however, instrumental differences in the microwave excitation and detection scheme in particular provide each of them with unique features that when combined become a powerful tool to prove the electronic structure of a range of molecular systems. These will be described in detail below.

The workflow in a typical MW spectroscopy project involves first the collection of a broadband CP-FTMW spectrum (usually from 8 to 18 GHz) to make preliminary assignations to transitions belonging to the different molecular species of the system. Once the frequencies of the most intense rotational transitions are known, final measurements are performed using the BF-FTMW instrument (from 4–26 GHz), which features higher resolution and sensitivity, to measure a broader range of transitions including those from minor isotopologues. The high resolution of the cavity-based BF instrument also allows narrow splittings such as those associated with the ^{14}N hyperfine structure and tunneling motions from internal dynamics to be completely resolved.

2.4.1 Sample Preparation and Injection

In both BF-FTMW and CP-FTMW experiments, the molecular targets are probed in the gas phase inside a high vacuum chamber (P ~ 10^{-7} kPa). For injection inside the chamber, a gas mixture containing a small amount of the sample (<1%) in an inert buffer gas, such as neon, helium or argon (stagnation pressure of ~100 kPa) needs to be prepared first at room temperature. The compounds studied in this thesis are all liquids at room temperature. For volatile samples with high vapour pressure and low boiling points, such as trimethylene oxide and sulfide (Chapter 6), thiophene (Chapter 7) and *N*-allylmethylamine (Chapter 8), their vapours can be directly collected in a gas cylinder and mixed with the buffer gas. For non-volatile compounds with relatively low vapour pressure and high boiling points, such as 3-mercaptopropionic acid (Chapter 4) and methyl 3-mercaptopropionate (Chapter 5), an aliquot of the liquid is transferred to a glass bubbler through which the inert gas can be passed through serving as a carrier to deliver the sample into the spectrometers. For the formation of water adducts, the mixture containing the monomer sample and the inert gas is bubbled through an additional reservoir containing water external to the chamber.

The expansion of the gas mixture into the high vacuum chambers of the instruments via a pulsed solenoid valve (circular orifice of 1 mm diameter) results in an isolated collision-free environment, known as the molecular beam or supersonic jet, where the sample is cooled down to a rotational temperature of a few Kelvin due to collisions of the molecules with the inert gas at the beginning of the expansion.[10,11] The low temperature of the molecular beam increases the population of the lowest rotational energy states and consequently, the spectrum in the jet is simplified in comparison to that collected at room temperature. In the latter, many states are usually

populated allowing even rotational transitions within vibrationally excited states to be observed. Peak broadening due to collisions is also decreased in the jet since the molecules are travelling in the same direction with the same velocity without further collision.[12]

2.4.2 Chirped-Pulse FTMW Spectrometer

The broadband CP-FTMW spectrometer works in the range of 8–18 GHz and follows the design of the first broadband microwave spectrometer developed by Professor Brooks Pate and co-workers[13] in 2008. The main advantage of the CP-FTMW instrument (Figure 2.2) is the use of microwave radiation from a microwave synthesizer coupled with a rapid linear frequency sweep (or chirp) generated by an arbitrary waveform generator (AWG) that allows the simultaneous excitation of transitions up to a 6 GHz frequency window in a single data acquisition. For the purpose of this thesis, most of the broadband spectra were collected in segments of 2 GHz each in which the chirped pulse sweeps through ± 1 GHz (ν_W) from a selected center frequency (ν_o) in 1–5 μs. The resulting excitation chirped pulse is amplified by a 20 W solid state amplifier before it is introduced into the chamber to provide sufficient excitation power in the absence of the resonant cavity. After the gas sample is inserted into the chamber by a pulsed nozzle which in this instrument is perpendicular to the excitation and detection axis, the chirped microwave pulse is broadcast in the sample cell by a high gain horn antenna to polarize the sample. Following polarization, the rotational frequencies corresponding to all transitions excited in the range of the chirp ($\nu_o \pm \nu_W$) is received by a second horn antenna located on the opposite side of the chamber. The broadband molecular signal can also be phase coherently averaged over several hours in a CP-FTMW experiment, usually collecting millions of FIDs (free induction decay), to improve the

quality of the spectrum. For the CP-FTMW experiments performed in this thesis, 25 FIDs were collected and averaged during each gas pulse (~1000 μs). Each FID event involves a microwave pulse (~ 1–5 μs) and the FID detection for ~16 μs. Typical linewidths in the spectrum can vary from ~150–200 kHz (FWHM, full width at half maximum). The experimental repetition rate is ~7 kHz and is limited by the signal digitization and/or vacuum throughput. A sample of a broadband CP-FTMW spectrum displaying many rotational transitions at once in the frequency range from 9 to 11 GHz (10 GHz $\pm$1 GHz) is given in the bottom of Figure 2.2.

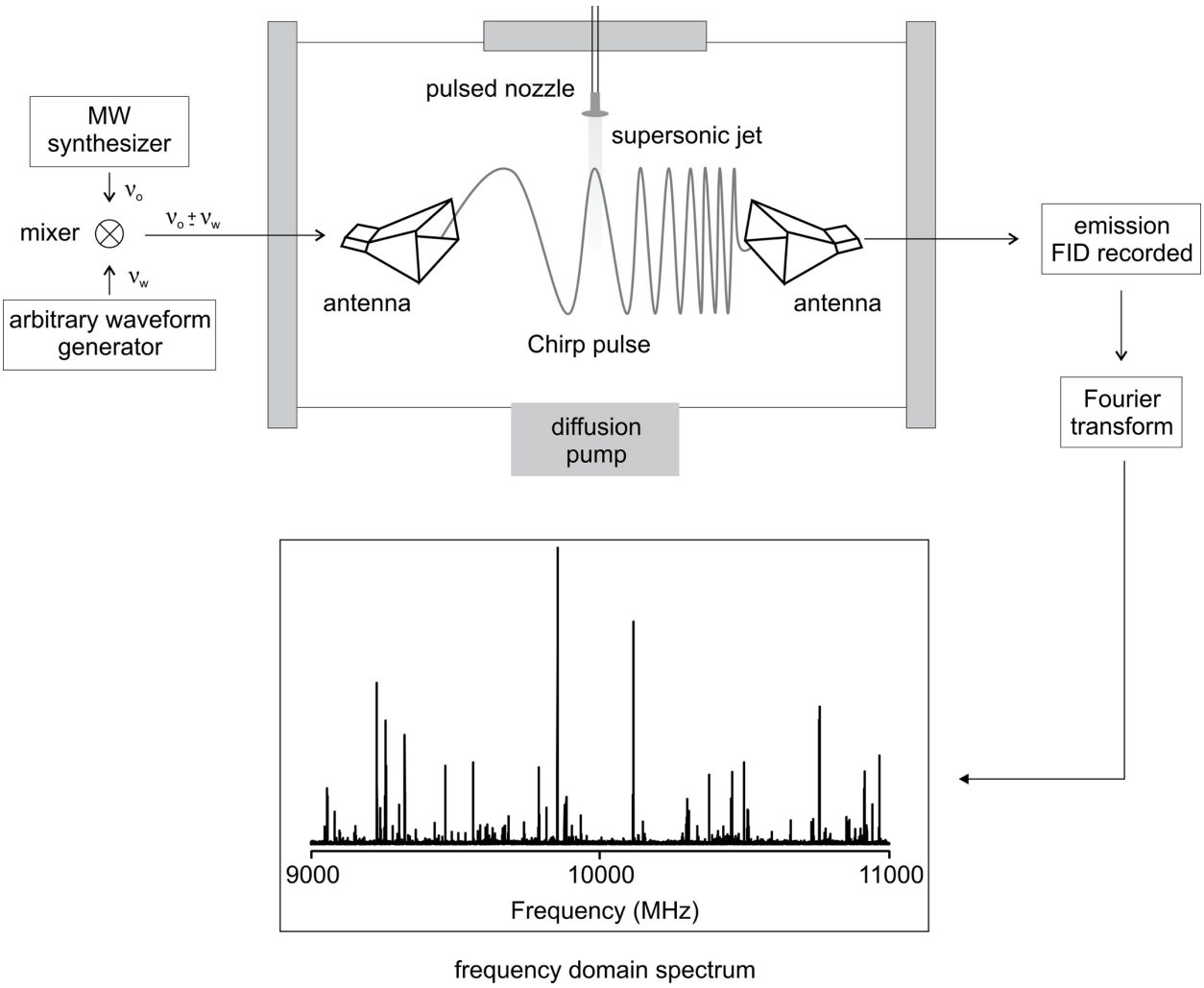

Figure 2.2 A simplified scheme of main events occurring during a broadband CP-FTMW experiment. The reader interested in the details of the excitation and detection can refer to the original manuscript in reference 9.

Although the CP-FTMW spectrometer facilitated the rapid collection of a broad spectrum over a large frequency window as described above, the absence of a resonant cavity sacrificed resolution and sensitivity. As the linewidth of the transitions in the CP-FTMW spectrum (~150–200 kHz) is much larger than that in the cavity BF-FTMW spectrum (~7 kHz), spectral splittings such as those from internal motions are often not resolvable in the broadband spectrum. That is the reason for using the CP-FTMW spectrum as a survey for preliminary assignments that guide

further measurements of transitions with higher resolution and sensitivity using the BF-FTMW instrument.

2.4.3 Cavity-Based Balle-Flygare FTMW Spectrometer

The cavity-based FTMW spectrometer works in the frequency range of 4–26 GHz and largely follows the design described by Grabow and Stahl[14] which is a modification of the first Balle-Flygare instrument described in 1981.[15] The instrument is used to collect individual rotational transitions in a frequency window of typically 1 MHz or less. A schematic of the instrumental setup is provided in Figure 2.3. Two 36 cm diameter concave aluminum mirrors (one movable and one stationary) comprise a Fabry-Pérot cavity which is built inside the 300 L stainless steel high vacuum chamber. The chamber is evacuated by a large diffusion pump and backed by a rotary pump during the experiments so that the background pressure inside the chamber is always on the order of 10^{-7} kPa. To collect the spectrum corresponding to a specific transition, the cavity needs to be physically tuned to the corresponding frequency (target molecular resonance) by moving the tunable mirror with the help of a servo motor installed behind it. Since the resonant cavity serves as a trap for the microwave field, transitions can be collected with very high resolution (linewidth of 7 kHz FWHM) and sensitivity (improved signal-to-noise ratio).

The pulsed nozzle is mounted near the center of the movable mirror and is responsible for introducing the gaseous sample inside the cavity. The gas pulse has a typical duration of ~1000 μs. Once the sample is delivered into the cavity, a microwave excitation pulse (1–5 μs duration), produced by a switch that gates the continuous wave radiation output from a radiofrequency and a microwave synthesizer, is provided by a L-shape wire hook antenna also located in the tunable

mirror as shown in Figure 2.3. The molecules interact with the excitation pulse which causes the dipole moments of the molecular targets to align (assuming the cavity is tuned to a molecular resonance) resulting in a rotating macroscopic polarization of the sample. After the excitation, the transient emission produced by the resultant oscillation of the dipole moment of the ensemble in the time domain (FID) is detected over 100–400 μs with the same wire hook antenna, processed via heterodyne mixing and the signal is Fourier transformed to give a spectrum in the frequency domain. Another antenna is present on the opposite side of the chamber, but it is connected to a diode detector and only used to verify the cavity resonance.

A single data acquisition event including one gas pulse, one excitation pulse and the FID detection takes about 1200 μs (or 120 ms). The pulse sequence can be repeated, and the emission signal can be phase coherently averaged as all pulse timings are linked to a frequency standard (10 MHz system clock). The experimental repetition rate is ~7 kHz and is mainly limited by the vacuum throughput. Since the emission signal is usually weak, many cycles are required to achieve a satisfactory sensitivity, specially for transitions due to minor isotopic species whose intensities are dependent on their natural abundances. As the sample insertion and the microwave pulse are coaxial, all observed frequencies appear as doublets in the FTMW spectrum due to the Doppler effect. A sample of a narrowband BF-FTMW spectrum is provided on the right side of Figure 2.3.

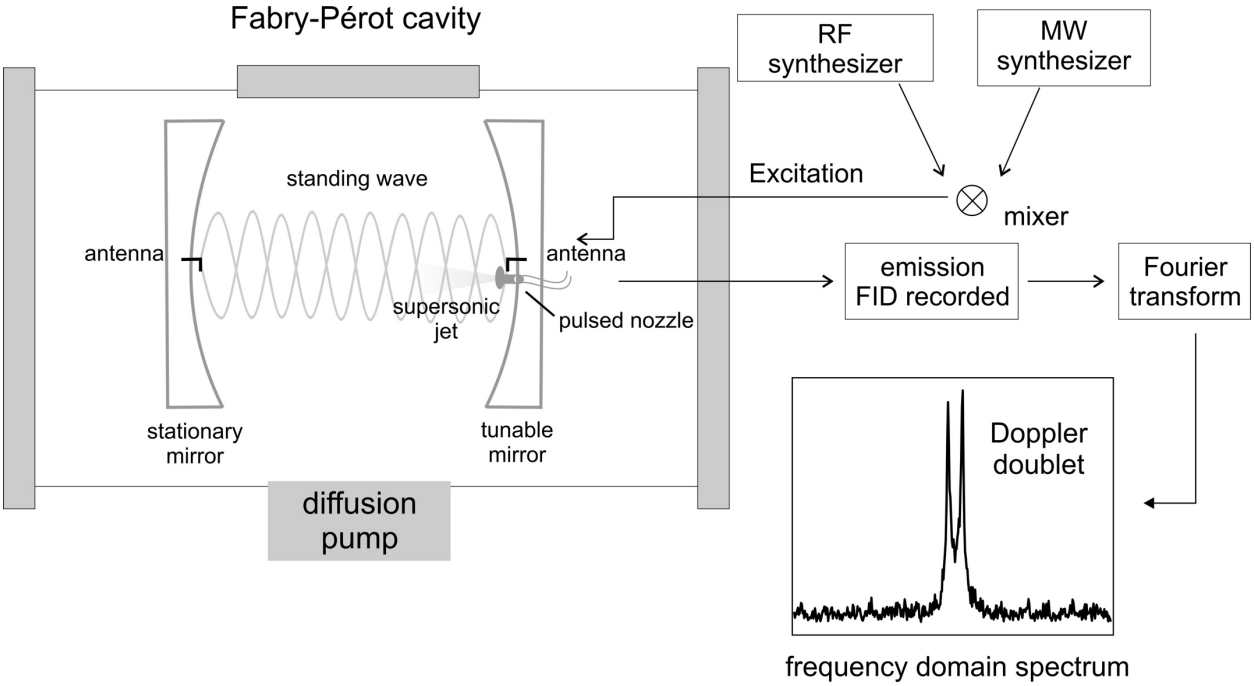

Figure 2.3 A simplified scheme of a Balle-Flygare FTMW experiment. The reader interested in the details of the excitation and detection can refer to the original manuscript in reference 8.

Although the cavity-based FTMW instrument has key advantages in terms of both resolution and sensitivity, the cavity itself limits its application since the excitation bandwidth is on the order of < 1 MHz. Imagine one wants to study a complex molecule having a dense spectrum with several dozens of transitions arising from multiple conformers in the range of 4–26 GHz. In order to detect each different transition, one would need to physically tune the cavity and record emission in segments of < 1 MHz (typically 0.2 MHz), which would result in 110,000 separate acquisitions making the study both time consuming and laborious. This highlights the advantages of combining the CP-FTMW instrument to collect the survey spectrum and the BF-FTMW instrument for higher resolution and sensitivity measurements in a typical rotational spectroscopic study.

As there were no previous reports on the molecular systems investigated in this thesis, extensive quantum chemical calculations were first carried out to predict the molecule's most stable geometries, relative energies and key spectroscopic parameters that are essential to guide the spectral searches. Theory was also used to explain features associated with observed conformers and to derive experimental parameters and molecular structures. A detailed description of the computational methods is provided in the next chapter.

2.5 References

(1) Walker, N. R. New Opportunities and Emerging Themes of Research in Microwave Spectroscopy. *Philos. Trans. R. Soc. A Math. Phys. Eng. Sci.* **2007**, *365* (1861), 2813–2828.

(2) Xu, Y.; Jäger, W. Microwave Rotational Spectroscopy. In *Encyclopedia of Inorganic and Bioinorganic Chemistry*; John Wiley & Sons, Ltd: Chichester, 2011.

(3) Hollas, J. M. *Modern Spectroscopy*, 4th ed.; John Wiley & Sons Ltd: Chichester, 2004.

(4) Gordy, W.; Cook, R. L.; Gordy, Walter; Cook, R. L. *Microwave Molecular Spectra*, 3rd ed.; John Wiley & Sons Inc.: New York, 1984.

(5) Bernath, P. F. *Spectra of Atoms and Molecules*, 1st ed.; Oxford University Press: Oxford, 1995.

(6) Watson, J. K. G. Determination of Centrifugal Distortion Coefficients of Asymmetric-Top Molecules. III. Sextic Coefficients. *J. Chem. Phys.* **1968**, *48* (10), 4517–4524.

(7) Gunther-Mohr, G. R.; White, R. L.; Schawlow, A. L.; Good, W. E.; Coles, D. K. Hyperfine Structure in the Spectrum of $N^{14}H_3$. I. Experimental Results. *Phys. Rev.* **1954**, *94* (5), 1184–1191.

(8) Evangelisti, L.; Sedo, G.; van Wijngaarden, J. Rotational Spectrum of 1,1,1-Trifluoro-2-Butanone Using Chirped-Pulse Fourier Transform Microwave Spectroscopy. *J. Phys. Chem. A* **2011**, *115* (5), 685–690.

(9) Sedo, G.; van Wijngaarden, J. Fourier Transform Microwave Spectra of a "New" Isomer of OCS-CO_2. *J. Chem. Phys.* **2009**, *131* (4), 044303.

(10) Smalley, R. E.; Ramakrishna, B. L.; Levy, D. H.; Wharton, L. Laser Spectroscopy of Supersonic Molecular Beams: Application to the NO_2 Spectrum. *J. Chem. Phys.* **1974**, *61* (10), 4363–4364.

(11) Smalley, R. E.; Wharton, L.; Levy, D. H. Molecular Optical Spectroscopy with Supersonic Beams and Jets. *Accounts. Chem. Res.* **1977**, *10* (4), 139–145.

(12) Imasaka, T.; Moore, D. S.; Vo-Dinh, T. Critical Assessment: Use of Supersonic Jet Spectrometry for Complex Mixture Analysis (IUPAC Technical Report). *Pure Appl. Chem.* **2003**, *75* (7), 975–998.

(13) Brown, G. G.; Dian, B. C.; Douglass, K. O.; Geyer, S. M.; Shipman, S. T.; Pate, B. H. A Broadband Fourier Transform Microwave Spectrometer Based on Chirped Pulse Excitation. *Rev. Sci. Instrum.* **2008**, *79* (5), 053103.

(14) Grabow, J.-U.; Stahl, W. Notizen: A Pulsed Molecular Beam Microwave Fourier Transform Spectrometer with Parallel Molecular Beam and Resonator Axes. *Zeitschrift für Naturforsch. A* **1990**, *45* (8), 1043–1044.

(15) Balle, T. J.; Flygare, W. H. Fabry–Perot Cavity Pulsed Fourier Transform Microwave Spectrometer with a Pulsed Nozzle Particle Source. *Rev. Sci. Instrum.* **1981**, *52* (1), 33–45.

Chapter 3. Computational Methods

Theoretical methods are fundamental for the success of any rotational spectroscopic study. Prior to the collection of the rotational spectrum, quantum chemical calculations are carried out to predict key spectroscopic parameters (e.g. rotational constants and dipole moment components) which allow simulations of spectral patterns to serve as guides for the initial spectral assignments. Since the systems studied in this work are flexible monomers or molecular adducts, the initial calculations involve conformational searches to locate all possible minima on the potential energy surface (PES) followed by geometry optimization and frequency calculations. This is necessary because each different geometry will have a unique rotational fingerprint as mentioned in Chapter 2.

Preliminary and final fittings of observed transition frequencies are performed with different open-source software dedicated to spectral analysis which allow us to derive key experimental parameters and molecular structures. Once such insights are attained, post optimization and frequency calculations are performed to rationalize the effects responsible for the observed conformational preferences and address additional phenomena. These usually include understanding the absence of certain conformers or the presence of splittings due to internal motions which require modeling of interconversion pathways with their associated barrier heights. Below, the computational methods are divided into three main parts and described in more detail: conformational searches and modelling the potential energy surface, spectral analysis and explaining conformational preferences.

3.1 Conformational Searches and Potential Energy Surfaces

The first step to understand the conformational landscape of a molecule or a molecular complex is to explore its PES which describes the energy of the system as a function of its atomic coordinates. For monomers comprised of several geometries, different points on the PES are modeled instead as a function of dihedral angles corresponding to rotatable angles that lead to different conformers. The PES is derived by performing quantum chemical calculations in which the angles of interest are varied in determined steps (usually 36 steps of 10° each for a full 360° rotation) and the molecular energy is obtained for each structure. These calculations are commonly known as scan calculations and can be performed using single point electronic structure calculations available in several popular computational chemistry packages.[1] In this thesis, the scan calculations were performed using electron correlated density functional theory (DFT) functionals, usually the B3LYP-D3(BJ),[2–4] with relatively large basis sets such as Dunning's cc-pVTZ[5] (which are needed to describe the molecular orbitals) as implemented in the Gaussian 16 software.[6] An example of a full PES for a system containing two dihedral angles (*N*-allylmethylamine, Chapter 8) is provided in Figure 3.1. Apart from locating twelve points of minimum in the blue and purple regions which correspond to nine unique conformers of AMA, the PES also locates points of maximum in the yellow and red regions which allow interconversion energy barriers between conformers to be calculated. This is essential to understand the internal dynamics of molecules that often leads to observable tunneling splittings.

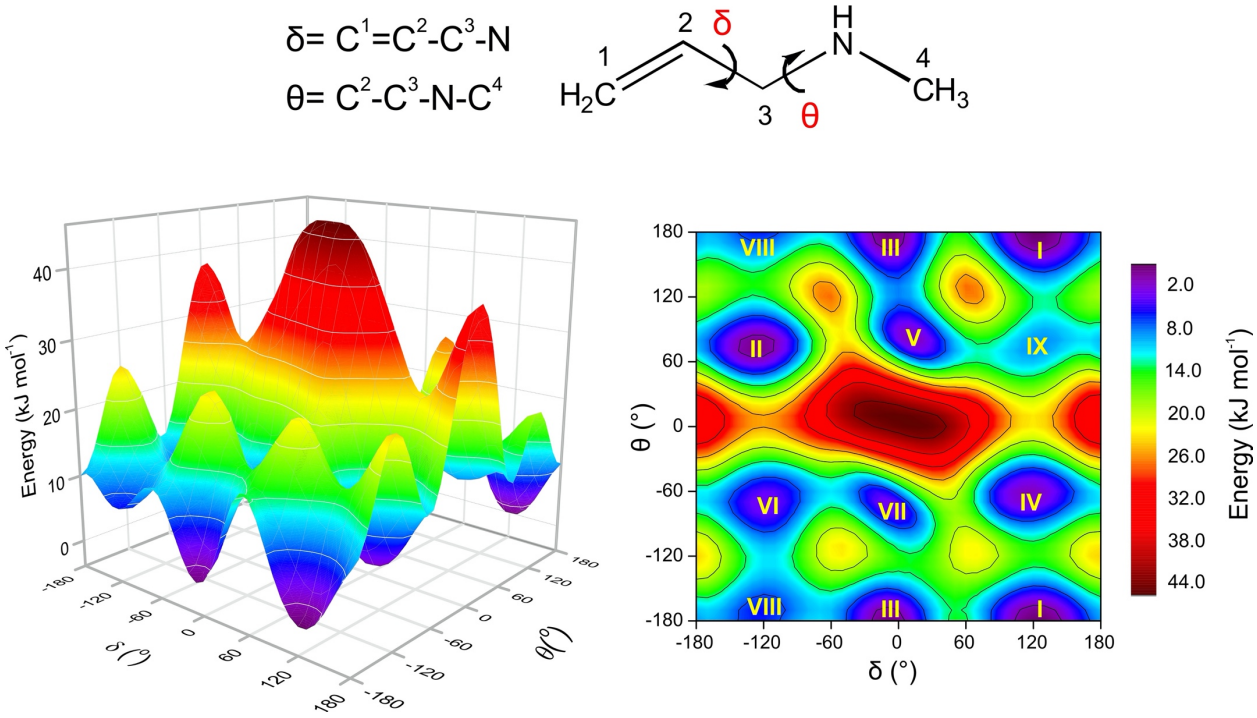

Figure 3.1 Full potential energy surface of AMA which arises due to internal rotations about the δ and θ dihedral angles. The PES was obtained through a scan calculation where both dihedral angles were varied from -180° to 180° in steps of 10° each at the B3LYP-D3(BJ)/cc-pVTZ level of theory. The points corresponding to the nine conformers of AMA are labeled in the top view of the PES on the right side.

Although scan calculations are an excellent tool to find conformers of molecules with one or two dihedrals, for larger systems and molecular clusters, generating their PES in this way is impractical since it involves a large number of dimensions. An alternative is the use of automated conformational sampling tools coupled with low-cost computational methods. The most popular approaches include calculations performed using force fields (FF) which are part of molecular mechanics (MM) theory. FF are empirical methods that use classical models to predict the energy of a molecule as a function of its conformation.[1] The energy is computed based on previously reported geometric parameters, such as bond distances and angles, of model structures from

experiments or high-level quantum chemistry calculations and those parameters are considered transferrable to larger and more complex systems. For example, if one assumes that a typical C–H bond length is always of about 1.05 Å to 1.1 Å with an associated stretching frequency between 2900 cm^{-1} and 3300 cm^{-1} for any molecular system, no additional calculations are needed to understand the energy associated with the C–H bond in an unknown system. This is what makes FF calculations extremely fast when compared to quantum mechanical methods such as those used during the scan calculations which are inherently more computationally expensive for including fewer approximations. On the other hand, since electronic correlation (interaction between electrons) is not included in MM, additional calculations (at higher levels of theory using correlated methods) on all predicted geometries from MM are crucial to define better electronic structures and to confirm their relative energy orderings.

Aiming to fill in the gap between FF and quantum mechanical theories, a group of theoreticians have focused on the development of the so-called semi-empirical quantum mechanical methods which are proposed to be simple, fast and reasonably accurate for the prediction of many molecular properties such as geometries, vibrational frequencies and non-covalent interactions. In particular, the GFN2-xTB method of Bannwarth, Ehlert and Grimme[7] features the inclusion of electrostatic interaction and exchange-correlation corrections to account for electron-electron interactions, and of a density-dependent dispersion model which becomes crucial when modeling non-covalent forces specially in weakly bound complexes. For conformational search purposes, Grimme et al. has implemented the GFN2-xTB method into an automated conformational search tool, known as conformer-rotamer ensemble sampling tool (CREST),[8,9] which not only explores the chemical space of monomers but also of molecular complexes which is a real advantage over the traditional FF methods which are mostly applied to

monomers. It is important to note that the conformational searches using FF and GFN2-xTB (through CREST) are not the final answers to the chemical problems considered here but are good initial inputs for further higher-level quantum mechanical calculations.

After finding plausible geometries for the monomer or complexes either by building their PES from scan calculations or through the automated searches, high level quantum mechanical methods are used to perform full optimization and frequency calculations of each starting structure. Once all geometries are optimized, the structures can be ranked in order of energy which resemble their relative stabilities and estimates of the rotational constants and dipole moment components are obtained which are crucial to guide the spectral searches. Frequency calculations, usually within the harmonic approximation, allow vibrational frequencies to be computed which in turn enables relative energies with zero-point energy (ZPE) corrections and quartic centrifugal distortion constants to be determined. Frequency calculations also confirm the nature of the stationary points as minimum geometries do not show any imaginary frequencies while transition states are characterized by the presence of a single imaginary vibrational frequency. This multi-step procedure is essential to reveal the most likely experimental candidates (low energy conformers) which are the first targets for assignment in the rotational spectrum.

3.2 Spectral Analysis

3.2.1 Pattern Recognition and Fitting Procedure

With insights about the conformer relative energy orderings, rotational constants and dipole moment components from the optimized geometries, a simulated spectrum for each species can be generated using the PGOPHER software,[10,11] a specialized program in simulating and fitting rotational, vibrational and electronic spectra. The preliminary assignment of candidate species is performed by recognizing its simulated spectral patterns in the broadband spectrum and assigning each experimental line manually to a set of corresponding transition quantum numbers. Even though the simulations are based on results from high level calculations, the predicted line positions do not always match well with the observed experimental transition frequencies and in such cases, extensive efforts are needed to assign the conformers. This is especially true for molecules containing several geometries which lead to very dense rotational spectra from which patterns are difficult to identify. The procedure of fitting the spectrum is exemplified in Figure 3.2 where the experimental and simulated spectrum of a simple pattern is compared before and after the lines are fitted.

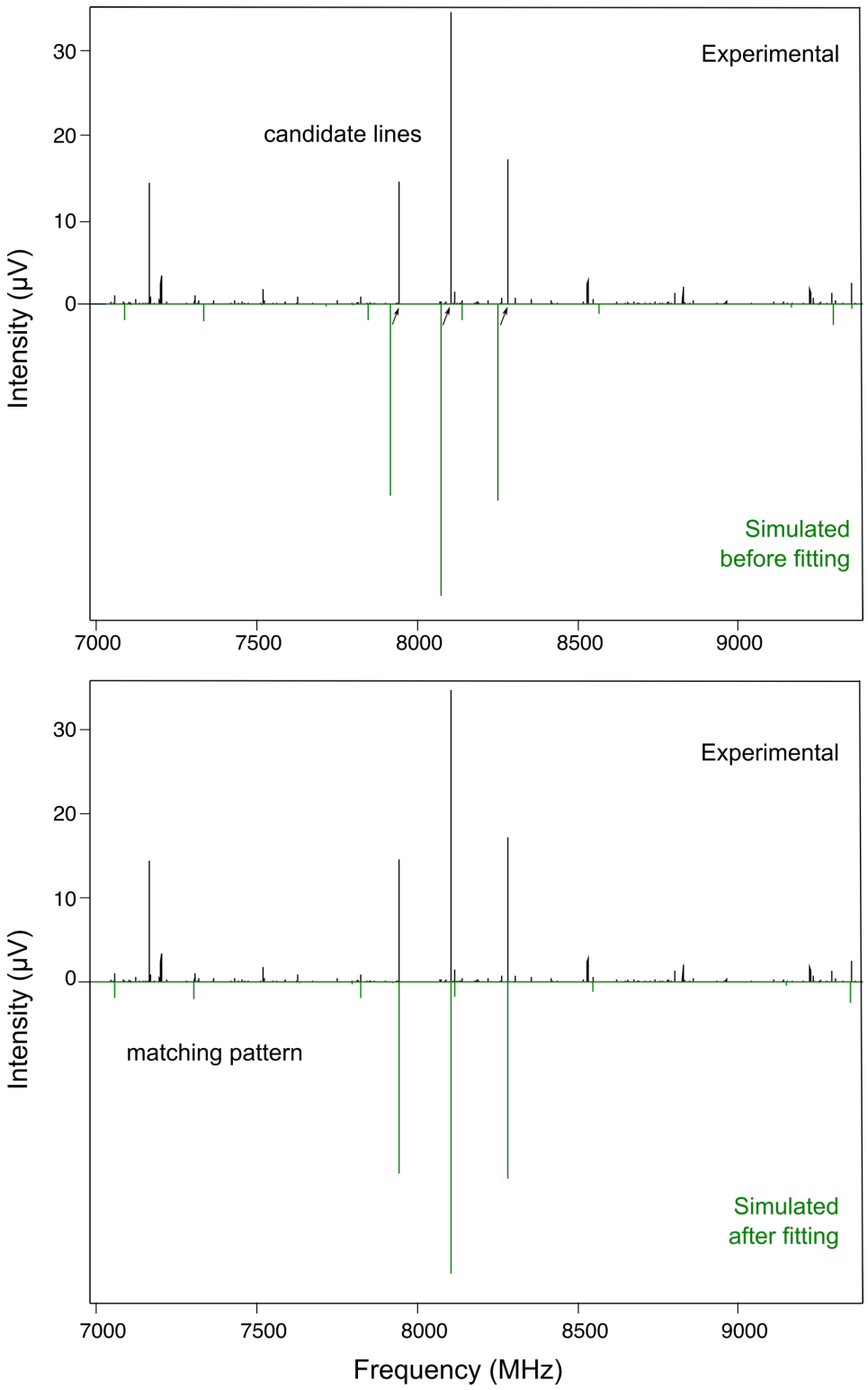

Figure 3.2 Comparison between experimental and simulated (based on predicted rotational constants and dipole moment components from quantum mechanical calculations) spectral patterns before (top) and after (bottom) the fitting procedure.

At the beginning, the candidate experimental lines are ~70 MHz apart from their simulated counterparts. Once a few of the predicted intense peaks are assigned to the spectral lines (strong lines in between 7800 – 8300 MHz in Figure 3.2), PGOPHER is used to least squares fit those lines to a suitable Hamiltonian to determine a set of experimental rotational constants. If the fit is correct, other transitions, not included in the initial fit, automatically shift and match an experimental line—note the three less intense transitions on the left side of the strong lines in the fitted spectrum in Figure 3.2. This confirms the initial assignments and allows more observables to be included in the subsequent fit resulting in better determined spectroscopic constants. In a similar way, transitions at higher and lower frequencies, which are out of the range of the broadband spectrum, can be predicted and sought using the cavity-based BF-FTMW instrument. It is important to note that since the linewidths of spectra collected with the BF-FTMW spectrometer (~7 kHz) are much smaller compared to those of the cp-FTMW (~100–200 kHz), final measurements are performed by collecting the BF spectrum for all transitions. This is also useful to resolve small splittings arising from the ^{14}N hyperfine structure and tunneling motions involving relatively high barriers. Instead of using the PGOPHER program, final fittings are carried out using Pickett's SPFIT[12] software to obtain refined rotational and centrifugal distortion constants. The least squares fits are done using Watson's symmetric (S)[13] or asymmetric (A)[14] reduced Hamiltonians which are usually chosen according to the relative moments of inertia of the asymmetric top molecule. For systems containing a methyl internal rotor which leads to an observable splitting, the fits were done using the XIAM[12,15] code which includes additional terms in the Hamiltonian suitable for dealing with the internal rotation.

When analyzing the rotational spectrum of flexible molecules with several possible conformations, often transitions belonging to certain conformers are absent in the spectrum even

though they are predicted to be populated and have sizeable dipole components. This phenomenon is usually a consequence of relaxation where high energy conformers can re-arrange and interconvert to lower energy forms due to collisions with the carrier gas at the beginning of the supersonic jet expansion. In the literature, energy barriers smaller than ~5 kJ mol^{-1} have been shown to allow for a nearly complete relaxation. The barrier heights are estimated using pathways identified from scan calculations or *via* transition state calculations.

3.2.2 Structure Determination

Apart from rotational transitions due to the parent species of the molecular systems, transitions due to singly substituted rare isotopologues may also be observed in natural abundance depending on the intensity of the parent transition. As the only difference between the isotopes of a given nucleus is in the number of neutrons, the molecular structures are not affected upon isotopic substitution. On the other hand, a change in the atomic masses alters the molecular moments of inertia and, consequently, the rotational constant values (remember the inversely proportional relationship between rotational constants and moments of inertia). This means that the transitions corresponding to the isotopes will also have their own rotational fingerprints. In this work, transitions due to the heavier ^{13}C (1.1 %) and ^{34}S (4.2 %) isotopes could be observed for some monomers in natural abundances while those corresponding to the ^{18}O (0.2 %) species of water were measured for some complexes using an enriched sample of water-^{18}O. The assignment and fitting procedure for the isotopic lines is analogous to that described above for the parent species with the exception that the calculated rotational constants for the isotopes, needed to simulate their

spectral patterns, are first estimated by substituting the masses of each atom one at a time in the molecule's optimized structures using Kisiel's PMIFST program.[12]

With experimentally derived rotational constants for the parent and heavy atom minor isotopologues and knowing the differences in the moments of inertia caused by the isotopic substitutions, the position of each substituted atom can be determined and the geometry of the molecule can be obtained. Although there are different approaches available, the ground state effective (r_0) and substitution (r_s) structures were derived in this work. The r_0 structure[16,17] is associated with the effective bond distances and angles in the ground state vibrational state and is fitted directly from the moments of inertia of the isotopologues (from the rotational constants determined experimentally) using the STRFIT program.[12] Non-substituted atoms are included in the r_0 treatment by fixing their atomic coordinates to their values from the equilibrium (r_e) structure (obtained from quantum mechanical calculations). The r_s method[18] determines the magnitude of the coordinates of each substituted atom along the *a*, *b* and *c* inertial axes of the parent molecule based on the so-called Kraitchman's equations.[19] The r_s structure is calculated using the KRA software.[12]

3.3 Conformational Preferences and Non-Covalent Interactions

Although the presence and properties of conformers of a molecular system can be verified experimentally, the underlying reasons for the observed conformational preferences (i.e. why one geometry is more favoured than the other) can only be obtained with theoretical calculations. In particular, four complementary approaches were used to characterize the non-covalent intramolecular and intermolecular interactions occurring in the studied systems: quantum theory

of atoms in molecules (QTAIM),[20] non-covalent interaction (NCI),[21] natural bond orbital (NBO)[22] and symmetry-adapted perturbation theory (SAPT)[23] analyses. The analyses are carried out using the AIMALL,[24] NCIPLOT,[25] NBO7[26] and Psi4[27] programs, respectively. A brief description of each analysis and the most relevant information they provide, for the purpose of the work presented here, is provided below. For a full theoretical description of the theories, one can refer to their specific references. These analyses are known as post-optimization calculations since they are usually performed on geometries corresponding to optimized minima.

3.3.1 Quantum Theory of Atoms in Molecules (QTAIM)

The QTAIM theory,[20] developed in the 1960s by Richard Bader, is a topological analysis of the molecular electron density (ρ) which aims to relate the concepts of molecular structure and chemical bonding by partitioning the molecular system into its atomic fragments. By analyzing each atom's ρ within the molecule, one can identify their atomic positions and evaluate the forces between them. The QTAIM method is suitable to characterize both covalent bonds and non-covalent intra- and/or intermolecular interactions. Based on the QTAIM concepts, two parameters must be visualized in the QTAIM molecular graphs (the output of the analysis) for two atoms to be considered chemically bound: the bond path (BP) and the bond critical point (BCP). The BP is analogous to the representation of a chemical bond in the Lewis-type structure and represents a line through space along which the ρ is maximum. The BCP is a saddle point in the tridimensional space corresponding to a minimum of ρ along the bonding direction, but a maximum in any other. The BP and BCP appear in the QTAIM graphs as a solid or dashed line and a green dot, respectively, as exemplified in the molecular graph of methyl

3-mercaptopropionate in Figure 3.3. Apart from these two indicators, additional critical points can be visualized in the graph such as ring critical points (RCP, Figure 3.3) which appear whenever a cyclic structure is present and correspond to the repulsive forces within the molecular ring. The analysis also provides quantitative information at each critical point such as the values of the electron density, its Laplacian and the potential energy (V). These values can then be used to estimate the strength of each individual contact by determining their energies. The energy of the interactions found for the systems studied in this thesis were calculated as $0.5V$ as proposed by Espinosa et al.[28]

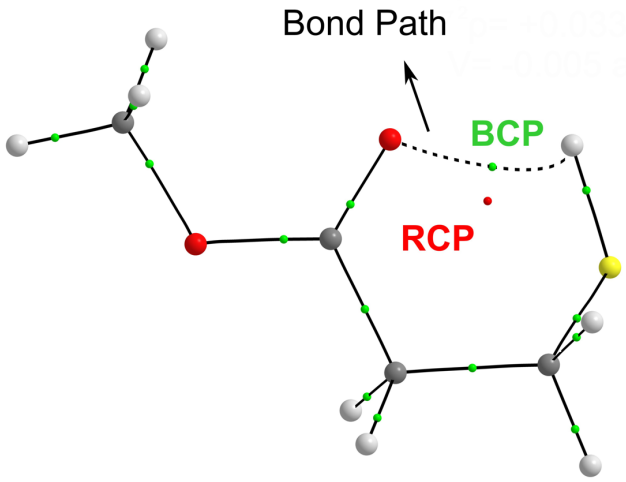

Figure 3.3 QTAIM molecular graph of methyl 3-mercaptopropionate highlighting the bond path (BP), bond critical point (BCP) and ring critical point (RCP) associated with the formation of the S–H···O hydrogen bond. Carbon, hydrogen, oxygen and sulfur atoms are depicted in grey, white, red and yellow, respectively.

While the QTAIM is a generally accepted and popular method, controversies are found in the literature regarding its accuracy for the study of long-range weak interactions. This include cases where a weak interaction is confirmed to exist experimentally, such as the O–H···O in 1,2-ethanediol, but that neither a BP nor a BCP regarding such interaction were observed in the

QTAIM molecular graphs.[29,30] Contrary observations have also been reported in which a BP and BCP have been predicted that correspond to a non-physically meaningful attractive interaction such as the H···H steric interactions in biphenyl derivatives.[31] This means that QTAIM results should be analyzed carefully also in the context of the user's chemical intuition. Aiming to propose a method specifically for describing non-covalent interactions, Johnson et al.[21] developed NCI analysis in 2010, which is a useful tool for characterizing weak intra- and intermolecular contacts.

3.3.2 Non-covalent Interaction (NCI)

Similar to the QTAIM approach, the NCI[21] analysis also uses the electron density topology as the key property to understand chemical bonding. However, the NCI method is based on the normalized reduced density gradient (*s*),

$$s = \frac{1}{[2(3\pi^2)^{\frac{1}{3}}]|\nabla\rho|/\rho^{4/3}}, \tag{3-1}$$

which comes from the ρ and its first derivative. Regions in which non-covalent interactions occur are defined as regions of both low ρ and *s*. The idea therefore is that by obtaining isosurfaces of *s* at low ρ, one can visualize the position and characteristics of the different non-covalent forces within a molecular system. Although the values of ρ are enough to locate the regions of the non-covalent contacts and indicate their strength, in order to distinguish whether a contact is weak, such as van der Waals, or a strong attractive or repulsive interaction, the sign of the Laplacian of the electron density ($\nabla^2\rho$) has been shown to be a better indicator. In particular, the sign of the second eigenvalue of the electron density Hessian matrix sign(λ_2)ρ can distinguish between attractive ($\lambda_2 < 0$) and repulsive ($\lambda_2 > 0$) interactions. While the NCI results can be shown graphically as plots of *s versus* sign(λ_2)ρ, it is a common practice to present the NCI outcomes as

pictorial gradient isosurfaces which are coloured based on the sign(λ_2)ρ values. In these NCI isosurfaces, strong attractive (sign(λ_2)ρ < 0) interactions are represented by blue, strong repulsive (sign(λ_2)ρ > 0) by red and weak van der Waals (sign(λ_2)ρ close to zero) by green coloured surfaces in the interatomic regions. For the benzene dimer in Figure 3.4, for example, the graph (Figure 3.4a) shows troughs with $S \sim 0$ corresponding to attractive π-π stacking interaction between the two aromatic rings and repulsive forces occurring within each benzene subunit. These interactions can also be simply visualized by the colour scheme in the NCI isosurface (Figure 3.4b).

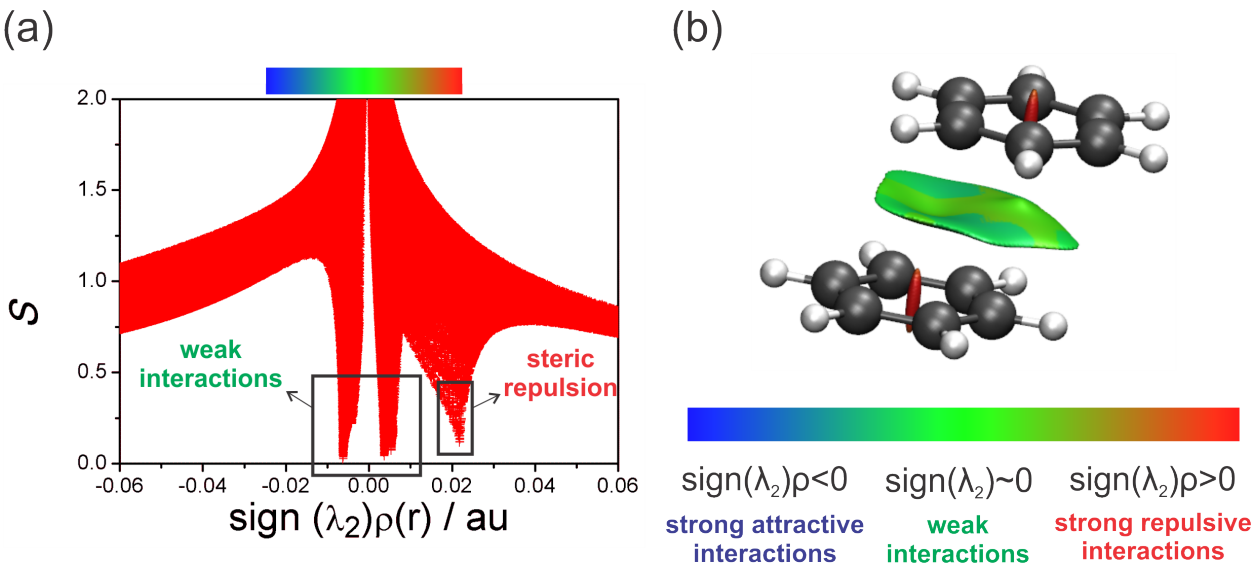

Figure 3.4 NCI graph (a) and isosurface (b) of the benzene dimer showing the troughs and colour scheme associated with the attractive π-π stacking interaction between the two aromatic rings and steric repulsion within each benzene monomer.

3.3.3 Natural Bond Orbital (NBO)

Natural bond orbitals[22] are representations of the electronic structure of the molecular system in the form of an idealized representation of the Lewis structure where localized molecular

orbitals and isolated electron pairs are doubly occupied. Apart from generating descriptions of the occupied (bonding and lone pairs) natural orbitals, the NBO analysis can also identify empty antibonding orbitals which are key to model hyperconjugative interactions (charge transfer from a filled to an empty orbital). These orbital interactions stabilize the molecule and their associated energies ($E^{(2)}$) can be obtained by means of second-order perturbation theory. The $E^{(2)}$ of an interaction between a donor and acceptor orbital is given by:

$$\Delta E_{i\to j}^{(2)} = q_i \frac{|F(i,j)|^2}{\varepsilon_j - \varepsilon_i}, \tag{3-2}$$

in which q_i is the occupancy of the donor orbital, $|F(i,j)|$ is the Kohn-Sham matrix element related to the orbital overlap between the donor and acceptor orbitals, and ε_i and ε_j are the energies of the donor and acceptor orbitals, respectively. Equation (3-2) indicates that a strong orbital interaction (large $E^{(2)}$ value) depends on both a favourable overlap and small energy gap between the interacting orbitals.

3.3.4 Symmetry-Adapted Perturbation Theory (SAPT)

To obtain detailed information on the intermolecular interactions forming weakly bound complexes (as found in Chapters 6, 7 and 9), SAPT calculations were invoked. This approach is also known as an energy decomposition method in which the complex calculated total interaction energy, also an indicator of the interaction's strength, can be further decomposed into four physically meaningful components (electrostatic, dispersion, exchange and induction). These terms reveal the physical nature of the intermolecular contacts and are used to understand the main energy contributor to explain the formation of a given complex. Comparisons of the SAPT results

for similar series of complexes are useful to understand the change in the interaction energy upon functional group or atomic substitutions. For example, in Chapter 6, SAPT analysis is used to understand the variations in hydrogen bonding character upon oxygen to sulfur substitution.

The subsequent chapters employ the computational methods introduced above in combination with rotational spectroscopy (Chapter 2) to study a range of flexible monomers and molecular aggregates. These methods are crucial to model the systems' PES and to reveal the stereoelectronic effects responsible for the conformational preferences.

3.4 References

(1) Cramer, C. J. *Essentials of Computational Chemistry: Theories and Models*, 2nd ed.; John Wiley & Sons, 2004.

(2) Becke, A. D. Density-functional Thermochemistry. III. The Role of Exact Exchange. *J. Chem. Phys.* **1993**, *98* (7), 5648–5652.

(3) Grimme, S.; Ehrlich, S.; Goerigk, L. Effect of the Damping Function in Dispersion Corrected Density Functional Theory. *J. Comput. Chem.* **2011**, *32* (7), 1456–1465.

(4) Grimme, S.; Antony, J.; Ehrlich, S.; Krieg, H. A Consistent and Accurate Ab Initio Parametrization of Density Functional Dispersion Correction (DFT-D) for the 94 Elements H-Pu. *J. Chem. Phys.* **2010**, *132* (15), 154104.

(5) Dunning, T. H. Gaussian Basis Sets for Use in Correlated Molecular Calculations. I. The Atoms Boron through Neon and Hydrogen. *J. Chem. Phys.* **1989**, *90* (2), 1007–1023.

(6) Frisch, M. J.; Trucks, G. W.; Schlegel, H. B.; Scuseria, G. E.; Robb, M. A.; Cheeseman, J. R.; Scalmani, G.; Barone, V.; Petersson, G. A.; Nakatsuji, H., et al. *Gaussian 16*, Revision

C.01; Gaussian, Inc.: Wallingford, CT, 2016.

(7) Bannwarth, C.; Ehlert, S.; Grimme, S. GFN2-XTB - An Accurate and Broadly Parametrized Self-Consistent Tight-Binding Quantum Chemical Method with Multipole Electrostatics and Density-Dependent Dispersion Contributions. *J. Chem. Theory Comput.* **2019**, *15* (3), 1652–1671.

(8) Pracht, P.; Bohle, F.; Grimme, S. Automated Exploration of the Low-Energy Chemical Space with Fast Quantum Chemical Methods. *Phys. Chem. Chem. Phys.* **2020**, *22* (14), 7169–7192.

(9) Grimme, S. Exploration of Chemical Compound, Conformer, and Reaction Space with Meta-Dynamics Simulations Based on Tight-Binding Quantum Chemical Calculations. *J. Chem. Theory Comput.* **2019**, *15* (5), 2847–2862.

(10) Western, C. M. PGOPHER: A Program for Simulating Rotational, Vibrational and Electronic Spectra. *J. Quant. Spectrosc. Radiat. Transf.* **2017**, *186*, 221–242.

(11) PGOPHER: A Program for Simulating Rotational, Vibrational and Electronic Spectra. http://pgopher.chm.bris.ac.uk/(accessed 2021-05-20).

(12) Kisiel, Z. PROSPE - Programs for ROtational SPEctroscopy http://www.ifpan.edu.pl/~kisiel/prospe.htm (accessed May 20, 2021).

(13) Watson, J. K. G. *In Vibrational Spectra and Structure a Series of Advances*; Durig, J. R.; Ed.; Elsevier: New York, 1977, Vol. 6, pp. 1–89.

(14) Watson, J. K. G. Determination of Centrifugal Distortion Coefficients of Asymmetric-Top Molecules. III. Sextic Coefficients. *J. Chem. Phys.* **1968**, *48* (10), 4517–4524.

(15) Hartwig, H.; Dreizler, H. The Microwave Spectrum of Trans-2,3-Dimethyloxirane in Torsional Excited States. *Zeitschrift für Naturforsch. A* **1996**, *51* (8), 923–932.

(16) Watson, J. K. G.; Roytburg, A.; Ulrich, W. Least-Squares Mass-Dependence Molecular Structures. *J. Mol. Spectrosc.* **1999**, *196* (1), 102–119.

(17) Kisiel, Z. Least-Squares Mass-Dependence Molecular Structures for Selected Weakly Bound Intermolecular Clusters. *J. Mol. Spectrosc.* **2003**, *218*, 58–67.

(18) Costain, C. C. Further Comments on the Accuracy of r_s Substitution Structures. Trans. Am. Crystallogr. Assoc. 1966, *2*, 157–164.

(19) Kraitchman, J. Determination of Molecular Structure from Microwave Spectroscopic Data. *Am. J. Phys.* **1953**, *21* (1), 17–24.

(20) Bader, R. F. W. Atoms in Molecules. *Acc. Chem. Res.* **1985**, *18* (1), 9–15.

(21) Johnson, E. R.; Keinan, S.; Mori-Sánchez, P.; Contreras-García, J.; Cohen, A. J.; Yang, W. Revealing Noncovalent Interactions. *J. Am. Chem. Soc.* **2010**, *132* (18), 6498–6506.

(22) Weinhold, F.; Landis, C. R.; Glendening, E. D. What Is NBO Analysis and How Is It Useful? *Int. Rev. Phys. Chem.* **2016**, *35* (3), 399–440.

(23) Jeziorski, B.; Moszynski, R.; Szalewicz, K. Perturbation Theory Approach to Intermolecular Potential Energy Surfaces of van Der Waals Complexes. *Chem. Rev.* **1994**, *94* (7), 1887–1930.

(24) Keith, T. A. *AIMAll*, version 17.11.14; TK Gristmill Software: Overland Park, KS, 2016.

(25) Contreras-García, J.; Johnson, E. R.; Keinan, S.; Chaudret, R.; Piquemal, J.-P.; Beratan, D. N.; Yang, W. NCIPLOT: A Program for Plotting Noncovalent Interaction Regions. *J. Chem. Theory Comput.* **2011**, *7* (3), 625–632.

(26) Glendening, E. D.; Badenhoop, J. K.; Reed, A. E.; Carpenter, J. E.; Bohmann, J. A.; Morales, C. M.; Karafiloglou, P.; Landis C. R.; Weinhold, F. *NBO 7.0*, Theoretical Chemistry Institute, University of Wisconsin: Madison, 2018.

(27) Parrish, R. M.; Burns, L. A.; Smith, D. G. A.; Simmonett, A. C.; DePrince, A. E.; Hohenstein, E. G.; Bozkaya, U.; Sokolov, A. Y.; Di Remigio, R.; Richard, R. M.; et al. Psi4 1.1: An Open-Source Electronic Structure Program Emphasizing Automation, Advanced Libraries, and Interoperability. *J. Chem. Theory Comput.* **2017**, *13* (7), 3185–3197.

(28) Espinosa, E.; Molins, E.; Lecomte, C. Hydrogen Bond Strengths Revealed by Topological Analyses of Experimentally Observed Electron Densities. *Chem. Phys. Lett.* **1998**, *285* (3–4), 170–173.

(29) Lane, J. R.; Contreras-García, J.; Piquemal, J. P.; Miller, B. J.; Kjaergaard, H. G. Are Bond Critical Points Really Critical for Hydrogen Bonding? *J. Chem. Theory Comput.* **2013**, *9* (8), 3263–3266.

(30) Silva, W. G. D. P.; Silla, J. M.; Cormanich, R. A.; Fernandes, S. A.; Freitas, M. P. The Role of Nonbonding Interactions and the Presence of Fluoride on the Conformational Isomerism of 1,2-Ethanediol. *Chem. Phys.* **2016**, *473*, 17–23.

(31) Cioslowski, J.; Mixon, S. T. Topological Properties of Electron Density in Search of Steric Interactions in Molecules: Electronic Structure Calculations on Ortho-Substituted Biphenyls. *J. Am. Chem. Soc.* **1992**, *114* (11), 4382–4387.

Chapter 4. Sulfur as a Hydrogen Bonding Donor in the Gas Phase: Rotational Spectroscopic and Computational Study of 3-Mercaptopropionic Acid[1]

In this chapter, the microwave and computational study of 3-mercaptopropionic acid (3-MPA, Figure 4.1) is discussed as an effort to overcome the lack of experimental data on sulfur hydrogen bonding. In particular, the hydrogen bond S–H···O=C between the mercapto (SH) and the carbonyl group (C=O) of the acid (–C(O)OH), which plays a major role in the biological environment, is of interest. The results obtained in this chapter reveal that although the sulfur hydrogen bond is weaker than those formed with oxygen and nitrogen, it is the principal effect that governs the conformational preferences of 3-MPA. This is supported by the observation of a single dominant structure in the rotational spectrum that is stabilized by the S–H···O=C interaction.

4.1 Abstract

Rotational spectra of 3-MPA were measured from 6-18 GHz using chirped pulse and cavity-based Fourier transform microwave (FTMW) spectroscopy. Theoretical calculations using the B3LYP-D3(BJ) and MP2 methods with the aug-cc-pVTZ basis set show the presence of seven energy minima of 3-MPA below 8.4 kJ mol^{-1}. Comparison of calculated rotational and centrifugal distortion constants with experimental data led to the unequivocal assignment of the global energy

[1]The content of this chapter is an adapted version of the article published in the Journal of Molecular Spectroscopy under the citation: Silva, W. G. D. P.; van Wijngaarden, J. Sulfur as a Hydrogen Bond Donor in the Gas Phase: Rotational and Spectroscopic Study of 3-Mercaptopropionic acid, *J. Mol. Spectrosc.* **2019**, *362*, 1–7.

minimum geometry. This conformer has the mercaptan hydrogen directly oriented towards the carbonyl oxygen of the carboxylic acid moiety suggesting the presence of a six-membered ring S–H···O=C intramolecular hydrogen bond. Quantum theory of atoms in molecules, non-covalent interactions, and natural bond orbital analyses confirm the stability of the sulfur hydrogen bond which plays a key role in the conformational preferences of 3-MPA.

4.2 Introduction

Hydrogen bonding (HB) is an important non-covalent interaction which plays a central role in several processes in chemistry and biology such as organic and enzymatic catalysis, protein folding, protein structure, and molecular recognition.[1] The strength of a HB A–H···B is generally proportional to the electronegativity of the HB donor (A) and HB acceptor (B) atoms. Due to the large electronegativity of oxygen (~3.4) and nitrogen (~3.0) and their versatility as both donors and acceptors, HBs formed by these atoms have been the subject of numerous studies. The characteristics of those interactions have also been used as basis for the definition of the HB concept.[2] On the other hand, less attention has been dedicated to HBs formed by atoms that have smaller electronegativities such as the chalcogens selenium (~2.5) and sulfur (~2.6).[3]

Sulfur HBs, where sulfur acts as proton donor and/or acceptor, are known to be weaker than traditional HBs; however, it was recently shown[3,4] that they can be as strong as oxygen and nitrogen HBs as in the case of the N–H···S interaction compared to N–H···O=C in methionine dipeptides.[3] They are also key to the stability and function of organic crystals and biological molecules.[3,5] One example is the role of the S–H···O=C HB in the stabilization of globular proteins in the natural environment.[5] Despite their unquestionable significance, the nature, strength, and

directionality of sulfur HBs are still topics of debate in the literature.[3] The lack of information on these important interactions inhibits their identification and the characterization of their function in different systems. For instance, computational algorithms which use HB geometries (distances and angles) and energetic criteria often fail to identify weak sulfur HBs in proteins since codes are parameterized with experimental data from typical and strong HBs such as those involving oxygen and nitrogen.[2]

The combination of molecular spectroscopy, particularly rotational spectroscopy, and quantum mechanical calculations has been shown to be an efficient approach to overcome the lack of experimental data on weak non-covalent interactions.[6–9] FTMW spectroscopy allows the determination of precise structural and energetic parameters of molecules in a supersonic jet expansion where species are studied in isolation of crystal packing and solvent effects. Additionally, the technique provides very accurate spectroscopic parameters for comparison to values obtained from theoretical calculations making rotational spectroscopy a powerful tool for benchmark purposes.[10]

A subset of sulfur-containing species has been studied in the gas phase using rotational spectroscopy to elucidate sulfur HBs.[11–14] The investigated systems are mostly dimers and molecular complexes where sulfur acts as HB donor and HB acceptor. Examples include the recent reports of Juanes et al[14] and Das et al[13] which reveal the competition between the HB donor and HB acceptor characters of sulfur in the monohydrate clusters of furfuryl mercaptan and the HB S–H···S interaction in the H_2S dimer, respectively. Although some studies have been carried out, there are still several classes of sulfur HBs that need clarification such as the S–H···O=C HB which plays a key role in biological systems.[5] As recently stated by Biswal[3] and reinforced by Juanes et al[14],

further investigations on unexplored sulfur-containing species at the molecular level are necessary to gain deeper insight on sulfur HBs.

Among sulfur-containing compounds, mercaptans (or thiols) (SH) are crucial in biological processes as well as in medicinal and food industries.[15] In particular, 3-mercaptopropionic acid (3-MPA) [HS–CH_2–CH_2–C(=O)OH] is an organic compound used in the synthesis of nanocrystals,[16] peptides, and protein thioesters,[17] and is a convulsant and important intermediate in biological studies.[15,18] Due to the potential of forming important metal complexes in seawater and sediments, 3-MPA complexes have also been used as prototypes for theoretical investigations[19] that aim to better understand the interaction between organic thiols and metal ions. A detailed understanding of the molecular structures adopted by the 3-MPA monomer, however, is crucial to gain insight into the binding mechanisms and formation of 3-MPA-metal complexes. As the presence of a thiol (SH) and a carboxylic acid moiety in its structure may permit formation of intramolecular S–H···O=C HBs, this compound is an interesting model for the study of sulfur non-covalent interactions.

Herein, we report the first microwave spectroscopic study of 3-MPA supported by density functional theory (DFT) and *ab initio* quantum mechanical calculations. The elucidation of the conformational preferences of 3-MPA expands the current understanding of sulfur HBs and reveals important differences in comparison to its oxygen analog 3-hydroxypropionic acid.

4.3 Methods

4.3.1 Experimental Methods

Rotational spectra of 3-MPA were measured in the frequency range of 6–18 GHz using both chirped-pulse (CP)[20] and cavity-based Balle-Flygare (BF)[21] type Fourier transform microwave (FTMW) spectrometers available at the University of Manitoba. The spectrometers have been previously described in the literature.[22,23] Initial measurements were carried out using the CP-FTMW instrument where the broadband spectra of 3-MPA were recorded in segments of 2 GHz from 6 GHz to 18 GHz. Afterwards, final frequency measurements were performed using the BF-FTMW instrument which provides better resolution and sensitivity. It is worth noting that in the cavity-based spectra, the rotational transitions are split into two components due to the Doppler effect of the molecular emission propagating collinearly with the jet expansion and have line widths of ~7 kHz (FWHM). The uncertainty in the line positions is of about $\pm$1 kHz.

For both experiments, 3-MPA (99%), purchased from Sigma-Aldrich Canada, was used without further purification. Since the compound is a liquid at room temperature with a high boiling point (110–111 ºC at 15 mmHg), a glass bubbler was used to deliver the sample into the spectrometers with neon (~1 bar) acting as a carrier gas. The mixture containing traces of the sample and the gas was supersonically expanded into the high vacuum chambers (P~10^{-6} Torr) of the instruments through a pulsed nozzle (1 mm diameter orifice).

4.3.2 Computational Details

The presence of multiple dihedral angles in the structure of 3-MPA make its conformational equilibrium rich as multiple conformations may arise from rotations around its single bonds as shown in Figure 4.1. To find all possible geometries of 3-MPA, an initial conformational search was carried out using the Merck Molecular Force Field (MMFF94)[24] method as implemented in the Marvin Sketch 16.10.10 program (ChemAxon version 6.1). The search led to thirty possible geometries of 3-MPA. Optimization calculations were then carried out for all structures at the B3LYP-D3(BJ)[25–27]/aug-cc-pVTZ[28] level of theory. These calculations resulted in seven energy minima with relative energies smaller than 8.4 kJ mol^{-1}. Based on recent reports[10,29] in rotational spectroscopy that highlight the importance of choosing appropriate theoretical methods for this type of study, we carried out optimization calculations at different levels of theory for the seven most stable conformers. The chosen methods include *ab initio* (MP2)[30] and DFT B3LYP, along with other three DFT functionals, including the M062-X[31], ωB97X-D[32] and the dispersion-corrected B3LYP functional with Becke-Johnson damping (B3LYP-D3(BJ)). The aug-cc-pVTZ basis set was used for all calculations.

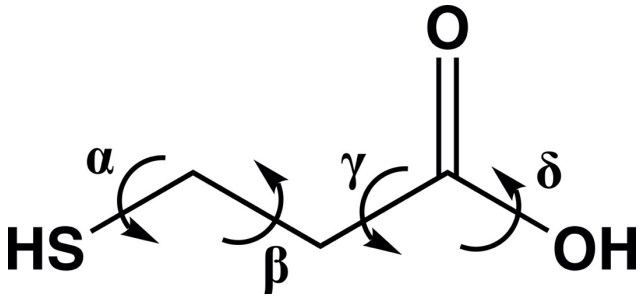

Figure 4.1 Chemical structure and dihedral angles of 3-MPA.

We also performed frequency calculations for all of the different methods to guarantee that imaginary frequencies were absent and also to obtain the electronic energies with zero-point corrections as well as the Gibbs free energies at 298K. All optimization and frequency calculations were carried out using the Gaussian 16 revision B.01 program.[33]

Finally, to investigate the presence and stability of intramolecular interactions in the conformers of 3-MPA, we completed quantum theory of atoms in molecules (QTAIM),[34] non-covalent interactions (NCI),[35] and natural bond orbital (NBO)[36] analyses. The QTAIM, NCI, and NBO analyses were performed using the AIMAll,[37] NCIPLOT,[38] and NBO 6.0[39] programs, respectively.

4.4 Results and Discussion

The seven conformers of 3-MPA having relative energies less than 8.4 kJ mol^{-1} are shown in Figure 4.2 while their Cartesian coordinates are provided in Tables S1–S7 in Appendix file. The structures are labeled by the name "mpa" which stands for 3-mercaptopropionic acid followed by an Arabic numeral, from 1 to 7, that represents their order of stability from B3LYP-D3(BJ) level calculations with basis set aug-cc-pVTZ, with 1 being the most stable conformer. As conformers with higher relative energies are not appreciably populated at room temperature before supersonic expansion, only these seven are considered for further discussion.

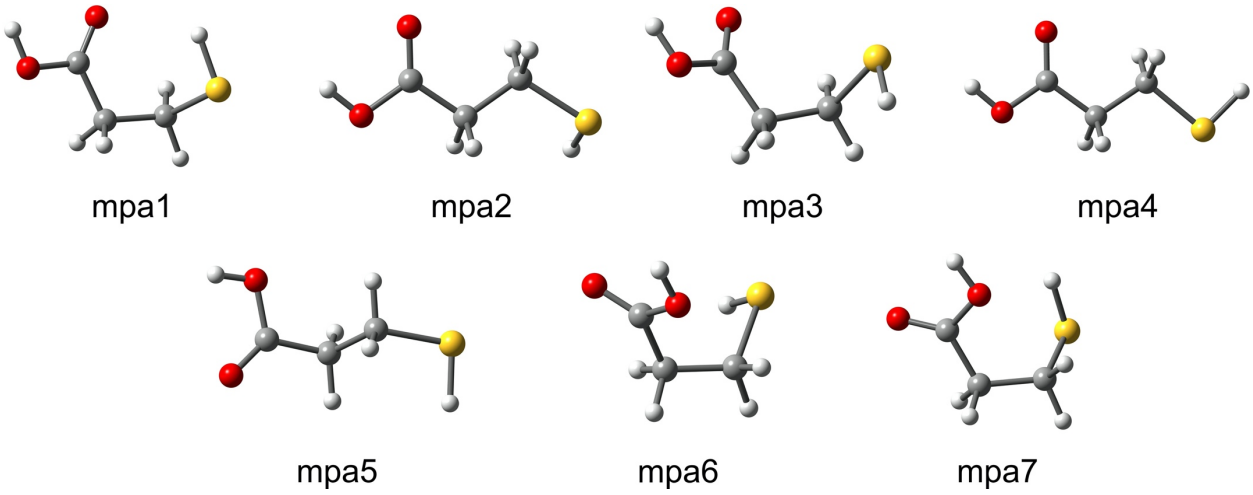

Figure 4.2 Seven most stable conformers of 3-MPA.

The role of theory in accurately capturing dispersive interactions in microwave spectroscopic investigations has been recently discussed in the literature.[10,29] As such, the relative energies and spectroscopic parameters of the seven most relevant conformers of 3-MPA were calculated at various levels of theory. Overall, the spectroscopic parameters calculated for each conformer from the different methods are consistent. The B3LYP-D3(BJ) functional presents the best agreement with the experimental data and a summary of these results is provided in Table 4.1 along with those from the popular *ab initio* MP2 method for comparison. The results obtained using the other three DFT methods (B3LYP, M062-X, and ωB97X-D) are provided in Table S10. The electronic energies with zero-point corrections (ΔE_{ZPE}) and the Gibbs free (ΔG) energies which account for entropic contributions at 298K are also provided.

Table 4.1 Calculated rotational parameters and relative energies (DFT B3LYP-B3(BJ) and MP2, aug-cc-pVTZ) for the most stable conformers of 3-MPA.

	B3LYP-D3(BJ)			MP2		
Conformer	***A*/*B*/*C*[a]**	**$\lvert\mu_a\rvert/\lvert\mu_b\rvert/\lvert\mu_c\rvert$[b]**	**ΔE_{ZPE}[c]/ΔG[d]**	***A*/*B*/*C***	**$\lvert\mu_a\rvert/\lvert\mu_b\rvert/\lvert\mu_c\rvert$**	**$\Delta E_{ZPE}/\Delta G$**
mpa1	5927/1572/1436	1.6/1.6/0.1	0.0/0.0	5836/1618/1479	1.7/1.8/0.1	0.0/0.0
mpa2	9027/1163/1049	1.0/1.4/0.6	3.8/1.7	8976/1179/1062	1.0/1.6/0.7	4.6/2.5
mpa3	5395/1559/1517	0.6/2.4/1.0	4.6/3.4	5277/1621/1577	0.5/2.6/1.3	4.6/3.3
mpa4	8972/1183/1058	0.6/0.4/0.0	6.3/4.2	8917/1200/1072	0.5/0.4/0.0	6.7/4.6
mpa5	8394/1181/1092	0.2/0.8/0.0	7.9/5.0	8338/1199/1108	0.1/0.8/0.0	8.4/5.0
mpa6	4904/1662/1627	0.4/2.0/0.8	7.1/6.3	4817/1738/1686	0.5/2.4/0.5	6.3/5.9
mpa7	5231/1618/1554	0.0/0.5/2.2	7.1/6.3	5087/1679/1626	0.1/0.9/2.4	6.3/5.9

[a]Rotational constants (*A*, *B*, and *C*) in MHz; [b]Absolute values of the electric dipole moment components in D; [c]Relative energies, in kJ mol^{-1}, with respect to the global energy minimum accounting for zero-point energy (ZPE) corrections; [d]Relative Gibbs free energies, in kJ mol^{-1}, with respect to the global energy minimum calculated at 298K.

From both the B3LYP-D3(BJ) and MP2 methods, conformer mpa1 is predicted to be the geometry corresponding to the global energy minimum and to be at least 1.7 kJ mol^{-1} (ΔG; B3LYP-D3(BJ)/aug-cc-pVTZ) more stable than the second lowest energy conformer (mpa2). This energy difference corresponds to abundances that are equivalent to 44.9% and 21.2% for mpa1 and mpa2 respectively, at room temperature. In the most stable conformer, the hydrogen atom of the SH group is directly oriented towards the carbonyl oxygen of the carboxylic acid moiety suggesting the presence of an S–H···O=C intramolecular hydrogen bond (IHB). This interaction would result in the formation of a six-membered ring (β of approximately 70º, Figure 4.1) in this conformation. The second lowest energy conformer adopts a "zig-zag" structure (β ~ 180º, Figure 4.1) where the oxygen, sulfur, and carbon atoms are all in the same plane while the hydrogens have out-of-plane orientations with the exception of the carboxylic acid hydrogen. The remaining

higher energy conformations also have values of β close to 180º (mpa4 and mpa5) or 70º (mpa3, mpa6, and mpa7). The geometry adopted by the global energy minimum of 3-MPA is similar to the one reported in the literature for the most stable conformer of thioglycolic or mercaptoacetic acid (HO–C(=O)–CH_2–SH) where the presence of the S–H···O=C intramolecular interaction results in the formation of a five-membered ring.[40,41]

Interestingly, none of the most populated conformers of 3-MPA exhibit a favorable geometry for the formation of a O–H···S IHB between the sulfur and the hydroxyl group of the carboxylic acid. This reveals that the character of sulfur in 3-MPA is that of a HB donor rather than acceptor. In the computational study of the oxygen analog of 3-MPA, 3-hydroxypropionic acid, the alcohol oxygen serves as a HB donor in both of the two lowest energy conformers. The lowest energy is analogous to that determined for mpa1 in this work and the second most stable conformer of 3-hydroxypropionic acid exhibits a O–H···O interaction with the alcohol oxygen acting as a HB donor to the hydroxy oxygen of the carboxylic acid moiety.[42] The latter resembles the structure of conformer mpa6, however, in 3-MPA this geometry is at least 5.9 kJ mol^{-1} higher in energy than mpa1 and is thus, considerably less stable.

As there are no previous reports on the microwave spectra of 3-MPA, the data collected in Table 4.1 were used to guide our experimental search. As the intensity of the rotational transitions in the microwave spectra is directly related to the electric dipole moment components (μ_a, μ_b, and μ_c) along the principal axes (*a*, *b*, and *c*) and the population of the ground state rotational energy levels, our spectral search focused first on the assignment of rotational transitions corresponding to the global minimum geometry. The simulated spectrum of mpa1 was compared to the experimental CP-FTMW spectra using the PGOPHER program[43]. The comparison led to the successful identification of mpa1 in the range from 6 GHz to 18 GHz. Both *a*- and *b*-type rotational

transitions were readily detected in good agreement with the sizeable $|\mu_a|$= 1.6 D–1.7 D and $|\mu_b|$= 1.6 D–1.8 D (B3LYP-D3(BJ) and MP2, aug-cc-pVTZ) dipole moment components predicted by theory. Despite accurate line positions, no *c*-type transitions could be observed for mpa1 which also agrees with the small predicted values of $|\mu_c|$= 0.1 D (B3LYP-D3(BJ) and MP2, aug-cc-pVTZ). A portion of the broadband microwave spectrum highlighting some rotational transitions assigned for mpa1 is provided in Figure 4.3A. To achieve higher resolution and sensitivity, the rotational transitions observed for the parent species of mpa1 in the broadband spectra were re-investigated using the cavity-based BF-FTMW spectrometer. In total, 45 Doppler doublets, including 26 *a*-type and 19 *b*-type rotational transitions, were measured for the parent species of mpa1. A sample of the BF-FTMW spectrum showing the Doppler splitting for the 3_{03}-2_{02} rotational transition is depicted in Figure 4.3B. The full list of assigned transitions is provided in Table S11. The observed transitions were fitted using Pickett's SPFIT program[44] set to Watson's A-reduced Hamiltonian[45] in the I^r representation. The derived experimental parameters are shown in Table 4.2.

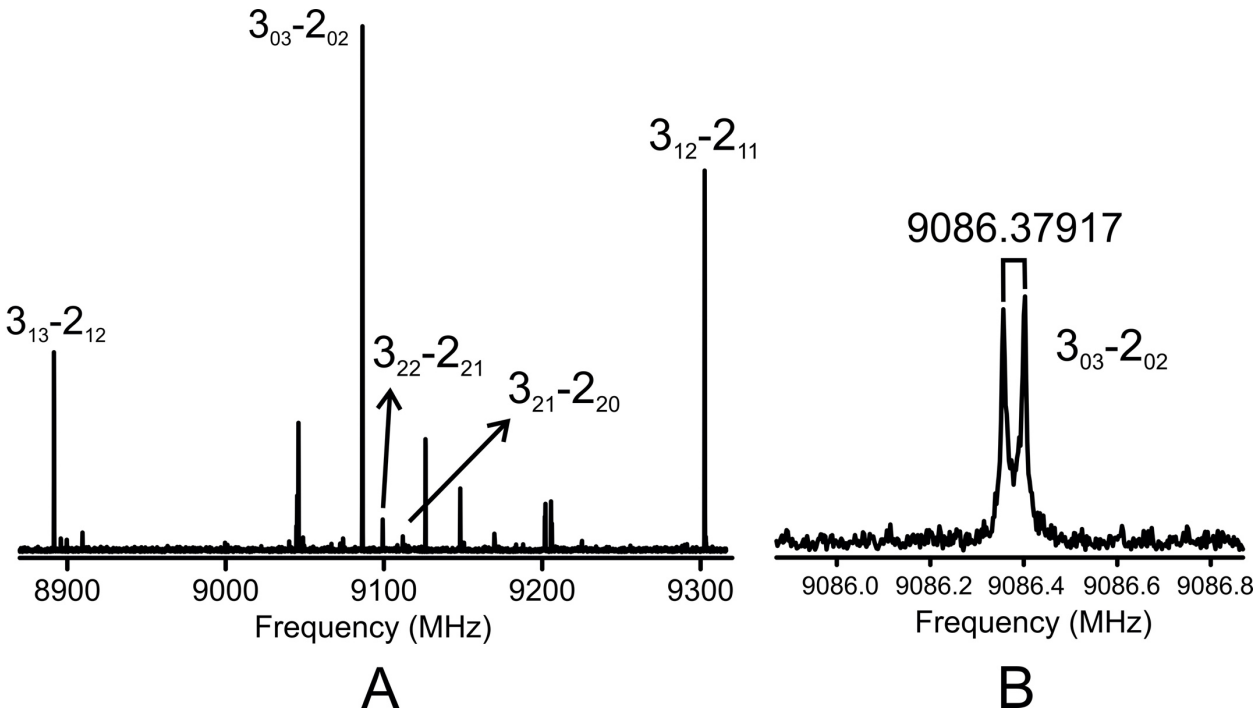

Figure 4.3 A) Portion of the broadband spectrum (1.5 million FIDs) of 3-mercaptopropionic acid displaying some rotational transitions observed for the parent species of mpa1; B) Sample of the cavity-based FTMW spectrum (778 cycles) of the 3_{03}-2_{02} rotational transition of mpa1.

Table 4.2 Comparison between experimental and theoretical (B3LYP-D3(BJ)/aug-cc-pVTZ) spectroscopic parameters for the parent species of conformer mpa1. The calculated distortion constants were obtained through anharmonic frequency calculations.

Parameter	Experimental	B3LYP-D3(BJ)
A /MHz	5946.15216(36)	5927
B /MHz	1585.04375(10)	1572
C /MHz	1448.00927(11)	1436
Δ_J /kHz	0.77709(61)	0.77
Δ_{JK} /kHz	-5.7705(39)	-5.59
Δ_K /kHz	33.179(72)	35.06
δ_j /kHz	-0.03159(51)	-0.03
δ_k /kHz	5.730(45)	6.24
σ /kHz	0.5	
N	45	

The ground state experimental rotational parameters are well-determined (σ= 0.5 kHz) and present good agreement with the equilibrium values derived from optimization and frequency calculations. The theoretical centrifugal distortion constants were estimated only using the B3LYP-D3(BJ) method due to the large computational cost of anharmonic frequency calculations at the MP2 level. The experimentally derived rotational constants A, B, and C show better agreement with the values calculated using B3LYP-D3(BJ) (within 1.5% for all rotational constants) which suggests that the equilibrium geometry (r_e) of mpa1 obtained at this level of theory is closer to its ground state structure. Comparison between experimental and theoretical centrifugal distortion constants provides an additional check for the unequivocal assignment of these transitions as arising from mpa1. It is worth noting that although a theoretical method can provide reasonable results for rotational constants, it does not always reproduce the values of the centrifugal distortion constants well.[46] Thus, the excellent match between experiment and theory in this work validates the consistency of the chosen level of theory.

Despite our experimental efforts, no other conformers of 3-MPA could be identified in the rotational spectra. Although mpa2 is predicted to have a population between 6.4% and 33.6% at room temperature (for different levels of theory), i.e. the predicted conformer distributions are very sensitive to the computation employed, the observed transitions of 3-MPA were extremely weak due to the compound's low volatility. This prevented the identification of the spectrum of mpa2 along with those of other conformers and minor isotopologues. Furthermore, it is well known that higher energy conformers may relax to lower energy forms during the supersonic jet expansion depending on the barriers to re-arrangement. Barriers above ~400 cm^{-1} restrict this relaxation and allow experimental observation of metastable conformers.[47] In this case, as the relaxation of mpa2 to mpa1 involves changes in all dihedral angles, the pathway is not simple to estimate, and we cannot conclude whether the absence of mpa2 is due to its low population (maybe as low as 6.4%) or facile relaxation to mpa1 in the cold jet.

To investigate the presence and stability of the six-membered ring S–H···O=C IHB in conformer mpa1, we performed quantum theory of atoms in molecules (QTAIM), non-covalent interactions (NCI), and natural bond orbital (NBO) analyses which are common approaches for the characterization of hydrogen bonds and other non-covalent interactions.[34–36] The QTAIM molecular graph (Figure 4.4A) exhibits a bond path (BP) and a bond critical point (BCP) between the carbonyl oxygen of the carboxylic acid moiety and the mercaptan hydrogen, supporting the existence of a S–H···O=C IHB in mpa1. Due to the formation of a six-membered ring, a ring critical point (RCP) is also observed in the QTAIM molecular graph. To confirm the stability of this interaction, the electron density (ρ), its Laplacian ($\nabla^2\rho$), and the local potential energy (V) at the BCP were analyzed using Bader's[48] criteria for the characterization of hydrogen bonds. The criteria establish that hydrogen bonds have values of $\rho(r)$ and $\nabla^2\rho(r)$ at the BCP between 0.002–

0.034 a.u. and 0.024–0.139 a.u., respectively[49] The values obtained for the QTAIM parameters (Table 4.3) at the BCP of the S–H···O=C interaction satisfy Bader's rules. Additionally, we also evaluated other criteria, established by Koch and Popelier[49] which compare the QTAIM properties of a H-bound and a non-H-bound hydrogen atom; these properties are the atomic charge q(H), atomic first dipole moment M_1(H), atomic energy E(H), and atomic volume V(H). By comparing the QTAIM parameters (Table 4.3) of the mercaptan hydrogens of mpa1 (which is involved in the IHB) and mpa2 (which does not experience the intramolecular interaction), it can be seen that the mercaptan hydrogen in the former has a larger q(H), has smaller M_1(H) and V(H), and is less stable than in the latter. Thus, as the mercaptan hydrogen of mpa1 satisfies the Koch and Popelier criteria, this conformer possesses a stable S–H···O=C IHB which indeed plays a significant role in the stabilization of mpa1 relative to the other forms.

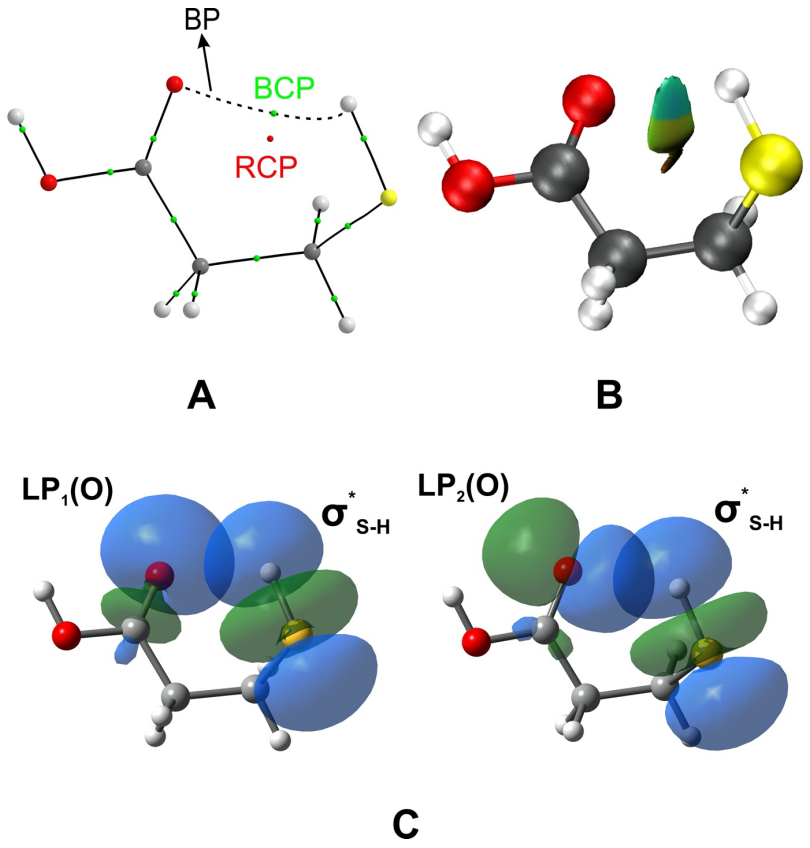

Figure 4.4 A) QTAIM molecular graph, B) NCI isosurface (s= 0.5 au; colour scale of -0.02 < ρ < 0.02); and C) NBO plots of mpa1.

Table 4.3 QTAIM parameters (in a.u.) obtained for conformers mpa1 and mpa2.

Parameter	mpa1	mpa2 (reference)
ρ(r)	0.009	–
$\nabla^2\rho(r)$	0.033	–
V(r)	-0.005	–
	H (SH)	H (SH)
q(H)	-0.028	-0.069
M_1(H)	0.053	0.063
E(H)	-0.607	-0.620
V(H)	49.06	54.36

In agreement with the QTAIM analysis, the NCI approach (Figure 4.4B) confirms the presence of a weak S–H···O=C IHB in mpa1 characterized by the blue-greenish isosurface between the carbonyl oxygen and the mercaptan hydrogen. The NCI isosurface is coloured based on the

values of sign(λ_2)ρ, where λ_2 is the second eigenvalue of the Hessian matrix of ρ. The colours are indicative of the types of interactions that are present in the chemical system under investigation where strong attractive, strong repulsive, and weak (van der Waals) interactions are represented by blue, red, and green isosurfaces, respectively.

The S–H···O=C IHB was also evaluated through natural bond orbital (NBO) analysis carried out at the B3LYP-D3(BJ)/aug-cc-pVTZ level of theory. The NBO output reveals charge transfer from the two lone-pairs of the carbonyl oxygen [LP_1(O) and LP_2(O)] to the anti-bonding orbital of the S–H bond ($\sigma^*_{S\text{-}H}$), characterized by the $LP_1(O) \rightarrow \sigma^*_{S–H}$ and $LP_2(O) \rightarrow \sigma^*_{S–H}$ hyperconjugative interactions. The second-order perturbation energies for such interactions are equal to 0.38 kJ mol^{-1} and 1.55 kJ mol^{-1}, respectively which implies greater involvement of LP_2(O) in the S–H···O=C IHB. For comparison, in 3-hydroxypropionic acid, the second-order perturbation energies of $LP_1(O) \rightarrow \sigma^*_{O–H}$ and $LP_2(O) \rightarrow \sigma^*_{O–H}$ are equivalent to 1.17 kJ mol^{-1} and 7.07 kJ mol^{-1} (B3LYP-D3(BJ)/aug-cc-pVTZ) (this work), respectively which reveals that the energies of the hyperconjugative interactions involved in the O–H···O=C IHB are approximately four times larger than those in the S–H···O=C IHB. This is of no surprise since oxygen often forms stronger hydrogen bonds when compared to sulfur. The $LP(O) \rightarrow \sigma^*_{S–H}$ hyperconjugative interactions play a key role in the stabilization of mpa1 which explains why it is the dominant conformer in the rich conformational landscape. A pictorial representation of the orbital overlaps of the $LP(O) \rightarrow \sigma^*_{S–H}$ hyperconjugative interactions is provided in the NBO plots of Figure 4.4C.

Regardless of whether sulfur acts as a HB donor or HB acceptor, it has been shown that sulfur HBs are characterized by different geometric parameters when compared to those formed by oxygen and nitrogen.[2] Thus, apart from quantum mechanical approaches, we also determined the effective geometric parameters of the S–H···O=C six-membered IHB by looking at the

equilibrium structure (r_e) of mpa1 (Figure 4.5). The length of the S–H···O=C IHB determined by the distance between the carbonyl oxygen and the mercaptan hydrogen is 2.553 Å which is smaller than the sum of the van der Waals radii of oxygen and hydrogen (~2.72 Å). The ∠SH···O angle is found to be 117.5º. For comparison, sulfur HBs in cysteine, where sulfur acts as proton donor S–H···B, have bond lengths that vary from 2.51 Å to 2.84 Å depending on the nature of the HB acceptor atom B.[2]

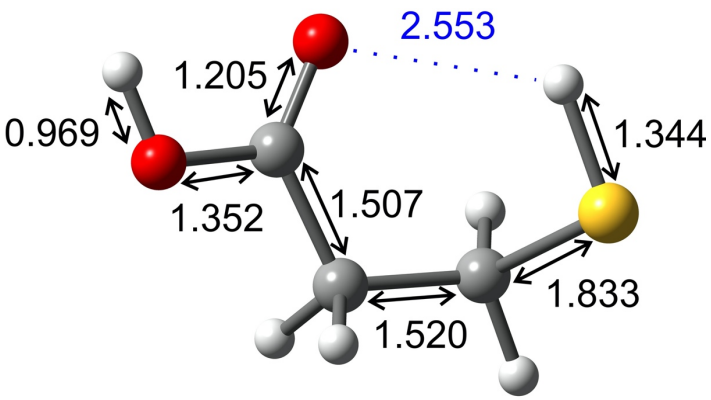

Figure 4.5 Equilibrium r_e structure of mpa1 obtained at the B3LYP-D3(BJ)/aug-cc-pVTZ level of theory.

In previous rotational spectroscopy studies[40,41] of thioglycolic acid (HO–C(=O)–CH_2–SH), which is the shorter hydrocarbon chain version of 3-MPA, the existence of a five-membered ring S–H···O=C IHB was suggested. Interestingly, splitting related to the torsion of the SH group was observed in the rotational spectra. This tunneling motion is characterized by a low-energy barrier double-well potential function that allows for the interconversion between two equivalent forms of thioglycolic acid. In the present study, we did not observe splitting associated with this tunneling motion in the rotational spectra of 3-MPA which we purport is related to a stronger S–H···O=C IHB in this compound. This leads to an increase in the energy barrier between the two equivalent forms of mpa1 restricting the torsion motion of the SH group in this conformation. To support our

assertion, we optimized and performed QTAIM and NBO (B3LYP-D3(BJ)/aug-cc-pVTZ) analyses for the geometry of the previous reported conformer of thioglycolic acid. In the QTAIM molecular graph, neither a BP nor a BCP were observed regarding the S–H···O=C IHB indicating the absence or the weak character of this interaction in thioglycolic acid. NBO calculations confirm that the S–H···O=C interaction in thioglycolic acid is weaker when compared to that in 3-MPA. This is evidenced by the calculated second-order perturbation energies of the $LP_2(O) \rightarrow \sigma^*_{S-H}$ hyperconjugative interaction which is equal to 0.21 kJ mol^{-1} in the former and 1.63 kJ mol^{-1} in the latter. Furthermore, it is well known that six-membered ring IHBs are stronger than the five-membered ones. This is explained by a greater ring strain in the five-membered cycles that affects the stability of the IHB formed as exemplified by the comparison of the O–H···O IHB in a series of substituted diols named 1,2-ethanediol,[50] 1,3-propanediol,[51] and 1,4-butanediol[52] that form five-, six-, and seven-membered ring IHBs, respectively.

4.5 Conclusions

In summary, the combination of quantum mechanical calculations and rotational spectroscopy in a supersonic jet expansion allowed the conformational study of 3-MPA for the first time. Theoretical calculations at both B3LYP-D3(BJ) and MP2 levels with the aug-cc-pVTZ basis set suggest the presence of seven populated energy minima in the conformational equilibrium of 3-MPA. Experimentally, one conformer was observed in the pure rotational spectra and the derived experimental rotational parameters agree very well with those predicted for the global energy minimum (mpa1) geometry whereby the sulfur behaves as a proton donor rather than acceptor. The excellent match of the experimental rotational and centrifugal distortion constants

with those calculated at the B3LYP-D3(BJ)/aug-cc-pVTZ not only unequivocally confirms the assignment of mpa1 but also reveals that its actual geometry is very close to the equilibrium structure r_e obtained at this level of theory. Topological NCI and QTAIM analyses show the presence of a stable S–H···O=C IHB in mpa1 which is confirmed by hyperconjugative LP(O) → $\sigma^*_{S–H}$ interactions obtained through NBO analysis. Although weak, the S–H···O=C IHB is proven to play a key role in the conformational preferences of 3-MPA. The detailed results obtained in this study contribute to a better understanding of the characteristics of sulfur HBs.

4.6 References

(1) Grabowski, S. J. What Is the Covalency of Hydrogen Bonding? *Chem. Rev.* **2011**, *111* (4), 2597–2625.

(2) van Bergen, L. A. H.; Alonso, M.; Palló, A.; Nilsson, L.; De Proft, F.; Messens, J. Revisiting Sulfur H-Bonds in Proteins: The Example of Peroxiredoxin AhpE. *Sci. Rep.* **2016**, *6* (1), 30369.

(3) Biswal H. S., Hydrogen Bonds Involving Sulfur: New Insights from ab Initio Calculations and Gas Phase Laser Spectroscopy, In *Noncovalent Forces*, *Challenges and Advances in Computational Chemistry and Physics*, 1st ed.; Springer International: Switzerland, 2015, 2, pp. 15–45.

(4) Rao Mundlapati, V.; Ghosh, S.; Bhattacherjee, A.; Tiwari, P.; Biswal, H. S.; Mundlapati, V. R.; Ghosh, S.; Bhattacherjee, A.; Tiwari, P.; Biswal, H. S. Critical Assessment of the Strength of Hydrogen Bonds between the Sulfur Atom of Methionine/Cysteine and Backbone Amides in Proteins. *J. Phys. Chem. Lett.* **2015**, *6* (8), 1385–1389.

(5) Gregoret, L. M.; Rader, S. D.; Fletterick, R. J.; Cohen, F. E. Hydrogen Bonds Involving Sulfur Atoms in Proteins. *Proteins Struct. Funct. Genet.* **1991**, *9* (2), 99–107.

(6) Seifert, N. A.; Zaleski, D. P.; Pérez, C.; Neill, J. L.; Pate, B. H.; Vallejo-López, M.; Lesarri, A.; Cocinero, E. J.; Castaño, F.; Kleiner, I. Probing the C–H···π Weak Hydrogen Bond in Anesthetic Binding: The Sevoflurane-Benzene Cluster. *Angew. Chemie Int. Ed.* **2014**, *53* (12), 3210–3213.

(7) Akmeemana, A. G.; Kang, J. M.; Dorris, R. E.; Nelson, R. D.; Anderton, A. M.; Peebles, R. A.; Peebles, S. A.; Seifert, N. A.; Pate, B. H. Effect of Aromatic Ring Fluorination on CH···π Interactions: Microwave Spectrum and Structure of the 1,2-Difluorobenzene···acetylene Dimer. *Phys. Chem. Chem. Phys.* **2016**, *18* (35), 24290–24298.

(8) Feng, G.; Evangelisti, L.; Favero, L. B.; Grabow, J. U.; Xia, Z.; Caminati, W. On the Weak O–H···halogen Hydrogen Bond: A Rotational Study of $CH_3CHClF\cdots H_2O$. *Phys. Chem. Chem. Phys.* **2011**, *13* (31), 14092–14096.

(9) Gougoula, E.; Medcraft, C.; Alkorta, I.; Walker, N. R.; Legon, A. C. A Chalcogen-Bonded Complex $H_3N\cdots S{=}C{=}S$ Formed by Ammonia and Carbon Disulfide Characterised by Chirped-Pulse, Broadband Microwave Spectroscopy. *J. Chem. Phys.* **2019**, *150* (8), 084307.

(10) Grimme, S.; Steinmetz, M. Effects of London Dispersion Correction in Density Functional Theory on the Structures of Organic Molecules in the Gas Phase. *Phys. Chem. Chem. Phys.* **2013**, *15* (38), 16031.

(11) Cole, G. C.; Møllendal, H.; Guillemin, J. C. Microwave Spectrum of 3-Butyne-1-Thiol: Evidence for Intramolecular S–H···π Hydrogen Bonding. *J. Phys. Chem. A* **2006**, *110* (30), 9370–9376.

(12) Xu, L.-H.; Liu, Q.; Suenram, R. D.; Lovas, F. J.; Hight Walker, A. R.; Jensen, J. O.; Samuels, A. C. Rotational Spectra, Conformational Structures, and Dipole Moments of Thiodiglycol by Jet-Cooled FTMW and Ab Initio Calculations. *J. Mol. Spectrosc.* **2004**, *228* (2), 243–250.

(13) Das, A.; Mandal, P. K.; Lovas, F. J.; Medcraft, C.; Walker, N. R.; Arunan, E. The H_2S Dimer Is Hydrogen-Bonded: Direct Confirmation from Microwave Spectroscopy. *Angew. Chemie Int. Ed.* **2018**, *57* (46), 15199–15203.

(14) Juanes, M.; Lesarri, A.; Pinacho, R.; Charro, E.; Rubio, J. E.; Enríquez, L.; Jaraíz, M. Sulfur Hydrogen Bonding in Isolated Monohydrates: Furfuryl Mercaptan versus Furfuryl Alcohol. *Chem. - A Eur. J.* **2018**, *24* (25), 6564–6571.

(15) Salgado, P.; Visnevschi-Necrasov, T.; Kiene, R. P.; Azevedo, I.; Rocha, A. C. S.; Almeida, C. M. R.; Magalhães, C. Determination of 3-Mercaptopropionic Acid by HPLC: A Sensitive Method for Environmental Applications. *J. Chromatogr. B* **2015**, *992*, 103–108.

(16) Zhuang, J.; Zhang, X.; Wang, G.; Li, D.; Yang, W.; Li, T. Synthesis of Water-Soluble ZnS : Mn^{2+} Nanocrystals by Using Mercaptopropionic Acid as Stabilizer. *J. Mater. Chem.* **2003**, *13* (7), 1853–1857.

(17) Kang, J.; Richardson, J. P.; MacMillan, D. 3-Mercaptopropionic Acid-Mediated Synthesis of Peptide and Protein Thioesters. *Chem. Commun.* **2009**, *6* (4), 407–409.

(18) Karlsson, A.; Fonnum, F.; Malthe-Sørenssen, D.; Storm-Mathisen, J. Effect of the Convulsive Agent 3-Mercaptopropionic Acid on the Levels of GABA, Other Amino Acids and Glutamate Decarboxylase in Different Regions of the Rat Brain. *Biochem. Pharmacol.* **1974**, *23* (21), 3053–3061.

(19) Belcastro, M.; Marino, T.; Russo, N.; Sicilia, E. Structure and Coordination Modes in the

Interaction between Cd2- and 3-Mercaptopropionic Acid. *J. Phys. Chem. A* **2004**, *108* (40), 8407–8410.

(20) Brown, G. G.; Dian, B. C.; Douglass, K. O.; Geyer, S. M.; Shipman, S. T.; Pate, B. H. A Broadband Fourier Transform Microwave Spectrometer Based on Chirped Pulse Excitation. *Rev. Sci. Instrum.* **2008**, *79* (5), 053103.

(21) Balle, T. J.; Flygare, W. H. Fabry–Perot Cavity Pulsed Fourier Transform Microwave Spectrometer with a Pulsed Nozzle Particle Source. *Rev. Sci. Instrum.* **1981**, *52* (1), 33–45.

(22) Sedo, G.; van Wijngaarden, J. Fourier Transform Microwave Spectra of a "New" Isomer of OCS-CO_2. *J. Chem. Phys.* **2009**, *131* (4), 044303.

(23) Evangelisti, L.; Sedo, G.; van Wijngaarden, J. Rotational Spectrum of 1,1,1-Trifluoro-2-Butanone Using Chirped-Pulse Fourier Transform Microwave Spectroscopy. *J. Phys. Chem. A* **2011**, *115* (5), 685–690.

(24) Halgren, T. A. Merck Molecular Force Field. I. Basis, Form, Scope, Parametrizations, and Performance of MMFF94. *J. Comput. Chem.* **1995**, *17*, 490–641.

(25) Grimme, S.; Ehrlich, S.; Goerigk, L. Effect of the Damping Function in Dispersion Corrected Density Functional Theory. *J. Comput. Chem.* **2011**, *32* (7), 1456–1465.

(26) Becke, A. D.; Johnson, E. R. A Density-Functional Model of the Dispersion Interaction. *J. Chem. Phys.* **2005**, *123* (15), 154101.

(27) Becke, A. D. Density-functional Thermochemistry. III. The Role of Exact Exchange. *J. Chem. Phys.* **1993**, *98* (7), 5648–5652.

(28) Dunning, T. H. Gaussian Basis Sets for Use in Correlated Molecular Calculations. I. The Atoms Boron through Neon and Hydrogen. *J. Chem. Phys.* **1989**, *90* (2), 1007–1023.

(29) Uriarte, I.; Insausti, A.; Cocinero, E. J.; Jabri, A.; Kleiner, I.; Mouhib, H.; Alkorta, I.

Competing Dispersive Interactions: From Small Energy Differences to Large Structural Effects in Methyl Jasmonate and Zingerone. *J. Phys. Chem. Lett.* **2018**, *9* (20), 5906–5914.

(30) Møller, C.; Plesset, M. S. Note on an Approximation Treatment for Many-Electron Systems. *Phys. Rev.* **1934**, *46* (7), 618–622.

(31) Zhao, Y.; Truhlar, D. G. The M06 Suite of Density Functionals for Main Group Thermochemistry, Thermochemical Kinetics, Noncovalent Interactions, Excited States, and Transition Elements: Two New Functionals and Systematic Testing of Four M06-Class Functionals and 12 Other Function. *Theor. Chem. Acc.* **2008**, *120* (1–3), 215–241.

(32) Chai, J.-D.; Head-Gordon, M. Long-Range Corrected Hybrid Density Functionals with Damped Atom–Atom Dispersion Corrections. *Phys. Chem. Chem. Phys.* **2008**, *10* (44), 6615.

(33) Frisch, M. J.; Trucks, G. W.; Schlegel, H. B.; Scuseria, G. E.; Robb, M. A.; Cheeseman, J. R.; Scalmani, G.; Barone, V.; Petersson, G. A.; Nakatsuji, H.; et al. *Gaussian 16*, Revision B.01; Gaussian, Inc.: Wallingford, CT, 2016.

(34) Bader, R. F. W. Atoms in Molecules. *Acc. Chem. Res.* **1985**, *18* (1), 9–15.

(35) Johnson, E. R.; Keinan, S.; Mori-Sánchez, P.; Contreras-García, J.; Cohen, A. J.; Yang, W. Revealing Noncovalent Interactions. *J. Am. Chem. Soc.* **2010**, *132* (18), 6498–6506.

(36) Weinhold, F.; Landis, C. R.; Glendening, E. D. What Is NBO Analysis and How Is It Useful? *Int. Rev. Phys. Chem.* **2016**, *35* (3), 399–440.

(37) Keith, T. A. *AIMAll*, version 17.11.14; TK Gristmill Software: Overland Park, KS, 2016.

(38) Contreras-García, J.; Johnson, E. R.; Keinan, S.; Chaudret, R.; Piquemal, J.-P.; Beratan, D. N.; Yang, W. NCIPLOT: A Program for Plotting Noncovalent Interaction Regions. *J. Chem. Theory Comput.* **2011**, *7* (3), 625–632.

(39) Glendening, E. D.; Badenhoop, J. K.; Reed, A. E.; Carpenter, J. E.; Bohmann, J. A.; Morales, C. M.; Landis C. R.; Weinhold, F. *NBO 6.0*, Theoretical Chemistry Institute, University of Wisconsin: Madison, 2012.

(40) Caminati, W.; Maris, A.; Favero, P. G. Free Jet Absorption Millimeter-Wave Spectrum of Thioglycolic Acid. *J. Mol. Spectrosc.* **1996**, *175* (1), 215–216.

(41) Yamaguchi, I.; Hasegawa, H.; Hirono, H.; Aizawa, Y.; Takagi, M.; Watanabe, H.; Sekiguchi, T.; Kobayashi, H.; Terasawa, H.; Watanabe, K. An Interpretation of the Microwave Spectrum of Mercaptoacetic Acid. *J. Mol. Spectrosc.* **1995**, *172* (1), 296–298.

(42) Alemán, C.; Casanovas, J.; Zanuy, D.; Hall, H. K. Systematic Evaluation of the Conformational Properties of Aliphatic ω-Hydroxy Acids. *J. Org. Chem.* **2005**, *70* (8), 2950–2956.

(43) Western, C. M. PGOPHER: A Program for Simulating Rotational, Vibrational and Electronic Spectra. *J. Quant. Spectrosc. Radiat. Transf.* **2017**, *186*, 221–242.

(44) Pickett, H. M. The Fitting and Prediction of Vibration-Rotation Spectra with Spin Interactions. *J. Mol. Spectrosc.* **1991**, *148* (2), 371–377.

(45) Watson, J. K. G. Determination of Centrifugal Distortion Coefficients of Asymmetric-Top Molecules. III. Sextic Coefficients. *J. Chem. Phys.* **1968**, *48* (10), 4517–4524.

(46) Alonso, J. L.; Peña, I.; López, J. C.; Alonso, E. R.; Vaquero, V. The Shape of the Simplest Non-Proteinogenic Amino Acid α-Aminoisobutyric Acid (Aib). *Chem. - A Eur. J.* **2019**, *25* (9), 2288–2294.

(47) Ruoff, R. S.; Klots, T. D.; Emilsson, T.; Gutowsky, H. S. Relaxation of Conformers and Isomers in Seeded Supersonic Jets of Inert Gases. *J. Chem. Phys.* **1990**, *93* (5), 3142–3150.

(48) Bader, R. F. W. A Bond Path: A Universal Indicator of Bonded Interactions. *J. Phys. Chem.*

A **1998**, *5639* (98), 7314–7323.

(49) Koch, U.; Popelier, P. L. A. Characterization of C-H-O Hydrogen Bonds on the Basis of the Charge Density. *J. Phys. Chem.* **1995**, *99* (24), 9747–9754.

(50) Silva, W. G. D. P.; Silla, J. M.; Cormanich, R. A.; Fernandes, S. A.; Freitas, M. P. The Role of Nonbonding Interactions and the Presence of Fluoride on the Conformational Isomerism of 1,2-Ethanediol. *Chem. Phys.* **2016**, *473*, 17–23.

(51) Karas, L. J.; Batista, P. R.; Viesser, R. V; Tormena, C. F.; Rittner, R.; de Oliveira, P. R. Trends of Intramolecular Hydrogen Bonding in Substituted Alcohols: A Deeper Investigation. *Phys. Chem. Chem. Phys.* **2017**, *19* (25), 16904–16913.

(52) Lane, J. R.; Contreras-García, J.; Piquemal, J. P.; Miller, B. J.; Kjaergaard, H. G. Are Bond Critical Points Really Critical for Hydrogen Bonding? *J. Chem. Theory Comput.* **2013**, *9* (8), 3263–3266.

Chapter 5. Internal Motions and Sulfur Hydrogen Bonding in Methyl 3-Mercaptopropionate[2]

While in chapter 4 the importance of the S–H···O=C interaction was confirmed to play a major role in the conformational stability of 3-MPA, no transitions belonging to singly substituted isotopic species could be observed in the spectrum which prevented experimental structures from being derived. In this chapter, the conformational analysis of methyl 3-mercaptopropionate (3-MP) is reported to derive accurate geometric parameters and to evaluate the influence of the ester group on the S–H···O=C hydrogen bonding. The rotational spectrum of 3-MP showed complex patterns due to the presence of the methyl internal rotor and torsional motions of the SH group which are also discussed in detail below.

5.1 Abstract

The effect of sulfur hydrogen bonding on the conformational equilibrium of methyl 3-mercaptopropionate (3-MP) was investigated using microwave spectroscopy in a supersonic jet expansion. The two most stable conformers (I and II) were assigned in the rotational spectra and complex splitting patterns owing to the methyl internal rotation and SH tunneling motion were resolved and analyzed in detail. For both conformers, the experimental torsional barriers for the methyl top are similar and of about 5.1 kJ mol^{-1}, which reveal that their geometrical differences do

[2]The content of this chapter is an adapted version of the article published in the Journal of Physical Chemistry A under the citation: Silva, W. G. D. P.; Evangelisti, L.; van Wijngaarden, J. Internal Motions and Sulfur Hydrogen Bonding in Methyl 3-Mercaptopropionate, *J. Phys. Chem. A* **2019**, *123*, 9840–9849.

not affect the methyl internal rotation. The experimentally-derived rotational and centrifugal distortion constants, along with the methyl internal rotation barriers are discussed in detail and compared with results from density functional theory and *ab initio* calculations. Quantum theory of atoms in molecules, non-covalent interaction, and natural bond orbital analyses show that the global minimum geometry (I), which has the thiol hydrogen oriented towards the carbonyl of the ester, is stabilized by an S–H···O=C hydrogen bond. The presence of a hydrogen bond is confirmed by the derivation of an accurate experimental geometry that reveals a hydrogen bond distance and angle S–H–O of 2.515(4) Å and 117.4(1)º, respectively. These results are key benchmarks to expand the current knowledge of sulfur hydrogen bonds and the relationship between internal motions and conformational preferences in esters.

5.2 Introduction

The laudable goal of developing an improved understanding of structural, energetic and physical characteristics of non-covalent interactions has driven a range of recent experimental and theoretical studies.[1–3] This is due to the importance of such interactions in molecular recognition, for example, which directs chemical, biological, and technological processes.[2,4] For many decades, hydrogen bonding (HB) has been known to be the principal effect that governs the three dimensional structures of proteins, organic and organometallic molecules, and play a key role in the modulation of important reaction pathways.[5,6] Consequently, the nature of HBs has motivated numerous scientific investigations but these have mainly focused on strong HBs formed by oxygen and nitrogen, while much less attention has been devoted to weak interactions, such as those involving sulfur. Sulfur HBs are dispersive in nature, and due to their strength, it had been assumed

that they are not the key factor that determines the structures of S-containing molecules. However, recent experiments have highlighted the influence of sulfur HBs in ruling processes and conformational preferences, such as the determination of the secondary structures of proteins.[4] Consequently, benchmarking, characterizing, and understanding the nature of sulfur HBs are of increasing interest in the literature.[7–9] As recently reviewed by Biswal,[4] many systems still need to be experimentally analyzed in order to correctly address the nature, strength, and directionality of sulfur interactions.

Important initial steps in the characterization of non-covalent interactions involve determining the structures of model systems and establishing their relative stabilities using spectroscopic techniques along with computational methods. When it comes to interactions with low binding energies, such as sulfur HBs, the experimental elucidation becomes challenging as the interactions are easily disrupted depending on the physical state or solvent, for example. Fourier transform microwave (FTMW) spectroscopy is a useful approach to address the dearth of experimental data in the literature on weak non-covalent interactions as the molecules are interrogated in the gas phase in a collision-free supersonic jet expansion isolated from crystal packing and solvent effects.[2] Hence, the FTMW technique is a powerful method for the accurate determination of geometrical parameters associated with weak interactions, and for benchmarking purposes as shown by a few recent reports dealing with the characterization of sulfur HBs.[7,8,10]

FTMW studies of S-containing compounds show that sulfur forms a variety of intra- and intermolecular non-covalent interactions in the gas phase, where it can act as a proton donor and/or proton acceptor, as shown for the S–H···S, S–H···O, and S–H···O=C HBs in the H_2S dimer,[7] monohydrated clusters of furfuryl mercaptan,[8] and in the monomer of 3-mercaptopropionic acid,[10] respectively. In the latest study, the biologically important interaction between a thiol and a

carbonyl group has been proven for the first time in the gas phase, where the importance of this interaction in ruling the conformational equilibrium of the investigated compound was highlighted. A related molecule for the study of intramolecular S–H···O=C HBs is methyl 3-mercaptopropionate [HS–CH_2–CH_2–(C=O)–O–CH_3]. The presence of a methyl group in the ester version can lead to complex splitting patterns in the rotational spectrum which also makes this molecule a prototype system for the investigation of methyl internal rotation barriers (V_3) in esters and for probing the relationship between V_3 and conformational preference.[11–13] For thioacetic acid,[11] for example, the *anti* conformation has an experimental V_3 barrier that is approximately five times larger than the *syn* one mainly due to both steric repulsion and conjugative effects. In contrast, conformational differences in the *cis* and *trans* conformers of 5-methyl furfural[14] were shown to not play a role in the barriers for the methyl internal rotor. Determining the experimental V_3 in a variety of systems is often difficult but necessary for the development of improved methodologies to accurately model the spectra and dynamics of molecules in the gas phase and beyond. For large, flexible molecular systems that adopt multiple conformations,[11] such as methyl 3-mercaptopropionate, understanding the effects that govern the V_3 barriers brings more challenges since their values can be a result of the competition between steric hindrance, electronic delocalization, and conformational relaxation.

In this paper, we report the first rotational spectroscopic investigation of methyl 3-mercaptopropionate (3-MP) using chirped-pulse and cavity-based FTMW spectroscopy supported by quantum mechanical calculations. The observed spectrum of 3-MP is dominated by features that arise from two conformers (I and II) where the lowest energy one (I) is stabilized by an intramolecular HB involving sulfur. Further insights into the S–H···O=C HB are provided through the determination of an accurate experimental geometry for conformer I from analyzing

the spectra of five heavy atom isotopologues, and from the energies derived from the topological quantum theory of atoms in molecules and non-covalent interaction analyses. The experimental methyl internal rotation barriers for conformers I and II and the conformational influences on their values are analyzed in detail aided by computational models. Together, these results expand the current understanding of both sulfur HBs and the relationship between tunneling motions and conformational preference in the gas phase.

5.3 Methods

5.3.1 Computational Methods

Theoretical calculations are first used to identify low-energy conformations and to derive relevant molecular properties, such as rotational constants and dipole moment components, which are crucial for the assignment of the conformers in the rotational spectrum. Based on the principle that each conformation has its unique rotational spectral fingerprint, comparison between experimental and calculated data is used to distinguish among the different species and to confirm the assignments.

For 3-MP, forty-one possible geometries were identified using the Merck Molecular Force Field (MMFF94),[15] implemented in the Marvin Sketch 16.10.10 program (ChemAxon version 6.1). These geometries were further optimized using the DFT dispersion-corrected B3LYP functional with Becke-Johnson (BJ) damping, named B3LYP-D3(BJ),[16–18] and the *ab initio* second-order Møller-Plesset (MP2)[19] perturbation theory method with the aug-cc-pVTZ[20] basis set. The chosen levels of theory have provided satisfactory results when compared to experimental

data for the carboxylic acid analog of 3-MP.[10] Frequency calculations were also carried out to verify the nature of the stationary points and to derive the electronic energy with zero-point energy (ZPE) corrections and the Gibbs free energies at 298 K. The optimization and frequency calculations led to nine true energy minima with relative energies below 11.0 kJ mol^{-1}. These calculations were carried out using the Gaussian 16 revision B.01[21] software.

Natural bond orbital (NBO),[22] quantum theory of atoms in molecules (QTAIM),[23] and non-covalent interaction (NCI)[24] analyses were performed to visualize and quantify intramolecular interactions in the observed conformers. These were carried out using the NBO 6.0,[25] AIMAll,[26] and NCIPLOT[27] programs, respectively.

5.3.2 Experimental Section

The pure rotational spectra of 3-MP (Sigma-Aldrich Canada, 98.0%) were recorded using chirped-pulse (CP) and Balle-Flygare[28] Fourier transform microwave (FTMW) spectrometers, which have been described in detail previously.[29,30] Briefly, liquid 3-MP (bp: 327 - 328K/ 1.8 kPa) was placed into a glass bubbler and neon (100 kPa) was used as a carrier gas to deliver the sample into the spectrometers' high vacuum (P ~10^{-6} Torr) chambers through a pulsed nozzle (1 mm diameter). The pressure difference between the sample manifold and the chambers results in a supersonic jet, where the rotational temperature of the sample is cooled down to a few Kelvin favoring low-energy conformers. Initial measurements were performed using the CP-FTMW instrument, where the broadband spectra of the compound were recorded from 8-18 GHz in segments of 2 GHz. Final measurements were performed in the same frequency range using the Balle-Flygare FTMW spectrometer which provides better resolution and sensitivity. In this design,

the molecular beam is coaxial with the resonator axis and thus, all rotational transitions are split into two Doppler components. The transitions typically have line widths of ~7 kHz (FWHM), while the line positions are determined to within about ±1 kHz.

5.4 Results

The nine conformers of 3-MP are depicted in Figure 5.1, while their Cartesian coordinates are given in Tables S12-S20. The calculated relative energies and rotational parameters (rotational constants and dipole moment components) are provided in Table 5.1. We report the conformers with relative energies below 11.0 kJ mol^{-1} since only low-energy conformations are expected to be sufficiently populated in the supersonic jet expansion and consequently, observed in the rotational spectra. The conformers are labeled using Roman numerals, from I to IX which represents their order of stability based on the relative Gibbs free energies (ΔG) from B3LYP-D3(BJ)/aug-cc-pVTZ.

The conformational behaviour of 3-MP reveals that the geometries adopted by its conformers have C–C–C–S dihedral angles of either approximately 60-70º or 180º, as exemplified by the structures of I and II in Figure 5.1, respectively. A similar conformational equilibrium has been recently observed for its carboxylic acid analog, 3-mercaptopropionic acid.[10] For 3-MP, the presence of a methyl group in its structure results in a competitive conformational equilibrium where nine energy minima are significantly populated at room temperature. The three most stable conformers (I, II, and III) closely resemble those obtained for its acid analog such that the global minimum geometry has the hydrogen of the thiol group directly oriented towards the carbonyl of the ester. Energy calculations show that the most stable geometry is favored by at least 2.1 kJ mol^{-1}

when compared to the remaining conformations. In the case of the higher energy conformations, close relative energies between specific geometries are observed, and their energy orderings and abundances vary depending on the level of theory, as exemplified by the theoretical results obtained for II and III (Table 5.1). Overall, the predicted rotational parameters for each conformer in the two levels of theory are consistent.

Based on the fact that the intensity of the rotational transitions depends on the dipole components along the principal axes system and population of the rotational energy levels, populated species with sizeable dipole moments are good candidates to start with the experimental investigations. As all have sufficient dipoles, we focused first on the assignment of rotational transitions belonging to the most stable geometries of 3-MP.

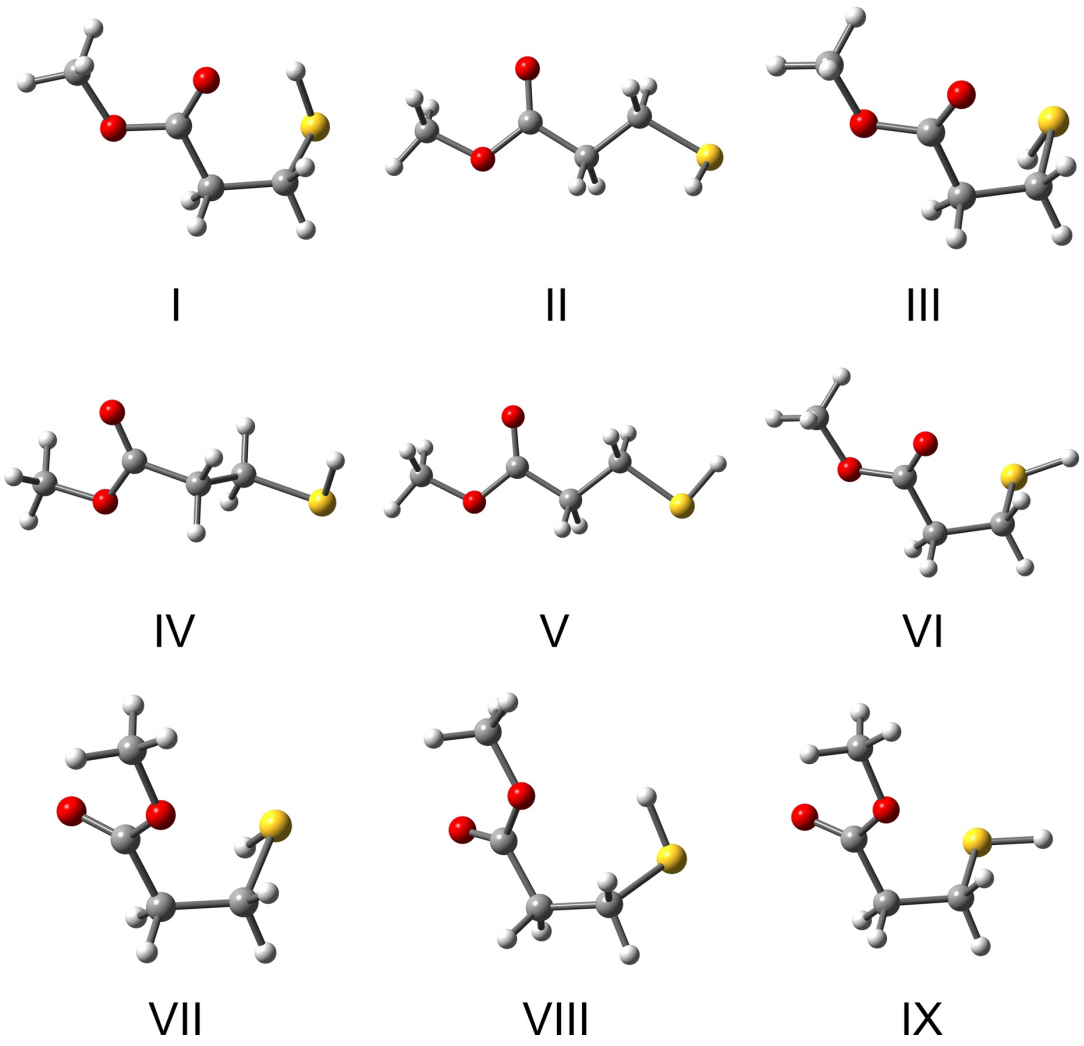

Figure 5.1 Nine conformers of methyl 3-mercaptopropionate. Carbons, oxygen, sulfur and hydrogen atoms are depicted in grey, red, yellow, and white colours, respectively.

Table 5.1 Calculated rotational parameters and relative energies (DFT B3LYP-B3(BJ) and *ab initio* MP2, aug-cc-pVTZ) for the conformers of methyl 3-mercaptopropionate.

	B3LYP-D3(BJ)				MP2			
Conformer	$A/B/C$[a]	$\|\mu_a\|/\|\mu_b\|/\|\mu_c\|$[b]	ΔE_{ZPE}[c]/ΔG[d]	$P(\Delta E_{ZPE})$[e]/ $P(\Delta G)$[f]	$A/B/C$[a]	$\|\mu_a\|/\|\mu_b\|/\|\mu_c\|$[b]	ΔE_{ZPE}[c]/ΔG[d]	$P(\Delta E_{ZPE})$/ $P(\Delta G)$
I	5046/1055/987	2.0/1.7/0.2	0.0/0.0	60.2/42.1	4916/1093/1021	2.0/1.9/0.2	0.0/0.0	61.0/44.6
II	8256/796/739	1.8/1.6/0.6	4.2/2.1	11.6/18.6	8267/806/748	1.7/1.7/0.7	5.0/2.9	7.8/14.1
III	4290/1101/1055	0.9/1.2/2.2	4.2/2.9	11.2/13.0	4099/1172/1107	0.6/1.2/2.5	4.2/2.9	11.0/14.6
IV	5984/864/796	0.9/1.1/0.1	7.9/3.8	2.4/8.8	6025/876/808	0.8/1.1/0.2	8.4/4.6	2.2/7.0
V	8160/807/745	1.3/0.5/0.0	6.3/4.2	2.3/3.9	8173/819/754	1.2/0.5/0.0	7.1/5.0	1.8/3.1
VI	4163/1124/1060	0.5/0.9/1.0	8.4/5.4	2.0/4.4	3921/1219/1119	0.0/0.8/1.1	8.8/6.3	2.0/3.8
VII	3422/1295/1180	0.2/0.2/2.1	6.3/5.8	4.7/4.2	3404/1346/1232	0.4/0.4/2.3	5.4/5.0	6.8/6.0
VIII	3483/1294/1124	0.5/0.7/2.3	6.3/5.8	4.8/4.2	3474/1331/1171	0.4/0.6/2.6	5.4/5.0	6.4/5.6
IX	3537/1249/1175	0.1/0.8/3.1	10.9/9.6	0.8/0.8	3519/1297/1231	0.4/0.6/3.4	10.0/9.2	1.0/1.2

[a]Rotational constants (A, B, and C) in MHz; [b]Absolute values of the electric dipole moment components in D; [c]Relative energies with respect to the global minimum accounting for zero-point energy (ZPE) corrections in kJ mol^{-1}; [d]Relative Gibbs free energies with respect to the global minimum calculated at 298K in kJ mol^{-1};[e]Population based on the relative energies with ZPE correction in %; [f] Population based on the relative Gibbs free energies in %.

To identify conformers in the rotational spectrum, we used the predicted data from Table 5.1 to obtain a simulated spectrum for each using the PGOPHER program.[31] Initial study of the CP-FTMW broadband spectrum led to the identification of two sets of R-branch *a*- and *b*-type rotational transitions belonging to two different conformers suggesting that the carriers are species with significant values of $|\mu_a|$ and $|\mu_b|$. To confirm the quantum number assignments and predict related transitions for each, initial fits were carried out using the PGOPHER program. By comparing the experimental rotational constants with the calculated ones in Table 5.1, the assigned transitions were attributed to the parent species of conformers I and II which both have sizeable $|\mu_a|$ and $|\mu_b|$ dipole components. Additional measurements were carried out using the cavity-based FTMW spectrometer to record transitions with higher resolution and sensitivity. Despite accurate line positions, no *c*-type transitions could be assigned in the spectra of I and II which is consistent with the small predicted values of $|\mu_c|$.

The cavity-based spectra observed for the parent species of both conformers show complex patterns due to the A/E splitting of the methyl internal rotor. Surprisingly, for the less intense set of transitions, attributed to II, additional splitting ascribed to a torsional motion of the SH group around the C–C–S–H dihedral angle was also observed. We describe the methyl top and SH tunnelling motions in detail below. For conformer I, the intensities of the transitions were sufficient to proceed with the identification of the rotational transitions of its singly substituted ^{34}S and all four ^{13}C isotopologues in natural abundance. The spectra of the minor isotopes also exhibit the complex A/E splitting pattern which is analogous to the pattern observed for the parent species of I. A sample of the broadband spectrum illustrating some assigned rotational transitions for the parent species of both conformers and for the isotopic species of I is presented in Figure 5.2. Two

specific *a*-type transitions showing the very different splitting patterns observed for the parent species of I and II using the Balle-Flygare instrument are shown in Figure 5.3.

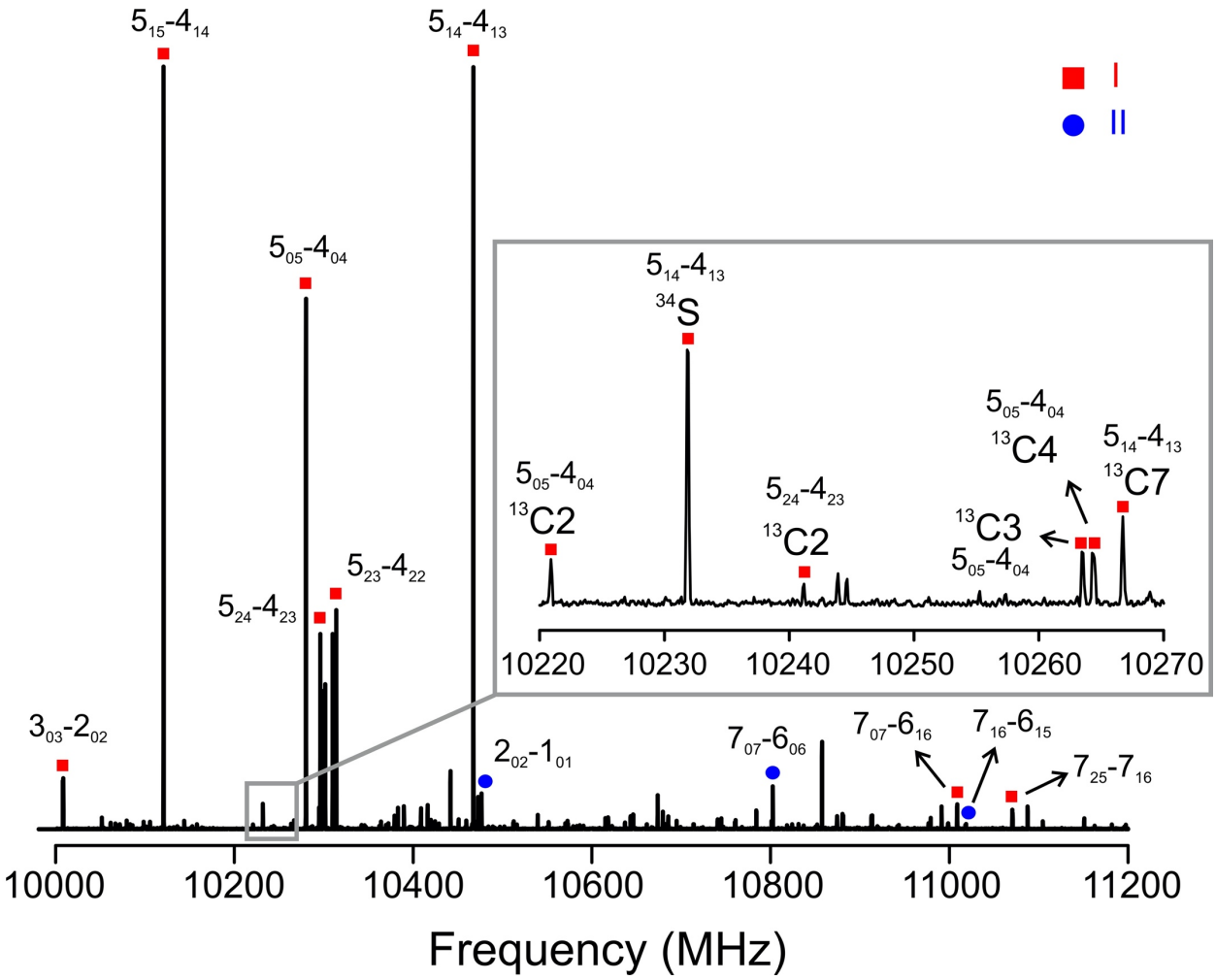

Figure 5.2 Portion of the broadband CP-FTMW spectrum of methyl 3-mercaptopropionate highlighting some rotational transitions observed for the species of conformers I and II. In the figure, the A/E splitting cannot be distinguished on this scale.

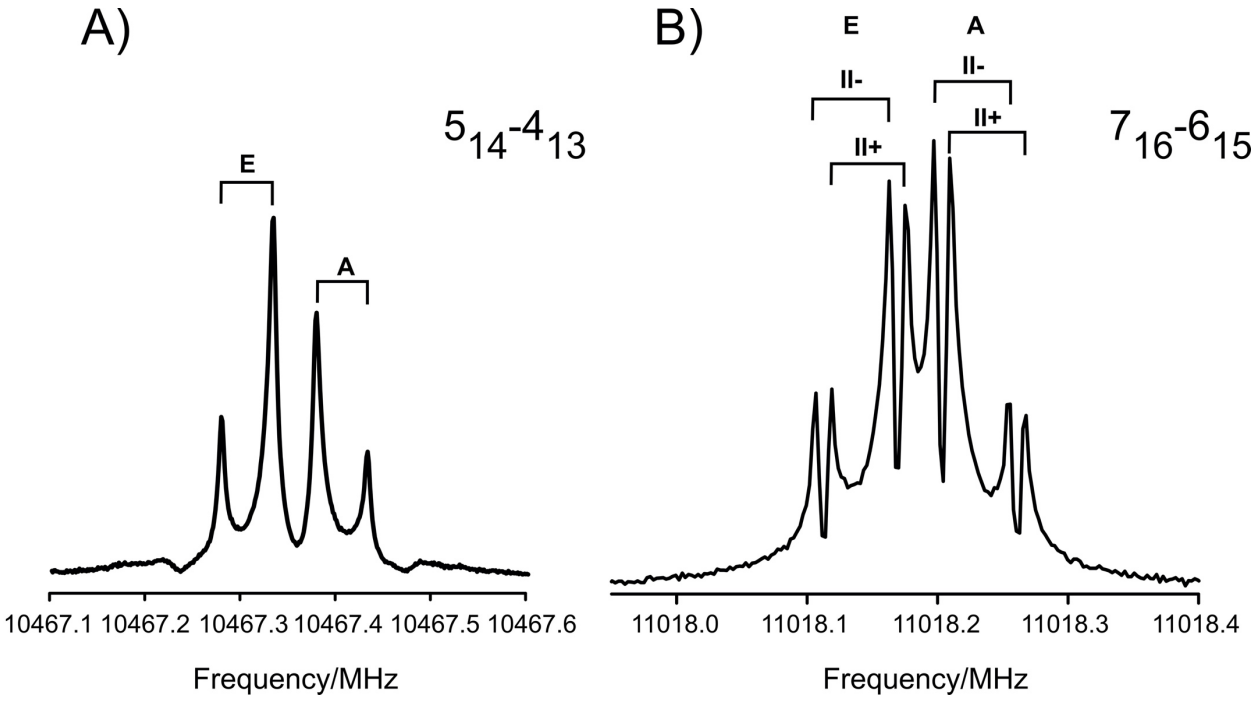

Figure 5.3 Sample of the cavity-based rotational spectra showing the different splitting patterns observed for the parent species of conformers A) I and B) II. The splitting is due to the internal rotation of the methyl top (A/E) and the torsion motion of the SH group (+/-).

The experimental transition frequencies for the parent and isotopic species of I were fit using the XIAM program[32] which applies the combined axis method (CAM) to account for the methyl internal rotation. The program is suitable for relatively high barrier cases such as those experienced here. For II, on the other hand, due to the presence of the additional splitting, two different approaches were used to test which would provide a better model. First, separate XIAM fits were performed for each of the two tunnelling states associated with the torsion of the SH group, labeled by us as II+ and II-. This approach has also been used in the study of monohydrate complexes containing similar internal motions.[33,34] Afterwards, we were also able to fit the A and E states independently using Pickett's SPFIT program.[35] Since the structures of both conformers are that of near prolate asymmetric tops, Watson's S-reduced Hamiltonian[36] in the I^r representation

was used for all performed fits. The experimental rotational, centrifugal distortion, and internal rotation constants for species I and II are shown in Table 5.2 and Table 5.3, respectively. The full lists of measured rotational transitions, assignments and residuals for the least squares fits are given in Tables S21-S30.

Table 5.2 Experimental spectroscopic parameters for the species of conformer I of 3-MP. Watson's S-reduced Hamiltonian (I^r representation).

	Parent	^{34}S	^{13}C2	^{13}C3	^{13}C4	^{13}C7	B3LYP-D3(BJ)
A (MHz)	5067.02148(76)	5026.1976(21)	5020.1700(33)	4992.109(40)	5063.684(51)	5049.805(66)	5046
B (MHz)	1064.48640(79)	1040.28494(17)	1058.63732(41)	1064.47025(18)	1062.77678(21)	1043.83172(19)	1055
C (MHz)	995.13673(89)	973.43053(18)	989.18841(39)	992.21527(17)	993.67461(23)	976.74003(22)	987
D_J (kHz)	0.40681(50)	0.39954(66)	0.3987(13)	0.40117(56)	0.40595(67)	0.39227(69)	0.39
D_{JK} (kHz)	-6.1099(29)	-6.1497(71)	-5.895(14)	-5.9614(65)	-6.1109(74)	-6.0213(85)	-6.00
D_K (kHz)	43.65(15)	44.27(37)	[43.65]	[43.65]	[43.65]	[43.65]	45.17
d_1 (kHz)	0.01276(53)	0.01050(75)	0.0106(19)	0.01026(87)	0.0136(10)	0.0124(11)	0.01
d_2 (kHz)	-0.00359(28)	-0.00231(46)	[-0.00359]	[-0.00359]	[-0.00359]	[-0.00359]	-0.003
V_3 (kJ/mol)	5.0696(87)	5.0696(13)	5.0858(47)	5.0782(18)	5.0821(21)	5.0887(21)	
F_0 (GHz)	161.12(26)	[161.12]	[161.12]	[161.12]	[161.12]	[161.12]	
δ (rad)	0.6330(13)	0.6376(16)	0.6115(55)	0.6210(21)	0.6234(24)	0.6123(24)	
I_α (uÅ^2)	3.1365(50)	[3.1365]	[3.1365]	[3.1365]	[3.1365]	[3.1365]	
N^a	117	101	53	51	47	41	
σ^b (kHz)	2.2	3.0	3.5	1.5	1.6	1.4	

[a] Number of lines in the fit; [b]Root-mean-square deviation of the fit; Values in [] were fixed to the calculated values.

Table 5.3 Experimental spectroscopic parameter for the parent species of conformer II of 3-MP. Watson's S-reduced Hamiltonian (I^r representation).

	XIAM		SPFIT		B3LYP-D3(BJ)
	II+ (A+/E+)	II- (A-/E-)	A+/A-	E+/E-	
A (MHz)	8242.8876(34)	8242.8885(43)	8244.1907(20)	8242.2278(57)	8256
B (MHz)	801.74647(17)	801.74804(19)	801.74070(21)	801.73912(23)	796
C (MHz)	744.12096(16)	744.12031(19)	744.12821(20)	744.12826(27)	739
D_J (kHz)	0.02566(73)	0.02556(86)	0.02659(98)	0.0250(11)	0.02
D_{JK} (kHz)	[0.21]	[0.21]	[0.21]	[0.21]	0.21
D_K (kHz)	[13.49]	[13.49]	[13.49]	[13.49]	13.49
d_1 (kHz)	[-0.002]	[-0.002]	[-0.002]	[-0.002]	-0.002
d_2 (kHz)	[0.00009]	[0.00009]	[0.00009]	[0.00009]	0.00009
V_3 (kJ/mol)	4.567(28)	4.563(36)			
F_0 (GHz)	144.67(74)	144.32(99)			
δ (rad)	0.236(20)	0.227(24)			
Da (MHz)				19.271(17)	
I_α (uÅ^2)	3.493(18)	3.502(24)			
N^a	57	59	60	53	
σ^b (kHz)	4.8	5.8	6.4	6.8	

[a] Number of lines in the fit; [b]Root-mean-square deviation of the fit; Values in [] were fixed to the calculated values.

5.5 Discussion

5.5.1 Rotational Spectroscopic Data

The highly accurate experimentally-derived ground state rotational constants (*A*, *B*, and *C*) for 3-MP show good agreement with those of the equilibrium geometries obtained theoretically. This unequivocally confirms the assignment of conformers I and II. The B3LYP-D3(BJ) method provides the best match with the experimental data, where the largest deviation (~21 MHz) is observed for the *A* rotational constant of the parent species of I. The quartic centrifugal distortion constants (D_J, D_{JK}, D_K, d_1, and d_2) agree very well with the calculated ones obtained through anharmonic frequency calculations at the B3LYP-D3(BJ)/aug-cc-pVTZ level of theory, providing an additional check for the assignments. The B3LYP-D3(BJ) method also showed the best results for the carboxylic acid version of 3-MP, 3-mercaptopropionic acid.[10] The experimental three-fold barrier to internal rotation V_3, along with other internal rotor parameters, such as the rotational constant of the methyl top (F_0), the angle between its α-axis and the principal *a*-axis of the molecule (δ), and its moment of inertia (I_α), were successfully obtained with the XIAM code.

The parameters that were not well-determined in the fits were fixed to either the parent species values, as in the case of some centrifugal distortion and internal rotation constants for the singly substituted isotopes of I, or the calculated ones, as for some centrifugal distortion constants of II. In the case of the latter, we also performed both the XIAM and SPFIT fits by varying only D_J, while the other centrifugal distortions constants were set to zero. For the SPFIT fits, the errors in the fits were similar to those reported in Table 5.3 (σ = 6.4 kHz for A^+/A^-, and σ = 6.3 kHz for E^+/E^-), while for the XIAM fits the values of σ were 2.8 kHz and 7.0 kHz for II+ and II-,

respectively. With the constants fixed, satisfactory fits were obtained, which confirms that isotopic substitution does not significantly change the parameter values, and that the employed level of theory describes the system under investigation well.

For conformer II, it is worth noting that the absence of cross-tunneling *c*-type rotational transitions in our spectrum prevented us from determining the energy difference between the A+/A- or E+/E- in the conformer II states in the SPFIT fits but the A and E states were fit independently. This fitting approach is typical for molecular systems having both an internal V_3 rotor and a separate tunnelling motion that involves the torsion of a water subunit in a complex, as specified previously in ref. 33 and 34. However, when the second tunneling involves ~120° rotation of a hydroxyl (-OH) or even bigger group,[37] the fits for the + and – states are coupled. Interestingly, this might be one of the first cases where a system containing tunneling splitting from both internal V_3 rotation and another torsional motion provide reasonable independent fits without the consideration of Coriolis coupling effects. For example, in the rotational spectroscopic study of the formic–acetic acid complex,[38] which presents complex splitting patterns due to coupled internal motions from methyl internal rotation and double proton transfer, the authors mention that they were not able to treat the A and E states independently since the fits for the E state were not satisfactory without the inclusion of transitions that connect the tunneling states.

5.5.2 Tunneling Motions

The potential energy surface for the internal rotation of a methyl group possess three equivalent energy minima and gives rise to a non-degenerate (A) and two-fold degenerate (E) state which result in rotational transitions that are tunneling split. Figure 5.4 shows the theoretical

potentials for the rotation of the methyl group in conformers I and II where both B3LYP-D3(BJ) and MP2 methods predict the two geometries to have similar barriers to internal rotation of approximately 3.6 kJ mol^{-1} and 4.8 kJ mol^{-1}, respectively. The experimentally determined three-fold barriers V_3 obtained for each conformer are indeed similar and have values of about 5.1 kJ mol^{-1} and 4.6 kJ mol^{-1} for I and II, respectively. Although it has been shown that conformational changes can lead to significant variations in V_3, as shown in the rotational study of thioacetic acid for example,[11] the differences in the geometries of I and II do not strongly affect the methyl internal rotation in 3-MP. Since the V_3 barriers depend on steric hindrance and the electronic structure of molecules,[11,14] the experimental outcomes in this work suggest that the electronic distribution of the methyl groups in I and II are very similar. Thus, even though I is expected to be stabilized by an S–H···O=C intramolecular hydrogen bond (IHB), this interaction does not seem to play an important role in the rotation of the methyl top. The experimental V_3 barriers obtained for the 3-MP conformers are also similar to values reported in the literature for its smaller version (methyl thioglycolate, $V_3 \sim 4.9$ kJ mol^{-1})[39] and other studied systems containing esters as functional groups, such as its hydrocarbon version: methyl propionate ($V_3 \sim 5.1$ kJ mol^{-1}).[40] By comparing the results, one can see that changes in the side chain of the molecule with respect to the ester group in those examples, such as the presence of a five-membered ring in the former, and the absence of the SH group in the latter, do not lead to significant variations in the internal of rotation of the methyl top.

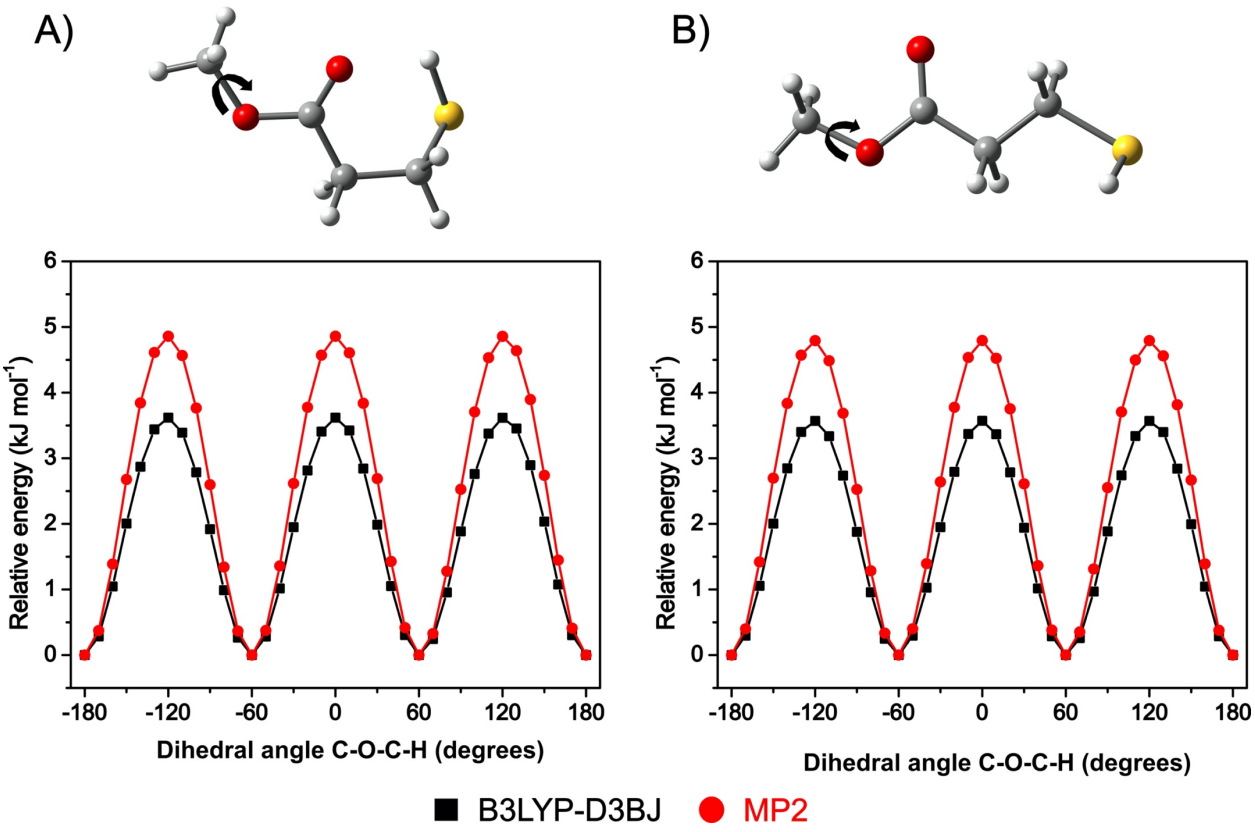

Figure 5.4 Potential energy curves for the methyl internal rotation in conformers A) I and B) II. The plots were obtained using the B3LYP-D3(BJ) and MP2 methods with the aug-cc-pVTZ basis set by varying the C–O–C–H dihedral angle in 36 steps of 10 degrees each.

To better understand the additional tunneling splitting observed in the rotational transitions of II, attributed to a torsional motion of the SH group, we performed scan calculations by rotating the C–C–S–H dihedral angle in 36 steps of 10 degrees each. This shows that the observed tunneling is characterized by a double-well potential energy function (Figure 5.5) that allows the interconversion between the two equivalent forms (mirror images) of II through a calculated energy barrier of approximately 7.0 kJ mol^{-1}. The predicted barriers are consistent with the small splitting observed experimentally.

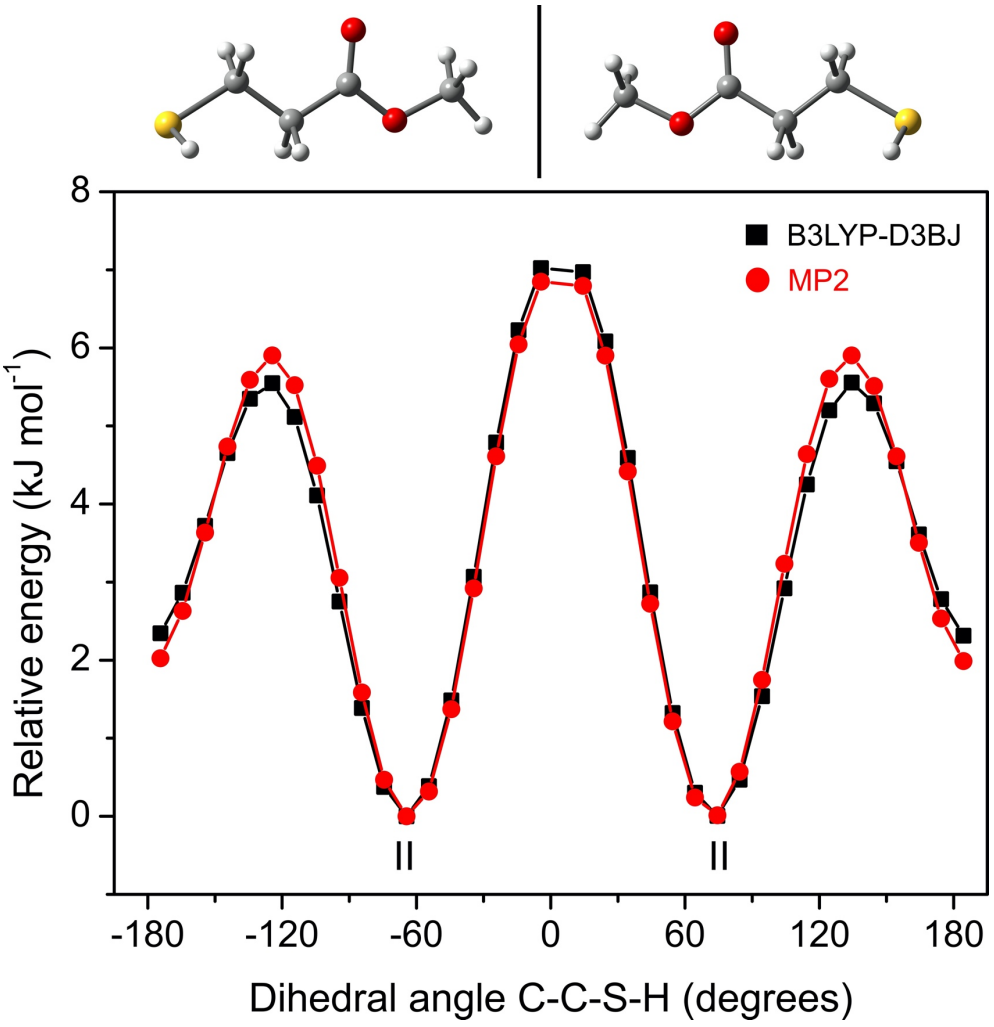

Figure 5.5 Potential energy curve for the torsional motion of the SH group in conformer II. The plot was obtained by the rotation of the SH group around the C–S bond in 36 steps of 10 degrees each using the B3LYP-D3(BJ) and MP2 methods with the aug-cc-pVTZ basis set.

5.5.3 Relaxation Pathways

Despite an extensive experimental search, transitions due to other conformers were not identified in the rotational spectrum of 3-MP. The experimentally observed conformers I and II are predicted to account for more than 58.7% (Table 5.1) of the total conformational equilibrium (100.0%) at room temperature, while the remaining population is spread among the other true energy minima. Since we were able to detect transitions belonging to the ^{13}C singly substituted isotopes of I which are about 1.0% of the intensity observed for the parent species, one may expect the observation of other higher energy conformations in the supersonic jet, such as conformer III (Table 5.1).

To explore the absence of transitions related to additional geometries in the rotational spectra, we carefully investigated the complex conformational distribution and predicted relaxation pathways for the conversion of higher energy conformations to lower energetic ones. It is well known from empirical studies that in the supersonic jet expansion, energy barriers of re-arrangements of ~4.8 kJ mol^{-1} or higher prevent relaxation and allow the observation of metastable conformers.[41] For example, the only difference in the geometries of II and V is in the orientation of the SH group and thus, relaxation from V to II could take place in the supersonic jet depending on the energy required for this SH torsional motion. The conversion pathway from V to II, calculated by the rotation of the SH group in 24 steps of 10 degrees each (Figure 5.6A), reveals an energy barrier of approximately 3.2 kJ mol^{-1} – 3.9 kJ mol^{-1}. Thus, V is expected to experience facile relaxation in the supersonic jet and will not be observed experimentally. Likewise, we carried out several scan calculations for possible relaxation pathways between other similar conformer pairs and the obtained potential energy curves are shown in Figure 5.7. The calculations

indicate that the following relaxations may occur during the experiments: V→II (3.2 kJ mol^{-1} – 3.9 kJ mol^{-1}), VI→I (0.0 kJ mol^{-1} – 0.3 kJ mol^{-1}), VIII→I (2.3 kJ mol^{-1} – 2.9 kJ mol^{-1}), and IX→VIII (1.1 kJ mol^{-1} – 1.6 kJ mol^{-1}). Therefore, conformers V, VI, VIII, and IX are not expected to be observed experimentally.

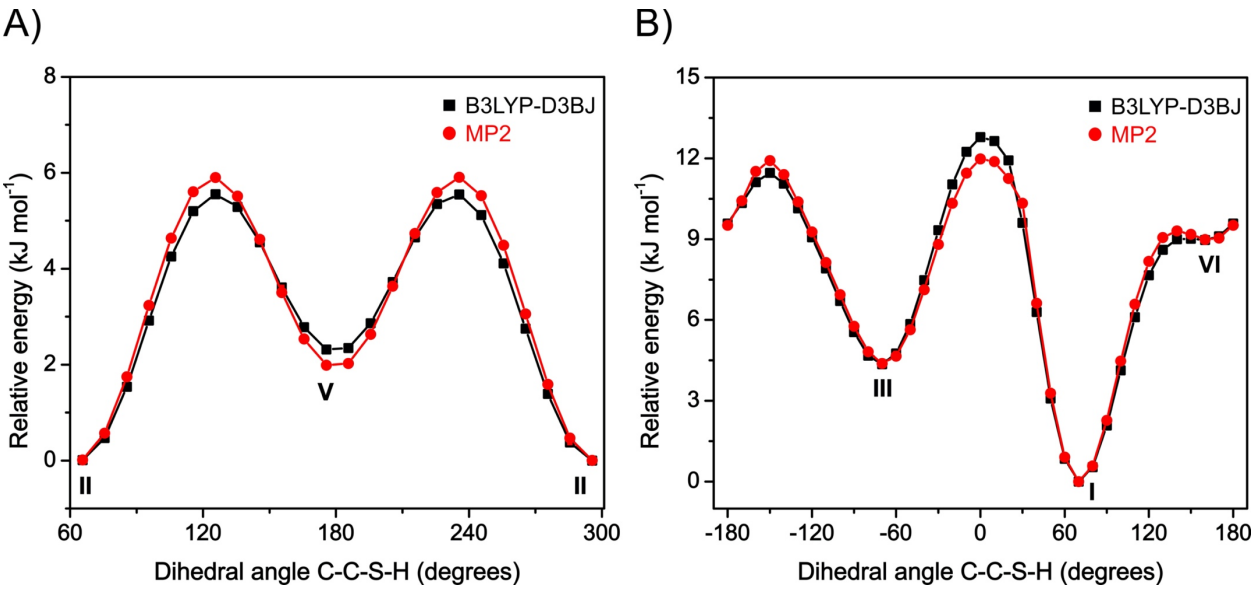

Figure 5.6 Conversion pathway between conformers A) II and V and B) III, I, and VI obtained by varying the torsional motion of the SH group. The potential energy curves were calculated using the B3LYP-D3(BJ) and MP2 methods with the aug-cc-pVTZ basis set.

Theoretically, the barrier of conversion (approximately 8.4 kJ mol^{-1} – 7.6 kJ mol^{-1}) from III to I (Figure 5.6B) would prevent its relaxation in the supersonic jet and III should be observed experimentally. It is worth noting that the conversion VI→I, which also involves the SH torsion motion, is estimated to be barrierless while that calculated from III→I is relatively high. The main reason for the high energy barrier in the latter is because in the conversion pathway from III to I, the transition state structure adopts a geometry where the SH group is oriented towards the non-carbonyl oxygen of the ester (C–C–S–H ≈ 0º) which likely increases the energy of conversion.

Although III should be metastable in the supersonic jet, its spectrum is dominated by *c*-type transitions and as only a few fall within the range of our spectrometer, a convincing assignment for conformer III was not attained.

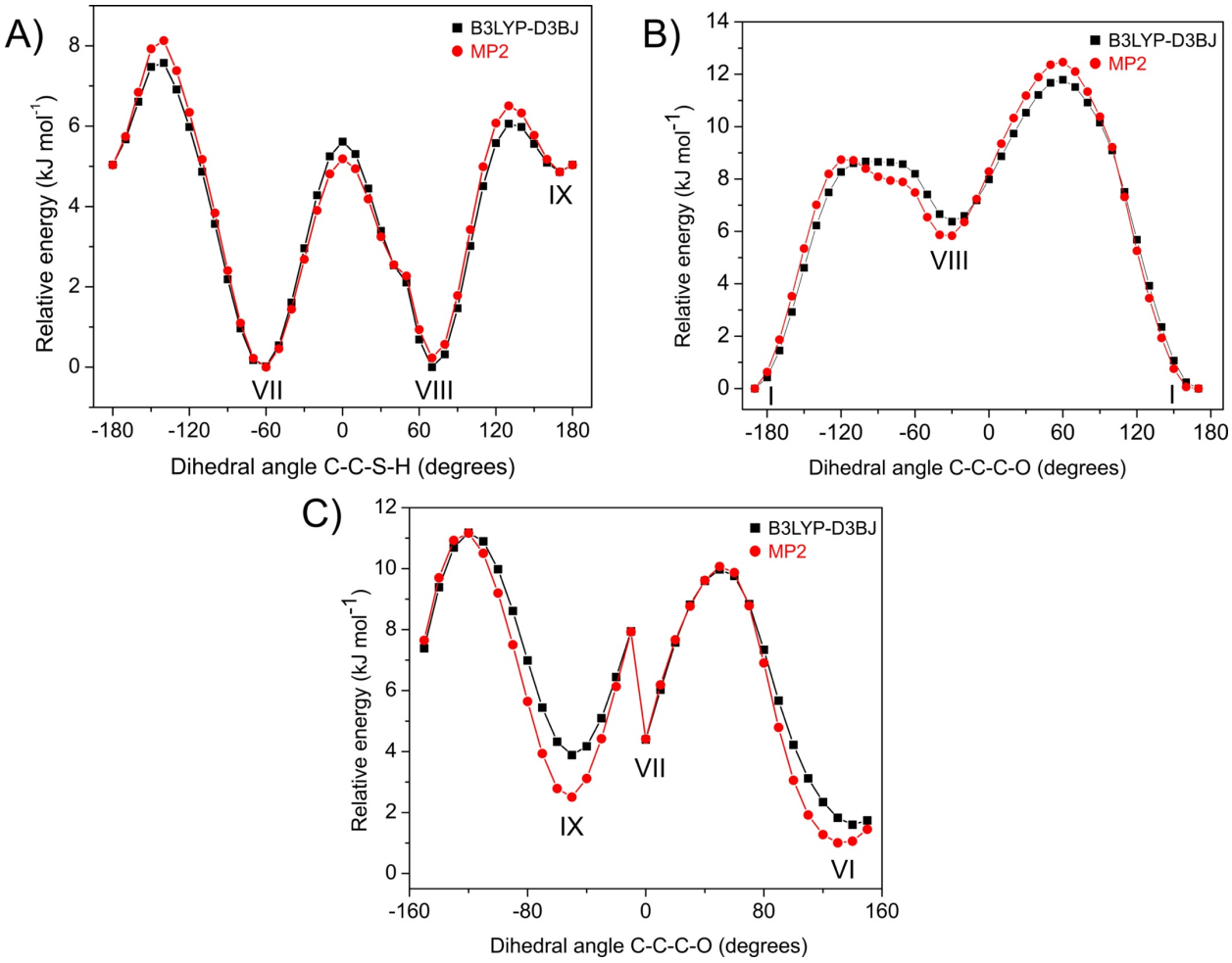

Figure 5.7 Conversion pathway between conformers A) VII, VIII, and IX B) I and VIII, C) VI, VII, and IX. The potential energy curves were calculated using the B3LYP-D3(BJ) and MP2 methods with the aug-cc-pVTZ basis set.

5.5.4 Intramolecular Hydrogen Bond and Structural Determination Analysis

To confirm the stability and to estimate the strength of the S–H···O=C intramolecular hydrogen bond (IHB) in conformer I, we carried out quantum theory of atoms in molecules (QTAIM) and non-covalent interactions (NCI) analyses. The NCI analysis (Figure 5.8A) shows a weak attractive (blue-greenish isosurface) interaction for the S–H···O=C close contact. The interaction is confirmed by the QTAIM analysis (Figure 5.8B) where a bond path (BP) and a bond critical point (BCP) are visualized between the thiol hydrogen and the carbonyl oxygen. The QTAIM molecular graph also shows a ring critical point (RCP) related to the repulsive interactions of the six-membered ring which arises upon HB formation. The energy of the S–H···O=C IHB can be estimated using the electronic potential energy at the BCP (V_{BCP}), as $E_{IHB} = 0.5|V_{BCP}|$.[42] The calculated E_{IHB} in I is of about 6.6 kJ mol^{-1} which confirms the weak character of the S–H···O=C IHB. In addition to the QTAIM and NCI topological analyses, we also carried out the natural bond orbital (NBO) calculations at the B3LYP-D3(BJ)/aug-cc-pVTZ level of theory. The NBO results show charge transfer from both lone–pairs [LP_1(O) and LP_2(O)] of the carbonyl oxygen to the anti-bonding orbital of the S–H bond ($\sigma^*_{S–H}$), evidenced by $LP_1(O) \rightarrow \sigma^*_{S–H}$ = 0.3 kJ mol^{-1} and $LP_2(O) \rightarrow \sigma^*_{S–H}$ = 1.4 kJ mol^{-1} hyperconjugative interactions, which also confirms the occurrence of the weak S–H···O=C IHB in I. Overall, the three computational approaches suggest that the presence of the sulfur IHB in I is the main reason for its higher stability over the other conformers. The role of this interaction has also been shown to be the explanation for the stabilization of the global minimum geometry of its acid analog.[10]

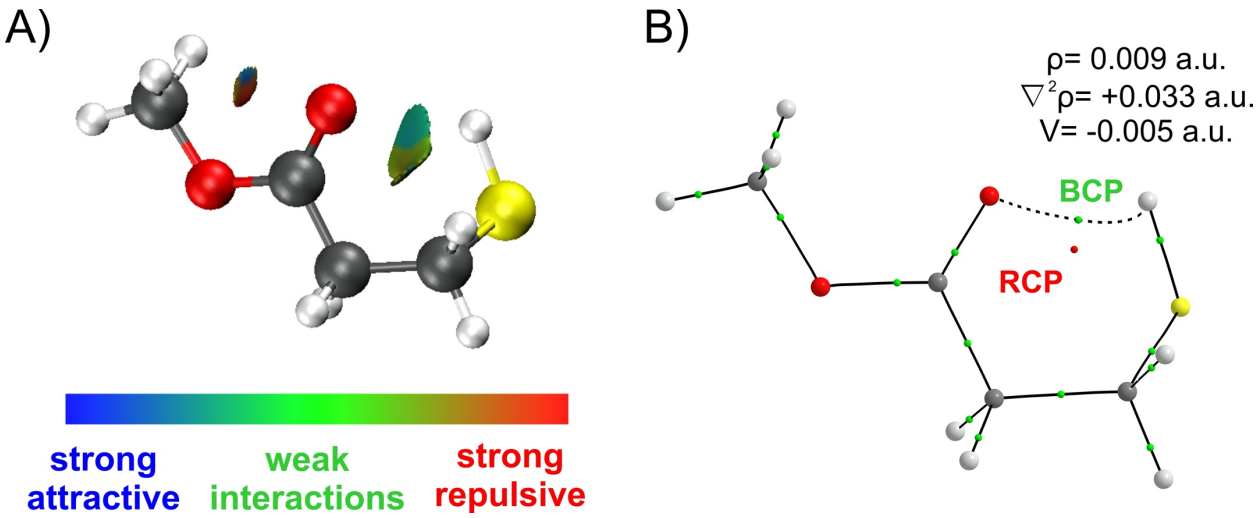

Figure 5.8 A) NCI isosurface (s= 0.5 au; colour scale of -0.02 < ρ < 0.02) and B) QTAIM molecular graph of conformer I. ρ, $\nabla^2\rho$, and V are the electron density, its Laplacian, and the potential energy at the BCP S–H···O=C.

Based on the experimental determination of the rotational constants for the parent species of I and its minor ^{34}S and ^{13}C singly substituted isotopic species, we derive key geometric parameters from its partial ground state geometry r_0 using Kisiel's STRFIT[43] least squares fitting program. Since our interest lies in understanding the IHB S–H···O=C, we focused our structural determination on the bond lengths and angles associated with the six-membered ring formed due to the IHB. The set of 18 rotational constants were used to fit six parameters which are the S1–C2, C2–C3, and C3–C4 bond distances, S1–C2–C3 and C2–C3–C4 bond angles, and the S1–C2–C3–C4 dihedral angle, while the other distances and angles were fixed to the values from B3LYP-D3(BJ)/aug-cc-pVTZ. By using the principal coordinates and their estimated uncertainties from the STRFIT outcome, the HB distance O5···H8 and angles C4–O5–H8 and S1–H8–O5, and the distance of the S1–H8 and C4=O5 bonds were determined trigonometrically along with their propagated uncertainties using the EVAL program.[44] The values for the fit parameters and their associated uncertainties along with the equilibrium geometries obtained theoretically are shown in

Table 5.4. The derived parameters confirm the *gauche* arrangement of the backbone where the dihedral angle S1–C2–C3–C4 is equal to -68.9(2)º and reveal that the HB distance H8···O5 and angle S1–H8–O5 are 2.515(4) Å and 117.4(1)º, respectively. The H8···O5 is less than the sum of their van der Waals radii (~2.72 Å), and the angle S1–H8–O5 is consistent with those observed for six-membered ring HBs. The HB distance involving the carbonyl oxygen in I is slightly smaller when compared to the intermolecular S–H···O HB distance of 2.44(3) Å observed in the monohydrated cluster of furfuryl mercaptan.[8] By comparing the hydrogen bond parameters obtained for the S–H···O=C in 3-MP with those for the six-membered ring O–H···O=C in 3-hydroxypropionic acid,[45] once can see that the HB distance S–H···O [2.515(4) Å] in the former is slightly longer when compared to the O–H···O (2.127Å) in the latter. On the other hand, the angle S–H–O [117.4(1)º] is slightly smaller than the O–H–O (129.6º). The observed differences in the HB distances and angles are consistent with the fact that the oxygen analog is expected to present stronger HBs when compared to the sulfur one. Although weaker than the O–H···O=C, the experimental results in this work clearly shows the importance of the S–H···O=C IHB in ruling the conformational equilibrium of S-containing compounds, in particular, 3-MP.

Table 5.4 Ground state effective (r_0) and equilibrium (r_e) (B3LYP-D3(BJ)/aug-cc-pVTZ) structural parameters determined for conformer I. Bond distances and angles are reported in angstroms (Å) and degrees, respectively.

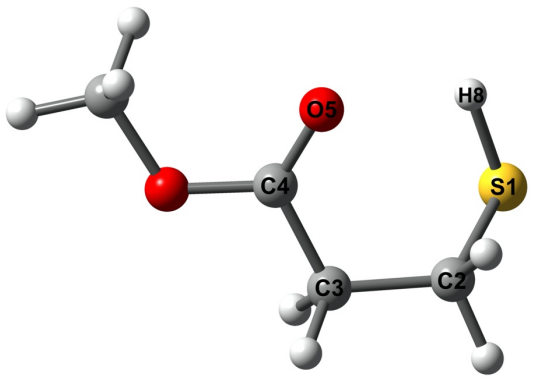

Parameter	r_0	r_e
S1–H8	1.344(3)	1.344
S1–C2	*1.819(2)*	1.834
C2–C3	*1.546(7)*	1.520
C3–C4	*1.491(4)*	1.510
C4=O5	1.206(3)	1.207
O5···H8	2.515(4)	2.552
S1–C2–C3	*114.1(1)*	114.2
C2–C3–C4	*112.1(3)*	113.1
S1–H8–O5	117.4(1)	117.5
C4–O5–H8	96.4(1)	95.6
S1–C2–C3–C4	*-68.9(2)*	-69.0

Values in *italics* were directly obtained from the STRFIT.

5.6 Conclusions

The ground state rotational spectrum of methyl 3-mercaptopropionate was measured and analyzed in detail using chirped-pulse and cavity-based Fourier transform microwave spectroscopy from 8–18 GHz. Rotational transitions belonging to the two most stable conformers (I and II) were successfully assigned in the rotational spectra, and the lines present complex splitting patterns due to the methyl internal rotation and/or SH tunneling motion. The similar experimental V_3 barriers for the two conformers reveal that the electronic distribution of I and II is not strongly affected by their geometrical differences. QTAIM, NCI, and NBO analyses show that conformer I is favored in the conformational equilibrium due to a stable S–H···O=C IHB, which is estimated to have an energy of about 6.6 kJ mol^{-1} based on the potential energy at the bond critical point. On the basis of the ground state effective (r_0) and equilibrium (r_e) geometries of I, we were able to derive the experimental geometric parameters associated with the sulfur HB, which reveals that the HB distance and angle S–H–O are 2.515(4) Å and 117.4(1)º, respectively. The non-observation of additional conformers was rationalized based on their conversion pathways to lower energy forms and/or low population in the supersonic jet expansion. The present study provides key experimental data on sulfur HBs at the molecular level in isolation of crystal packing and solvent effects and serves as a benchmark for improved understanding and modelling of these important non-covalent interactions.

5.7 References

(1) Oswald, S.; Suhm, M. A. Soft Experimental Constraints for Soft Interactions: A Spectroscopic Benchmark Data Set for Weak and Strong Hydrogen Bonds. *Phys. Chem. Chem. Phys.* **2019**, *21*, 18799–18810.

(2) Juanes, M.; Saragi, R. T.; Caminati, W.; Lesarri, A. The Hydrogen Bond and Beyond: Perspectives for Rotational Investigations of Non-Covalent Interactions. *Chem. - A Eur. J.* **2019**, *25* (49), 11402–11411.

(3) Li, W.; Spada, L.; Tasinato, N.; Rampino, S.; Evangelisti, L.; Gualandi, A.; Cozzi, P. G.; Melandri, S.; Barone, V.; Puzzarini, C. Theory Meets Experiment for Noncovalent Complexes: The Puzzling Case of Pnicogen Interactions. *Angew. Chemie Int. Ed.* **2018**, *57* (42), 13853–13857.

(4) Biswal H. S., Hydrogen Bonds Involving Sulfur: New Insights from ab Initio Calculations and Gas Phase Laser Spectroscopy, In *Noncovalent Forces*, *Challenges and Advances in Computational Chemistry and Physics*, 1st ed.; Springer International: Switzerland, 2015, 2, pp. 15–45.

(5) Alkorta, I.; Rozas, I.; Elguero, J. Non-Conventional Hydrogen Bonds. *Chem. Soc. Rev.* **1998**, *27* (2), 163.

(6) Grabowski, S. J. What Is the Covalency of Hydrogen Bonding? *Chem. Rev.* **2011**, *111* (4), 2597–2625.

(7) Das, A.; Mandal, P. K.; Lovas, F. J.; Medcraft, C.; Walker, N. R.; Arunan, E. The H_2S Dimer Is Hydrogen-Bonded: Direct Confirmation from Microwave Spectroscopy. *Angew. Chemie Int. Ed.* **2018**, *57* (46), 15199–15203.

(8) Juanes, M.; Lesarri, A.; Pinacho, R.; Charro, E.; Rubio, J. E.; Enríquez, L.; Jaraíz, M. Sulfur Hydrogen Bonding in Isolated Monohydrates: Furfuryl Mercaptan versus Furfuryl Alcohol. *Chem. - A Eur. J.* **2018**, *24* (25), 6564–6571.

(9) Mundlapati, V. R.; Ghosh, S.; Bhattacherjee, A.; Tiwari, P.; Biswal, H. S. Critical Assessment of the Strength of Hydrogen Bonds between the Sulfur Atom of Methionine/Cysteine and Backbone Amides in Proteins. *J. Phys. Chem. Lett.* **2015**, *6* (8), 1385–1389.

(10) Silva, W. G. D. P.; van Wijngaarden, J. Sulfur as a Hydrogen Bond Donor in the Gas Phase: Rotational Spectroscopic and Computational Study of 3-Mercaptopropionic Acid. *J. Mol. Spectrosc.* **2019**, *362*, 1–7.

(11) Smith, C. J.; Huff, A. K.; Zhang, H.; Mo, Y.; Leopold, K. R. A Strong Dependence of the CH_3 Internal Rotation Barrier on Conformation in Thioacetic Acid: Microwave Measurements and an Energy Decomposition Analysis. *J. Chem. Phys.* **2019**, *150* (13), 134302.

(12) Eibl, K.; Stahl, W.; Kleiner, I.; Nguyen, H. V. L. Conformational Effect on the Almost Free Internal Rotation in 4-Hexyn-3-ol Studied by Microwave Spectroscopy and Quantum Chemistry. *J. Chem. Phys.* **2018**, *149* (14), 144306.

(13) Andresen, M.; Kleiner, I.; Schwell, M.; Stahl, W.; Nguyen, H. V. L. Sensing the Molecular Structures of Hexan-2-one by Internal Rotation and Microwave Spectroscopy. *ChemPhysChem* **2019**, *20*, 2063–2073.

(14) Hakiri, R.; Derbel, N.; Nguyen, H. V. L.; Mouhib, H. Communication through the Furan Ring: The Conformational Effect on the Internal Rotation of 5-Methyl Furfural Studied by Microwave Spectroscopy. *Phys. Chem. Chem. Phys.* **2018**, *20* (40), 25577–25582.

(15) Halgren, T. A. Merck Molecular Force Field. I. Basis, Form, Scope, Parametrizations, and Performance of MMFF94. *J. Comput. Chem.* **1995**, *17*, 490–641.

(16) Becke, A. D. Density-functional Thermochemistry. III. The Role of Exact Exchange. *J. Chem. Phys.* **1993**, *98* (7), 5648–5652.

(17) Becke, A. D.; Johnson, E. R. A Density-Functional Model of the Dispersion Interaction. *J. Chem. Phys.* **2005**, *123* (15), 154101.

(18) Grimme, S.; Ehrlich, S.; Goerigk, L. Effect of the Damping Function in Dispersion Corrected Density Functional Theory. *J. Comput. Chem.* **2011**, *32* (7), 1456–1465.

(19) Møller, C.; Plesset, M. S. Note on an Approximation Treatment for Many-Electron Systems. *Phys. Rev.* **1934**, *46* (7), 618–622.

(20) Dunning, T. H. Gaussian Basis Sets for Use in Correlated Molecular Calculations. I. The Atoms Boron through Neon and Hydrogen. *J. Chem. Phys.* **1989**, *90* (2), 1007–1023.

(21) Frisch, M. J.; Trucks, G. W.; Schlegel, H. B.; Scuseria, G. E.; Robb, M. A.; Cheeseman, J. R.; Scalmani, G.; Barone, V.; Petersson, G. A.; Nakatsuji, H.; et al. *Gaussian 16*, Revision B.01; Gaussian, Inc.: Wallingford, CT, 2016.

(22) Weinhold, F.; Landis, C. R.; Glendening, E. D. What Is NBO Analysis and How Is It Useful? *Int. Rev. Phys. Chem.* **2016**, *35* (3), 399–440.

(23) Bader, R. F. W. Atoms in Molecules. *Acc. Chem. Res.* **1985**, *18* (1), 9–15.

(24) Johnson, E. R.; Keinan, S.; Mori Sánchez, P.; Contreras García, J.; Cohen, A. J.; Yang, W. NCI : Revealing Non-Covalent Interactions. *J. Am. Chem. Soc.* **2010**, *132* (18), 6498–6506.

(25) Glendening, E. D.; Badenhoop, J. K.; Reed, A. E.; Carpenter, J. E.; Bohmann, J. A.; Morales, C. M.; Landis C. R.; Weinhold, F. *NBO 6.0*, Theoretical Chemistry Institute, University of Wisconsin: Madison, 2012.

(26) Keith, T. A. *AIMAll*, version 17.11.14; TK Gristmill Software: Overland Park, KS, 2016.

(27) Contreras-García, J.; Johnson, E. R.; Keinan, S.; Chaudret, R.; Piquemal, J.-P.; Beratan, D. N.; Yang, W. NCIPLOT: A Program for Plotting Noncovalent Interaction Regions. *J. Chem. Theory Comput.* **2011**, *7* (3), 625–632.

(28) Balle, T. J.; Flygare, W. H. Fabry–Perot Cavity Pulsed Fourier Transform Microwave Spectrometer with a Pulsed Nozzle Particle Source. *Rev. Sci. Instrum.* **1981**, *52* (1), 33–45.

(29) Evangelisti, L.; Sedo, G.; van Wijngaarden, J. Rotational Spectrum of 1,1,1-Trifluoro-2-Butanone Using Chirped-Pulse Fourier Transform Microwave Spectroscopy. *J. Phys. Chem. A* **2011**, *115* (5), 685–690.

(30) Sedo, G.; van Wijngaarden, J. Fourier Transform Microwave Spectra of a "New" Isomer of OCS-CO_2. *J. Chem. Phys.* **2009**, *131* (4), 044303.

(31) Western, C. M. PGOPHER: A Program for Simulating Rotational, Vibrational and Electronic Spectra. *J. Quant. Spectrosc. Radiat. Transf.* **2017**, *186*, 221–242.

(32) Hartwig, H.; Dreizler, H. The Microwave Spectrum of Trans-2,3-Dimethyloxirane in Torsional Excited States. *Zeitschrift für Naturforsch. A* **1996**, *51* (8), 923–932.

(33) Gall, J. T. A.; Thomas, J.; Xie, F.; Wang, Z.; Jäger, W.; Xu, Y. Rotational Spectroscopy of the Methyl Glycidate-Water Complex: Conformation and Water and Methyl Rotor Tunnelling Motions. *Phys. Chem. Chem. Phys.* **2017**, *19* (43), 29508–29515.

(34) Schnitzler, E. G.; Seifert, N. A.; Ghosh, S.; Thomas, J.; Xu, Y.; Jäger, W. Hydration of the Simplest α-Keto Acid: A Rotational Spectroscopic and Ab Initio Study of the Pyruvic Acid–Water Complex. *Phys. Chem. Chem. Phys.* **2017**, *19* (6), 4440–4446.

(35) Pickett, H. M. The Fitting and Prediction of Vibration-Rotation Spectra with Spin Interactions. *J. Mol. Spectrosc.* **1991**, *148* (2), 371–377.

(36) Watson, J. K. G. *In Vibrational Spectra and Structure a Series of Advances*; Durig, J. R.; Ed.; Elsevier: New York, 1977, Vol. 6, pp. 1–89.

(37) Evangelisti, L.; Caminati, W. Internal Dynamics in Complexes of Water with Organic Molecules. Details of the Internal Motions in Tert-Butylalcohol–Water. *Phys. Chem. Chem. Phys.* **2010**, *12* (43), 14433.

(38) Tayler, M. C. D.; Ouyang, B.; Howard, B. J. Unraveling the Spectroscopy of Coupled Intramolecular Tunneling Modes: A Study of Double Proton Transfer in the Formic-Acetic Acid Complex. *J. Chem. Phys.* **2011**, *134* (5), 054316.

(39) Fantoni, A. C.; Caminati, W.; Favero, P. G. The SH Torsion Double Minimum Potential in Methylthioglycolate as Studied by Millimeterwave Free Jet Absorption Spectroscopy and Ab Initio Investigations. *J. Mol. Spectrosc.* **1996**, *176* (2), 364–368.

(40) Nguyen, H. V. L.; Stahl, W.; Kleiner, I. Structure and Rotational Dynamics of Methyl Propionate Studied by Microwave Spectroscopy. *Mol. Phys.* **2012**, *110* (17), 2035–2042.

(41) Ruoff, R. S.; Klots, T. D.; Emilsson, T.; Gutowsky, H. S. Relaxation of Conformers and Isomers in Seeded Supersonic Jets of Inert Gases. *J. Chem. Phys.* **1990**, *93* (5), 3142–3150.

(42) Espinosa, E.; Molins, E.; Lecomte, C. Hydrogen Bond Strengths Revealed by Topological Analyses of Experimentally Observed Electron Densities. *Chem. Phys. Lett.* **1998**, *285* (3–4), 170–173.

(43) Kisiel, Z. Least-Squares Mass-Dependence Molecular Structures for Selected Weakly Bounds Intermolecular Clusters, *J. Mol. Spectrosc*., **2003**, 218, 58–67.

(44) Kisiel, Z. Evaluation Of Internal From Cartesians, EVAL Code, PROSPE-Programs For Rotational Spectroscopy. http://info.ifpan.edu.pl/~kisiel/prospe.htm (accessed July 10, 2019).

(45) Alemán, C.; Casanovas, J.; Zanuy, D.; Hall, H. K. Systematic Evaluation of the Conformational Properties of Aliphatic ω-Hydroxy Acids. *J. Org. Chem.* **2005**, *70* (8), 2950–2956.

Chapter 6. Hydrogen Bonding Networks and Cooperativity Effects in the Aqueous Solvation of Trimethylene Oxide and Sulfide Rings by Microwave Spectroscopy and Computational Chemistry[3]

This chapter reports on the microsolvation of the flexible four-membered rings trimethylene oxide (TMO) and sulfide (TMS) with one and two water molecules. As TMO and TMS rings have an effectively planar and a puckered structure, respectively, as a result of large amplitude ring puckering motions, different binding topologies are observed between each ring and the water molecules. The impact of water on the ring structures and the hydrogen bonding networks occurring in the hydrated complexes are reported in detail. In the last section of the chapter, theoretical calculations for analogous complexes formed with trimethylene selenide (TMSe) are included to evaluate the influence of the chalcogen atom substitution (O, S and Se) on the interaction energy of the complexes.

6.1 Abstract

The intermolecular interactions responsible for the microsolvation of the highly flexible trimethylene oxide (TMO) and trimethylene sulfide (TMS) rings with one and two water (w) molecules were investigated using rotational spectroscopy (8–22 GHz) and quantum chemical

[3] The content of this chapter is an adapted version of the article published in the Journal of Chemical Physics: Silva, W. G. D. P.; van Wijngaarden, J. Hydrogen Bonding Networks and Cooperativity Effects in the Aqueous Solvation of Trimethylene Oxide and Sulfide Rings by Microwave Spectroscopy and Computational Chemistry, *J. Chem. Phys.* **2021**, 155, 034305.

calculations. The observed patterns of transitions are consistent with the most stable geometries of the TMO–w, TMO–$(w)_2$ and TMS–w complexes at the B2PLYP-D3(BJ)/aug-cc-pVTZ level and were confirmed using spectra of the ^{18}O isotopologue. Due to its effectively planar backbone, TMO offers one unique binding site for solvation while water can bind to the puckered TMS ring in either an *axial* or *equatorial* site of the heteroatom. In all clusters, the first water molecule binds in the σ_v symmetry plane of the ring monomer and serves as a hydrogen bond donor to the heteroatom. The second water molecule is predicted to form a cooperative hydrogen bonding network between the three moieties. Secondary C–H···O interactions are a key stabilizing influence in the trimers and also drive the preferred binding site in the TMS clusters with the *axial* binding site preferred in TMS–w and the *equatorial* form calculated to be more stable in the dihydrate. Using an energy partition scheme from symmetry-adapted perturbation theory for the O, S and Se containing mono- and dihydrates, the intermolecular interactions are revealed to be mainly electrostatic but the dispersive character of the contacts is enhanced with increasing size of the ring's heteroatom due to the key role of longer-range secondary interactions.

6.2 Introduction

Accurate descriptions of non-covalent interactions are critical to achieve a comprehensive understanding of the driving forces behind important chemical phenomena including self-assembly, molecular recognition and the formation of supramolecular entities.[1,2] As a first step in characterizing intermolecular interactions, key properties related to structure and dynamics can be derived from experimental studies of prototypical monomers and their complexes formed with partner molecules in supersonic jets.[1,3] Clusters in which the binding partner is water are of

particular interest to model the first stages of aqueous solvation. A number of examples are found in the literature including studies of hydrates formed with linear species,[4,5] rings[6–8] or other small compounds including amines,[9,10] ethers,[11] thiols and alcohols.[12] When high-resolution spectroscopy and quantum chemical calculations are combined and applied to such clusters, a detailed picture of the preferred binding sites, geometry, dynamics and the fundamental nature of the non-covalent interactions on a microscopic scale begins to emerge.

Intermolecular interactions involving the four-membered rings trimethylene oxide (c-C_3H_6O)(TMO) and trimethylene sulfide (c-C_3H_6S)(TMS) add an additional degree of complexity as the free monomers themselves are known to undergo a large amplitude ring puckering motion.[13] In both cases, the underlying potential energy surfaces along this coordinate are known to be double-well potentials with two equivalent minima corresponding to a non-planar ring backbone. In TMO, the barrier to planarity (15.52(5) cm^{-1})[14] based on spectroscopic studies is well below the zero point energy resulting in an effectively planar geometry for the heavy atom backbone.[15–23] As a result, the two lone pairs of electrons on oxygen offer equivalent binding sites for a partner molecule as seen through experimental measurements of the rotational spectrum of TMO complexes with Ar,[24] HF,[25] HCl[26] and H_2O.[27] In TMS, the barrier to ring planarity (274(2) cm^{-1})[28] is much higher by comparison and the ground state geometry is that of a flexed ring as confirmed by tunnelling splitting in the microwave and rotationally-resolved infrared spectrum.[28–31] As the ring backbone is puckered, the lone pairs on sulfur, which are oriented axially or equatorially to the ring, provide two potential binding sites for the partner molecule. This has been confirmed via the rotational spectra of TMS–HF[32] and TMS–HCl[33] which contain signatures due to two separate isomers. In addition to providing interesting model systems to probe the contribution of the heteroatom (O versus S) to the character of the non-covalent interaction, the TMO and TMS

monomers afford the opportunity to investigate the degree to which the binding partner quenches the large amplitude motion of the ring which may lead to subtle changes in its effective geometry. While the common assumption is that monomer geometries are not disrupted upon complexation,[3] Ottaviani *et al*. suggested that a 3° deviation from planarity of the ring was discernable from the millimeterwave spectrum of TMO–water (TMO–w) using deuterium and ^{18}O enriched samples.[27]

We describe herein a comprehensive study of the non-covalent interactions occurring in a series of water complexes formed with TMO and TMS in an effort to deduce how the geometry of the ring and the identity of the heteroatom affect the binding sites upon microsolvation by one and two water molecules. Using Fourier transform microwave (FTMW) spectroscopy, we report the first experimental observation of TMO–$(w)_2$ and TMS–w including measurements with ^{18}O enriched water for confirmation of the assignments. Furthermore, we have extended the work of Ottaviani *et al.*[27] to the microwave region by measuring new transitions for TMO–w (and ^{18}O water) including the first observation of the ^{13}C isotopologues in natural abundance. For the three complexes, the observed spectral patterns are consistent with quantum chemical models at the B2PLYP-D3(BJ) and *ab initio* MP2 levels of theory which are extended to include predictions for TMS-$(w)_2$ and the selenium containing analogs for comparison. To enhance our understanding of the physical origins of the non-covalent contacts responsible for each cluster, we employed multiple computational approaches including topological and energy decomposition methods.

6.3 Methods

6.3.1 Experimental Methods

The rotational spectra of TMO–w, TMO–$(w)_2$ and TMS–w were measured using a chirped-pulse (cp) and a cavity-based Balle-Flygare (BF) type Fourier transform microwave (FTMW) spectrometer which have been described previously.[34,35] In each experiment, a gas mixture containing 1% of the monomer vapour from above a liquid sample of the compound (Sigma-Aldrich Canada) in neon (100–300 kPa) was prepared at room temperature and seeded with water by passing it through a glass reservoir containing water or ^{18}O enriched water (97%). The gas mixture was expanded into the high vacuum chambers using a pulsed nozzle (1 mm orifice) to create a rotationally-cooled, supersonic jet expansion. Broadband CP-FTMW spectra were initially recorded in 2 GHz segments from 8–18 GHz from which the most intense rotational transitions for the parent species of the complexes were identified. In the case of the TMO–w dimer, the spectral features were sufficiently intense to also observe sets of transitions consistent with the corresponding ^{13}C isotopologues in natural abundance. Once a preliminary fit was obtained from the broadband spectrum, final frequency measurements were performed using the BF-FTMW instrument from 8–22 GHz which affords higher resolution and sensitivity. As the molecular beam and the resonator axis are coaxial in the BF-FTMW instrument, all rotational transitions appeared as doublets due to the Doppler effect. The measured transitions have linewidths of ~7 kHz (FWHM) and their positions were determined to within ~2 kHz.

6.3.2 Computational Methods

Initial conformational searches for TMO–$(w)_n$, TMS–$(w)_n$ and TMSe–$(w)_n$ (n=1,2) complexes were carried out at the GFN2-xTB[36] level using the Conformer-Rotamer Ensemble Sampling Tool (CREST) available in the extended tight binding (xTB) program package.[37,38] Following the searches, optimization and harmonic frequency calculations were performed for all possible geometries using the density functional theory (DFT) B3LYP[39]-D3(BJ)[40,41] method with Dunning's aug-cc-pVTZ[42] basis sets. For the TMO and TMS complexes, the geometries with relative energies within 10 kJ mol^{-1} were then subjected to optimization and frequency calculations using the double-hybrid B2PLYP[43]-D3(BJ) and *ab initio* MP2[44] methods with the aug-cc-pVTZ and Ahlrichs' def-2TZVP[45] basis set. The Boys and Bernardi's counterpoise correction method[46] was included in all optimization and frequency calculations to account for the basis set superposition error (BSSE). All optimization and frequency calculations were performed using the Gaussian 16 program.[47]

To visualize and quantify intermolecular interactions in the complexes, non-covalent interaction (NCI) and quantum theory of atoms in molecules (QTAIM) analyses were done using the NCIPLOT[48] and AIMAll[49] programs, respectively. Symmetry-adapted perturbation theory (SAPT) at the sapt2+(3)δMP2[50]/aug-cc-pVTZ was performed using the Psi4[51] to comprehend the physical origins of the interactions behind the formation of the complexes.

6.4 Results

A summary of the relative energies and spectroscopic parameters of the mono- and dihydrated complexes of TMO and TMS at the B2PLYP-D3(BJ) level is provided in Table 6.1 while the results from MP2 calculations are given in Table S43. The corresponding equilibrium structures for the lowest energy forms are presented in Figure 6.1 (monohydrates) and Figure 6.2 (dihydrates). As reported earlier by Ottaviani *et al*.,[27] the optimized geometry of TMO–w is heavily dependent on the level of theory employed with DFT calculations identifying a near planar TMO subunit with one binding site at oxygen to form a O···H–O hydrogen bond (HB) with water in the *ac*-plane of the TMO monomer and MP2 calculations predicting a TMO ring that is puckered by ~18° with two potential binding sites. This discrepancy is a result of the flatness of the potential energy surface along the TMO ring puckering coordinate and highlights the challenge of modelling compounds of this type. For the TMO–$(w)_2$ trimer (Figure 6.2), the second water molecule binds on the same side of the TMO ring (in the *ac*-plane of the monomer) and is oriented as a HB donor to the first.

As expected from studies of related weakly bound dimers with TMS,[32,33] the quantum chemical results for TMS–w identify two potential binding sites (*axial* and *equatorial*, Figure 6.1) in the *ac*-plane of the puckered ring monomer to form a S···H–O interaction with the former being slightly lower in energy. In this case, *axial* and *equatorial* designation refer to the orientation of the lone pair on S which can be intuited by analogy to the position of the H atom on the opposite side of the puckered TMS ring. Interestingly, in the TMS–$(w)_2$ trimer (Figure 6.2), by comparison, the lowest energy arrangement involves *equatorial* binding of the first water to sulfur with the second arranged as in the TMO analogue.

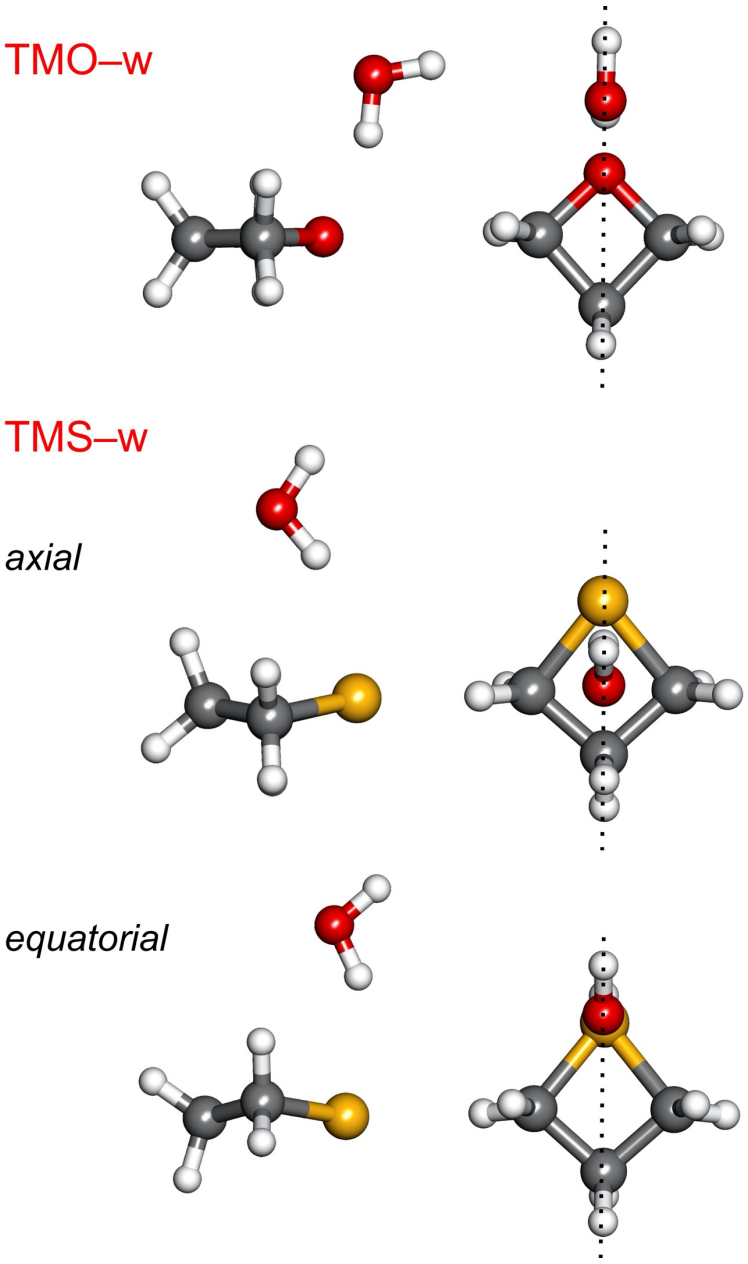

Figure 6.1 Equilibrium geometries (B2PLYP-D3(BJ)/aug-cc-pVTZ) of the conformers of TMO–w and TMS–w from a side (left) and a top (right) view. In the side view, the monomer *ac*-plane is in the plane of the page while in the top this plane is represented by a dotted line. The axial and equatorial binding sites of TMS–w refer to the orientation of the lone pair on S which is analogous to that of the H atom on the opposite side of the ring.

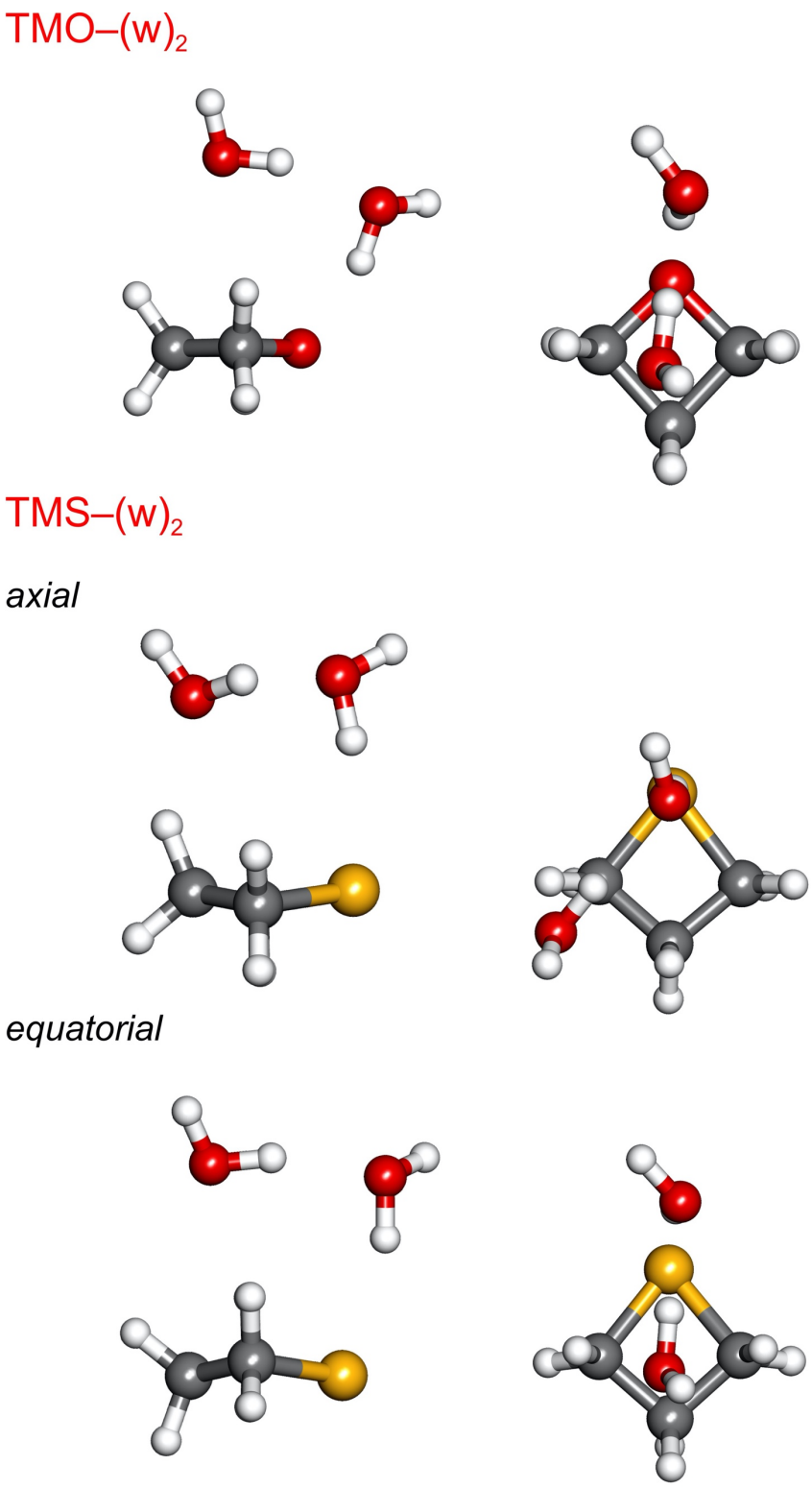

Figure 6.2 Equilibrium geometries (B2PLYP-D3(BJ)/aug-cc-pVTZ) of the conformers of TMO–$(w)_2$ and TMS–$(w)_2$ from a side (left) and a top (right) view.

Table 6.1 Calculated relative energies and spectroscopic parameters for the conformers of the mono- and dihydrated complexes of TMO and TMS.

	TMO–w	TMO–$(w)_2$	TMS–w		TMS–$(w)_2$	
Parameter[a]			*axial*	*equatorial*	*axial*	*equatorial*
A/MHz	8415/8151[b]	3559/3522	4389/4401	4640/4638	2784/2760	2697/2701
B/MHz	2624/2628	2042/2027	2522/2514	2365/2366	1505/1507	1675/1653
C/MHz	2444/2470	1608/1589	2223/2219	2152/2151	1210/1204	1264/1251
$\lvert\mu_a\rvert$/D	2.1/2.1	0.6/0.5	0.8/0.7	0.7/0.6	0.2/0.0	0.3/0.4
$\lvert\mu_b\rvert$/D	0.0/0.0	0.1/0.0	0.3/0.1	0.2/0.1	0.0/0.3	0.3/0.1
$\lvert\mu_c\rvert$/D	0.4/0.5	0.4/0.4	0.0/0.0	0.0/0.0	0.5/0.5	0.5/0.5
Complexation energy/kJ mol^{-1}	-29.4/-28.2	-68.4/-68.2	-23.8/-23.1	-23.1/-22.3	-57.5/-58.2	-59.0/-59.3
ΔE_{ZPE}/kJ mol^{-1}	—	—	0.0/0.0	0.7/0.8	1.1/1.0	0.0/0.0

[a]Rotational constants (*A*, *B* and *C*), absolute electric dipole moment components ($\lvert\mu_a\rvert$, $\lvert\mu_b\rvert$ and $\lvert\mu_c\rvert$), complexation energies accounting for basis set superposition errors and relative ZPE-corrected electronic (ΔE_{ZPE}) energies; [b]B2PLYP-D3(BJ), aug-cc-pVTZ/def2-TZVP basis set.

Based on the predicted spectroscopic parameters from Table 6.1, rotational transitions for the most stable conformers of TMO–$(w)_2$ and TMS–w were observed for the first time using both normal and ^{18}O enriched water samples. In the experiments involving gas mixtures with TMO, additional transitions due to TMO–w and its two singly substituted ^{13}C species in natural abundance were also assigned using the millimeterwave spectrum of the parent as a guide.[27] For this dimer, the ^{13}C transitions exhibited a relative intensity ratio of ~2:1 (C_α:C_β) due to the equivalence of the two α carbon atoms in the complex by symmetry. There was insufficient signal to detect the minor isotopologues of TMO–$(w)_2$ and TMS–w in natural abundance as the overall transition intensities were nearly two orders of magnitude lower than for TMO–w as shown in Figure 6.3. Each set of rotational transitions were fit independently with Pickett's SPFIT program[52] using Watson's S-reduced Hamiltonian (I^r representation).[53] The determined spectroscopic parameters for TMO–w are provided in Table 6.2 while those for TMO–$(w)_2$ and TMS–w are shown in Table 6.3. The observed transition frequencies are listed in Tables S44–S46.

In an effort to observe transitions arising from the *equatorial* conformer of TMS–w, as reported for the dimers with HF[32] and HCl,[33] the CP-FTMW spectrum was recorded with helium as the carrier gas. Although this form is only slightly higher in energy (0.5–0.7 kJ mol^{-1}, Table 6.1), no candidate lines corresponding to the *equatorial* conformer were observed. This may be a consequence, to some extent, of the smaller *a*-dipole but likely indicates that relaxation to the lower energy *axial* form is feasible.

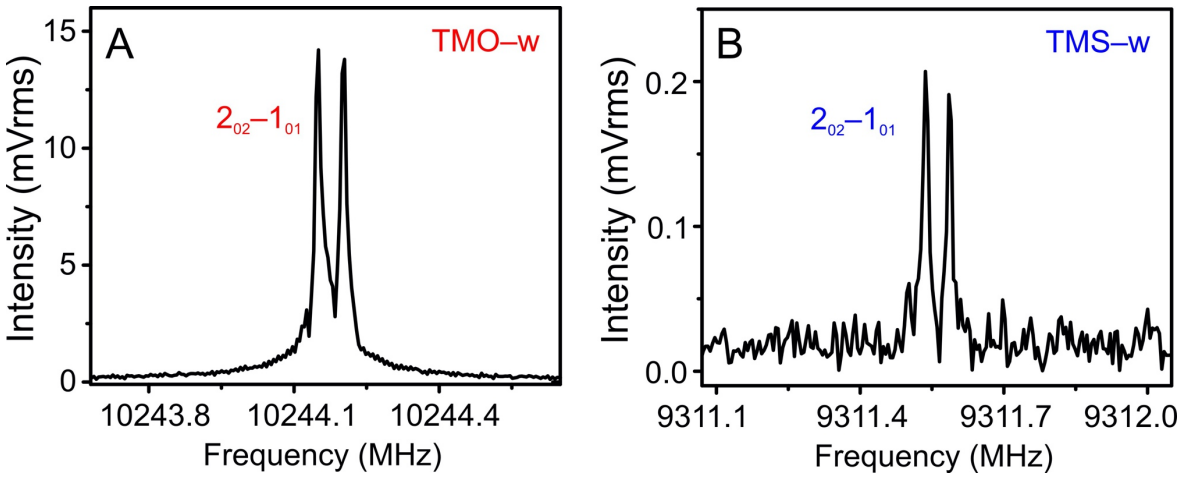

Figure 6.3 Cavity BF-FTMW spectrum for the J_{KaKc}' – J_{KaKc}" = 2_{02} – 1_{01} transition observed for A) TMO–w, 20 cycles and B) TMS–w, 220 cycles.

Table 6.2 Spectroscopic parameters for the assigned species of TMO–w

Parameter[a]	Parent	^{18}O	C_α (equivalent)	C_β
A/MHz	8097.89(99)	8069.52(85)	7974.10(99)	8016.70(68)
B/MHz	2635.78669(99)	2478.6300(12)	2628.34996(42)	2597.2756(17)
C/MHz	2488.11083(75)	2350.0202(12)	2468.67065(50)	2460.4851(49)
D_J/kHz	20.716(26)	18.778(16)	[20.716][b]	[20.716]
D_{JK}/kHz	-69.10(14)	-63.939(68)	[-69.10]	[-69.10]
d_1/kHz	2.433(23)	2.034(22)	[2.433]	[2.433]
d_2/kHz	-0.070(16)	-0.042(10)	[-0.070]	[-0.070]
N	10	14	5	4
σ/kHz	0.9	2.1	1.1	2.1
$\mu_a/\mu_b/\mu_c$	y/n/n	y/n/n	y/n/n	y/n/n
P_{aa}/amu Å^2	166.23	178.17	166.82	168.48
P_{bb}/amu Å^2	36.89	36.90	37.91	36.93
P_{cc}/amu Å^2	25.51	25.74	25.47	26.11

[a]Rotational constants (*A*, *B* and *C*), quartic centrifugal distortion constants (D_J, D_{JK}, d_1, d_2), number of fitted transitions (*N*), standard deviation of the fit (σ); electric dipole moment components $\mu_a/\mu_b/\mu_c$ "y" if transitions related to the dipole were observed and "n" if not observed; planar moments of inertia (P_{aa}, P_{bb} and P_{cc}) obtained based on the rotational constants. [b]Values in brackets [ ] were fixed to the value determined for the corresponding parent species. The full set of calculations spectroscopic parameters at the B2PLYP-D3(BJ) level is provided in Table S47. The fits were done based on BF-FTMW measurements.

Table 6.3 Spectroscopic parameters for the assigned conformers of TMO–$(w)_2$ and TMS–w.

Parameter[a]	TMO–$(w)_2$		TMS–w	
	Parent	^{18}O	Parent	^{18}O
A/MHz	3487.4632(91)	3304.9560(82)	4427.9958(52)	4427.168(70)
B/MHz	2015.34068(93)	1916.26887(79)	2474.9504(16)	2323.79959(72)
C/MHz	1572.87970(60)	1476.30949(56)	2194.9170(14)	2074.92694(71)
D_J/kHz	1.7636(81)	1.5674(79)	5.178(22)	4.671(18)
D_{JK}/kHz	13.695(64)	12.944(65)	61.02(16)	58.47(53)
d_1/kHz	-0.3733(70)	-0.3491(65)	-0.576(29)	-0.482(12)
d_2/kHz	-0.0148(55)	-0.0397(56)	0.411(28)	0.351(26)
N	13	16	12	10
σ/kHz	1.7	2.0	2.4	0.9
$\mu_a/\mu_b/\mu_c$	y/n/n	y/n/n	y/y/n	y/n/n
P_{aa}/amu Å^2	213.59	226.58	160.16	173.45
P_{bb}/amu Å^2	107.73	115.76	70.10	70.12
P_{cc}/amu Å^2	37.19	37.16	44.04	44.03

[a]Rotational constants (*A*, *B* and *C*), quartic centrifugal distortion constants (D_J, D_{JK}, d_1, d_2), number of fitted transitions (*N*), standard deviation of the fit (σ); electric dipole moment components $\mu_a/\mu_b/\mu_c$ "y" if transitions related to the dipole were observed and "n" if not observed; planar moments of inertia (P_{aa}, P_{bb} and P_{cc}) obtained based on the rotational constants. The full set of calculations spectroscopic parameters at the B2PLYP-D3(BJ) level is provided in Table S47. The fits were done based on BF-FTMW measurements.

Using the rotational constants for the observed isotopologues of TMO–w and TMS–w, substitution coordinates (r_s) were derived using Kraitchman's equations[54] as implemented in the KRA routine.[55] For TMO–w, experimental information for the ^{13}C (this work) and deuterium isotopologues were available but were insufficient to derive the ring geometry without substitution at the position of the heteroatom. The labelled $H_2{}^{18}O$ sample, however, made it possible to experimentally confirm the position of water within the hydrated clusters both in the inertial frame of the complex and in the reference frame of the monomer. The latter was achieved by treating the water as a point mass (18.01056 amu) relative to the ring. A comparison between the calculated and substituted coordinates is provided in Table 6.4.

Table 6.4 Kraitchman substituted atomic coordinates (Å) for the water oxygen in TMO–w and TMS–w.

O atom - coordinate	$\|a\|$		$\|b\|$		$\|c\|$	
	Exp.	Calc.[a]	Exp.	Calc.	Exp.	Calc.
TMO–w	2.4704(8)	2.48	0.00[b]	0.00	0.350(6)	-0.35
TMS–w	2.6024(6)	2.58	0.13(1)	0.14	0.00	0.00

[a]B2PLYP-D3(BJ)/aug-cc-pVTZ; [b]Imaginary values were set to zero.

Table 6.5 Kraitchman coordinates (Å) for the center of mass (COM) of water relative to the principal axis system of the TMO and TMS monomers.

	COM water		
Coordinate	$\|a\|$	$\|b\|$	$\|c\|$
TMO	1.951(3)	0.00	2.6967(6)
TMS	0.00[a]	0.00	3.2697(5)

[a]Imaginary values were set to zero.

6.5 Discussion

The experimentally-derived rotational constants of the TMO–w, TMO–$(w)_2$ and TMS–w complexes are consistent with the lowest energy geometries predicted at the B2PYLP level of theory with both aug-cc-pVTZ and def2-TZVP basis sets in Table 6.1 and with the results from MP2 calculations (Table S43) (with the exception of TMO–w as mentioned above). The successful observation of transitions related to minor isotopic species based on these equilibrium geometries confirms that the effectively planar geometry of TMO and the puckered geometry of TMS (dihedral ∠C–C–C–S of ~18°) is retained following complexation with water. In the monohydrated clusters (Figure 6.1), the water molecule is positioned in the *ac*-plane (σ_v) of the heterocycle as supported by the close agreement between the planar moments associated with this plane (P_{bb}) in the TMO (36.99 amu Å^2)[20] and TMS (43.98 amu Å^2)[30] monomers and those corresponding to P_{cc}, the mirror plane of the TMO–w (36.89 amu Å^2) and TMS–w (44.04 amu Å^2) dimers. Further confirmation that the first water lies in the *ac*-plane of the TMO and TMS rings comes from the substitution coordinates in Table 6.5 which show that the center of mass of water has an imaginary *b*-coordinate (implying a near zero value).[56] In the TMO–$(w)_2$ trimer, the slightly larger P_{cc} value (37.19 amu Å^2) relative to that of TMO–w is consistent with the slight rotation of the first water molecule in the trimer to move one hydrogen out of the symmetry plane as seen in Figure 6.2. This slight re-orientation presumably stabilizes the HB formed between the two water molecules.

Key information regarding the stability of the TMO–w and TMS–w dimers can be extracted from the QTAIM molecular graphs in Figure 6.4 that represent the non-covalent interactions as bond paths (black solid or dashed lines) between atoms. The primary contact in TMO–w is approximately three times stronger than the sulfur HB in TMS–w. This highlights the

weaker acceptor character of sulfur compared to that of oxygen and is consistent with the distances between the center of mass of water and the S (3.38 Å) or O (2.87 Å) heteroatoms of the ring from the Kraitchman analysis (adopting the equilibrium monomer geometries of TMO and TMS from B2PLYP-D3(BJ)/aug-cc-pVTZ calculations). The puckered geometry of TMS, however, permits the establishment of a secondary contact in TMS–w with a stabilizing energy of ~5.0 kJ mol^{-1} from the QTAIM results and is confirmed in the NCI calculations (Figure 6.4) by the presence of a green isosurface between C$_\beta$–H and the O of water. It is interesting to note that although the *axial* conformer of TMS–w is ~0.5–0.7 kJ mol^{-1} (Table 6.1) more stable than the *equatorial* form, its dominant S···H–O interaction is slightly smaller by ~0.3 kJ mol^{-1} suggesting that the substantial secondary C$_\beta$–H···O contact is the determining factor for the preferred *axial* binding site in TMS–w. A similar experimental finding was reported for TMS dimers with HF[32] and HCl.[33]

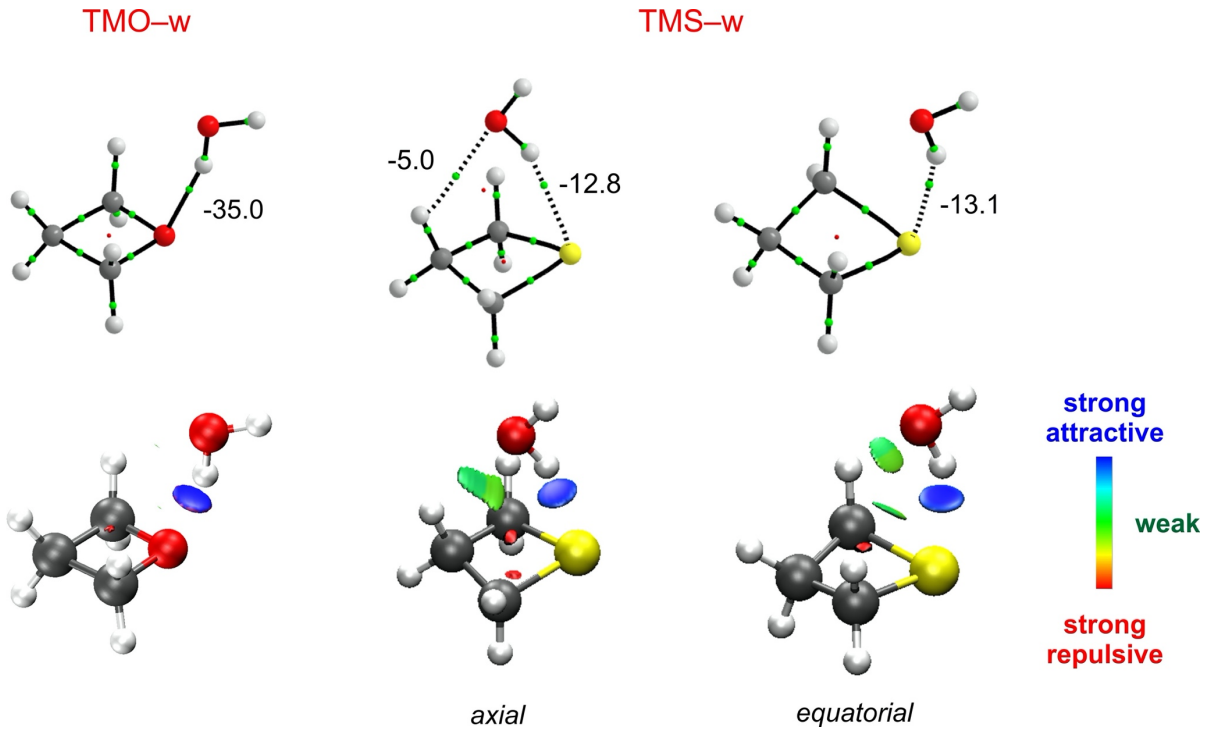

Figure 6.4 QTAIM molecular graphs with identified HB energies in kJ mol^{-1} (top) and NCI isosurfaces (bottom, s= 0.5, colour scale BGR -0.02 < ρ < +0.02) for the conformers of the TMO–w and TMS–w.

In moving to the dihydrated clusters (Figure 6.5), the topology of the HB interactions is significantly altered to accommodate the additional water molecule. While the first water serves as a HB donor to the ring heteroatom to form O···H–O or S···H–O primary interactions, it also acts as a HB acceptor for the second water molecule as depicted in Figure 6.5. In turn, the second water acts as both donor and acceptor as it binds to the first via O···H–O HB interactions and to the methylene groups of the rings through smaller secondary C_β–H···O contacts. The intermolecular contacts established between the three components are examples of cooperative HB networks as observed for other water complexes.[11,57] The result is the strengthening of the primary contact by more than 10 kJ mol^{-1} relative to the corresponding dimers due to the decreased HB distances (~0.1 Å (B2PLYP-D3(BJ)/aug-cc-pVTZ) shorter for both trimers). Note that the primary interaction is

more pronounced in the TMO trimers than in the TMS trimers which is consistent with the weaker acceptor character of sulfur.

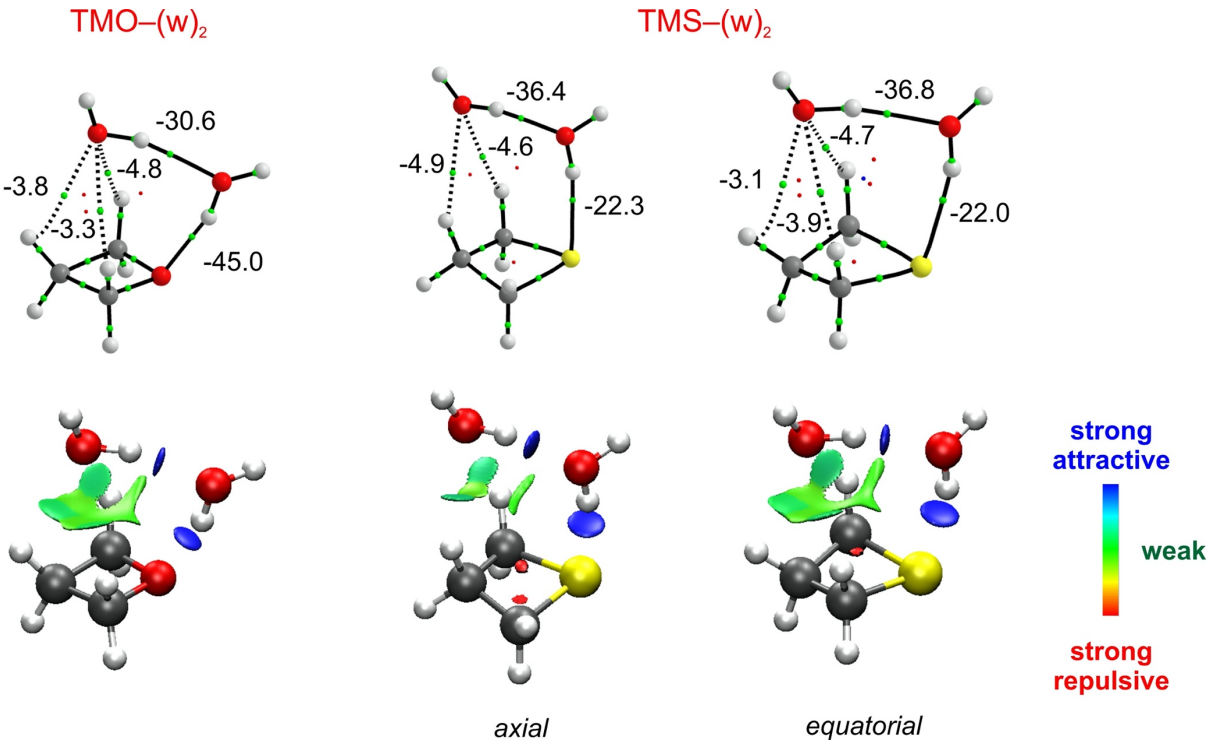

Figure 6.5 QTAIM molecular graphs with identified HB energies in kJ mol^{-1} (top) and NCI isosurfaces (bottom, s= 0.5, colour scale BGR -0.02 < ρ < +0.02) for the conformers of the TMO–(w)$_2$ and TMS–(w)$_2$.

While the *axial* binding site was preferred in the TMS–w dimer, a surprising change is predicted in the relative energy ordering of the TMS–(w)$_2$ as the *equatorial* form is ~1 kJ mol^{-1} (Table 6.1) more favourable. As seen in Figure 6.5, this increased stability is due to the three weak contacts established between the second water and the methylene hydrogen atoms. In the *axial* conformer by comparison, the second water is not centered on the *ac*-plane of the TMS ring and forms non-covalent interactions with only two C–H groups (Figure 6.2 and Figure 6.5). This key

difference in the position of the second water is captured using the rotational constants based on the equilibrium geometries from Table 6.1 (B2PLYP-D3(BJ)/aug-cc-pVTZ) to estimate the P_{cc} values for the *axial* (49.83 amu Å^2) and *equatorial* (44.64 amu Å^2) conformers of TMS–$(w)_2$, which show that, in the *equatorial* form, the second water molecule is more centered over the ring and close to the symmetry plane of the TMS monomer (43.98 amu Å^2) and TMS–w (44.04 amu Å^2) dimer.

Finally, SAPT calculations provide deeper insights regarding the nature of the intermolecular interactions as the interaction energies are partitioned in terms of electrostatic, dispersive, inductive and exchange-repulsive components. In Table 6.6, SAPT results for the TMO, TMS, and TMSe hydrates are provided to evaluate the effect of the chalcogen atom on the stability of the complexes. As in the TMS clusters, the two most stable geometries of the Se containing complexes are predicted to adopt both *axial* and *equatorial* configurations (Figure 6.6) with the former being the most stable monohydrate and the latter favoured in the presence of two waters. For all complexes, the total interaction energies show a stability ordering of O > S > Se in accordance with the non-covalent interaction strengths derived from the QTAIM analysis (Figure 6.4, Figure 6.5 and Figure 6.6 for the Se derivatives). From the partitioned energies, the electrostatic term is the main contributor to the stability of all clusters, but its role diminishes as the size of the heteroatom increases and this trend is partially offset by an increase in the % contribution from dispersion. This is particularly true for the monohydrates of the S and Se heterocycles which exhibit the longer range C_β–H···O contacts due to the puckered geometry of the ring. Although these secondary interactions are smaller than the primary HB with the heteroatom of the ring, they clearly drive the energetic preference for the *axial* form of TMS-w and TMSe–w and the *equatorial* conformers of TMS–$(w)_2$ and TMSe–$(w)_2$.

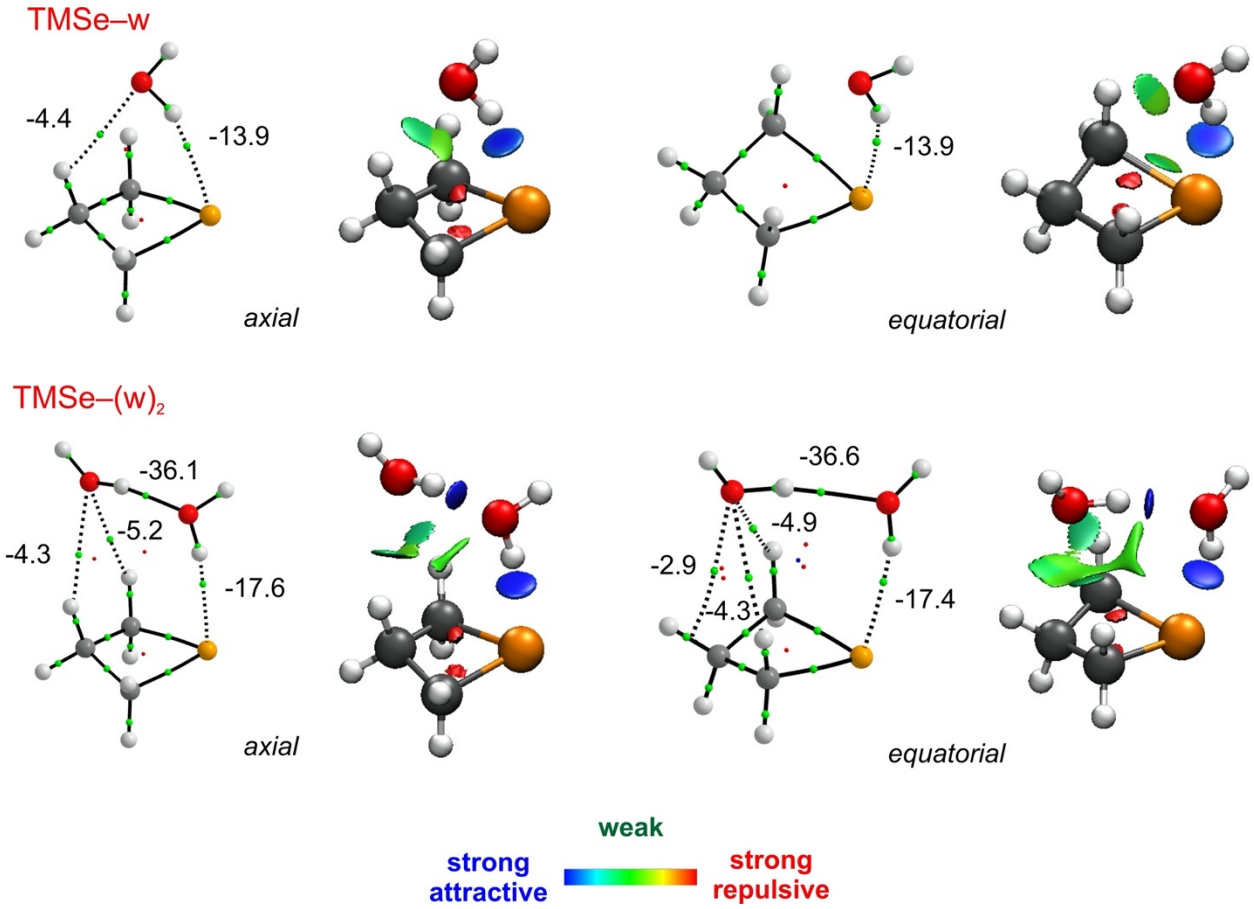

Figure 6.6 . QTAIM molecular graphs (left) and NCI isosurfaces (right, *s*= 0.5, colour scale BGR -0.02 < ρ < +0.02) for the conformers of TMSe–(w) and TMSe–$(w)_2$.

Table 6.6 SAPT results (in kJ mol^{-1}) for the mono- and dihydrates of TMO, TMS and TMSe obtained at the SAPT2+(3)δMP2/aug-cc-pVTZ level of theory.

Complex	Electrostatic	Induction	Dispersion	Exchange	Total
TMO–w	-44.1 (57.0)[a]	-16.3 (21.1)	-17.0 (22.0)	48.0	-29.4
TMO–$(w)_2$	-63.1 (54.4)	-25.6 (22.1)	-27.3 (23.5)	67.2	-48.9
TMS–w *axial*	-31.9 (51.9)	-12.4 (20.2)	-17.2 (28.0)	38.1	-23.4
TMS–w *equatorial*	-29.3 (50.7)	-11.9 (20.6)	-16.6 (28.7)	34.8	-23.0
TMS–$(w)_2$ *axial*	-47.1 (50.6)	-21.7 (23.3)	-24.3 (26.1)	56.4	-36.7
TMS–$(w)_2$ *equatorial*	-48.0 (49.0)	-23.2 (23.7)	-26.8 (27.3)	58.9	-39.1
TMSe–w *axial*	-30.0 (51.2)	-11.9 (20.3)	-16.7 (28.5)	36.3	-22.4
TMSe–w *equatorial*	-28.3 (49.3)	-11.8 (20.5)	-17.3 (30.2)	35.3	-22.1
TMSe–$(w)_2$ *axial*	-46.0 (49.6)	-22.2 (23.9)	-24.6 (26.5)	57.0	-35.7
TMSe–$(w)_2$ *equatorial*	-45.6 (48.2)	-22.5 (23.8)	-26.4 (27.9)	56.6	-37.9

[a]Values in brackets ( ) represent the contribution of that term (in percentage) to the total stabilizing energy (electrostatic + induction + dispersion).

6.6 Conclusions

The factors governing the aqueous microsolvation of the four-membered heterocycles TMO and TMS were explored using FTMW spectroscopy and quantum chemistry. The establishment of intermolecular contacts with water does not appear to have a discernable effect on the geometry of the ring monomers and the preferred binding sites for the solvent depend on the capacity to form primary and secondary HB contacts with the heteroatom and methylene groups of the ring, respectively. The latter interactions were found to be a strong influence on the position of water in the TMS containing clusters due to its puckered ring geometry. For the dihydrated rings, cooperative hydrogen bonding networks identified through QTAIM calculations

provide additional stability for the clusters through an increase of the primary HB contacts by more than 10 kJ mol^{-1} and through formation of additional secondary HB contacts which were confirmed by NCI calculations. SAPT analysis captures the nature of these secondary interactions as an increase in the % dispersion character and also confirms that the greater stability of the TMO complexes over those formed with the S (and Se) analogues is due to greater electrostatic contributions to the interaction energy. These seemingly small but significant differences highlight the importance of modelling the stepwise solvation of flexible molecules and the central role of long-range interactions in driving this process.

6.7 References

(1) Juanes, M.; Saragi, R. T.; Caminati, W.; Lesarri, A. The Hydrogen Bond and Beyond: Perspectives for Rotational Investigations of Non-Covalent Interactions. *Chem. – A Eur. J.* **2019**, *25* (49), 11402–11411.

(2) Grabowski, S. J. What Is the Covalency of Hydrogen Bonding? *Chem. Rev.* **2011**, *111* (4), 2597–2625.

(3) Xu, Y.; Wijngaarden, J. Van; Jäger, W. Microwave Spectroscopy of Ternary and Quaternary van Der Waals Clusters. *Int. Rev. Phys. Chem.* **2005**, *24* (2), 301–338.

(4) Barclay, A. J.; Pietropolli Charmet, A.; McKellar, A. R. W.; Moazzen-Ahmadi, N. Exploring the next Step in Micro-Solvation of CO in Water: Infrared Spectra and Structural Calculations of $(H_2O)_4$-CO and $(D_2O)_4$-CO. *J. Chem. Phys.* **2021**, *154* (4).

(5) Bogomolov, A. S.; Roucou, A.; Bejjani, R.; Herman, M.; Moazzen-Ahmadi, N.; Lauzin, C. The Rotationally Resolved Symmetric 2OH Excitation in H_2O-CO_2 Observed Using Pulsed

Supersonic Expansion and CW-CRDS. *Chem. Phys. Lett.* **2021**, *774* (March), 138606.

(6) Mackenzie, R. B.; Dewberry, C. T.; Cornelius, R. D.; Smith, C. J.; Leopold, K. R. Multidimensional Large Amplitude Dynamics in the Pyridine-Water Complex. *J. Phys. Chem. A* **2017**, *121* (4), 855–860.

(7) Silva, W. G. D. P.; van Wijngaarden, J. Characterization of Large-Amplitude Motions and Hydrogen Bonding Interactions in the Thiophene–Water Complex by Rotational Spectroscopy. *J. Phys. Chem. A* **2021**, *125* (16), 3425–3431.

(8) Wang, J.; Spada, L.; Chen, J.; Gao, S.; Alessandrini, S.; Feng, G.; Puzzarini, C.; Gou, Q.; Grabow, J.; Barone, V. The Unexplored World of Cycloalkene–Water Complexes: Primary and Assisting Interactions Unraveled by Experimental and Computational Spectroscopy. *Angew. Chemie Int. Ed.* **2019**, *58* (39), 13935–13941.

(9) Silva, W. G. D. P.; Poonia, T.; van Wijngaarden, J. Exploring the Non-Covalent Interactions behind the Formation of Amine–Water Complexes: The Case of N-Allylmethylamine Monohydrate. *Phys. Chem. Chem. Phys.* **2021**, *23* (12), 7368–7375.

(10) Chen, J.; Zheng, Y.; Melli, A.; Spada, L.; Lu, T.; Feng, G.; Gou, Q.; Barone, V.; Puzzarini, C. Theory Meets Experiment for Elucidating the Structure and Stability of Non-Covalent Complexes: Water-Amine Interaction as a Proof of Concept. *Phys. Chem. Chem. Phys.* **2020**, *22* (9), 5024–5032.

(11) Fatima, M.; Maué, D.; Pérez, C.; Tikhonov, D. S.; Bernhard, D.; Stamm, A.; Medcraft, C.; Gerhards, M.; Schnell, M. Structures and Internal Dynamics of Diphenylether and Its Aggregates with Water. *Phys. Chem. Chem. Phys.* **2020**, *22* (48), 27966–27978.

(12) Juanes, M.; Saragi, R. T.; Pinacho, R.; Rubio, J. E.; Lesarri, A. Sulfur Hydrogen Bonding and Internal Dynamics in the Monohydrates of Thenyl Mercaptan and Thenyl Alcohol.

Phys. Chem. Chem. Phys. **2020**, *22* (22), 12412–12421.

(13) Legon, A. C. Equilibrium Conformations of Four- and Five-Membered Cyclic Molecules in the Gas Phase: Determination and Classification. *Chem. Rev.* **1980**, *80* (3), 231–262.

(14) Jokisaari, J.; Kauppinen, J. Vapor-Phase Far-Infrared Spectrum and Double Minimum Potential Function of Trimethylene Oxide. *J. Chem. Phys.* **1973**, *2260* (May 2013), 2260–2263.

(15) Fernandez, J.; Myers, R. J.; Gwinn, W. D. Microwave Spectrum and Planarity of the Ring of Trimethylene Oxide. *J. Chem. Phys.* **1955**, *23* (4), 758–759.

(16) Chan, S. I.; Zinn, J.; Fernandez, J.; Gwinn, W. D. Trimethylene Oxide. I. Microwave Spectrum, Dipole Moment, and Double Minimum Vibration. *J. Chem. Phys.* **1960**, *33* (6), 1643–1655.

(17) Chan, S. I.; Borgers, T. R.; Russell, J. W.; Strauss, H. L.; Gwinn, W. D. Trimethylene Oxide. III. Far-Infrared Spectrum and Double-Minimum Vibration. *J. Chem. Phys.* **1966**, *44* (3), 1103–1111.

(18) Creswell, R. A.; Mills, I. M. Microwave Spectra and Centrifugal Distortion Constants of Oxetane. *J. Mol. Spectrosc.* **1974**, *52* (3), 392–412.

(19) Creswell, R. A. Molecular Structure of Oxetane. *Mol. Phys.* **1975**, *30* (1), 217–222.

(20) Lesarri, A.; Blanco, S.; López, J. C. The Millimetre-Wave Spectrum of Oxetane. *J. Mol. Struct.* **1995**, *354* (3), 237–243.

(21) Winnewisser, M.; Kunzmann, M.; Lock, M.; Winnewisser, B. . The High-Resolution FIR-Spectrum of Oxetane. *J. Mol. Struct.* **2001**, *561* (1–3), 1–15.

(22) Moruzzi, G.; Kunzmann, M.; Winnewisser, B. P.; Winnewisser, M. Ritz Assignment and Watson Fits of the High-Resolution Ring-Puckering Spectrum of Oxetane. *J. Mol.*

Spectrosc. **2003**, *219* (1), 152–162.

(23) Mahassneh, O.; van Wijngaarden, J. Analysis of the Coriolis Perturbed Rovibrational Spectrum of the C–O Asymmetric Stretch and C–C Symmetric Stretch of Trimethylene Oxide. *J. Mol. Spectrosc.* **2020**, *371*.

(24) Lorenzo, F.; Lesarri, A.; Lopez, J. C.; Alonso, J. L. Rotational Spectrum and Structure of the Oxetane-Argon Van Der Waals Complex. *Chem. Phys. Lett.* **1998**, *286*, 272–276.

(25) Sanz, M. E.; Sanz, V. M.; López, J. C.; Alonso, J. L. Oxetane-Hydrogen Fluoride Complex: A Rotational Study. *Chem. Phys. Lett.* **2001**, *342* (1–2), 31–38.

(26) Antolínez, S.; López, J. C.; Alonso, J. L. Rotational Spectra and Structure of the Hydrogen-Bonded Complex Oxetane···HCl. *Chem. Phys. Lett.* **2001**, *334* (4–6), 250–256.

(27) Ottaviani, P.; Giuliano, M.; Velino, B.; Caminati, W. Interactions Between Organic Molecules and Water: Rotational Spectrum of the 1:1 Oxetane?Water Complex. *Chem. - A Eur. J.* **2004**, *10* (2), 538–543.

(28) Harris, D. O.; Harrington, H. W.; Luntz, A. C.; Gwinn, W. D. Microwave Spectrum, Vibration-Rotation Interaction, and Potential Function for the Ring-Puckering Vibration of Trimethylene Sulfide. *J. Chem. Phys.* **1966**, *44* (9), 3467–3480.

(29) White, M. S.; Beeson, E. L. Microwave Spectrum of Trimethylene Sulfide. *J. Chem. Phys.* **1965**, *43* (5), 1839–1841.

(30) Hinze, R.; Guarnieri, A.; Alonso, J. L.; López, J. C. Electric Dipole Moments of Thietane in Excited States of the Ring Puckering Vibration: An Experimental and Ab Initio Study. *J. Mol. Struct.* **1995**, *350* (3), 195–204.

(31) van Wijngaarden, J.; Desmond, D.; Leo Meerts, W. Analysis of High Resolution FTIR Spectra from Synchrotron Sources Using Evolutionary Algorithms. *J. Mol. Spectrosc.* **2015**,

315, 107–113.

(32) Sanz, M. E.; López, J. C.; Alonso, J. L. Axial and Equatorial Hydrogen-Bond Conformers and Ring-Puckering Motion in the Trimethylene Sulfide·Hydrogen Fluoride Complex. *Chem. - A Eur. J.* **2002**, *8* (18), 4265–4271.

(33) Sanz, M. E.; Lesarri, A.; López, J. C.; Alonso, J. L. Hydrogen Bond in Molecules with Large-Amplitude Motions: A Rotational Study of Trimethylene Sulfide···HCl. *Angew. Chemie Int. Ed.* **2001**, *40* (5), 935–938.

(34) Evangelisti, L.; Sedo, G.; van Wijngaarden, J. Rotational Spectrum of 1,1,1-Trifluoro-2-Butanone Using Chirped-Pulse Fourier Transform Microwave Spectroscopy. *J. Phys. Chem. A* **2011**, *115* (5), 685–690.

(35) Sedo, G.; van Wijngaarden, J. Fourier Transform Microwave Spectra of a "New" Isomer of OCS-CO2. *J. Chem. Phys.* **2009**, *131* (4), 044303.

(36) Bannwarth, C.; Ehlert, S.; Grimme, S. GFN2-XTB - An Accurate and Broadly Parametrized Self-Consistent Tight-Binding Quantum Chemical Method with Multipole Electrostatics and Density-Dependent Dispersion Contributions. *J. Chem. Theory Comput.* **2019**, *15* (3), 1652–1671.

(37) Pracht, P.; Bohle, F.; Grimme, S. Automated Exploration of the Low-Energy Chemical Space with Fast Quantum Chemical Methods. *Phys. Chem. Chem. Phys.* **2020**, *22* (14), 7169–7192.

(38) Grimme, S. Exploration of Chemical Compound, Conformer, and Reaction Space with Meta-Dynamics Simulations Based on Tight-Binding Quantum Chemical Calculations. *J. Chem. Theory Comput.* **2019**, *15* (5), 2847–2862.

(39) Becke, A. D. Density-functional Thermochemistry. III. The Role of Exact Exchange. *J.*

Chem. Phys. **1993**, *98* (7), 5648–5652.

(40) Grimme, S.; Antony, J.; Ehrlich, S.; Krieg, H. A Consistent and Accurate Ab Initio Parametrization of Density Functional Dispersion Correction (DFT-D) for the 94 Elements H-Pu. *J. Chem. Phys.* **2010**, *132* (15), 154104.

(41) Grimme, S.; Ehrlich, S.; Goerigk, L. Effect of the Damping Function in Dispersion Corrected Density Functional Theory. *J. Comput. Chem.* **2011**, *32* (7), 1456–1465.

(42) Dunning, T. H. Gaussian Basis Sets for Use in Correlated Molecular Calculations. I. The Atoms Boron through Neon and Hydrogen. *J. Chem. Phys.* **1989**, *90* (2), 1007–1023.

(43) Grimme, S. Semiempirical Hybrid Density Functional with Perturbative Second-Order Correlation. *J. Chem. Phys.* **2006**, *124* (3), 034108.

(44) Møller, C.; Plesset, M. S. Note on an Approximation Treatment for Many-Electron Systems. *Phys. Rev.* **1934**, *46* (7), 618–622.

(45) Weigend, F.; Ahlrichs, R. Balanced Basis Sets of Split Valence, Triple Zeta Valence and Quadruple Zeta Valence Quality for H to Rn: Design and Assessment of Accuracy. *Phys. Chem. Chem. Phys.* **2005**, *7* (18), 3297–3305.

(46) Boys, S. F.; Bernardi, F. The Calculation of Small Molecular Interactions by the Differences of Separate Total Energies. Some Procedures with Reduced Errors. *Mol. Phys.* **1970**, *19* (4), 553–566.

(47) Frisch, M. J.; Trucks, G. W.; Schlegel, H. B.; Scuseria, G. E.; Robb, M. A.; Cheeseman, J. R.; Scalmani, G.; Barone, V.; Petersson, G. A.; Nakatsuji, H., et al. *Gaussian 16*, Revision C.01; Gaussian, Inc.: Wallingford, CT, 2016.

(48) Contreras-García, J.; Johnson, E. R.; Keinan, S.; Chaudret, R.; Piquemal, J.-P.; Beratan, D. N.; Yang, W. NCIPLOT: A Program for Plotting Noncovalent Interaction Regions. *J.*

Chem. Theory Comput. **2011**, *7* (3), 625–632.

(49) Keith, T. A. *AIMAll*, version 17.11.14; TK Gristmill Software: Overland Park, KS, 2016.

(50) Hohenstein, E. G.; Sherrill, C. D. Density Fitting of Intramonomer Correlation Effects in Symmetry-Adapted Perturbation Theory. *J. Chem. Phys.* **2010**, *133* (1), 014101.

(51) Parrish, R. M.; Burns, L. A.; Smith, D. G. A.; Simmonett, A. C.; DePrince, A. E.; Hohenstein, E. G.; Bozkaya, U.; Sokolov, A. Y.; Di Remigio, R.; Richard, R. M.; et al. Psi4 1.1: An Open-Source Electronic Structure Program Emphasizing Automation, Advanced Libraries, and Interoperability. *J. Chem. Theory Comput.* **2017**, *13* (7), 3185–3197.

(52) Pickett, H. M. The Fitting and Prediction of Vibration-Rotation Spectra with Spin Interactions. *J. Mol. Spectrosc.* **1991**, *148* (2), 371–377.

(53) Watson, J. K. G. Determination of Centrifugal Distortion Coefficients of Asymmetric-Top Molecules. III. Sextic Coefficients. *J. Chem. Phys.* **1968**, *48* (10), 4517–4524.

(54) Kraitchman, J. Determination of Molecular Structure from Microwave Spectroscopic Data. *Am. J. Phys.* **1953**, *21* (1), 17–24.

(55) Kisiel, Z. PROSPE - Programs for ROtational SPEctroscopy http://www.ifpan.edu.pl/~kisiel/prospe.htm (accessed Nov 8, 2019).

(56) Gordy, W.; Cook, R. L.; Gordy, Walter; Cook, R. L. *Microwave Molecular Spectra*, 3rd ed.; John Wiley & Sons Inc.: New York, 1984.

(57) Loru, D.; Steber, A. L.; Pinacho, P.; Gruet, S.; Temelso, B.; Rijs, A. M.; Pérez, C.; Schnell, M. How Does the Composition of a PAH Influence Its Microsolvation? A Rotational Spectroscopy Study of the Phenanthrene–Water and Phenanthridine–Water Clusters. *Phys. Chem. Chem. Phys.* **2021**, *23* (16), 9721–9732.

Chapter 7. Characterization of Large Amplitude Motions and Hydrogen Bonding Interactions in the Thiophene–Water Complex by Rotational Spectroscopy[4]

In the previous chapter, it was shown that the complex formed between water and the saturated heterocycles TMO and TMS are driven primarily *via* O–H···S and O–H···O hydrogen bonds in which the heteroatoms constitute the preferred binding site for the water molecule. In this chapter, the intermolecular complex between water and a sulfur heteroaromatic compound (thiophene) is discussed and compared to results from the literature for its oxygen (furan) and nitrogen (pyrrole) counterparts. The thiophene–water complex was shown to be very dynamic undergoing large amplitude motions associated with internal dynamics of the water molecule which made the determination of the location of water within the complex very challenging. By modelling the energy barriers related to the water motions and observing transitions for the singly substituted ^{18}O isotopologue, the geometry of the complex is determined to be highly averaged over the interconversion between two forms of the global minimum. The details of the observed geometry and its non-covalent interactions are discussed below. Surprisingly, while water still binds to furan and pyrrole through hydrogen bonding interactions involving the heteroatoms, the topology of the interactions in the thiophene–w complex is unique with the π-electron cloud of the ring being the most favoured interaction site for the water subunit while the sulfur atom is involved in secondary interaction.

[4]The content of this chapter is an adapted version of the article published in the Journal of Physical Chemistry A under the citation: Silva, W. G. D. P.; van Wijngaarden, J. Characterization of Large-Amplitude Motions and Hydrogen Bonding Interactions in the Thiophene–Water Complex by Rotational Spectroscopy, *J. Phys. Chem. A* **2021**, *125*, 3425–3431.

7.1 Abstract

The rotational fingerprint of the thiophene–water complex was investigated for the first time using Fourier transform microwave spectroscopy (7–20 GHz) aided by quantum mechanical calculations. Transitions for a single species were observed and the rotational constants for the parent and ^{18}O isotopomers are consistent with a geometry that is highly averaged over a barrierless large amplitude motion of water that interconverts two equivalent forms corresponding to the global minimum (B2PLYP-D3(BJ)/def2-TZVP). In this effective geometry, the water lies above the thiophene ring close to its σ_v plane of symmetry. The observed transitions are split by a second water-centered tunneling motion that exchanges its two protons by internal rotation about its C_2 axis with a calculated barrier of ~2.7 kJ mol^{-1} (B2PLYP-D3(BJ)/def2-TZVP). Based on quantum theory of atoms in molecules, non-covalent interaction and symmetry-adapted perturbation theory analyses, the observed geometry enables two intermolecular interactions (O–H···π and O–H···S) whose electrostatic and dispersive contributions favour formation of the thiophene–water complex.

7.2 Introduction

Non-covalent interactions involving aromatic rings play a key role in many chemical and biological processes such as molecular recognition, aggregation and protein folding.[1,2] Despite their importance, accurate experimental and computational descriptions of the molecular level forces involved in solvation of an aromatic molecule remain challenging even for small prototypical systems such as 1:1 solvent–solute molecular aggregates.[3–5] When a solvent molecule

approaches an aromatic ring, interactions may be formed with the π-electron clouds of the ring, either at its center or on a C=C bond, or with the aromatic hydrogens in which the solvent may serve as a proton donor and/or acceptor.[6] The scenario is more complicated for aromatic heterocycles as additional contacts may be established with the heteroatom.[3–5,7,8] The presence of multiple potential binding sites with interaction energies that are often sensitive to the computational levels chosen affirm the importance of experimental studies of isolated solvent–solute complexes.

Coupled with the complexity described above, rotational spectroscopic studies of the monohydrated complexes of pyrrole (pyrrole–w)[4,9], pyridine (pyridine–w)[5] and thiazole (thiazole–w)[8] revealed that due to a shallow potential energy surface around the global minimum geometry, the ground state structures of these complexes, stabilized by N–H···O (pyrrole–w) and N···H–O (pyridine–w and thiazole–w) hydrogen bonds (HB) in which the oxygen atom of water lies in the same plane as the heterocyclic structure, are highly influenced by large amplitude motions. These motions (not typically captured by routine computational methods) are associated with the internal dynamics of water and may lead to tunneling splittings in the rotational spectrum depending on the barrier height. Although the water complexes of the oxygen and sulfur counterparts of pyrrole, namely furan and thiophene, have not been investigated by rotational spectroscopy, their vibrational spectra were reported by Ar matrix FTIR (Fourier transform infrared) spectroscopy.[10] While for furan–w the IR spectrum was consistent with a single geometry with the oxygen of water in the plane of the ring and stabilized by a O–H···O HB in agreement with computational results,[7] for thiophene–w, the dominant species in the matrix is governed by a weak C–H···O interaction with all heavy atoms in one plane. This was rather unexpected as the lowest energy conformer is predicted to have the water molecule above the plane of the thiophene ring and to be stabilized by

a O–H···π interaction.[10] The vibrational spectrum of thiophene–w thus raises the question of whether the preferred binding site of water in this complex is in fact ruled by a C–H···O interaction or if the observed results were affected by matrix effects. In any case, previous investigations have shown that water preferentially binds to the more electronegative heteroatoms in pyrrole, pyridine, thiazole and furan (with the oxygen of water lying in the same plane as the ring) whereas interactions with thiophene are intrinsically different in nature. This is likely due to the less electronegative sulfur atom.

Herein, we describe the first investigation of the thiophene–w complex using high resolution rotational spectroscopy to resolve the discrepancy between experiment (matrix IR) and theory in terms of the most stable geometry of the dimer. Rotational spectroscopy is the ideal tool for this as the patterns of transitions are governed by the moments of inertia providing confirmation of the underlying geometry. Additionally, the supersonic jet is a collision-free environment where species are studied in isolation of solvent and matrix effects. Our combined quantum chemical and spectroscopic study establishes that the ground state structure of thiophene–w is highly averaged over a barrierless large amplitude motion that interconverts two equivalent forms of the complex corresponding to the global minimum. The interactions governing the formation of the complex were investigated using quantum theory of atoms in molecules (QTAIM)[11] and non-covalent interaction (NCI)[12] analyses. The nature of the intermolecular interactions forming the thiophene–w complex were studied using symmetry-adapted perturbation theory (SAPT)[13] calculations and are compared with theoretical results derived here for the related species pyrrole–w, furan–w and benzene–w. The analyses show that the observed complex is stabilized by O–H···π and O–H···S HB while SAPT calculations show that thiophene behaves more like a benzene molecule when binding to water than other heterocycles.

7.3 Methods

7.3.1 Experimental Methods

The rotational fingerprints of the thiophene–w complex were investigated from 7–20 GHz using a broadband chirped-pulse (CP) and a cavity-based Balle-Flygare (BF) type Fourier transform microwave (FTMW) spectrometer. Both instruments have been described in detail previously.[14,15] To produce the complex, a gas mixture of ~1% thiophene (99%, bp: 357K, Sigma-Aldrich Canada) seeded in neon was prepared at room temperature and subsequently bubbled through a reservoir containing water (or water enriched with ^{18}O for isotopic measurements). The resulting gas mixture (thiophene + water) was then delivered inside the high vacuum chambers (P ~ 10^{-7} kPa) of the instruments using a pulsed nozzle (1 mm orifice) which creates a supersonic jet expansion. In the jet, the molecules are probed in a collision-free environment where the rotational temperature is cooled to a few Kelvin. Initially, a broadband survey spectrum was collected with the CP-FTMW instrument from 8–18 GHz in segments of 2 GHz from which the most intense rotational transitions of the parent and ^{18}O species of the thiophene–w complex were identified. Final frequency measurements were performed using the BF-FTMW spectrometer from 7–20 GHz which features higher resolution and sensitivity. In a typical BF-FTMW experiment, the recorded transitions have widths of ~7 kHz (FWHM) while the uncertainty in line positions is ±2 kHz. The transitions are split into two Doppler components due to the collinear arrangement of the molecular beam and the resonator axis.

7.3.2 Computational Methods

The possible geometries of the thiophene–w complex were identified by performing a conformational search using the conformer-rotamer ensemble sampling tool (CREST)[16] as implemented in the extended tight binding (xTB) program.[17] The search found 28 plausible structures for the complex which were fully optimized at the double-hybrid B2PLYP[18]-D3(BJ)[19,20]/def2-TZVP[21] level of theory. For the optimization calculations, we used a tight convergence criteria given the characteristic shallow potential energy surface of related water complexes and included the Boys and Bernardi's counterpoise[22] method to account for the basis set superposition error (BSSE). Harmonic frequency calculations were also carried out at the same level of theory to verify the nature of the stationary points and to obtain relative energies with zero-point correction (ZPE) and quartic centrifugal distortion constants. The optimization and frequency calculations confirmed the presence of only four unique conformers (out of the 28 initial geometries from CREST) for thiophene–w at the B2PLYP-D3(BJ)/def2-TZVP level. To obtain energy barriers associated with the interconversion between conformers, transition state structures were optimized at the B2PLYP-D3(BJ)/def2-TZVP level and were confirmed to be true by the presence of a single imaginary frequency. All optimization and frequency calculations were carried out using the Gaussian 16 program.[23]

To visualize the intermolecular interactions occurring in thiophene–w, we performed QTAIM[11] and NCI[12] analyses using the AIMALL[24] and NCIPLOT[25] programs, respectively. The nature behind the formation of the thiophene–w dimer was further investigated by decomposing the complex interaction energy into four physically meaningful components (electrostatic, dispersion, induction and exchange) using a SAPT analysis.[13] We also carried out SAPT

calculations for related complexes such as furan–w, pyrrole–w and benzene–w and compare the results with those obtained for thiophene–w. All SAPT calculations were performed at the SAPT2+(3)δMP2[26]/def2-TZVP level using the Psi4 code.[27]

7.4 Results

The conformational search using CREST followed by higher level quantum chemical calculations suggest that water can interact with thiophene to form four stable conformers (I, II, III and IV, Figure 7.1) numbered in order of increasing energy. The Cartesian coordinates for their equilibrium structures at the B2PLYP-D3(BJ)/def2-TZVP level are given in Appendix D in Tables S48–S51 of the supporting information (SI) file. The calculated zero-point corrected relative energies, rotational constants and electric dipole moment components of each conformer are provided in Table 7.1. Although these four conformers have been reported[10] theoretically, we decided to extend the computational work on the thiophene–w complex to include B2PLYP-D3(BJ)/def2-TZVP calculations. This level of theory is known[4,8,28] to provide accurate estimates for the rotational parameters of water complexes facilitating the assignment of the different species in the rotational spectrum.

Based on the quantum mechanical calculations from Table 7.1, conformer I is predicted to be the global minimum geometry for the complex and appears to be stabilized by O–H···π interactions in which one hydrogen of water binds to the π-orbital of a C=C bond while the other hydrogen atom is directed above the middle of the ring (Figure 7.1). This is contrary to the most stable conformer reported for the monohydrates of furan (O···H–O),[7] pyrrole (N–H···O)[4], thiazole (N···H–O)[8] and pyridine (N···H–O)[5] where the center of mass of water lies in the plane of the ring

such that water binds to the most electronegative heteroatom or with the hydrogen attached to it in the case of pyrrole. The structure reported to be the most abundant based on the Ar matrix IR spectrum,[10] forming a C–H···O HB (conformer II in this work), is predicted to be at least 2.4 kJ mol^{-1} (Table 7.1) less stable than conformer I at the B2PLYP-D3(BJ)/def2-TZVP level.

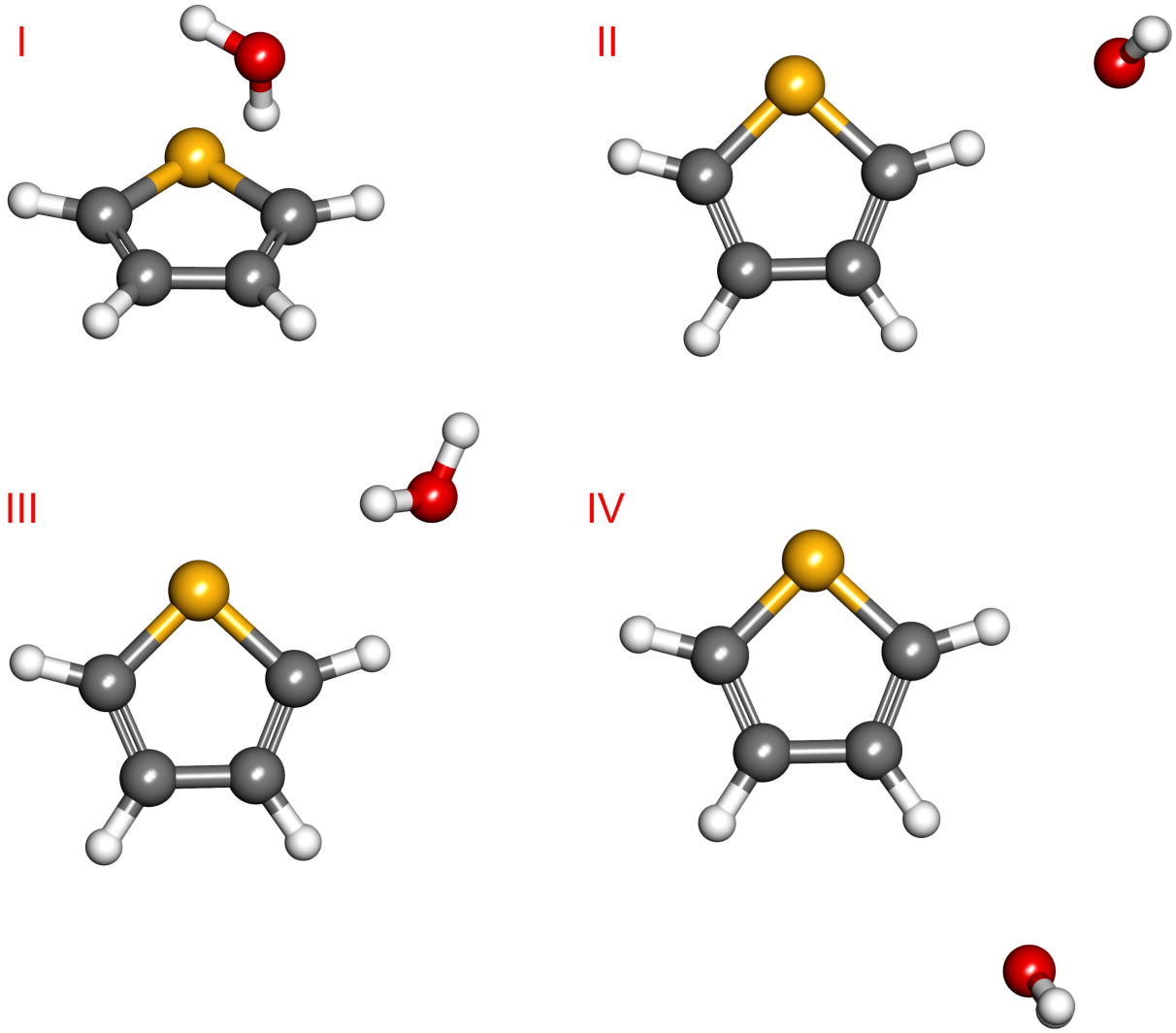

Figure 7.1 Four conformers of the thiophene–w complex obtained at the B2PLYP-D3(BJ)/def2-TZVP level of theory.

Table 7.1 Calculated relative energies with zero-point correction (ΔE_{ZPE}), rotational constants (*A*, *B*, *C*) and electric dipole moment components for the conformers of the thiophene–w complex obtained at the B2PLYP-D3(BJ)/def2-TZVP level of theory.

Conformer	ΔE_{ZPE} (kJ mol^{-1})	*A*/*B*/*C* (MHz)	$\mu_a/\mu_b/\mu_c$ (Debye)
I	0.0	3461/1983/1788	2.2/0.5/0.7
II	2.4	5550/1325/1075	2.4/0.3/0.0
III	2.5	5845/1587/1287	0.8/0.9/1.1
IV	4.4	7030/1092/949	3.0/0.0/0.0

As the rotational signature of the thiophene–w complex has not been previously reported, the calculated parameters from Table 7.1 were used to guide the spectroscopic assignment. In the rotational spectrum, we observed transitions belonging to the thiophene monomer and new sets of lines which were assigned to conformer I of thiophene–w. The assigned lines were *a*-type R-branch transitions, consistent with the large $|\mu_a|$= 2.2 D for conformer I and showed a tunneling splitting which was readily recognized in the CP-FTMW spectrum. The assignments were confirmed by measuring transitions for the singly substituted ^{18}O species (obtained from experiments using $H_2{}^{18}O$) which were also split into tunneling doublets. For both parent and ^{18}O species, the tunneling components presented an intensity ratio of ~3:1 based on the cavity BF-FTMW measurements. The two tunnelling states for each isotopomer were fitted independently with Pickett's SPFIT program[29] using a Watson's S-reduced Hamiltonian (I^r representation)[30] to yield the spectroscopic parameters shown in Table 7.2. The complete line lists containing the transition frequencies and fit residuals are given in Tables S52–S53. The transitions for the two tunneling states were labeled as 'lower' and 'upper' in Table 7.2 which refer to the sets of lines observed at lower and higher frequency, respectively. Despite the sizeable $|\mu_b|$= 0.5 D and $|\mu_c|$= 0.7 D dipole components predicted for conformer I and a careful search, neither *b*- nor *c*-type transitions could be observed

in the spectrum. Transitions consistent with other conformers of thiophene–w were not observed despite the fact that the μ_a-dipole of conformer II is predicted to be greater than that of conformer I.

Table 7.2 Spectroscopic parameters obtained for the observed species of the thiophene–w complex.

	Parent			^{18}O			
Parameter	Lower	Upper	Average	Lower	Upper	Average	B2PLYP-D3(BJ)[f]
A/MHz[a]	3300.1290(71)	3340.8600(76)	3320.4945	3294.40(11)	3334.33(24)	3314.365	3461
B/MHz	2089.06830(34)	2093.94782(35)	2091.50806	1961.2425(25)	1965.9168(27)	1963.57965	1983
C/MHz	1879.73050(24)	1885.01782(25)	1882.37416	1773.7528(25)	1778.5700(35)	1776.1614	1788
D_J/kHz[b]	6.5214(48)	6.0429(52)	12.5643	5.73(12)	5.19(16)	5.46	8.612
D_{JK}/kHz	39.537(47)	34.503(50)	37.020	[39.537][e]	[34.503]	37.020	5.282
d_1/kHz	-1.2704(44)	-1.1675(44)	1.21895	[-1.2704]	[-1.1675]	1.21895	1.214
d_2/kHz	0.2545(36)	0.1234(54)	0.18895	[0.2545]	[0.1234]	0.18895	-0.425
N[c]	29			13			
σ/kHz[d]	0.7			4.8			

[a]Rotational constants (A, B and C), [b]quartic distortion constants (D_J, D_{JK}, d_1, d_2), [c]number of fitted transitions (N), [d]standard deviation of the fit (σ); [e]Values in brackets [ ] were fixed to the value derived for the parent species. [f]def2-TZVP basis set.

7.5 Discussion

Based on comparison of the experimentally-derived rotational constants with the quantum chemical predictions from Table 7.1, it is evident that the measured spectrum of thiophene–w is closest to that expected for conformer I, the global minimum geometry. This establishes that the O–H···π HB is the dominant interaction that favours complex formation. Our results, based on the rotational spectrum of the isolated dimer, differ from those derived from IR experiments in which the C–H···O bound conformer II was purported to be the major species, however, this may have been influenced by matrix effects.[10] Although the experimental rotational constants (Table 7.2) for conformer I are consistent with the calculated values (Table 7.1), the discrepancies are larger than one might expect as are the differences in the centrifugal distortion constants (Table 7.2). From the absence of *b*- and *c*-type transitions and the observation of a tunneling splitting in the spectrum, it is clear that internal motions associated with the water molecule must be investigated to understand the spectrum of thiophene–w. In previous studies of the related pyrrole–w,[4,9] thiazole–w[8] and pyridine–w[5] complexes, for example, no *c*-type transitions were detected in the rotational spectrum despite sizeable $|\mu_c|$ due to internal dynamics of water which average the dipole along the *c*-axis to zero.

Based on the geometry of conformer I as shown in Figure 7.2, there is an equivalent form in which the O–H···π interaction is established on the opposite side of thiophene's σ_v plane. In Figure 7.2, we investigate two possible pathways (Path 1 and Path 2) for interconversion between Ia and Ib and their corresponding transition states whose natures are confirmed by the observation of a single imaginary frequency at the B2PLYP-D3(BJ)/def2-TZVP. The calculated energy barriers for Path 1 and Path 2 are very low; on the order of 0.4 kJ mol^{-1} and 0.8 kJ mol^{-1} (B2PLYP-

D3(BJ)/def2-TZVP). When ZPE corrections are taken into consideration, the interconversion between Ia and Ib is essentially barrierless as the barriers are lowered to -0.2 kJ mol^{-1} for Path 1 and 0.4 kJ mol^{-1} for Path 2. This implies that the ground state structure is an effective one lying somewhere between that of Ia and Ib. The observation of averaged ground state structures as a consequence of large amplitude motions have been previously reported for monohydrated complexes of small heterocycles[4,8] and flexible molecules such as 2-fluoroethanol.[31]

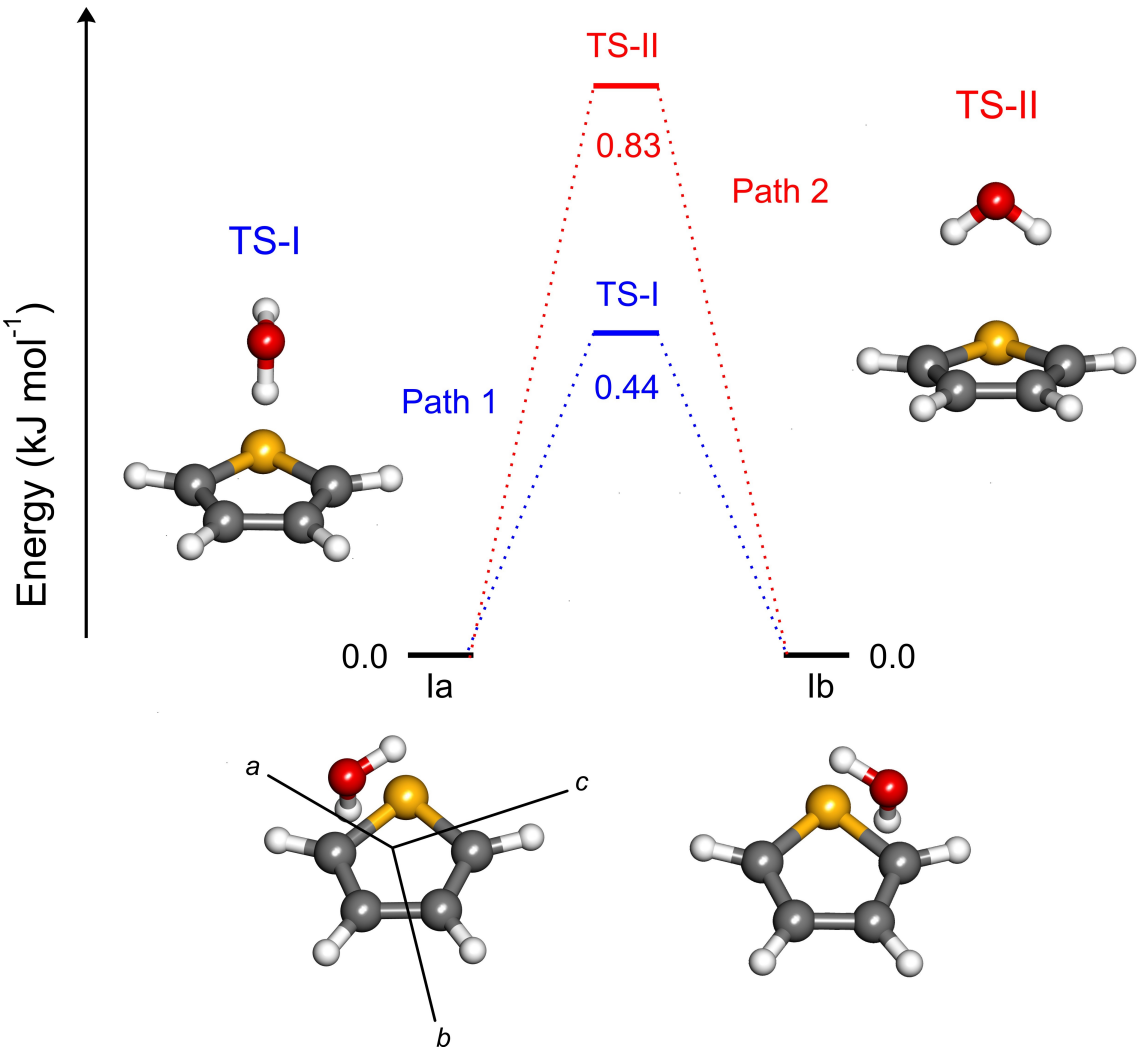

Figure 7.2 Possible pathways (Path 1 and Path 2) and transitions states (TS-I and TS-II) for the interconversion between the two equivalent forms of conformer I (Ia and Ib) obtained at the B2PLYP-D3(BJ)/def2-TZVP level.

To better characterize the ground state geometry, we first used the experimental rotational constants of the singly substituted ^{18}O isotopomer to derive Kraitchman's[32] substituted r_s atomic coordinates (Table 7.3) for the oxygen of water using the KRA program.[29] It is important to note that the obtained $|c|$ coordinate was set to zero since it yielded an imaginary value in the analysis suggesting that the oxygen atom is close to the *ab*-plane of the complex. In Figure 7.3, we compare the position of water in the equilibrium geometry of conformer I and in the two transitions states (TS-I and TS-II); the atomic coordinates for these geometries are also given in Table 7.3. From the *c*-coordinates in particular, it is evident that the ground state geometry is closer to that of TS-I and TS-II (but slightly closer to that of TS-I) than to the equilibrium geometry of conformer I. To describe the geometry of thiophene–w in terms of the principal axis system of the thiophene monomer,[33] a Kraitchman analysis was also performed treating the water molecule (mass 18.01056 amu) as a substitution site of the thiophene monomer. This provided substitution coordinates {*a*, *b*, *c*} with absolute values of 0.523(3) Å, 0.267(6) Å and 3.3801(5) Å which places the center of mass of water slightly out of the *ac*-plane (σ_v) of thiophene (0.267(6) Å) which would be analogous to the *c*-coordinate in the TS of the thiophene–w complex (Figure 7.3 top). While this value may seem consistent with the magnitude of the *c*-coordinate of conformer I in its equilibrium form in Table 7.3, it is important to note that the axis system is shifted and rotated slightly in conformer I by comparison as shown in Figure 7.2. A more realistic picture of the position of water relative to the σ_v plane of thiophene in conformer I is seen in Figure 7.3 in the bottom left corner. As the oxygen atom (and its center of mass) is above the C=C bond, we can estimate that the distance to the σ_v plane of thiophene is around half the C–C bond distance (~1.4 Å). This result from treating water as a point is consistent with the other Kraitchman results in Table 7.3 that the ground state geometry is closer to that of a TS geometry than the equilibrium geometry.

Table 7.3 Kraitchman's coordinates (in Ångstroms) with associated Costain errors obtained for the oxygen atom of water from the observed tunnelling states (Lower, Upper) and quantum chemical calculations (I, TS-I, TS-II). Refer to Figure 7.2 and Figure 7.3 for the axis systems from the equilibrium and transition state structures.

	$\|a\|$	$\|b\|$	$\|c\|$
Lower	2.8293(6)	0.411(4)	0[a]
Upper	2.8245(7)	0.432(5)	0[a]
I	2.91	0.45	0.28
TS-I	2.87	0.51	0.00
TS-II	2.80	0.56	0.00

[a]Set to zero due to the presence of an imaginary value.

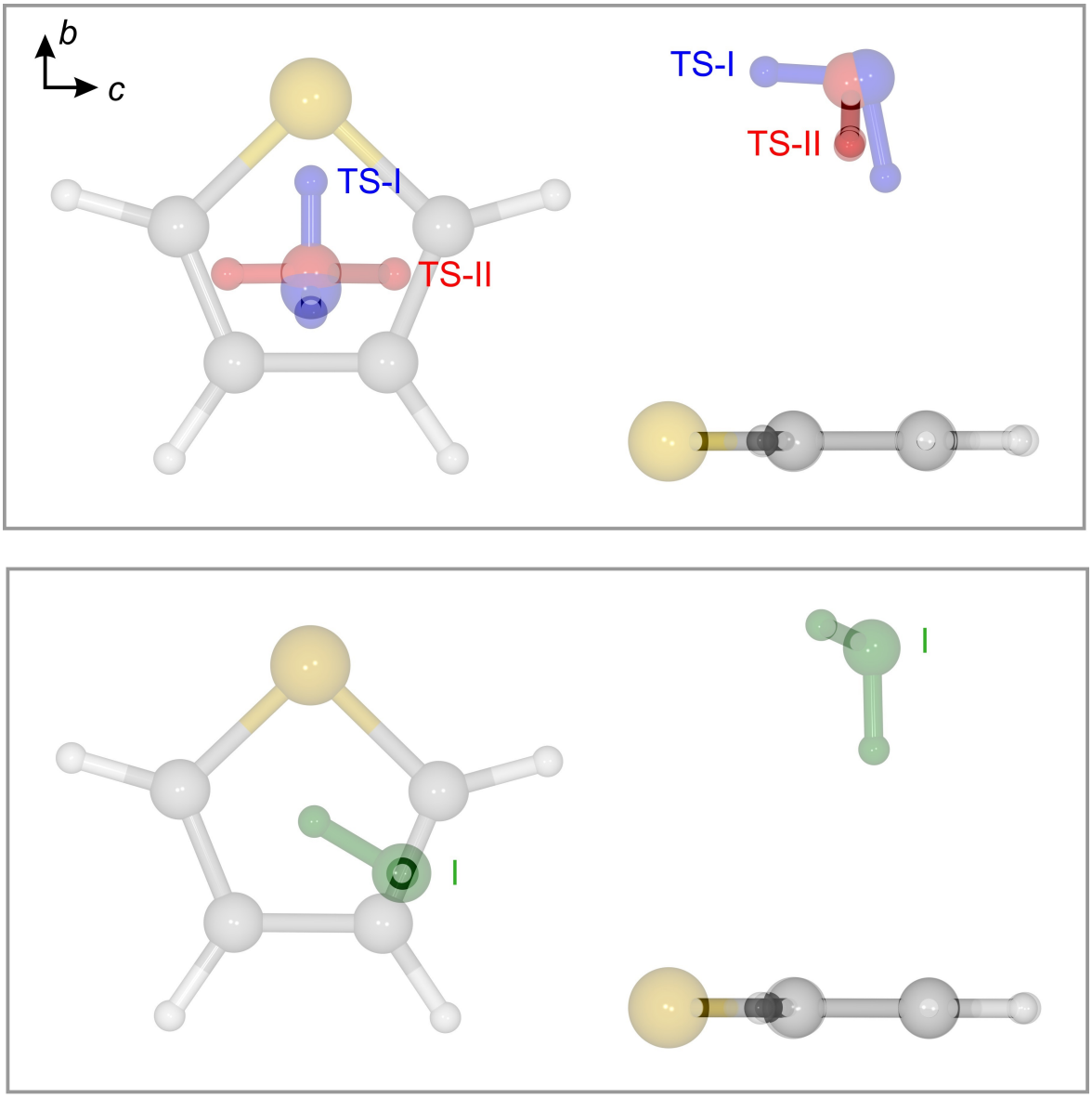

Figure 7.3 Comparison of the position of water in the equilibrium geometry of conformer I (green), TS-I (blue) and TS-II (red). Note that the axis system in the equilibrium geometry (bottom) is that given in Figure 7.2.

Additional information about the location of the water molecule within the complex can be derived from the planar moments of inertia obtained from the rotational constants. The P_{cc} values for the parent (62.26 amu Å^2 and 63.10 amu Å^2 for the upper and lower tunneling states, respectively) and ^{18}O species (62.25 amu Å^2 and 63.10 amu Å^2) of thiophene–w, are very similar to the P_{bb} value reported for the thiophene monomer (62.87 amu Å^2).[34] This suggests that the water molecule lies largely in thiophene's σ_v plane of symmetry. Similar results have been observed for the thiophene–HBr and thiophene–HCl complexes in which the HBr and HCl subunits are located on the σ_v plane of the thiophene ring.[34] By comparing the experimental P_{cc} values of thiophene–w with those predicted computationally for conformer I (59.12 amu Å^2), TS-I (62.57 amu Å^2) and TS-II (63.65 amu Å^2), the P_{cc} values of TS-I and TS-II (in particular TS-I) are closer to the experimentally derived values which lends further support to the position of the oxygen atom in the highly averaged ground state structure.

The observation of a structure with the oxygen centered above the thiophene ring as in TS-I and TS-II is also consistent with the lack of *c*-type transitions in the spectrum as a motion *via* these transition states would average the dipole along the *c*-axis to zero as reported for pyrrole–w,[4,9] thiazole–w[8] and pyridine–w.[5] The absence of *b*-type transitions indicates that the ground state structure is more similar to TS-I as the predicted μ_b for this geometry is -0.1 D (B2PLYP-D3(BJ)/def2-TZVP) (compared with 0.5 D in conformer I and 1.2 D in TS-II). While the μ_b dipole component does not average to zero if the thiophene–w complex passes through TS-I, its magnitude would be a very small relative to that of the μ_a dipole of 2.2 D which is consistent with our inability to observe *b*-type transitions. Collectively, the above observations from Kraitchman's analysis, planar moments and selection rules, suggest that the water subunit undergoes a large amplitude motion within the thiophene–w complex *via* TS-I (Figure 7.2).

The rotational transitions of thiophene–w also displayed a tunneling splitting and as the large amplitude motion between Ia and Ib is essentially barrierless, this is likely associated with exchange of the two hydrogens of water *via* inertial rotation along its C_2 axis. We estimated the barrier of this motion in the thiophene–w complex to be of about 2.7 kJ mol^{-1} (B2PLYP-D3(BJ)/def2-TZVP) based on the geometry of TS-I. An analogous internal rotation of water led to tunneling splittings in the pyrrole–w[4,9] and pyridine–w[5] dimers.

With novel insights regarding the effective ground state structure of the thiophene–w complex (compared with those of other heterocycles), we analyzed the interactions responsible for the formation of the dimer using QTAIM,[11] NCI,[12] and SAPT[13] calculations. The calculations were performed for the optimized TS-I geometry since it is a reasonable model of the observed averaged ground state structure. In the QTAIM molecular graph of thiophene–w (Figure 7.4), a bond path (black dotted line) and a bond critical point (BCP, green dot) are observed between one hydrogen of water which acts as a HB donor and the C=C bond suggesting that a primary O–H···π interaction is responsible for the formation of the complex. Based on the electron potential energy (V) at the BCP, an interaction strength of ~5.1 kJ mol^{-1} (E= 0.5V)[35] is obtained for the O–H···π HB which is approximately 4.6 times weaker than the O–H···N HB reported for thiazole–w[8] for comparison. Although the observed geometry of thiophene–w seems to favour an additional S···H–O interaction, the QTAIM analysis did not detect it. This means that this interaction is either absent in thiophene–w or not strong enough to be captured by the QTAIM method. Thus, we also performed NCI calculations which is a more suitable approach for describing weaker, long-range interactions. The NCI isosurfaces (Figure 7.4), obtained from the electron density and its derivatives, confirm the primary O–H···π HB but also show the existence of the secondary O–H···S

contact in the complex in which water also acts as a HB donor. Both interactions are visualized by the blue-green isosurfaces in the interacting regions.

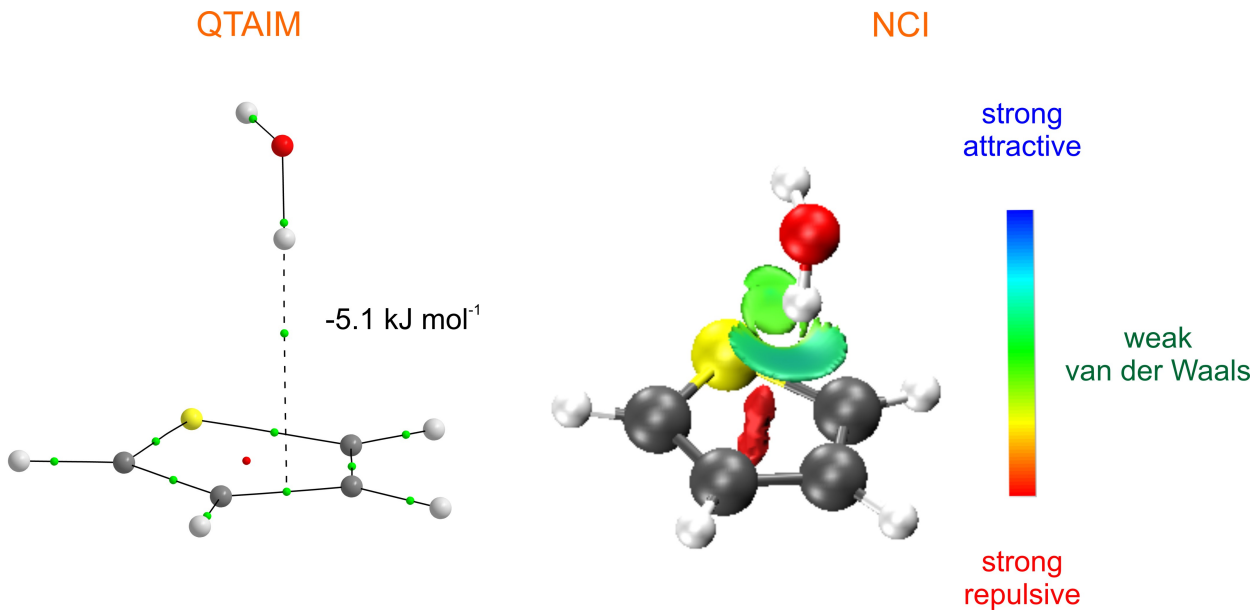

Figure 7.4 QTAIM molecular graph (left) and NCI isosurface (right, s=0.5 and colour scale BGR: $0.02 < \rho < +0.02$) for the observed conformer of the thiophene–w complex.

While the QTAIM and NCI analyses provide descriptions of each intermolecular interaction, SAPT analysis gives more quantitative knowledge of the nature behind the formation of the complex. We compare the SAPT results of thiophene–w with those for pyrrole–w, furan–w and benzene–w in Table 7.4. The total SAPT energies indicate that pyrrole and furan form the most stable complexes with water due to larger contributions from the electrostatic term. The preferred stability of these two complexes is consistent with the stronger N–H···O and O–H···O HBs they form with water in contrast to the weaker O–H···S and/or O–H···π HBs in thiophene–w and benzene–w. Although all complexes have the electrostatic energy as the most stabilizing term, representing at least ~48% of the total stabilization energy (electrostatic + repulsion + induction), a noticeable increase in the contributions from dispersion is observed from pyrrole–w (15.4%) <

furan–w (22%) < thiophene–w (36.8%) ~ benzene–w (38.0%). In the monohydrates of thiophene and benzene, the electrostatic and dispersive contributions are much more balanced which supports the idea that the O–H···π HBs are weaker, longer-range interactions and more dispersive in nature. Overall, from the SAPT results in Table 7.4, the nature of the interactions binding thiophene to water are more similar to those of benzene–w than for those of heterocycles such as furan and pyrrole. The preference of water to interact primarily with the π-system in thiophene rather than to the heteroatom as in furan,[7] pyrrole[4,9] and thiazole[8] is explained by key differences in the electron density distribution in the heterocycles. While in furan and pyrrole the negative charges are concentrated around O and N due to their high electronegativity, in thiophene, the negative charge from the heteroatom is more dispersed into the ring making the π-systems the preferred binding site for the water molecule.[10,34]

Table 7.4 Symmetry-adapted perturbation theory results for thiophene–w, benzene–w, furan–w and pyrrole–w obtained at the SAPT2+(3)δMP2/def2-TZVP level of theory. The values in brackets ( ) represent the contribution of that term (in percentage) to the total stabilizing energy (electrostatic + induction + dispersion).

Complex	Total	Electrostatic	Induction	Dispersion	Exchange
Thiophene–w	-10.8	-11.6 (48.6%)	-3.5 (14.6%)	-8.8 (36.8%)	13.1
Benzene–w	-11.6	-13.5 (48.4%)	-3.8 (13.6%)	-10.6 (38.0%)	16.3
Furan–w	-12.1	-20.6 (59.6%)	-6.4 (18.4%)	-7.6 (22.0%)	22.5
Pyrrole–w	-22.4	-34.7 (65.9%)	-9.9 (18.7%)	-8.1 (15.4%)	30.3

7.6 Conclusions

Combining rotational spectroscopy and quantum mechanical calculations, the geometry of the thiophene–w complex was established for the first time in isolation of solvent and matrix effects. The observed spectrum is consistent with a geometry that is highly averaged over a barrierless large amplitude motion which interconverts the two equivalent forms of conformer I corresponding to the predicted global minimum at the B2PLYP-D3(BJ)/def2-TZVP level of theory. In this effective geometry, the water molecule lies above the thiophene ring close to its σ_v plane of symmetry and forms the complex *via* O–H···π and S···H–O HBs as supported by the experimentally-derived planar moments, substitution coordinates for the water oxygen (from ^{18}O measurements), QTAIM and NCI analyses. In addition to the above large amplitude motion, the transitions for the thiophene–w complex showed a tunneling splitting that is attributed to a water-centered internal rotation about its C_2 axis which exchanges the protons of water with a calculated barrier of ~2.7 kJ mol^{-1} (B2PLYP-D3(BJ)/def2-TZVP). Based on SAPT results, we show that a balance of electrostatic and dispersive forces contributes to the stabilization of the thiophene–w complex while for pyrrole–w and furan–w, the electrostatic term is dominant. This work on the thiophene–w dimer serves as a guide for future investigations on larger molecular complexes of thiophene with larger solvent shells.

7.7 References

(1) Nishio, M.; Umezawa, Y.; Fantini, J.; Weiss, M. S.; Chakrabarti, P. CH-π Hydrogen Bonds in Biological Macromolecules. *Phys. Chem. Chem. Phys.* **2014**, *16* (25), 12648–12683.

(2) Brandl, M.; Weiss, M. S.; Jabs, A.; Sühnel, J.; Hilgenfeld, R. C-H···π-Interactions in Proteins. *J. Mol. Biol.* **2001**, *307* (1), 357–377.

(3) Gottschalk, H. C.; Poblotzki, A.; Fatima, M.; Obenchain, D. A.; Pérez, C.; Antony, J.; Auer, A. A.; Baptista, L.; Benoit, D. M.; Bistoni, G.; et al. The First Microsolvation Step for Furans: New Experiments and Benchmarking Strategies. *J. Chem. Phys.* **2020**, *152* (16), 164303.

(4) Wu, B.; Xie, F.; Xu, Y. The Pyrrole-Water Complex: Multidimensional Large Amplitude Dynamics and Rotational Spectra of Its ^{13}C Isotopologues. *J. Mol. Spectrosc.* **2020**, *374*, 111381.

(5) Mackenzie, R. B.; Dewberry, C. T.; Cornelius, R. D.; Smith, C. J.; Leopold, K. R. Multidimensional Large Amplitude Dynamics in the Pyridine-Water Complex. *J. Phys. Chem. A* **2017**, *121* (4), 855–860.

(6) Li, S.; Cooper, V. R.; Thonhauser, T.; Puzder, A.; Langreth, D. C. A Density Functional Theory Study of the Benzene−Water Complex. *J. Phys. Chem. A* **2008**, *112* (38), 9031–9036.

(7) Lockwood, S. P.; Fuller, T. G.; Newby, J. J. Structure and Spectroscopy of Furan:H_2O Complexes. *J. Phys. Chem. A* **2018**, *122* (36), 7160–7170.

(8) Li, W.; Chen, J.; Xu, Y.; Lu, T.; Gou, Q.; Feng, G. Unveiling the Structural and Energetic

Properties of Thiazole-Water Complex by Microwave Spectroscopy and Theoretical Calculations. *Spectrochim. Acta - Part A Mol. Biomol. Spectrosc.* **2020**, *242*, 118720.

(9) Tubergen, M. J.; Andrews, A. M.; Kuczkowski, R. L. Microwave Spectrum and Structure of a Hydrogen-Bonded Pyrrole-Water Complex. *J. Phys. Chem.* **1993**, *97* (29), 7451–7457.

(10) Wasserman, J. G.; Murphy, K. J.; Newby, J. J. Evidence of C–H···O Interactions in the Thiophene:Water Complex. *J. Phys. Chem. A* **2019**, *123* (48), 10406–10417.

(11) Bader, R. F. W. Atoms in Molecules. *Acc. Chem. Res.* **1985**, *18* (1), 9–15.

(12) Johnson, E. R.; Keinan, S.; Mori-Sánchez, P.; Contreras-García, J.; Cohen, A. J.; Yang, W. Revealing Noncovalent Interactions. *J. Am. Chem. Soc.* **2010**, *132* (18), 6498–6506.

(13) Jeziorski, B.; Moszynski, R.; Szalewicz, K. Perturbation Theory Approach to Intermolecular Potential Energy Surfaces of van Der Waals Complexes. *Chem. Rev.* **1994**, *94* (7), 1887–1930.

(14) Evangelisti, L.; Sedo, G.; van Wijngaarden, J. Rotational Spectrum of 1,1,1-Trifluoro-2-Butanone Using Chirped-Pulse Fourier Transform Microwave Spectroscopy. *J. Phys. Chem. A* **2011**, *115* (5).

(15) Sedo, G.; van Wijngaarden, J. Fourier Transform Microwave Spectra of a New Isomer of OCS-CO_2. *J. Chem. Phys.* **2009**, *131* (4), 044303.

(16) Pracht, P.; Bohle, F.; Grimme, S. Automated Exploration of the Low-Energy Chemical Space with Fast Quantum Chemical Methods. *Phys. Chem. Chem. Phys.* **2020**, *22* (14), 7169–7192.

(17) Bannwarth, C.; Ehlert, S.; Grimme, S. GFN2-XTB - An Accurate and Broadly Parametrized Self-Consistent Tight-Binding Quantum Chemical Method with Multipole Electrostatics and Density-Dependent Dispersion Contributions. *J. Chem. Theory Comput.* **2019**, *15* (3),

1652–1671.

(18) Grimme, S. Semiempirical Hybrid Density Functional with Perturbative Second-Order Correlation. *J. Chem. Phys.* **2006**, *124* (3), 034108.

(19) Grimme, S.; Ehrlich, S.; Goerigk, L. Effect of the Damping Function in Dispersion Corrected Density Functional Theory. *J. Comput. Chem.* **2011**, *32* (7), 1456–1465.

(20) Grimme, S.; Antony, J.; Ehrlich, S.; Krieg, H. A Consistent and Accurate Ab Initio Parametrization of Density Functional Dispersion Correction (DFT-D) for the 94 Elements H-Pu. *J. Chem. Phys.* **2010**, *132* (15), 154104.

(21) Weigend, F.; Ahlrichs, R. Balanced Basis Sets of Split Valence, Triple Zeta Valence and Quadruple Zeta Valence Quality for H to Rn: Design and Assessment of Accuracy. *Phys. Chem. Chem. Phys.* **2005**, *7* (18), 3297–3305.

(22) Boys, S. F.; Bernardi, F. The Calculation of Small Molecular Interactions by the Differences of Separate Total Energies. Some Procedures with Reduced Errors. *Mol. Phys.* **1970**, *19* (4), 553–566.

(23) Frisch, M. J.; Trucks, G. W.; Schlegel, H. B.; Scuseria, G. E.; Robb, M. A.; Cheeseman, J. R.; Scalmani, G.; Barone, V.; Petersson, G. A.; Nakatsuji, H., et al. *Gaussian 16*, Revision C.01; Gaussian, Inc.: Wallingford, CT, 2016.

(24) Keith, T. A. *AIMALL*, version 17.11.14; TK Gristmill Software: Overland Park, KS, 2016.

(25) Contreras-García, J.; Johnson, E. R.; Keinan, S.; Chaudret, R.; Piquemal, J.-P.; Beratan, D. N.; Yang, W. NCIPLOT: A Program for Plotting Noncovalent Interaction Regions. *J. Chem. Theory Comput.* **2011**, *7* (3), 625–632.

(26) Hohenstein, E. G.; Sherrill, C. D. Density Fitting of Intramonomer Correlation Effects in Symmetry-Adapted Perturbation Theory. *J. Chem. Phys.* **2010**, *133* (1), 014101.

(27) Parrish, R. M.; Burns, L. A.; Smith, D. G. A.; Simmonett, A. C.; DePrince, A. E.; Hohenstein, E. G.; Bozkaya, U.; Sokolov, A. Y.; Di Remigio, R.; Richard, R. M.; et al. Psi4 1.1: An Open-Source Electronic Structure Program Emphasizing Automation, Advanced Libraries, and Interoperability. *J. Chem. Theory Comput.* **2017**, *13* (7), 3185–3197.

(28) Juanes, M.; Lesarri, A.; Pinacho, R.; Charro, E.; Rubio, J. E.; Enríquez, L.; Jaraíz, M. Sulfur Hydrogen Bonding in Isolated Monohydrates: Furfuryl Mercaptan versus Furfuryl Alcohol. *Chem. - A Eur. J.* **2018**, *24* (25), 6564–6571.

(29) Kisiel, Z. PROSPE - Programs for ROtational SPEctroscopy http://www.ifpan.edu.pl/~kisiel/prospe.htm (accessed Jan 15, 2021).

(30) Watson, J. K. G. *In Vibrational Spectra and Structure: A Series of Advances*; Durig, J. R., Ed.; Elsevier: New York, 1977, Vol. 6, pp. 1–89.

(31) Huang, W.; Thomas, J.; Jäger, W.; Xu, Y. Tunnelling and Barrier-Less Motions in the 2-Fluoroethanol–Water Complex: A Rotational Spectroscopic and Ab Initio Study. *Phys. Chem. Chem. Phys.* **2017**, *19* (19), 12221–12228.

(32) Kraitchman, J. Determination of Molecular Structure from Microwave Spectroscopic Data. *Am. J. Phys.* **1953**, *21* (1), 17–24.

(33) van Wijngaarden, J.; Van Nest, S. J.; van Dijk, C. W.; Tokaryk, D. W. Rovibrational Spectrum and Analysis of the N8 Band of Thiophene Using Infrared Synchrotron Radiation. *J. Mol. Spectrosc.* **2010**, *259* (1), 56–59.

(34) Legon, A. C.; Ottaviani, P. The Rotational Spectrum of Thiophene···HBr and a Comparison of the Geometries of the Complexes B···HX, Where B Is Benzene, Furan or Thiophene and X Is F, Cl or Br. *Phys. Chem. Chem. Phys.* **2004**, 488–494.

(35) Espinosa, E.; Molins, E.; Lecomte, C. Hydrogen Bond Strengths Revealed by Topological

Analyses of Experimentally Observed Electron Densities. *Chem. Phys. Lett.* **1998**, *285* (3–4), 170–173.

Chapter 8. Targeting the Rich Conformational Landscape of *N*-Allylmethylamine Using Rotational Spectroscopy and Quantum Mechanical Calculations[5]

In this chapter, the geometries of *N*-allylmethylamine (AMA), which is an allylic amine of astrochemical and atmospheric interest, are discussed. The results of this chapter will constitute the basis for the investigation of the AMA–water complex in Chapter 9. As the previous chapters have focused on interactions in O and S containing compounds such as the S···H–O and O···H–O hydrogen bonds, studying interactions between AMA and water will provide important information on N···H–O for comparison. Although the study of the monomer is essential to understand the spectrum of its monohydrated complex, this chapter provides interesting results regarding the effects ruling the geometries of the monomer species. AMA shows a surprisingly competitive equilibrium whose conformational preferences are governed by a subtle balance between attractive and repulsive interactions. The rotational spectrum was shown to be relatively dense containing lines from four different conformers. Below, the geometries, dynamics and stereoelectronic effects present in AMA are considered in detail.

[5]The content of this chapter is an adapted version of the article published in ChemPhysChem under the citation: Silva, W. G. D. P.; Poonia, T.; van Wijngaarden, J. Targeting the Rich Conformational Landscape of *N*-allylmethylamine Using Rotational Spectroscopy and Quantum Mechanical Calculations, *ChemPhysChem* **2020**, *21*, 2515–2522.

8.1 Abstract

The highly variable conformational landscape of *N*-allylmethylamine (AMA) was investigated using Fourier transform microwave spectroscopy aided by high-level theoretical calculations to understand the energy relationship governing the interconversion between nine stable conformers. Spectroscopically, transitions belonging to four low energy conformers were identified and their hyperfine patterns owing to the ^{14}N quadrupolar nucleus were unambiguously resolved. The rotational spectrum of the global minimum geometry, conformer I, shows an additional splitting associated with a tunneling motion through an energy barrier interconnecting its enantiomeric forms. A two-step tunneling trajectory is proposed by finding transition state structures corresponding to the allyl torsion and NH inversion. Natural bond orbital and non-covalent interaction analyses reveal that an interplay between steric and hyperconjugative effects rules the conformational preferences of AMA.

8.2 Introduction

Amines are ubiquitous in nature. In biological media, for instance, the amino group is a key component in peptides, neurotransmitters and nucleosides, while in the atmosphere and interstellar medium (ISM), amino containing molecules are known participants in the chemistry of aerosols and evolution of stars, respectively.[1,2] In astrochemistry, amines are of great interest as potential precursors for the formation of amino acids and peptides under astrophysical conditions.[3,4] Prebiotic aminoacetonitrile (H_2NCH_2CN)[5] and methylamine (CH_3NH_2)[6,7], for example, are suggested to play a role in the formation of the simplest amino acid glycine.[3,4]

Although amino acids and peptides are well-known in biological environments, none have been unequivocally detected in the ISM making the hunt for a connection which links biology and astronomy an open scientific pursuit of significant importance. The careful study of additional nitrogen containing molecules that may lead to direct astronomical detections, or to laboratory synthesis of potential astrochemical targets, is therefore central to advance our understanding of the chemistry of the ISM.

Previous gas phase pyrolysis reports using allyl containing precursors, such as *N*-allylmethylamine (AMA, $H_2C{=}CH{-}CH_2{-}NH{-}CH_3$) and its oxygen and sulfur counterparts,[8,9] have shown that the thermal decomposition of this class of compounds led to the formation of species of astrochemical and atmospheric interest. In the case of AMA,[8] the main kinetically favored products at temperatures of 602–694K are propylene (CH_2CHCH_3)[10] and methanimine (CH_2NH)[11] which are known prebiotic molecules found in the TMC-1 and Sagittarius B2 molecular clouds, respectively.[2,8] This suggests that AMA is a good candidate to form novel molecular species which can then be characterized by rotational spectroscopy under laboratory conditions. Before understanding the products and processes in which AMA participates, a complete characterization of its conformational landscape, spectroscopic fingerprints and internal motions is compulsory.

Allyl derivatives of the type $H_2C{=}CH{-}CH_2{-}X$ tend to show a diverse conformational behavior which arises from internal rotations around its two single bonds.[12–14] Depending on the nature of the X substituent, a variety of effects, including steric hindrance, London dispersive forces and hydrogen bonding, can rule their conformational preferences. One example is the many theoretical[14] and experimental[15–19] investigations required to partially understand the relative energy ordering of the four observed conformers of allylamine ($H_2C{=}CH{-}CH_2{-}NH_2$). For AMA,

a previous low-resolution rotational spectroscopic study[20] at dry-ice temperature identified one rotamer which was attributed to the global minimum. This geometry was assumed to be at least 3.0 kJ mol^{-1} more stable than any other conformer due to an intramolecular hydrogen bond between the allyl and amino groups. At that time, no quantum mechanical calculations were performed to verify this and, due to experimental limitations, the hyperfine structure owing to the ^{14}N quadrupolar nucleus and internal motions were not resolved.

Herein, we investigate the rich conformational space of AMA using modern Fourier transform microwave (FTMW) spectroscopy aided by density functional theory (DFT) and *ab initio* quantum mechanical calculations. Transitions from four unique conformations were observed in the rotational spectrum and their characteristic hyperfine splittings due to the ^{14}N quadrupolar nucleus were assigned. To understand the effects governing the conformational preferences, natural bond orbital (NBO)[21] and non-covalent interaction (NCI)[22] analyses were invoked. The results define the underlying factors that govern the conformational stability of AMA which will guide spectroscopic investigations in other regions of the electromagnetic spectrum.

8.3 Methods

8.3.1 Experimental Methods

A commercially available sample of *N*-allylmethylamine (96% purity) was purchased from Alfa Aesar Canada and used without further purification. Given that the sample is a liquid at room temperature with a relatively low boiling point (61–62°C), a gas mixture containing 1.0% of the title compound in neon (100 kPa) was prepared at room temperature and expanded into the high

vacuum chamber of the spectrometers using a pulsed nozzle (1 mm diameter orifice) to create a supersonic jet. The rotational spectrum of AMA was collected using a chirped pulse and a cavity-based Balle-Flygare type Fourier transform microwave spectrometer, which were described in detail previously.[23,24] Initially, the broadband CP-FTMW spectrum was recorded from 8–18 GHz in segments of 2 GHz from which the most intense rotational transitions due to different conformers of AMA were identified. Later, to collect transitions at higher frequencies and to resolve the hyperfine structure due to the ^{14}N quadrupolar nucleus, final frequency measurements were performed using the BF-FTMW instrument from 8–22 GHz which provides higher resolution and sensitivity. Rotational transitions recorded using the cavity-based spectrometer normally have line widths of ~7 kHz (FWHM) when the free induction decay is recorded for 400 μs allowing the uncertainty in the line positions to be determined to within ± 2 kHz. Due to the collinear arrangement of the molecular beam and the resonator axis in the BF-FTMW spectrometer, all rotational transitions collected using this instrument show a doublet splitting due to the Doppler effect.

8.3.2 Computational Methods

To identify the conformers of AMA, we initially performed a conformational search at the GFN2-xTB[25] level of theory using the Conformer-Rotamer Ensemble Sampling Tool (CREST) available in the extended tight binding (xTB) program package.[26,27] The conformational search identified 17 possible geometries of AMA. In the meantime, a three-dimensional potential energy surface was obtained by scanning the δ (C1=C2–C3–N) and θ (C2–C3–N–C4) dihedral angles simultaneously in 36 steps of 10º for each at the B3LYP[28]-D3(BJ)[29,30]/cc-pVTZ[31] level. During

the scan calculations, all other geometric parameters were allowed to relax. The resulting PES, shown in Figure 8.1, yielded nine unique energy minima. All of the 17 and nine geometries obtained from the aforementioned approaches were then fully optimized at higher levels of theory using the density-functional theory B3LYP[28]-D3(BJ)[29,30] and double-hybrid B2PLYP[32]-D3(BJ)[29,30] functionals along with the *ab initio* MP2[33] method. All optimizations were performed using Dunning's aug-cc-pVTZ basis sets.[31] Harmonic frequency calculations were also carried out to verify the nature of the stationary points. In the end, these calculations resulted in a total of nine true minima for AMA whose relative energies lie within an energy window of 10 kJ mol^{-1}.

Several relaxed potential energy curves were subsequently computed using both DFT and MP2 methods by varying the geometric coordinates of interest in steps of 10º to model possible interconversion and tunnelling pathways between minima. As needed, transition state structures were optimized and confirmed by the presence of a single imaginary frequency. All scan, optimization and harmonic frequency calculations were computed using the Gaussian 16 program.[34] The effects governing the conformational preferences of the observed conformers were subsequently evaluated using natural bond orbital[21] and non-covalent interaction[22] analyses carried out with the NBO 7.0[35] and NCIPLOT[36] programs, respectively.

8.4 Results

8.4.1 Conformational Searches

The conformational landscape of AMA was computationally explored using a joint approach involving molecular dynamics and high-level quantum mechanical calculations. A

conformational search using the molecular dynamics GFN2-xTB method led to 17 possible geometries while the construction of a potential energy surface (PES) obtained at the B3LYP-D3(BJ)/cc-pVTZ level (Figure 8.1) located nine energy minima. The diversity of conformers found by both methods arise from internal rotations about the δ (C1=C2–C3–N) and θ (C2–C3–N–C4) dihedral angles (Figure 8.1). All possible minima were subjected to optimization and harmonic frequency calculations at the B3LYP-D3(BJ), B2PLYP-D3(BJ) and MP2 levels with the aug-cc-pVTZ basis set.

The results from the three levels of quantum chemical theory converge to yield nine unique energy minima—their geometries are similar to the ones located in the PES—whose natures are confirmed by the absence of imaginary frequencies. This is consistent with the hypothetical geometries from the assumption that the total number of unique conformers is 3^n ($3^2 = 9$) with being n the number of dihedral angles which lead to different conformations. Pictorial representations of the nine optimized geometries of AMA are shown in Figure 8.1 while their Cartesian coordinates are provided in Appendix E. Relative electronic energies with zero-point energy (ZPE) corrections and spectroscopic parameters for the nine stable conformers of AMA obtained at the B2PLYP-D3(BJ) and MP2 methods are given in Table 8.1, whereas the results from B3LYP-D3(BJ) are provided in Table S65 for comparison. The conformers are labeled using Roman numerals from I–IX which represent their order of stability in MP2 being I the most stable conformer. Overall, although the conformational energy ordering and predicted spectroscopic constants from the three different levels of theory are consistent with each other, the rotational constants from B2PLYP-D3(BJ) presented a better match with the experimentally determined values (Table S66).

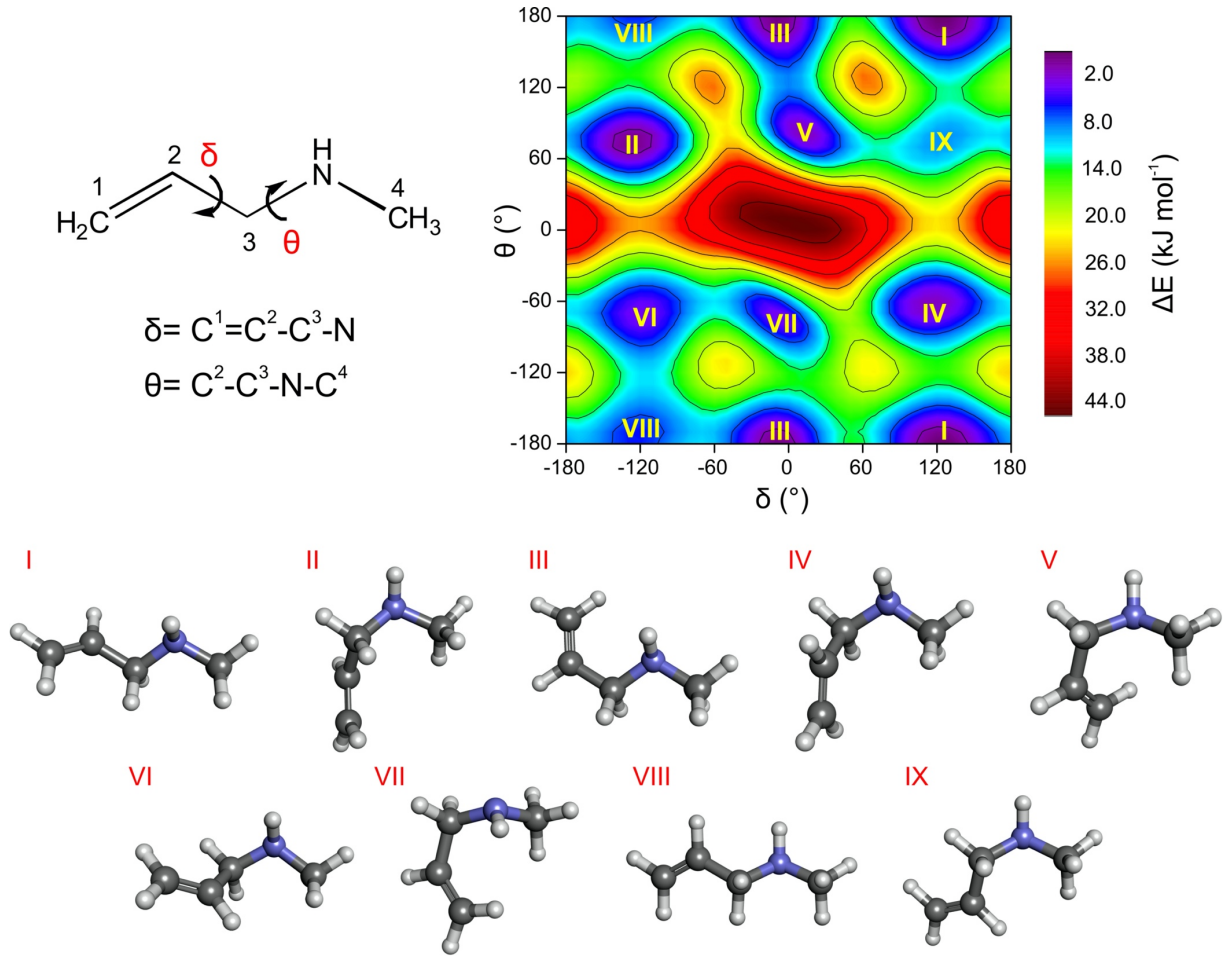

Figure 8.1 Potential energy surface (B3LYP-D3(BJ)/cc-pVTZ) and nine optimized conformers of AMA (B2PLYP-D3(BJ)/aug-cc-pVTZ) which arise through rotations around its δ and θ dihedral angles.

Table 8.1 Calculated energies with zero-point (ZPE) corrections in kJ mol^{-1}, populations at 298K in %, electric dipole moment components in Debye and rotational constants in MHz for the nine conformers of AMA obtained using the B2PLYP-D3(BJ) and MP2 methods with the aug-cc-pVTZ basis set.

Conformer	B2PLYP-D3(BJ)				MP2			
	ΔE_{ZPE}	P	$A/B/C$	$\lvert\mu_a\rvert/\lvert\mu_b\rvert/\lvert\mu_c\rvert$	ΔE_{ZPE}	P	$A/B/C$	$\lvert\mu_a\rvert/\lvert\mu_b\rvert/\lvert\mu_c\rvert$
I	0.0	34.2	20135/2243/2213	0.1/0.6/0.6	0.0	30.3	19637/2263/2237	0.1/0.8/0.6
II	1.1	21.8	10203/3061/2651	0.4/0.1/0.9	0.4	26.0	10008/3137/2695	0.3/0.0/1.0
III	2.0	15.5	14730/2703/2368	0.5/0.5/0.7	1.9	14.3	14636/2730/2386	0.5/0.6/0.8
IV	3.1	9.9	9612/3174/2700	0.5/0.3/0.7	2.5	11.0	9466/3247/2741	0.6/0.4/0.7
V	4.2	6.3	8842/3539/2937	0.8/0.8/0.4	3.3	7.9	8748/3613/2989	0.8/0.8/0.5
VI	5.0	4.5	13446/2637/2452	0.3/0.8/0.2	5.4	3.5	13089/2685/2492	0.4/0.9/0.2
VII	5.8	3.2	8654/3573/2916	0.5/0.4/0.2	5.6	3.2	8562/3648/2965	0.6/0.4/0.2
VIII	5.6	3.6	20847/2230/2177	0.4/0.1/1.0	5.7	3.0	20516/2246/2196	0.4/0.1/1.0
IX	9.2	0.8	13916/2627/2413	0.6/0.4/0.9	9.2	0.7	13388/2689/2463	0.6/0.3/1.0

8.4.2 Spectral Analysis

According to the high-level quantum mechanical calculations in this work (Table 8.1), apart from the global minimum (conformer I), AMA has another four low-energy conformers (II–V) with $\Delta E_{ZPE} < 5.0$ kJ mol^{-1} which possess non-zero electric dipole components and thus, should be observable by FTMW spectroscopy in a supersonic jet. The predicted rotational constants (*A*, *B*, and *C*) for each conformer are sufficiently unique so as to allow their unambiguous identification.

Transitions due to conformer I were readily identified in the broadband chirped pulse (CP) FTMW spectrum. Those were predominantly *b*- and *c*-type Q-branch transitions, lying in the upper limit of our CP-FTMW instrument around 17–18 GHz. Despite the small magnitude of the μ_a dipole (0.1 D), we were able to detect a few *a*-type rotational transitions for conformer I. Although the transitions due to conformer I dominated the spectrum, three additional sets of rotational transitions were observed in the survey spectrum (Figure 8.2A). The observed patterns were consistent with conformers II, III and V based on the supporting quantum chemical predictions. All assigned transitions were confirmed through measurements of their characteristic ^{14}N hyperfine structure using the Balle-Flygare (BF) FTMW instrument. Based on careful measurements using the cavity-based instrument and considering the calculated dipole moment components for each identified conformer, we estimate the experimental abundances of conformers I, II, III and V to be approximately 40%, 36%, 22% and 2%, respectively. This is a rough estimate as transitions with comparable quantum numbers for each conformer lie more than 2 GHz apart.

Interestingly, additional splittings were detected for some transitions with higher J rotational quantum number for conformer I. The splitting pattern (~1:1 ratio) is consistent with a tunneling motion associated with interconversion between two equivalent forms of I (I+ and I-) which would require internal motions of both the allyl and amino groups (Figure 8.3). A sample of the cavity-based spectrum, showing the F'–F = 3–2 ^{14}N hyperfine component and the tunneling splitting for the 2_{11}–2_{02} transition of conformer I, is provided in Figure 8.2B. For conformer III, although the $|\mu_c|$ component is calculated to be greater than the $|\mu_a|$ and $|\mu_b|$ components (Table 8.1), no *c*-type transitions were observed. This is likely caused by an inversion motion of the NH group that is symmetric along the *c*-axis perpendicular to the heavy atom backbone of AMA in Figure 8.1 which averages μ_c to zero if the ground state of III is above the barrier to this motion. A similar case has been reported in previous rotational spectroscopic studies of other amino containing compounds, such as 3-aminophenol.[37] Despite a careful search, transitions due to other conformers of AMA were not detected.

All measured rotational transitions were fitted with Pickett's SPFIT program[38] using Watson's A-reduced Hamiltonian in the I^r representation to yield experimental rotational, quartic centrifugal distortion and ^{14}N quadrupole coupling constants. The determined spectroscopic parameters for each conformer are provided in Table 8.2, while the complete line lists including individual hyperfine components and residuals are given as supplementary data (Tables S68–S71). The two tunneling states were fitted independently and are labeled in Table 8.2 as I+ and I-.

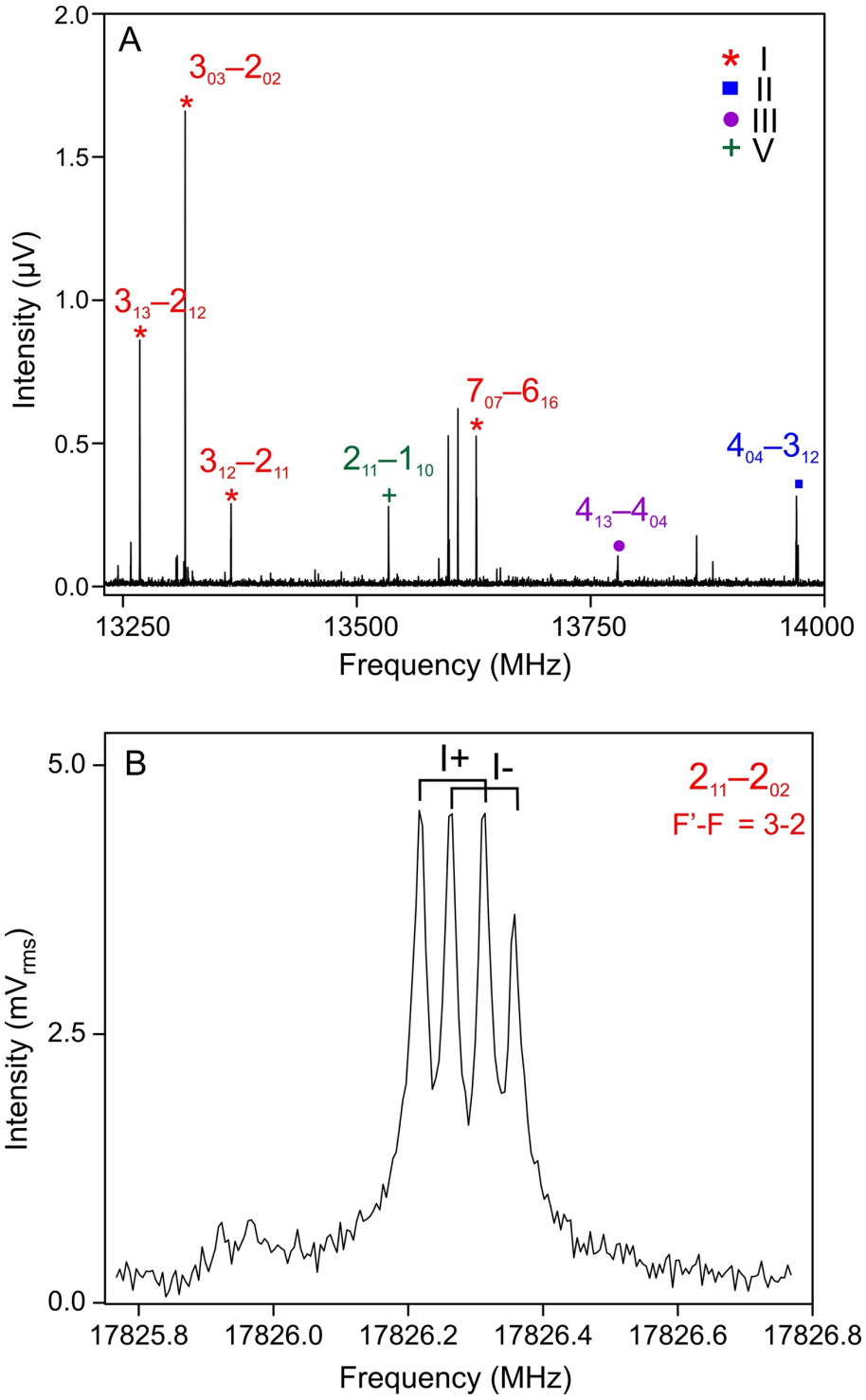

Figure 8.2 A) Sample of the broadband CP-FTMW spectrum (1.5 million FIDs) showing rotational transitions belonging to the parent species of conformers I, II, III and V. B) BF-FTMW spectrum (200 cycles) of the 2_{11}–2_{02} transition (F'–F = 3–2 hyperfine component) of conformer I highlighting the tunneling splitting.

Table 8.2 Experimental spectroscopic parameters for the four observed conformers of AMA

Parameter	I+	I-	II	III	V
A/MHz[a]	19998.1762(21)	19998.2173(20)	10173.23585(46)	14539.2746(48)	8773.1220(25)
B/MHz	2235.73639(58)	2235.73865(58)	3050.66194(22)	2699.7120(10)	3533.8400(17)
C/MHz	2203.14081(59)	2203.14302(58)	2641.63405(16)	2362.97445(96)	2932.5425(15)
Δ_J/kHz[b]	[0.63140769]	[0.63140769]	3.2139(80)	0.593(30)	3.337(50)
Δ_{JK}/kHz	-23.31(14)	-23.68(15)	-25.240(71)	-2.90(42)	-11.49(40)
Δ_K/kHz	[433.87203]	[433.87203]	[87.552397]	[36.947153]	[23.483135]
δ_J/kHz	[-0.090601327]	[-0.090601327]	0.9530(53)	[0.100861]	0.942(75)
δ_K/kHz	[40.889685]	[40.889685]	[5.0103483]	[1.20664]	[4.0555968]
1.5 (χ_{aa})/MHz[c]	4.3037(52)	4.3045(55)	3.7874(14)	3.707(11)	1.4243(82)
0.25 (χ_{bb}- χ_{cc})/MHz	-0.4038(24)	-0.3995(25)	1.87302(44)	0.7150(60)	0.2337(27)
$\mu_a/\mu_b/\mu_c$[d]	y/y/y	y/y/y	y/y/y	y/y/n	y/y/n
N[e]	111		60	27	21
σ/kHz[f]	6.4		1.4	5.8	3.2

[a]Rotational constants; [b]quartic centrifugal distortion constants; [c]^{14}N nuclear quadrupole coupling constants; [d]electric dipole moment components ("y" if observed and "n" if not observed); [e]total number of lines (N) in the fit; [f]root-mean-square deviation of the fit (σ). Values in brackets were fixed to the calculated values at B2PLYP-D3(BJ)/aug-cc-pVTZ. The full set of calculated constants are provided in Table S66. In table S67, the % deviation between the experimental and calculated rotational and ^{14}N quadrupole coupling constants for the three different levels of theory are provided.

8.5 Discussion

The conformational analysis of AMA by high-level quantum mechanical calculations and modern FTMW spectroscopy reveals a rich and competitive conformational behaviour for this seemingly simple molecule. From nine stable conformers (ΔE_{ZPE} < 10 kJ mol^{-1}, Table 8.1) predicted at 298K, four (I, II, III and V, Figure 8.1) were observed in the supersonic jet expansion. The previous assertion that conformer I is at least 3.0 kJ mol^{-1} more stable than any other rotamer of AMA[20] is inaccurate as supported by the observation of transitions from the four conformers whose intensities are consistent with the calculated dipole moments and relative energies from both DFT and *ab initio* calculations—I (0.0 kJ mol^{-1}), II (~1.0 kJ mol^{-1}), III (2.0 kJ mol^{-1}) and V

(~3.0–4.0 kJ mol^{-1}) in this work. As mentioned above, no transitions for conformers IV, VI, VII, VIII and IX were identified in the rotational spectrum. There are two common explanations invoked[39] to justify the absence of stable conformers in a molecular beam experiment: (1) the higher energy conformers are not abundant in the sample from the start and/or (2) they experience facile relaxation to lower energy forms through collisions with the carrier gas during the expansion.

At room temperature, conformers with relative energies higher than 5.0 kJ mol^{-1} (VI, VII, VIII and IX) are expected to be less than 6.0% populated based on the Boltzmann formula and, coupled with the dipole moment components in Table 8.1, are unlikely to be observed in the supersonic jet even if they are metastable. Nevertheless, to better characterize the conformational space of AMA, we considered relaxation pathways connecting the various conformers at both B2PLYP-D3(BJ)/aug-cc-pVTZ and MP2/aug-cc-pVTZ levels as shown in Figure 8.4. These are in essence cross sections of the full three-dimensional PES displayed in Figure 8.1. Considering the estimated energy barrier heights (Figure 8.4), relaxation from VIII→I (~4.0–5.0 kJ mol^{-1}) and IX→II (~3.0 kJ mol^{-1}) is possible, while all the other conformers should be metastable as they correspond to deeper pockets on the PES. The non-observation of transitions of conformer IV is somewhat surprising based on its low relative energy (~2.5–3.1 kJ mol^{-1}) and electric dipole moment components (Table 8.1). Even though the calculations indicate that IV is metastable, there is still a possibility of conformational cooling from IV to II given their geometric similarities (Figure 8.1). The conformational relaxations of the above-mentioned higher energy conformers into I and II are supported by their enriched conformational abundances of 40% and 36%, respectively, observed in the supersonic jet.

Interconversion pathways also provide useful insight into the tunnelling splitting observed for conformer I. The intensity ratio (Figure 8.2B) of the two components is consistent with

tunnelling between two equivalent forms of I (I+ and I-, Figure 8.3) which requires motion of both the allyl and amino groups in the same direction. A possible tunneling trajectory, modeled in a sequential two-step fashion, is proposed in Figure 8.3. By starting with the amino inversion followed by the allyl torsion, or vice-versa, the lowest energy tunneling path requires passing through two transition states (TS). These are connected by an intermediate energy minimum structure (conformer VIII) in which the allyl group and the amino hydrogen point out of the molecular plane in opposite directions to each other. In the TS for the allyl torsion, the terminal double bond and the amino hydrogen are arranged in a way that minimizes steric repulsions, while in the TS for the amino inversion, these groups are spatially closer. This results in a lower barrier height for the allyl torsion compared to the NH inversion (Figure 8.3). Previous studies of related compounds, for example, have shown that a pathway involving changes in two geometric coordinates of a molecule can occur not only via two steps but also in a concerted way as proposed for the amine azetidine.[40,41] For conformer I, a concerted route would involve a planar TS geometry with C_s symmetry which is an unlikely pathway given the high estimated barrier of ~70.0 kJ mol^{-1} from B2PLYP-D3/aug-cc-pVTZ.

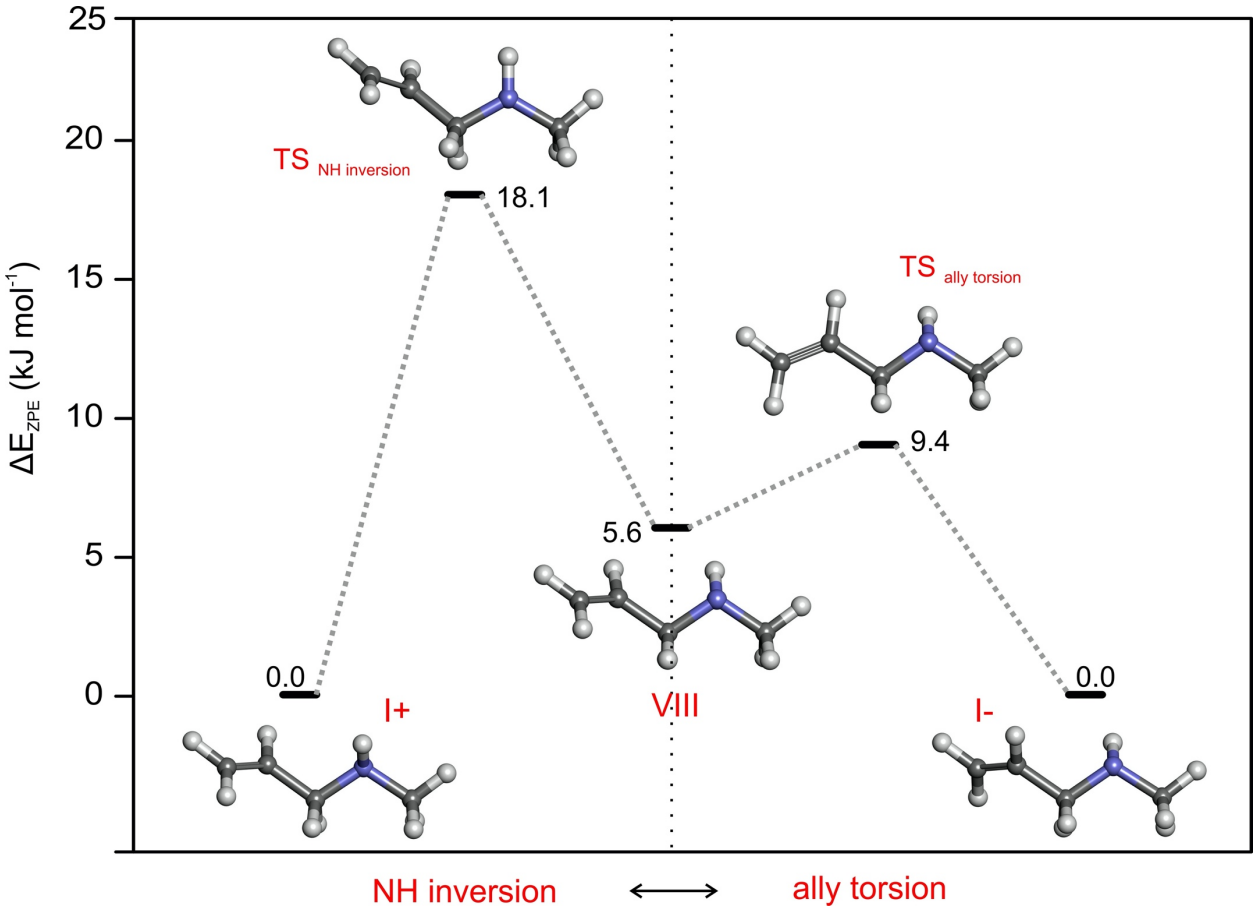

Figure 8.3 Possible two-step tunneling pathway for the interconversion between the equivalent forms of I obtained at the B2PLYP-D3(BJ)/aug-cc-pVTZ level of theory.

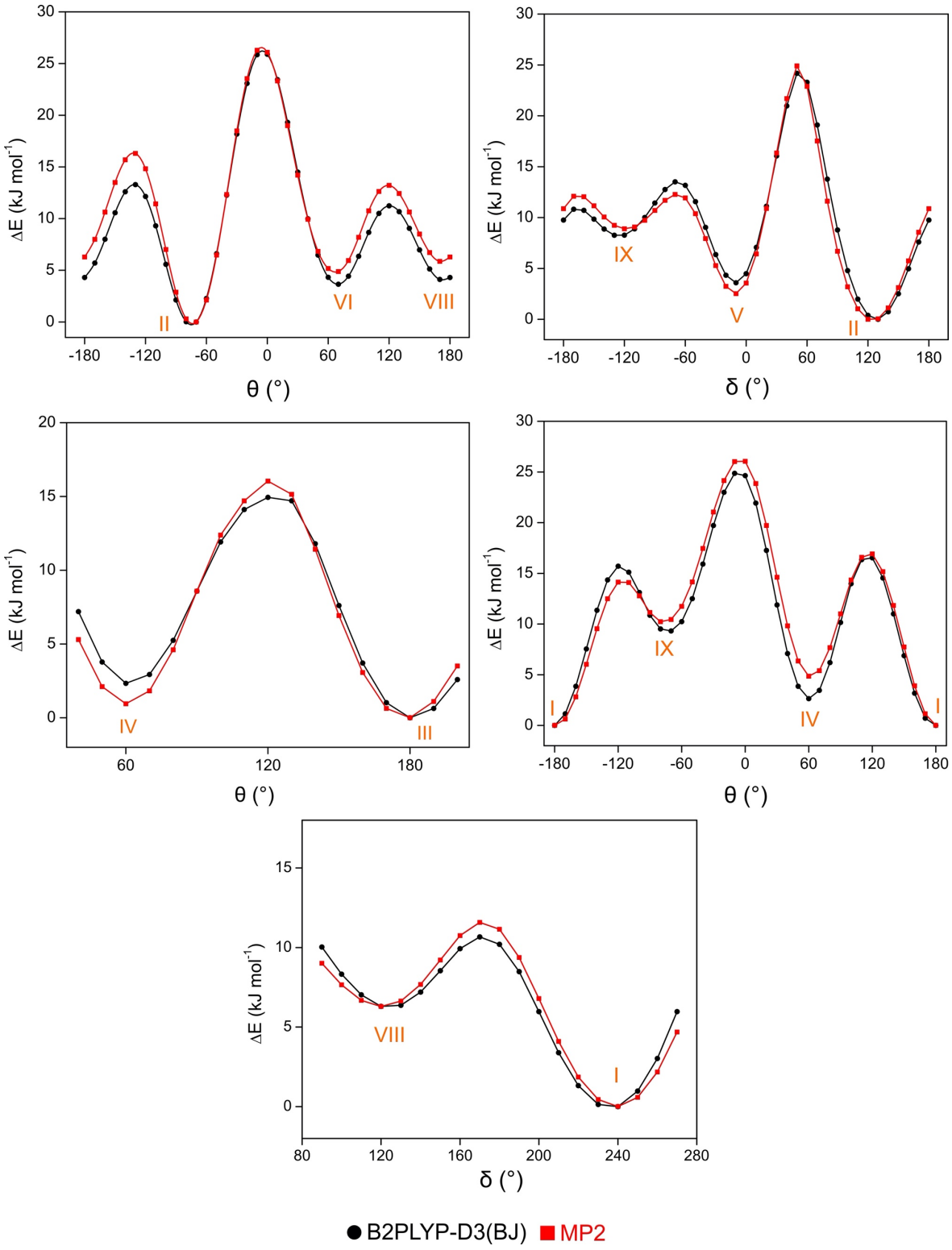

Figure 8.4 Possible relaxation pathways interconnecting specific conformers of AMA obtained theoretically using the MP2 and B2PLYP-D3(BJ) methods with the aug-cc-pVTZ basis set.

To identify possible non-covalent interactions that influence the conformer energy ordering of AMA, we used natural bond orbital and non-covalent interaction analyses. The results suggest a complex interplay of competing effects that stabilize and destabilize the individual conformers. The NCI analysis (Figure 8.5), for example, does not show any attractive or repulsive contacts in conformers I, V and VIII, but reveals weak CH···π attractive interactions in II, IV, VI and IX, CH···N in III and NH···π in VII. These contacts are seen by the blue-green regions on the isosurfaces between the atoms involved in the interaction. It is worth noting that each of these contacts is accompanied by destabilizing repulsive effects (reddish part in the isosurfaces) of similar magnitude. Most importantly, the global minimum geometry is not stabilized by CH···π interactions suggesting that intramolecular hydrogen bonding is not the dominant factor governing the conformational behaviour of AMA as previously thought.[20]

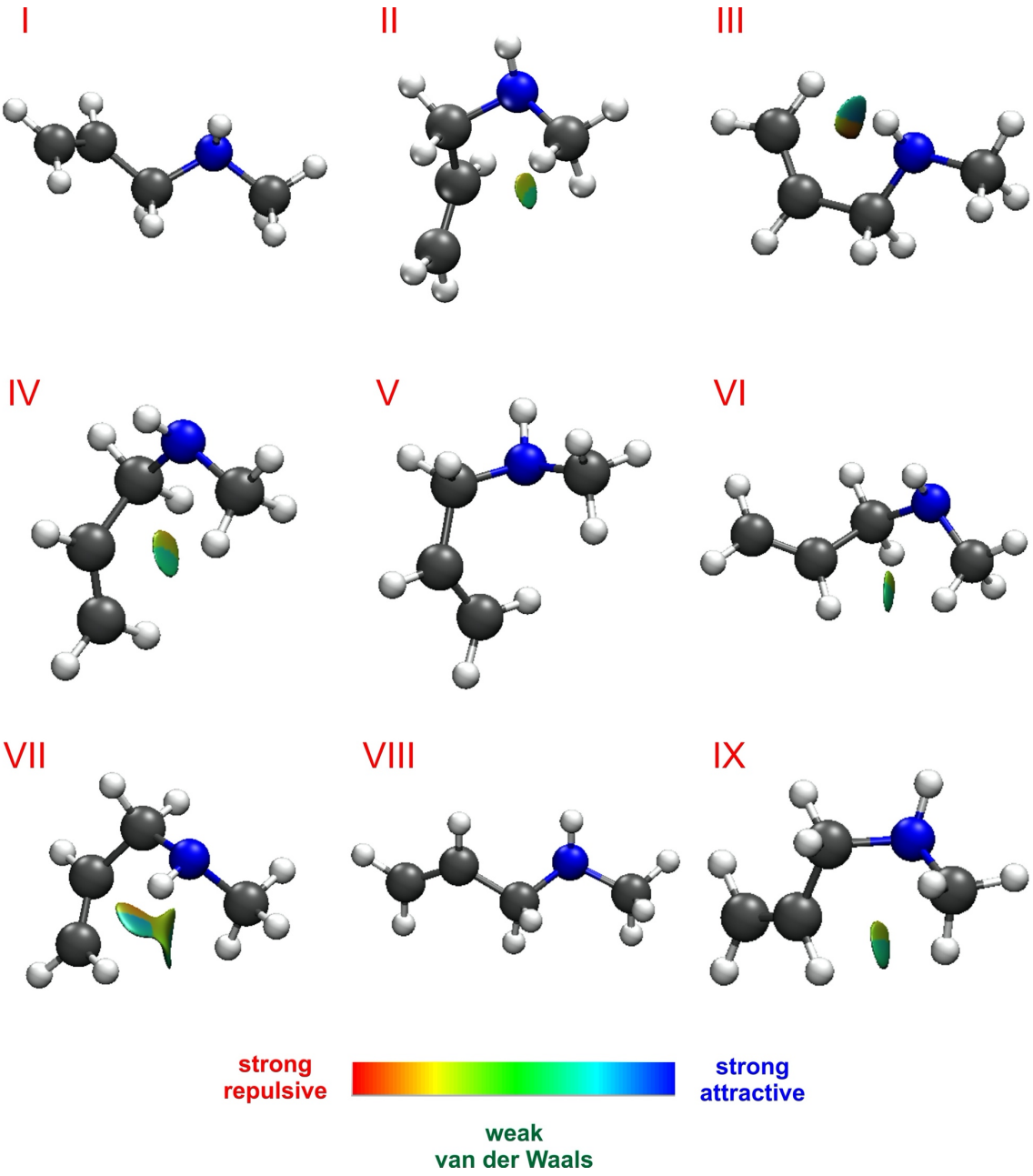

Figure 8.5 NCI isosurfaces (s= 0.05, colour scale of -0.02 < ρ < 0.02 au for the SCF densities) for the nine stable conformers of AMA.

NBO calculations (Table 8.3) also confirm the absence of a NH···π hydrogen bond in I, but do reveal that the arrangement of the allyl group and the amino hydrogen favors electron transfer

from the lone-pair on nitrogen n_N into the antibonding π* and σ* orbitals of the C=C and C–C bonds, respectively. In fact, charge-transfer interactions involving the lone-pair at nitrogen and the vicinal methylene and methyl groups are observed for all nine conformers (Table 8.3). The magnitudes of the interactions vary depending on the geometric relationship between the lone-pair and the CH_2 and CH_3 moieties. The central role of hyperconjugation in stabilizing conformer I is apparent when comparing its interaction perturbation energies with those of conformer VIII which has a similar geometry but lacks both $n_N \rightarrow \pi^*_{C=C}$ and $n_N \rightarrow \sigma^*_{C-C}$ interactions due to the opposite disposition of the allyl and amino groups. The energy difference of ~5.0–6.0 kJ mol^{-1} between I and VIII is analogous to the sum of the second-order perturbation energies for the $n_N \rightarrow \pi^*_{C=C}$ and $n_N \rightarrow \sigma^*_{C-C}$ hyperconjugative interactions (~5.5 kJ mol^{-1}) observed in I. Although in other conformers the hyperconjugative interactions present similar or even larger values (Table 8.3), their geometries are also more destabilized by repulsive contacts as visualized from the NCI isosurfaces which makes them slightly less stable than I. The multifaceted conformational preferences of AMA can therefore be rationalized in terms of a delicate balance of destabilization due to steric effects and stabilization from hyperconjugative interactions.

Table 8.3 Charge-transfer interactions involving the lone-pair (n_N) at nitrogen exhibited by the nine conformers of AMA obtained at the B3LYP-D3(BJ)/aug-cc-pVTZ level. The second-order perturbation energies are given in kJ mol^{-1}.

Interaction	**I**	**II**	**III**	**IV**	**V**	**VI**	**VII**	**VIII**	**IX**
$n_N \rightarrow \pi^*_{C1-C2}$	2.4	2.7	0.0	5.8	0.0	6.1	0.0	0.0	0.0
$n_N \rightarrow \sigma^*_{C2-C3}$	3.2	8.5	3.5	32.4	12.6	31.8	38.0	0.0	8.2
$n_N \rightarrow \sigma^*_{C3-H}$	8.6	32.6	8.2	6.7	30.6	9.7	11.5	11.0	30.1
$n_N \rightarrow \sigma^*_{C3-H'}$	32.7	2.3	33.6	7.5	0.0	4.5	4.5	30.7	0.0
$n_N \rightarrow \sigma^*_{C4-H}$	32.2	4.2	32.6	4.5	4.4	5.1	3.9	4.2	3.3
$n_N \rightarrow \sigma^*_{C4-H'}$	4.3	9.5	4.2	9.1	9.6	8.5	10.5	10.0	11.1
$n_N \rightarrow \sigma^*_{C4-H''}$	9.7	31.8	9.9	33.6	31.5	34.7	35.1	32.0	31.8

8.6 Conclusions

A detailed conformational study of AMA was completed using Fourier transform microwave spectroscopy and high-level quantum mechanical calculations. Rotational transitions for four stable conformers (I, II, III and V) were observed whose patterns agree with predictions from both DFT and *ab initio* calculations and show the characteristic hyperfine structure due to the ^{14}N quadrupolar nucleus. A two-step pathway is presented as the most energetically favourable route for the interconversion between the two equivalent forms of I (I+ and I-) to justify the observed tunneling splitting. The stable geometries of AMA are not governed by an isolated effect, but are rather the consequence of a tight competition between destabilizing steric effects and stabilizing hyperconjugative interactions as supported by the NCI and NBO calculations. This is the driving force behind the rich conformational landscape of AMA. The experimental and theoretical results presented here lay a critical foundation for further investigations of AMA and its decomposition products of atmospheric and astrochemical interest.

8.7 References

(1) Ge, X.; Wexler, A. S.; Clegg, S. L. Atmospheric Amines – Part I. A Review. *Atmos. Environ.* **2011**, *45* (3), 524–546.

(2) McGuire, B. A. 2018 Census of Interstellar, Circumstellar, Extragalactic, Protoplanetary Disk, and Exoplanetary Molecules. *Astrophys. J. Suppl. Ser.* **2018**, *239* (2), 17.

(3) Miller, S. L. A Production of Amino Acids Under Possible Primitive Earth Conditions. *Science* **1953**, *117* (3046), 528–529.

(4) Holtom, P. D.; Bennett, C. J.; Osamura, Y.; Mason, N. J.; Kaiser, R. I. A Combined Experimental and Theoretical Study on the Formation of the Amino Acid Glycine (NH_2CH_2COOH) and Its Isomer ($CH_3NHCOOH$) in Extraterrestrial Ices. *Astrophys. J.* **2005**, *626* (2), 940–952.

(5) Belloche, A.; Menten, K. M.; Comito, C.; Müller, H. S. P.; Schilke, P.; Ott, J.; Thorwirth, S.; Hieret, C. Detection of Amino Acetonitrile in Sgr B2(N). *Astron. Astrophys.* **2008**, *482* (1), 179–196.

(6) Kaifu, N.; Morimoto, M.; Nagane, K.; Akabane, K.; Iguchi, T.; Takagi, K. Detection of Interstellar Methylamine. *Astrophys. J.* **1974**, *191*, L135.

(7) Fourikis, N.; Takagi, K.; Morimoto, M. Detection of Interstellar Methylamine by Its $2_{02} \rightarrow 1_{10}$ A_a-State Transition. *Astrophys. J.* **1974**, *191*, L139.

(8) Vitins, P.; Egger, K. W. The Thermochemical Kinetics of the Retro-'Ene' Reactions of Molecules with the General Structure (Allyl)XYH in the Gas Phase. Part IX. Unimolecular Thermal Decompostion of Allylmethylamine. *J. Chem. Soc., Perkin Trans. 2* **1974**, No. 11, 1289–1291.

(9) Oliaey, A. R.; Shiroudi, A.; Zahedi, E.; Deleuze, M. S. Theoretical Study on the Elimination Kinetics in the Gas Phase of Allyl Methyl Compounds. *Monatshefte für Chemie - Chem. Mon.* **2018**, *149* (8), 1389–1400.

(10) Marcelino, N.; Cernicharo, J.; Agúndez, M.; Roueff, E.; Gerin, M.; Martín-Pintado, J.; Mauersberger, R.; Thum, C. Discovery of Interstellar Propylene (CH_2CHCH_3): Missing Links in Interstellar Gas-Phase Chemistry. *Astrophys. J.* **2007**, *665* (2), L127–L130.

(11) Godfrey, P. D.; Brown, R. D.; Robinson, B. J.; Sinclair, M. W. Discovery of Interstellar Methanimine (Formaldimine). *Astrophys. Lett.* **1973**, *13*, 119.

(12) Sun, W.; Sogeke, O. P.; Silva, W. G. D. P.; van Wijngaarden, J. Dispersion-Driven Conformational Preference in the Gas Phase: Microwave Spectroscopic and Theoretical Study of Allyl Isocyanate. *J. Chem. Phys.* **2019**, *151* (19), 194304.

(13) Stitsky, J.; Silva, W. G. D. P.; Sun, W.; van Wijngaarden, J. Conformers of Allyl Isothiocyanate: A Combined Microwave Spectroscopy and Computational Study. *J. Phys. Chem. A* **2020**, *124* (19), 3876–3885.

(14) Galabov, B.; Kim, S.; Xie, Y.; Schaefer, H. F.; Leininger, M. L.; Durig, J. R. Conformations of Allyl Amine: Theory vs Experiment. *J. Phys. Chem. A* **2008**, *112* (10), 2120–2124.

(15) Herrebout, W. A.; Zheng, C.; van der Veken, B. J.; Durig, J. R. Conformational Stability of Allyl Amine from Temperature Dependent Infrared Spectra of Rare Gas Solutions, Ab Initio Calculations, r_0 Structural Parameters, and Vibrational Assignment. *J. Mol. Struct.* **2003**, *645* (2–3), 109–132.

(16) Botskor, I.; Rudolph, H. D.; Roussy, G. The Microwave Spectrum of One N-Gauche Rotamer of Allylamine. *J. Mol. Spectrosc.* **1974**, *53* (1), 15–36.

(17) Botskor, I.; Rudolph, H. D.; Roussy, G. The Microwave Spectrum of a Second N-Gauche

Rotamer of Allylamine. *J. Mol. Spectrosc.* **1974**, *52* (3), 457–484.

(18) Roussy, G.; Demaison, J.; Botskor, I.; Rudolph, H. D. Microwave Spectrum of One Rotamer of Allylamine. *J. Mol. Spectrosc.* **1971**, *38* (3), 535–544.

(19) Botskor, I.; Rudolph, H. D. The Microwave Spectrum of the Fourth Distinct Rotameric Form of Allylamine. *J. Mol. Spectrosc.* **1978**, *71* (1–3), 430–445.

(20) Marstokk, K.-M.; Møllendal, H. Microwave Spectrum, Conformation and Internal Hydrogen Bonding in N-Methylallylamine. *Acta Chem. Scand.* **1986**, *40a*, 615–621.

(21) Weinhold, F.; Landis, C. R.; Glendening, E. D. What Is NBO Analysis and How Is It Useful? *Int. Rev. Phys. Chem.* **2016**, *35* (3), 399–440.

(22) Johnson, E. R.; Keinan, S.; Mori-Sánchez, P.; Contreras-García, J.; Cohen, A. J.; Yang, W. Revealing Noncovalent Interactions. *J. Am. Chem. Soc.* **2010**, *132* (18), 6498–6506.

(23) Evangelisti, L.; Sedo, G.; van Wijngaarden, J. Rotational Spectrum of 1,1,1-Trifluoro-2-Butanone Using Chirped-Pulse Fourier Transform Microwave Spectroscopy. *J. Phys. Chem. A* **2011**, *115* (5), 685–690.

(24) Sedo, G.; van Wijngaarden, J. Fourier Transform Microwave Spectra of a “New” Isomer of OCS-CO_2. *J. Chem. Phys.* **2009**, *131* (4), 044303.

(25) Bannwarth, C.; Ehlert, S.; Grimme, S. GFN2-XTB - An Accurate and Broadly Parametrized Self-Consistent Tight-Binding Quantum Chemical Method with Multipole Electrostatics and Density-Dependent Dispersion Contributions. *J. Chem. Theory Comput.* **2019**, *15* (3), 1652–1671.

(26) Grimme, S. Exploration of Chemical Compound, Conformer, and Reaction Space with Meta-Dynamics Simulations Based on Tight-Binding Quantum Chemical Calculations. *J. Chem. Theory Comput.* **2019**, *15* (5), 2847–2862.

(27) Pracht, P.; Bohle, F.; Grimme, S. Automated Exploration of the Low-Energy Chemical Space with Fast Quantum Chemical Methods. *Phys. Chem. Chem. Phys.* **2020**, *22* (14), 7169–7192.

(28) Becke, A. D. Density-functional Thermochemistry. III. The Role of Exact Exchange. *J. Chem. Phys.* **1993**, *98* (7), 5648–5652.

(29) Grimme, S.; Ehrlich, S.; Goerigk, L. Effect of the Damping Function in Dispersion Corrected Density Functional Theory. *J. Comput. Chem.* **2011**, *32* (7), 1456–1465.

(30) Grimme, S.; Antony, J.; Ehrlich, S.; Krieg, H. A Consistent and Accurate Ab Initio Parametrization of Density Functional Dispersion Correction (DFT-D) for the 94 Elements H-Pu. *J. Chem. Phys.* **2010**, *132* (15), 154104.

(31) Dunning, T. H. Gaussian Basis Sets for Use in Correlated Molecular Calculations. I. The Atoms Boron through Neon and Hydrogen. *J. Chem. Phys.* **1989**, *90* (2), 1007–1023.

(32) Grimme, S. Semiempirical Hybrid Density Functional with Perturbative Second-Order Correlation. *J. Chem. Phys.* **2006**, *124* (3), 034108.

(33) Møller, C.; Plesset, M. S. Note on an Approximation Treatment for Many-Electron Systems. *Phys. Rev.* **1934**, *46* (7), 618–622.

(34) Frisch, M. J.; Trucks, G. W.; Schlegel, H. B.; Scuseria, G. E.; Robb, M. A.; Cheeseman, J. R.; Scalmani, G.; Barone, V.; Petersson, G. A.; Nakatsuji, H., et al. *Gaussian 16*, Revision C.01; Gaussian, Inc.: Wallingford, CT, 2016.

(35) Glendening, E. D.; Badenhoop, J. K.; Reed, A. E.; Carpenter, J. E.; Bohmann, J. A.; Morales, C. M.; Karafiloglou, P.; Landis C. R.; Weinhold, F. *NBO 7.0*, Theoretical Chemistry Institute, University of Wisconsin: Madison, 2018.

(36) Contreras-García, J.; Johnson, E. R.; Keinan, S.; Chaudret, R.; Piquemal, J.-P.; Beratan, D.

N.; Yang, W. NCIPLOT: A Program for Plotting Noncovalent Interaction Regions. *J. Chem. Theory Comput.* **2011**, *7* (3), 625–632.

(37) Filsinger, F.; Wohlfart, K.; Schnell, M.; Grabow, J.-U. Precise Dipole Moments and Quadrupole Coupling Constants of the Cis and Trans Conformers of 3-Aminophenol : Determination of the Absolute Conformation W. *Phys. Chem. Chem. Phys.* **2008**, *10*, 666–673.

(38) Kisiel, Z. PROSPE - Programs for ROtational SPEctroscopy http://www.ifpan.edu.pl/~kisiel/prospe.htm (accessed Nov 8, 2019).

(39) Loru, D.; Quesada-Moreno, M. M.; Avilés-Moreno, J. R.; Jarman, N.; Huet, T. R.; López-González, J. J.; Sanz, M. E. Conformational Flexibility of Limonene Oxide Studied By Microwave Spectroscopy. *ChemPhysChem* **2017**, *18* (3), 274–280.

(40) López, J. C.; Blanco, S.; Lesarri, A.; Alonso, J. L. Internal Dynamics in Azetidine: A Microwave and Ab Initio Study. *J. Chem. Phys.* **2001**, *114* (5), 2237–2250.

(41) Domingos, S. R.; Pérez, C.; Medcraft, C.; Pinacho, P.; Schnell, M. Flexibility Unleashed in Acyclic Monoterpenes: Conformational Space of Citronellal Revealed by Broadband Rotational Spectroscopy. *Phys. Chem. Chem. Phys.* **2016**, *18* (25), 16682–16689.

Chapter 9. Exploring the Non-Covalent Interactions Behind the Formation of Amine–Water Complexes: The Case of the *N*-Allylmethylamine Monohydrate[6]

Following the conformational study of AMA in Chapter 8, the geometries of the AMA–water complex are reported in this chapter in an effort to model the microsolvation of this prototypical secondary amine. Apart from observing transitions belonging to the four reported conformers of AMA, lines due to two geometries of AMA–w were detected in the rotational spectrum. The assigned conformers were shown to be stabilized by two intermolecular interactions consisting of a dominant N···H–O and a secondary C–H···O hydrogen bond in which water acts as both hydrogen bond donor and acceptor. Although water does not change the geometry of the AMA conformers significantly, it affects their relative energy orderings with the effects being more pronounced for higher energy conformations. By investigating a series of monohydrated primary, secondary and tertiary amines using quantum chemical methods, the nature behind the formation of these complexes were investigated in detail. AMA–water is shown to be the most strongly bound complex within the studied series.

[6]The content of this chapter is an adapted version of the article published in Physical Chemistry Chemical Physics under the citation: Silva, W. G. D. P.; Poonia, T.; van Wijngaarden, J. Exploring the Non-Covalent Interactions Behind the Formation of Amine–Water Complexes: The Case of the *N*-allylmethylamine Monohydrate, *Phys. Chem. Chem. Phys.* **2021**, *23*, 7368–7375.

9.1 Abstract

The conformational landscape of the monohydrated complex of *N*-allylmethylamine (AMA–w) was investigated for the first time using rotational spectroscopy from 8–20 GHz and quantum chemistry calculations. From a total of nine possible energy minima within 10 kJ mol^{-1}, transitions for the two most stable conformers of AMA–w were detected and assigned aided by DFT and *ab* initio MP2 predictions. The observed rotational transitions displayed characteristic hyperfine splittings due to the presence of the ^{14}N quadrupolar nucleus. Quantum theory of atoms in molecules (QTAIM), non-covalent interaction (NCI) and natural bond orbital (NBO) analyses showed that the observed conformers of AMA–w are stabilized by two intermolecular interactions consisting of a dominant N···H–O and a secondary C–H···O hydrogen bond (HB) in which the water molecule acts simultaneously as a HB donor and acceptor. The HBs formed with water do not change the relative energy ordering of the most stable conformers of AMA but do affect the stability of higher energy conformations by disrupting the intramolecular forces responsible for their geometries. By comparing the intermolecular interaction energies with those of the monohydrates of the simplest primary (methylamine, MA), secondary (dimethylamine, DMA) and tertiary (trimethylamine, TMA) amines using symmetry-adapted perturbation theory (SAPT) calculations, we find that AMA forms the strongest bound complex with water. This is rationalized through the identification of subtle differences in stabilizing and destabilizing contributions across the amine–w series of complexes.

9.2 Introduction

A comprehensive understanding of the non-covalent interactions governing the stability of hydrates is of great interest because of the ubiquitous nature of water. Molecular aggregates formed between water and amines, for example, play a crucial role in biology—being essential to the existence of life—and in the chemistry of the atmosphere where amines are involved in key processes such as aerosol nucleation.[1] The undeniable importance of these clusters has motivated both theoretical and spectroscopic studies[2–8] of the hydrogen bonding networks between the amino group and water which have largely focused on water microsolvation of small N-containing molecules such as ammonia (ammonia–w),[2,3] methylamine (MA–w),[5] dimethylamine (DMA–w)[4–6] and trimethylamine (TMA–w).[7,8] These reports have shown that the interaction between the water molecule and the amino group occurs via an intermolecular N···H–O hydrogen bond (HB) in which the water typically acts as the HB donor while the N serves as a HB acceptor. The strength of the binding interactions increases with the number of methyl substituents around the N atom following a general stability trend of TMA–w > DMA–w > MA–w > ammonia–w.

Chen *et al*[9] evaluated the impact of two larger alkyl substituents on the HB parameters of primary amine–w complexes by studying *n*-propylamine–water (PA–w) and isopropylamine–water (IPA–w) using computational chemistry and rotational spectroscopy. It was found that the larger side chains of PA and IPA in comparison to that of MA and ethylamine do not have a significant impact on the interaction energies of the monohydrates.[9] These findings provide useful information to understand binding involving larger alkyl primary amines such as those present in biological environments. Investigation of the monohydrates of secondary and tertiary amines is essential to the development of a systematic understanding of the influence of diverse side chains

on the formation of amine–w clusters. This enhanced knowledge promises to shed light on the fundamental processes driving the chemistry of amines in aqueous environments.

N-allylmethylamine (CH_2=CH–CH_2–NH–CH_3, AMA) is an amine of astrochemical and atmospheric relevance.[10,11] A recent microwave spectroscopic study[10] reported transitions belonging to four conformers in the rotational spectrum of AMA whose stabilities have been rationalized by a complex interplay between steric and attractive interactions. The examination of the AMA–w complex is a crucial first step to understanding the changes in its conformational behaviour in the presence of water and to elucidate the effect of the allyl group on the intermolecular interaction. In comparison to the simplest secondary amine DMA, the presence of the vinyl substituent in AMA may alter the electron density around N through intramolecular interaction and offers an additional potential binding site for the water molecule which would directly impact the interaction energy of the AMA–w complex.

In this study, we investigated the conformational behaviour of AMA–w for the first time using a combination of rotational spectroscopy and high-level quantum chemical calculations. Transitions arising from two unique conformers of the complex were observed in the rotational spectrum and their assignments were confirmed by the presence of a hyperfine splitting related to the quadrupolar ^{14}N nucleus. To understand the nature of the intra- and intermolecular interactions that govern the observed conformers, we used quantum theory of atoms in molecules (QTAIM),[12] non-covalent interaction (NCI)[13] and natural bond orbital (NBO)[14] analyses. The interaction energies were decomposed into four components (electrostatic, dispersion, induction and exchange or Pauli repulsion) using symmetry-adapted perturbation theory (SAPT)[15] calculations and the results compared with those derived in this work for the water dimer, ammonia–w, MA–w, DMA–w and TMA–w.

9.3 Methods

9.3.1 Experimental Methods

AMA (96%, bp: 334–335 K) is commercially available from Alfa Aesar and was used without further purification. To produce the monohydrated complex, a gas mixture containing ~1% of AMA in neon (100 kPa) was prepared at room temperature and subsequently bubbled through a reservoir containing water. The mixture (AMA + water) was then delivered to the high vacuum ($P \approx 10^{-7}$ kPa) chamber of the instruments via a supersonic jet expansion through a pulsed nozzle (1 mm diameter). Rotational spectra of the complex were collected using a chirped-pulse (CP) and a Balle-Flygare (BF) Fourier transform microwave (FTMW) spectrometer which have been described in detail previously.[16,17] Initial measurements were performed using the CP-FTMW instrument to record a broadband spectrum from 8–18 GHz in segments of 2 GHz each. On the basis of the survey spectra, the most intense rotational transitions belonging to the different conformers of the AMA–w complex were identified. These transitions showed partially resolved hyperfine splittings due to the presence of the ^{14}N quadrupolar nucleus. Final frequency measurements were performed using the BF-FTMW spectrometer (8–20 GHz) which features higher resolution and sensitivity. This allowed the hyperfine structure to be better resolved and the less intense spectral features to be recorded. Transitions collected with the BF-FTMW instrument have linewidths (FWHM) of ~7 kHz while the uncertainty in the line positions is ±2 kHz. In the BF-FTMW setup, all transitions are split into two Doppler components due to the coaxial arrangement of the molecular beam and the resonator axis.

9.3.2 Computational Methods

To identify possible conformers of AMA–w, a molecular dynamics approach was used at the GFN2-xTB[18] level of theory using the Conformer-Rotamer Ensemble Sampling Tool (CREST) available in the extended tight binding (xTB) program package.[19,20] This initial search led to 56 possible geometries for AMA–w. All 56 structures were optimized using the dispersion-corrected density functional theory (DFT) B3LYP[21]-D3(BJ)[22,23] functional with Dunning's aug-cc-pVTZ[24] basis set. The B3LYP-D3(BJ)/aug-cc-pVTZ calculations led to 25 unique minima as some of the initial structures converged to the same energy minimum. Next, the optimized geometries from B3LYP-D3(BJ) whose relative energies were within 10 kJ mol^{-1} were re-optimized at higher levels of theory including the double hybrid B2PLYP[25] method with D3(BJ)[22,23] dispersion corrections (referred to as B2PLYP-D3 hereafter) and the *ab initio* MP2[26] methods both combined with the aug-cc-pVTZ basis set. It is worth noting that conformers with relative energies larger than 10 kJ mol^{-1} are not expected to be sufficiently populated for observation using our spectroscopic methods. Vibrational frequency calculations within the harmonic approximation were performed for all optimized geometries at the same levels of theory to validate the nature of the stationary points, to compute energies with zero-point corrections (ZPE) and to estimate quartic centrifugal distortion constants. The Boys and Bernardi's counterpoise method[27] was included in all optimization and frequency calculations to account for basis set superposition (BSSE) error. The optimization and frequency calculations were performed using the Gaussian 16 program.[28]

Non-covalent interaction (NCI),[13] quantum theory of atoms in molecules (QTAIM)[12] and natural bond orbital (NBO, B3LYP-D3(BJ)/aug-cc-pVTZ)[14] analyses were performed to identify and quantify the intra- and intermolecular interactions responsible for the conformers of AMA–w

using the NCIPLOT,[29] AIMALL[30] and NBO 7 programs,[31] respectively. The interaction energy between the water and AMA monomers for each observed conformer was further decomposed into physically meaningful terms (electrostatic, exchange or Pauli repulsion, induction and dispersion) using the symmetry-adapted perturbation theory (SAPT)[15] energy decomposition analysis (EDA). For comparison, we also performed EDA for related amine–w complexes and compare the results with those of the water dimer and ammonia–w. The SAPT calculations were done at the SAPT2+(3)δMP2[32]/aug-cc-pVTZ level using the Psi4 code.[33] Atomic charges were also computed using the Voronoi deformation density (VDD)[34] method as implemented in the Multiwfn software.[35]

9.4 Results

9.4.1 Potential Energy Surface

For the AMA monomer itself, a total of nine energy minima were reported[10] on the potential energy surface and were labeled using a Roman numeral from I–IX which describes their decreasing order of stability with I being the most stable geometry. Experimentally, rotational transitions for the four low energy conformers ($\Delta E_{ZPE} < 2.1$ kJ mol^{-1}) I, II, III and V were observed in a supersonic jet expansion and their populations were estimated to be 40%, 36%, 22% and 2%, respectively. Since the interaction with a water molecule may induce changes in the relative energy ordering of the monomer geometries upon complexation, all conformers of AMA must be considered when searching for the energy minima of the AMA–w complex. This is done automatically during the initial steps of the conformational searches in the CREST procedure

through the iMTD-GC algorithm which considers all possible orientations of the monomer geometries and binding sites for the water molecule. After the conformational searches, optimizations at higher levels of theory led to nine conformers for AMA–w, depicted in Figure 9.1, whose relative energies are within 10 kJ mol^{-1}. Although higher energy conformers exist, only those below 10 kJ mol^{-1} are expected to be sufficiently populated for detection by FTMW spectroscopy in a supersonic jet. The atomic coordinates for each of the nine conformers are provided in Tables S72–S80 of Appendix F. Their calculated energetic and spectroscopic parameters from both the B2PLYP-D3 and MP2 methods are given in Table 9.1. The geometries of the monohydrated complexes were named using the acronym AMA followed by a first Roman numeral which represents the monomer geometry, the letter "w" for water and a second Roman numeral to denote the order of stability of the complex with AMA-I-w-I being the most stable conformer. Overall, the calculated relative energy orderings, rotational constants (*A*, *B* and *C*), quadrupole coupling constants [$1.5\chi_{aa}$ and $0.25\ (\chi_{bb}- \chi_{cc})$] and electric dipole moment components (μ_a, μ_b, μ_c) for the conformers of AMA–w from the B2PLYP-D3 and MP2 methods are consistent with each other.

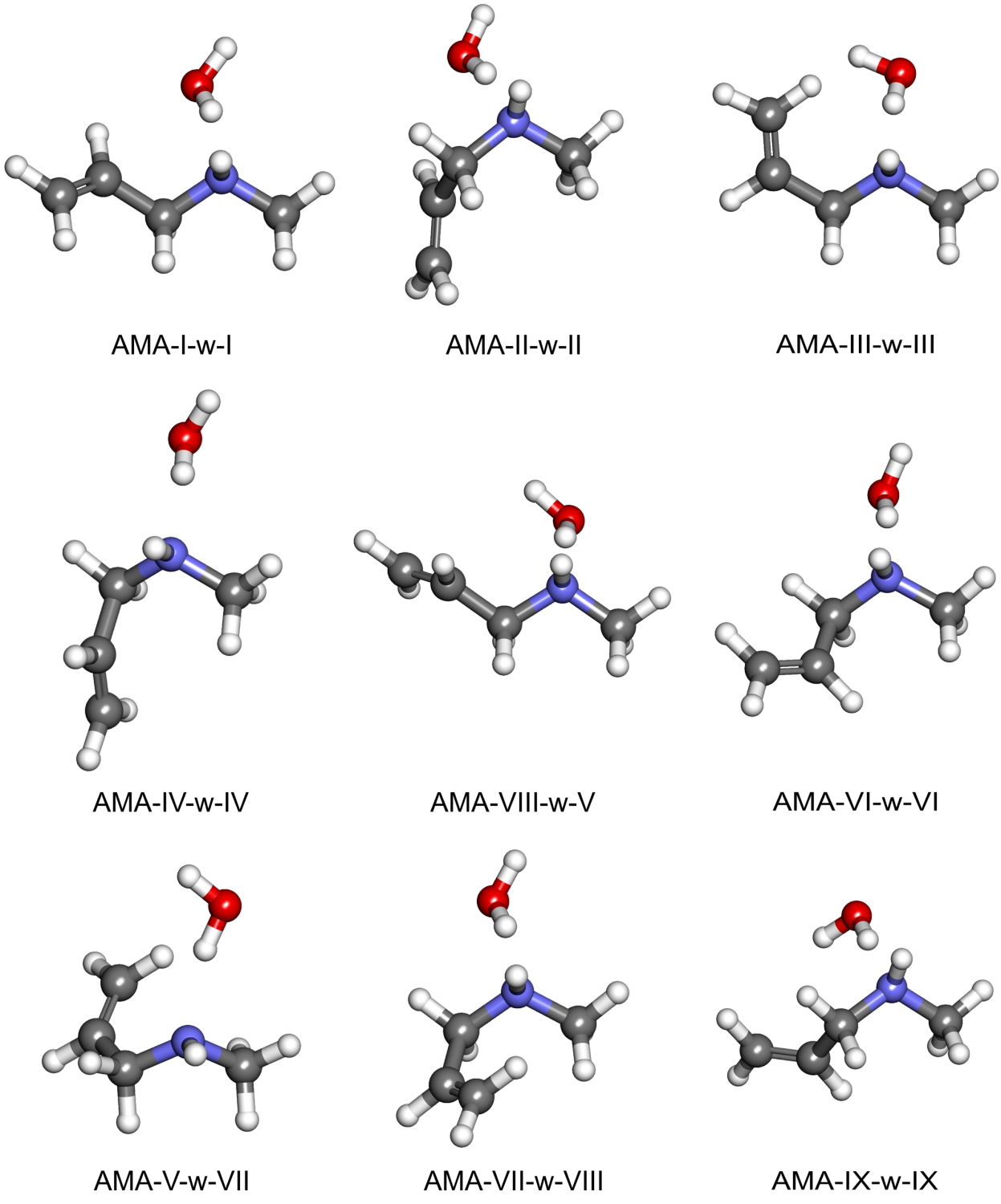

Figure 9.1 Nine conformers of the AMA–w complex identified within an energy window of 10 kJ mol^{-1} using quantum chemical calculations (B2PLYP-D3/aug-cc-pVTZ).

Table 9.1 Calculated relative energies with zero-point corrections (ZPE) ΔE_0 in kJ mol^{-1}, population P at 298K in %, rotational (A, B and C) and ^{14}N quadrupole coupling [1.5 (χ_{aa}) and 0.25 (χ_{bb}- χ_{cc})] constants in MHz, and electric dipole moment components (μ_a, μ_b and μ_c) in Debye for the nine most stable conformers of the AMA–w complex obtained at the B2PLYP-D3 and MP2 levels with the aug-cc-pVTZ basis set.

Conformer	B2PLYP-D3					MP2				
	ΔE_0	P_{298K}	$A/B/C$	1.5 (χ_{aa})/0.25 (χ_{bb}- χ_{cc})	$\mu_a/\mu_b/\mu_c$	ΔE_0	P_{298K}	$A/B/C$	1.5 (χ_{aa})/0.25 (χ_{bb}- χ_{cc})	$\mu_a/\mu_b/\mu_c$
AMA-I-w-I	0.0	41.3	3441/1984/1345	1.84/-1.40	0.1/2.5/1.3	0.0	39.4	3504/1998/1365	1.70/-1.26	0.0/2.4/1.3
AMA-II-w-II	1.7	20.9	3255/2134/1568	-0.80/-0.83	0.2/2.9/0.7	1.2	23.8	3260/2167/1594	-1.16/-0.73	0.3/2.9/0.8
AMA-III-w-III	2.5	14.9	3197/2290/1511	3.71/-1.70	2.0/2.6/0.2	2.5	14.2	3298/2277/1559	3.60/-1.64	1.9/2.4/0.3
AMA-IV-w-IV	4.1	8.0	5336/1474/1292	-6.11/0.03	1.7/2.0/1.5	3.7	8.7	5223/1519/1347	-5.87/0.00	1.6/1.9/1.5
AMA-VIII-w-V	5.0	5.4	3361/2105/1400	4.21/-1.79	1.4/2.7/1.0	5.0	5.2	3458/2128/1427	3.99/-1.60	1.1/2.4/1.1
AMA-VI-w-VI	6.1	3.6	4979/1484/1213	-5.18/-0.22	1.8/1.9/1.5	6.5	2.8	5226/1488/1237	-4.80/-0.19	1.8/1.6/1.6
AMA-V-w-VII	6.9	2.5	3288/2232/1656	0.56/-1.30	2.5/1.3/1.3	6.7	2.7	3433/2196/1655	0.83/-1.26	2.2/1.3/1.3
AMA-VII-w-VIII	7.0	2.4	5643/1543/1308	-7.12/0.10	2.0/1.5/1.0	6.9	2.4	5806/1569/1330	-6.60/0.14	1.9/1.4/1.1
AMA-IX-w-IX	9.3	1.0	2919/2375/1528	4.11/-1.70	1.3/3.2/0.2	9.6	0.8	2937/2416/1554	3.88/-1.67	1.4/3.3/0.2

9.4.2 Spectral Analysis

The broadband CP-FTMW spectrum of the AMA and water mixture is very dense including lines from the four conformers (I, II, III and V) of the monomer reported previously.[10] Once these known transitions were excluded, two sets of *R*-branch *b*-type transitions were rapidly identified. This suggested the formation of two new species in the supersonic jet with sizeable μ_b dipole components. By comparing the experimental rotational constants with the predicted values for each individual conformer (Table 9.1), the patterns were assigned to the parent species of the two most stable conformers predicted for the complex, AMA-I-w-I and AMA-II-w-II. The initial assignments were confirmed using the BF-FTMW instrument which allowed the ^{14}N hyperfine structure to be better resolved. No extra tunneling splittings due to methyl internal rotation or N–H inversion within AMA (as seen for the monomer)[10] or to the movement of the water subunit were observed. A portion of the CP-FTMW spectrum of AMA–w is given in Figure 9.2 while the BF-FTMW spectrum for the 6_{16}-5_{05} transition of AMA-I-w-I highlighting ^{14}N hyperfine components is provided in Figure 9.3.

The final fitting of all measured transitions was carried out with Pickett's SPFIT program[36] using Watson's S-reduced Hamiltonian[37] (I^r representation) to obtain accurate rotational, quartic centrifugal distortion and quadrupole coupling constants. A summary of the resulting values is given in Table 9.2. The consistency with the theoretical predictions in Table 9.1 confirms the assignment of conformers AMA-I-w-I and AMA-II-w-II. The complete line lists of measured transitions and residuals are provided in Tables S81–S82. No transitions belonging to other AMA–w species were detected which may be a consequence of insufficient population or relaxation to lower energy forms.

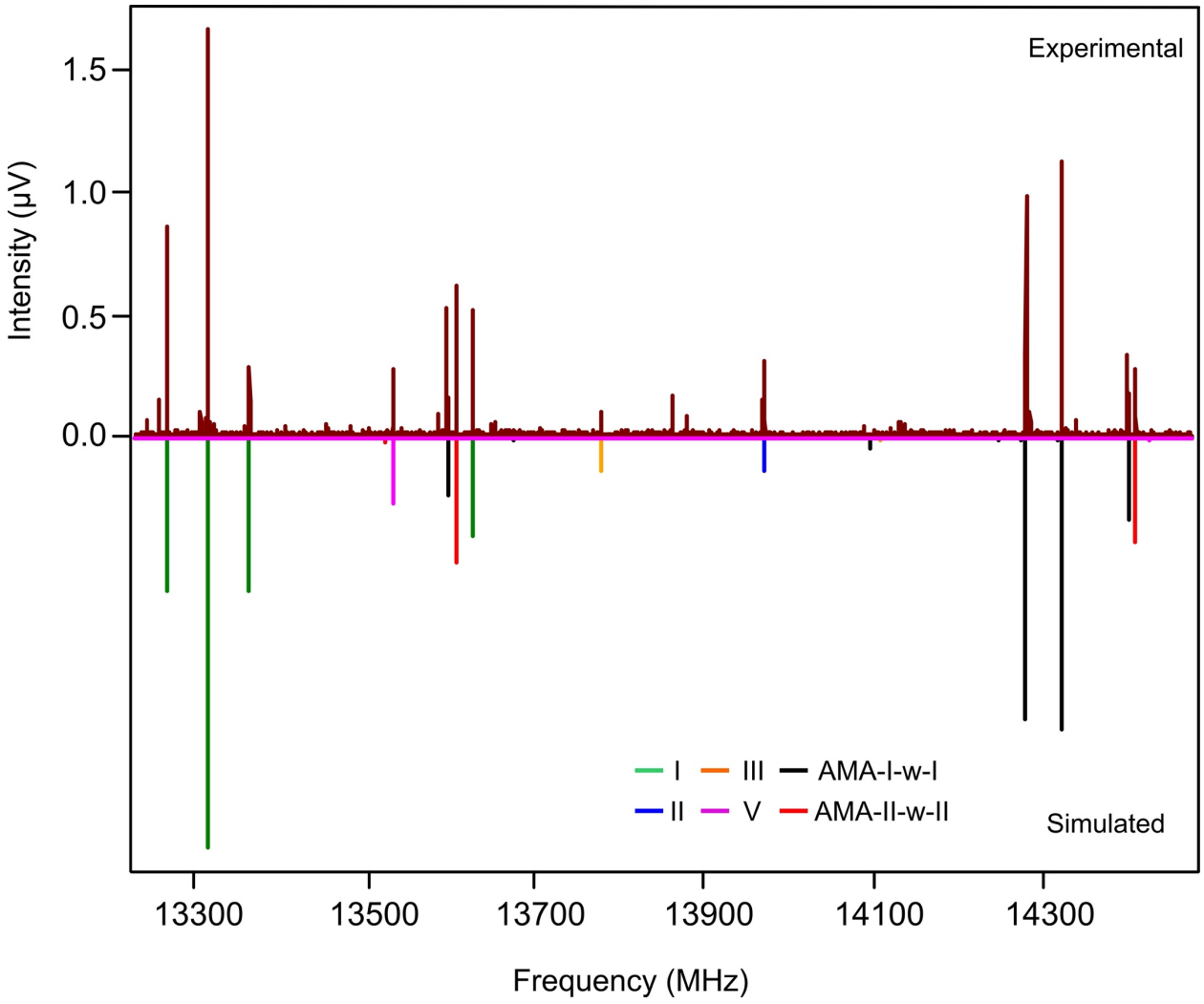

Figure 9.2 Section of the CP-FTMW spectrum (1.5 million FIDs). The upper trace (maroon) represents the experimental spectrum while the lower traces (in colour) show simulations of the spectra of the known conformers of AMA and AMA–w. The intensity of the simulated transitions is based on calculated electric dipole moment components and populations.

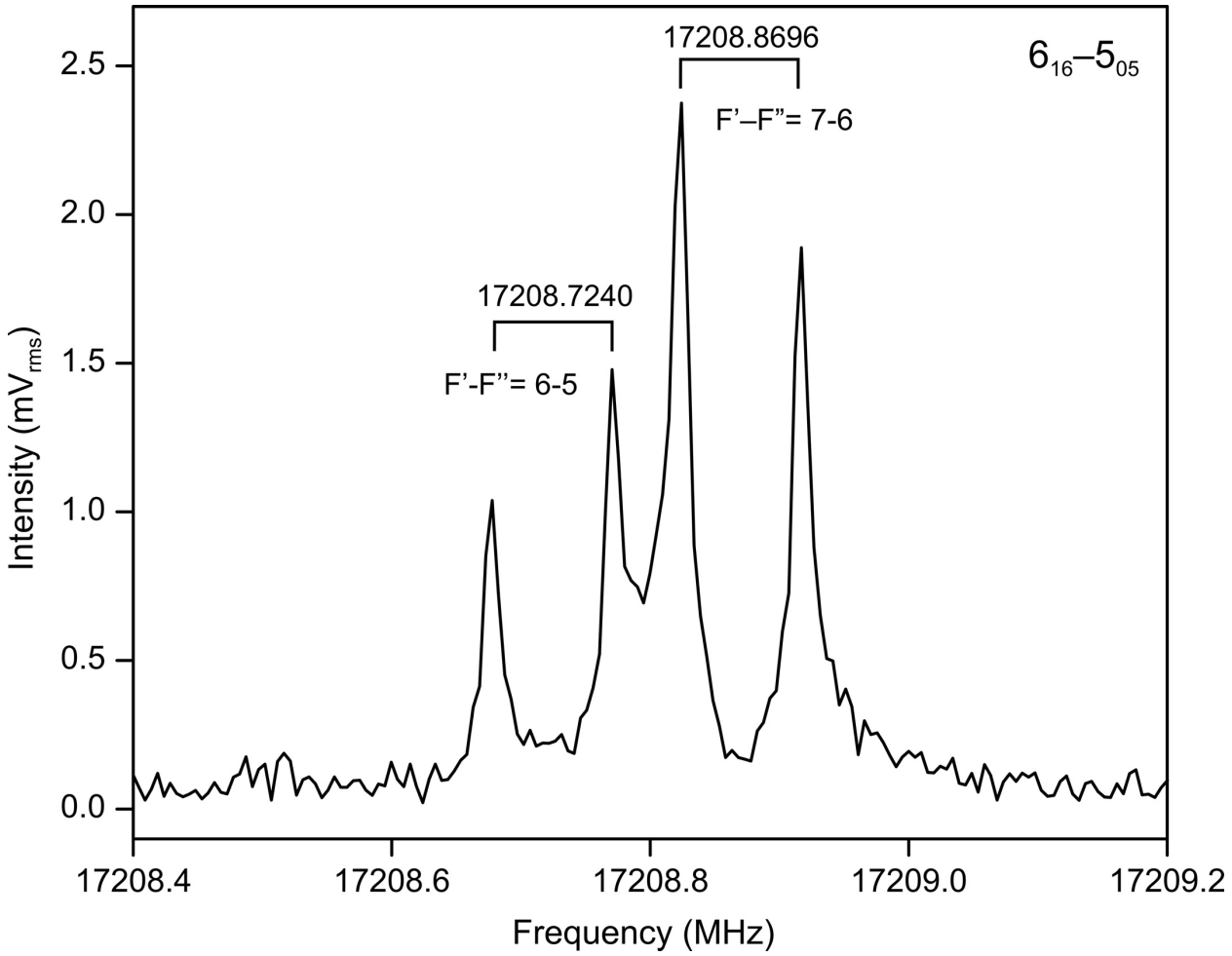

Figure 9.3 BF-FTMW spectrum for the 6_{16}–5_{05} rotational transition of conformer AMA-I-w-I highlighting two ^{14}N hyperfine components.

Table 9.2 Experimentally derived spectroscopic parameters for the two observed conformers of the AMA–w complex.

Parameter	AMA-I-w-I	AMA-II-w-II
A/MHz[a]	3442.84817(33)	3260.33627(73)
B/MHz	1959.50815(24)	2082.50939(77)
C/MHz	1330.95365(11)	1542.36365(25)
D_J/kHz[b]	2.6641(44)	3.423(12)
D_{JK}/kHz	-3.171(20)	-4.470(65)
D_K/kHz	29.706(35)	12.879(78)
d_1/kHz	-1.3021(31)	-1.059(12)
d_2/kHz	-0.2410(21)	-0.041(11)
1.5 (χ_{aa})/MHz[c]	1.6642(37)	-0.9239(67)
0.25 (χ_{bb}- χ_{cc})/MHz	-1.31271(70)	-0.7976(11)
$\mu_a/\mu_b/\mu_c$[d]	n/y/y	n/y/n
N[e]	82	36
σ/kHz[f]	2.1	2.1

[a]Rotational constants; [b]quartic centrifugal distortion constants; [c]^{14}N nuclear quadrupole coupling constants; [d]electric dipole moment components ("y" if observed and "n" if not observed); [e]total number of lines (N) in the fit; [f]root-mean-square deviation of the fit (σ). The full set of calculated constants at both B2PLYP-D3 and MP2 methods are provided in Table S83.

9.5 Discussion

All nine AMA–w conformers, identified by the B2PLYP-D3 and MP2 calculations, are stabilized by a primary N···H–O intermolecular HB in which the nitrogen atom serves as a HB acceptor while the water molecule acts as a HB donor (Figure 9.1). This is consistent with the greater nucleophilic character of nitrogen compared to that of oxygen. The favoured HB acceptor role of nitrogen has also been highlighted in previous studies dealing with the monohydrated complexes of primary, secondary and tertiary amines such as MA–w,[5] DMA–w,[4–6] TMA–w,[4,5,7]

PA–w and IPA–w.[9] Depending on the geometry adopted by the AMA monomer, the water molecule can simultaneously act as a HB acceptor as in conformers AMA-I-w-I and AMA-II-w-II where a secondary C–H···O HB is established between the vinylic hydrogen and the oxygen atom of water. The nature and strength of the intermolecular interactions occurring in the conformers of AMA–w will be discussed in detail below.

The relative energy ordering for the four most stable geometries of AMA–w follows the same trend observed in the isolated amine.[10] Significant changes are observed, however, in the stability ordering of higher energy conformers following complexation. This is exemplified, for example, by the stabilization of the eighth most stable conformer of the AMA monomer to form the fifth most stable hydrate (AMA-VIII-w-V) and by the destabilization of the AMA monomer V to form AMA-V-w-VII. In this sense, interactions with water disrupt the conformational equilibrium of AMA to some extent with the effects being most pronounced for AMA species lying ~5 kJ mol^{-1} or more above the global minimum. The detection of AMA-I-w-I and AMA-II-w-II confirms that the intramolecular interactions responsible for the low energy conformers I (40%) and II (36%) of AMA remain important in the presence of water while higher energy dimers were not produced in sufficient quantities to be detected despite their sizeable dipole moments (Table 9.1).

To understand why conformers AMA-I-w-I and AMA-II-w-II are the two most stable complexes, one must explore the intrinsic nature of the interactions responsible for these geometries. As the calculated rotational constants from B2PLYP-D3/aug-cc-pVTZ for AMA-I-w-I and AMA-II-w-II matched the experimental ground state values, it is reasonable to assume that the equilibrium structures at this level of theory provide a good description of these conformers. The HB parameters extracted from the equilibrium structures, namely the N···H–O and C–H···O

distances, are 1.89 Å and 2.76 Å, and 1.91 Å and 2.57 Å in conformers AMA-I-w-I and AMA-II-w-II, respectively. This suggests that the strength of the N···H–O interaction is similar in AMA-I-w-I and AMA-II-w-II (slightly shorter N···H–O distance in AMA-I-w-I) while the secondary C–H···O interaction is more favoured in AMA-II-w-II based on the shorter HB. To further characterize the underlying effects leading to such subtle differences, we used the three well-known QTAIM, NCI and NBO approaches.

The QTAIM molecular plots and associated parameters for the nine conformers of AMA–w are given in Figure 9.4 and Table S84, respectively. These show that all conformers exhibit a primary N···H–O HB as evidenced by the presence of a bond critical point (BCP, green dot) along the interaction path between the nitrogen and hydrogen atoms. In addition, AMA-I-w-I, AMA-II-w-II and AMA-V-w-VII display a secondary C–H···O HB. Using the electronic potential energy at the BCP, V_{BCP}, the strength of each HB can be obtained by $E_{HB} = 0.5V_{BCP}$.[38] The energies of the primary N···H–O and secondary C–H···O HBs in the different conformers vary from -37 to -39 kJ mol^{-1} and from -4 to -6 kJ mol^{-1}, respectively. When focusing on the QTAIM graphs of the two observed conformers (Figure 9.5A), the primary contact is indeed stronger in AMA-I-w-I than in AMA-II-w-II (by ~1.2 kJ mol^{-1}) while the reverse is true for the secondary interaction (~1.1 kJ mol^{-1} stronger in AMA-II-w-II) in agreement with the aforementioned HB distances. Nevertheless, the overall contribution from these intermolecular HBs to the stabilization of the two lowest energy conformers seem to cancel each other implying that their relative energy difference is not solely dependent on the strength of the intermolecular contacts but also on stabilizing and destabilizing intramolecular effects within the monomers themselves.

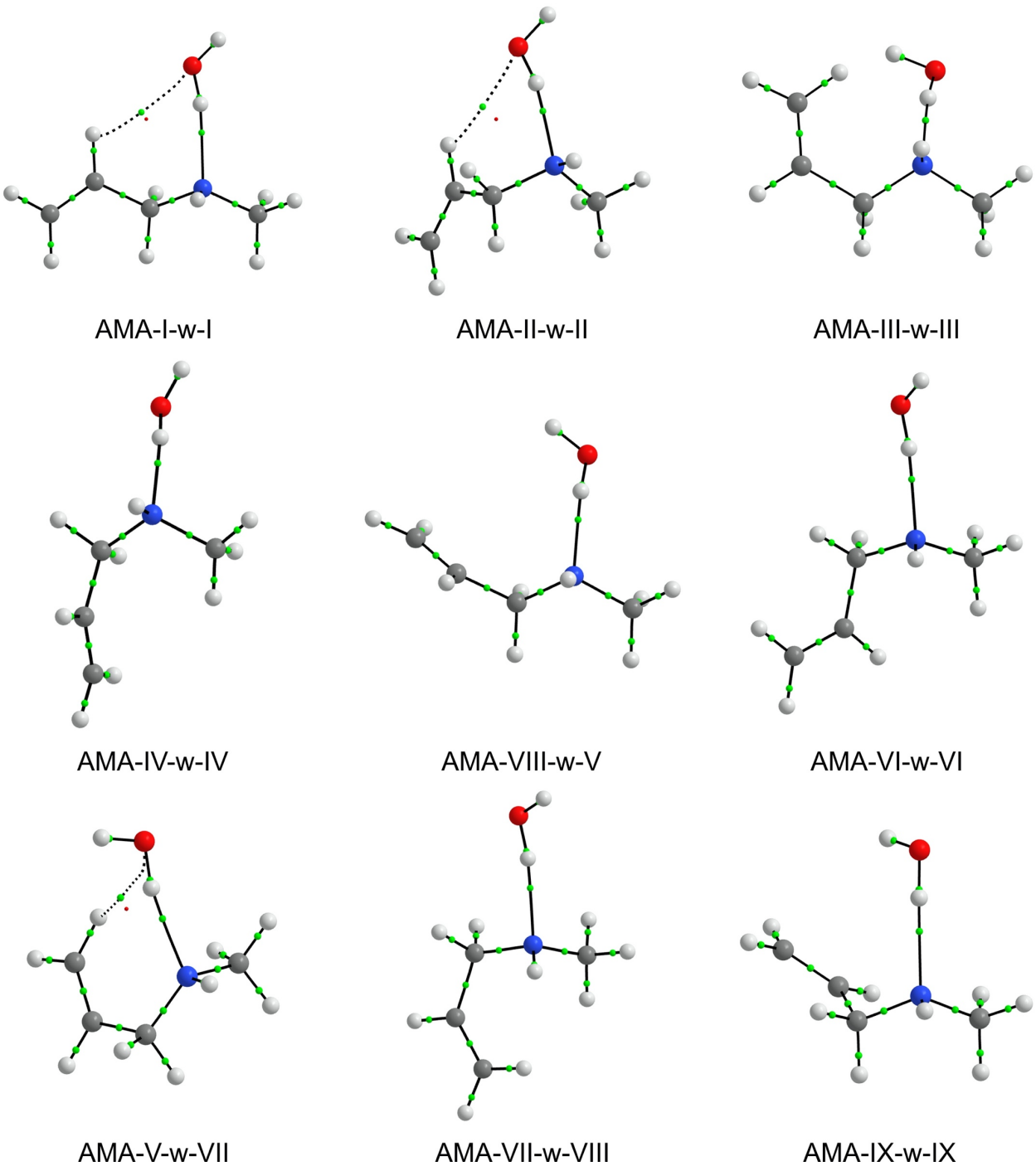

Figure 9.4 QTAIM molecular graphs for the nine most stable conformers of AMA–w.

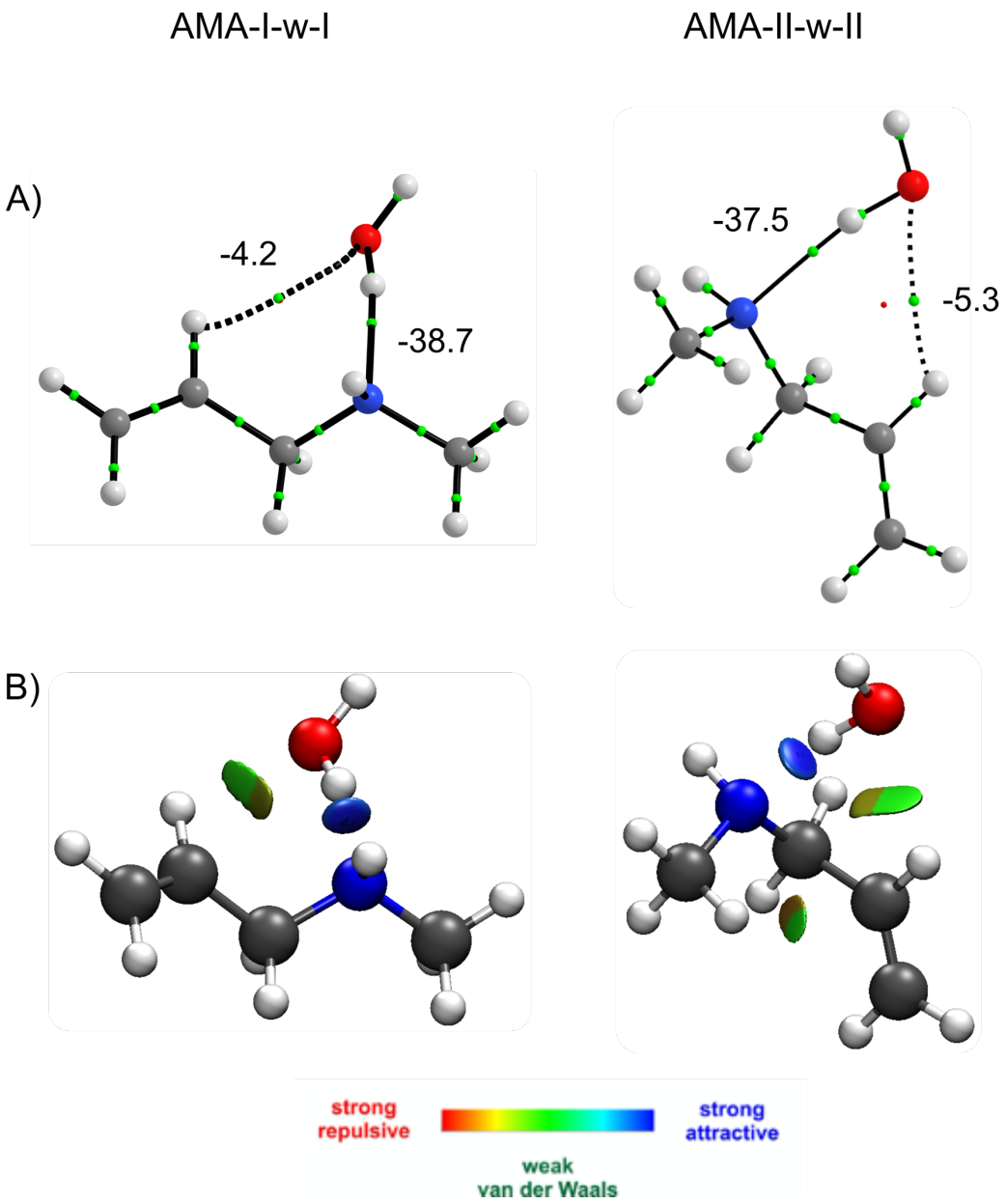

Figure 9.5 A) QTAIM molecular graphs containing the energies (in kJ mol^{-1}) for the N···H–O and C–H···O HB and B) NCI isosurfaces (s=0.5 and colour scale BGR: 0.02 < ρ < +0.02) for the two observed conformers of the AMA–w complex.

While the QTAIM approach is useful to characterize short to medium range HBs, NCI calculations can identify weaker interactions.[39] The NCI results, shown in Figure 9.6 for all conformers and in Figure 9.5B for AMA-I-w-I and AMA-II-w-II, confirm the strong N···H–O HB (blue coloured surfaces in the interacting regions) in all conformers and a weaker C–H···O HB (green coloured isosurfaces) in AMA-I-w-I, AMA-II-w-II and AMA-V-w-VII. The NCI outcomes also identify weaker secondary C–H···O contacts in AMA-III-w-III and AMA-VIII-w-V which were not captured by the QTAIM method. The intramolecular forces are similar to those first identified in the isolated molecule[10] in most of the conformers of AMA–w (specifically in the four lowest energy ones), lending support to the notion that these internal interactions are the primary influencers of the relative energy ordering of the most stable hydrates. Interestingly, complexation with water alters the nature of the intramolecular contacts in the higher energy forms of AMA and disrupts their stability ordering in agreement with the DFT and MP2 calculations. A noteworthy example arises from the comparison of the previously reported NCI plot of AMA conformer V (ref 10) with the one of its monohydrate AMA-V-w-VII (Figure 9.6, this work). Although the monomer geometry within the complex is largely maintained, the HBs established with water in AMA-V-w-VII leads to the formation of a 7-membered ring (involving atoms from the amino and allyl groups) resulting in the appearance of attractive and repulsive isosurfaces (absent in the isolated AMA conformer V). It is evident from the relative energy of the complex, that the combination of these effects leads to overall destabilization within the AMA V partner itself as the strength of the intermolecular contacts (Table S84, QTAIM) with water are actually greater than in some of the other hydrates. In contrast, the formation of a longer-range C–H···O HB in AMA-VIII-w-V does not lead to new destabilizing intramolecular interactions within conformer VIII (Figure 9.6) but suggests that this weak secondary contact (not captured by QTAIM) is sufficient

to bind the water molecule preferentially to monomer geometry VIII over others (namely V, VI, VII) based on the relative energies in Table 9.1. These two examples highlight the disruptive role that water can play through complex subtle effects that ultimately rule the conformational landscape of the AMA–w.

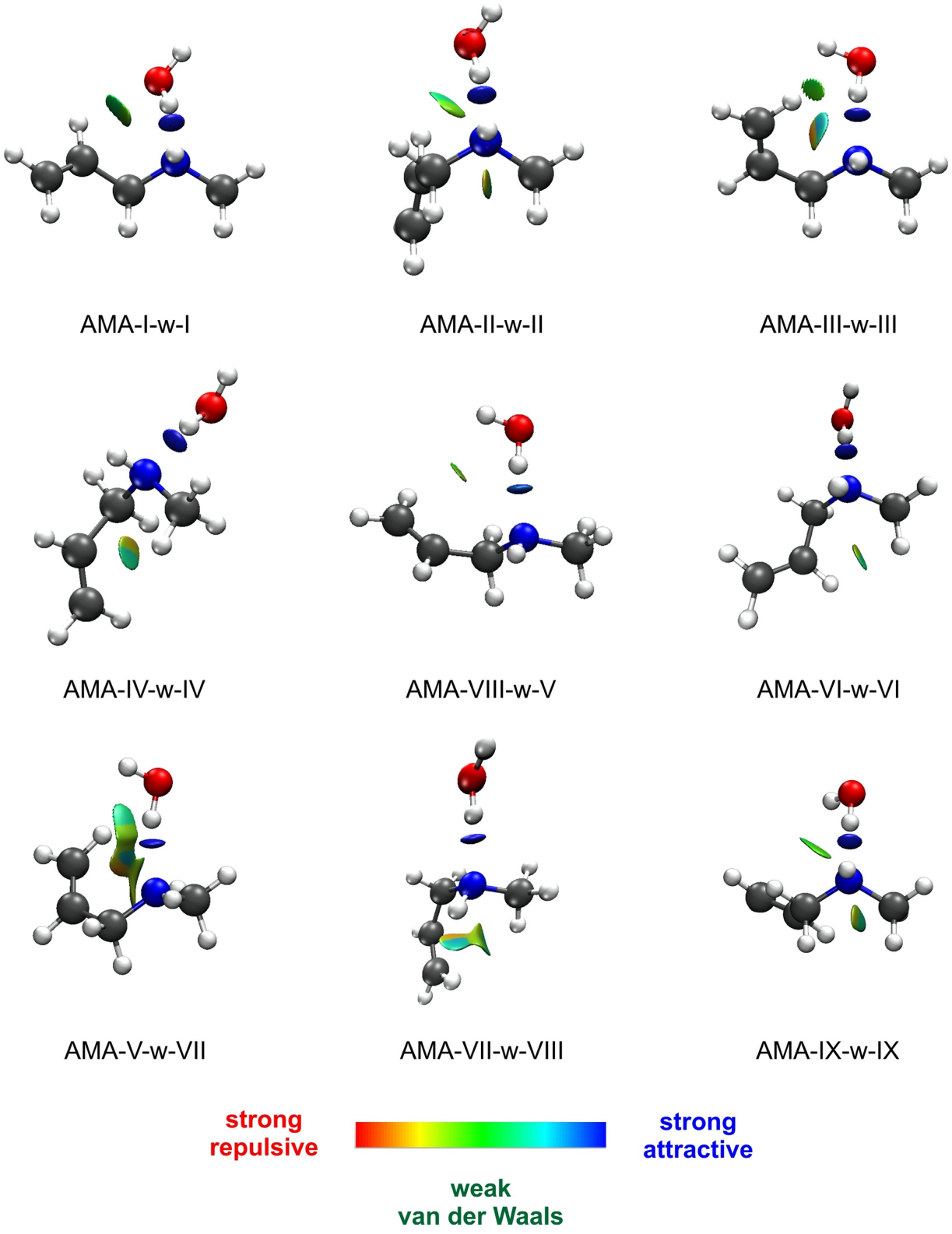

Figure 9.6 NCI isosurfaces (s=0.5 and colour scale BGR: 0.02 < ρ < +0.02) for the nine most stable conformers of AMA–w.

The results from the topological QTAIM and NCI analyses for the observed conformers are inline with NBO calculations in which charge transfer between electron donor (lone-pair) and acceptor (σ*) orbitals corresponding to these interactions is found to contribute to their second-order perturbation energies $E^{(2)}$. A summary of the NBO results for conformers AMA-I-w-I and AMA-II-w-II is given in Table 9.3.

Table 9.3 Second-order perturbation energies, $E^{(2)}$, for the $n_N \rightarrow \sigma^*_{O-H}$ and $n_O \rightarrow \sigma^*_{C-H}$ charge transfer interactions in the two most stable conformers of AMA–w obtained with the NBO calculations at the B3LYP-D3(BJ)/aug-cc-pVTZ level of theory.

Conformer	Charge transfer	$E^{(2)}$ (kJ mol^{-1})
AMA-I-w-I	$n_N \rightarrow \sigma^*_{O-H}$	55.5
	$n_O \rightarrow \sigma^*_{C-H}$	0.8
AMA-II-w-II	$n_N \rightarrow \sigma^*_{O-H}$	55.9
	$n_O \rightarrow \sigma^*_{C-H}$	1.3

Once the individual intra- and intermolecular interactions were identified, to understand the physical origins behind the formation of the AMA–w complex, the interaction energies (E_{total}) were decomposed using the SAPT analysis at the SAPT2+(3)δMP2/aug-cc-pVTZ level of theory as summarized in Table 9.4. The SAPT results confirm the slightly greater stability of AMA-I-w-I (larger negative E_{total} value) over AMA-II-w-II. For both, the largest stabilizing contribution is the electrostatic term which is related to favourable Coulombic interactions occurring between the negative charges around the nitrogen (-0.137 in AMA-I-w-I and -0.134 in AMA-II-w-II) and oxygen atoms (-0.307 in AMA-I-w-I and -0.306 in AMA-II-w-II) with the positive atomic charges surrounding the hydrogens (+0.096 and +0.047 in AMA-I-w-I and +0.092 and +0.051 in AMA-II-w-II) involved in the N···H–O and C–H···O HB, respectively. The induction and dispersion terms

further stabilize the AMA–w complex but their contributions are approximately three times smaller than the electrostatic one. The difference in the E_{total} between AMA-I-w-I and AMA-II-w-II arises from the destabilizing Pauli repulsion term (exchange) which is smaller in AMA-I-w-I.

Finally, to evaluate the impact of different substituents on the interaction energies of amine–w complexes, we compared the SAPT results from AMA–w with those of other amine monohydrates and with the ammonia–w adduct and the water dimer (Table 9.4). It is apparent that even the simplest ammonia–w complex has an interaction energy E_{total} that is ~1.3 times stronger than the water dimer suggesting that in water rich environments, such as the Earth's atmosphere, a water molecule binds preferentially to ammonia over self-aggregation. When the hydrogen atoms of ammonia are substituted by methyl groups in a stepwise fashion from MA to TMA, a gradual increase in the stability (smaller E_{total}) of the complexes is observed with TMA–w being the most stable of this family. It is interesting to note that while AMA is a secondary amine like DMA, the E_{total} for conformer AMA-I-w-I is 1.6 kJ mol^{-1} stronger than in DMA–w and also more stable by 1.4 kJ mol^{-1} than the tertiary amine complex TMA–w. The greater stability of AMA–w in comparison with DMA-w is mainly caused by a slight increase in the contributions from dispersion (Table 9.4) which is likely from the secondary long-range C–H···O HB established with the vinyl group in AMA–w. On the other hand, the surprisingly larger stability of AMA–w compared to TMA–w is not governed by the stabilizing contributors but rather by the Pauli repulsion term. While the sum of the three stabilizing terms is -107.4 kJ mol^{-1} in TMA–w and -105.8 kJ mol^{-1} in AMA–w, TMA–w is 3.0 kJ mol^{-1} more destabilized by Pauli repulsion (Table 9.4) by comparison. These subtle differences observed in the stabilizing and destabilizing effects within the clusters in Table 9.4 reinforce the importance of evaluating the impact of different side chains on the formation of amine–w complexes. A comprehensive conformational study of the homologous

series of complexes including, for example, allylamine–water and dimethylallylamine–water would provide interesting insights in this regard.

Table 9.4 Symmetry-adapted perturbation theory (SAPT) results, in kJ mol^{-1}, (SAPT2+(3)δMP2/aug-cc-pVTZ) for the two observed conformers of AMA–w and related complexes.

Complex	E_{total}	$E_{electrostatic}$	$E_{exchange}$	$E_{induction}$	$E_{dispersion}$
AMA-I-w-I	-34.3	-60.5	71.5	-23.0	-22.3
AMA-II-w-II	-33.6	-60.6	72.3	-22.9	-22.4
TMA–w	-32.9	-61.0	74.5	-24.9	-21.5
DMA–w	-32.7	-59.6	70.2	-23.5	-19.7
MA–w	-31.0	-56.3	64.0	-21.5	-17.2
ammonia–w[a]	-27.2	-49.1	53.0	-17.5	-13.6
water dimer[a]	-20.8	-34.7	35.2	-11.0	-10.3

[a]From reference 40.

9.6 Conclusions

The conformational landscape and the intermolecular interactions stabilizing the monohydrated complexes of AMA were revealed in this work for the first time using rotational spectroscopy. Aided by DFT and *ab initio* MP2 predictions, transitions for the two most stable conformers (AMA-I-w-I and AMA-II-w-II) were unequivocally assigned and their hyperfine splittings owing to the ^{14}N quadrupolar nucleus were resolved. In the observed complexes, the water molecule interacts with AMA as both a HB donor and acceptor forming primary N···H–O and a secondary C–H···O HBs on the order of -37 to -39 kJ mol^{-1} and -4 to -6 kJ mol^{-1}, respectively.

While the formation of HBs with water are not sufficient to overcome the internal forces governing the conformational landscape of the most stable monomers, they certainly affect the intramolecular interactions responsible for the energy ordering of higher energy conformations. Based on the energy components identified via SAPT analysis, the nature of the complex formation is mainly electrostatic with smaller contributions from induction and dispersion. By comparing the results for AMA–w with those from the water dimer, ammonia–w, MA–w, DMA–w and TMA–w clusters, we show that AMA is more readily hydrated. Relative to other primary and secondary amines, the presence of the vinyl group in AMA favours the formation of secondary contacts such as the C–H···O HB and thus tunes the overall interaction energy. For the tertiary case of TMA–w, the fewer substituents at N in AMA offer less stabilizing effects in comparison but the reduced exchange term in AMA–w yields greater stability overall. In closing, this study highlights the need for enhanced understanding of the unique influences that govern the interactions between amines and water on a microscopic scale including the number and identity of the organic sidechains and lays groundwork for modelling their chemistry in atmospheric and biological processes.

9.7 References

(1) Ge, X.; Wexler, A. S.; Clegg, S. L. Atmospheric Amines – Part I. A Review. *Atmos. Environ.* **2011**, *45* (3), 524–546.

(2) Herbine, P.; Dyke, T. R. Rotational Spectra and Structure of the Ammonia-Water Complex. *J. Chem. Phys.* **1985**, *83* (8), 3768–3774.

(3) Engdahl, A.; Nelander, B. The Intramolecular Vibrations of the Ammonia Water Complex. A Matrix Isolation Study. *J. Chem. Phys.* **1989**, *91* (11), 6604–6612.

(4) Kjaersgaard, A.; Vogt, E.; Hansen, A. S.; Kjaergaard, H. G. Room Temperature Gas-Phase Detection and Gibbs Energies of Water Amine Bimolecular Complex Formation. *J. Phys. Chem. A* **2020**, *124* (35), 7113–7122.

(5) Mmereki, B. T.; Donaldson, D. J. Ab Initio and Density Functional Study of Complexes between the Methylamines and Water. *J. Phys. Chem. A* **2002**, *106* (13), 3185–3190.

(6) Tubergen, M. J.; Kuczkowski, R. L. Hydrogen Bonding to Dimethylamine: The Microwave Spectrum and Structure of the Dimethylamine-Water Complex. *J. Mol. Struct.* **1995**, *352–353*, 335–344.

(7) Tubergen, M. J.; Kuczkowski, R. L. Microwave Spectroscopic Characterization of a Strong Hydrogen Bond: Trimethylamine-Water. *J. Am. Chem. Soc.* **1993**, *115* (20), 9263–9266.

(8) Rozenberg, M.; Loewenschuss, A.; Nielsen, C. J. H-Bonded Clusters in the Trimethylamine/Water System: A Matrix Isolation and Computational Study. *J. Phys. Chem. A* **2012**, *116* (16), 4089–4096.

(9) Chen, J.; Zheng, Y.; Melli, A.; Spada, L.; Lu, T.; Feng, G.; Gou, Q.; Barone, V.; Puzzarini, C. Theory Meets Experiment for Elucidating the Structure and Stability of Non-Covalent Complexes: Water-Amine Interaction as a Proof of Concept. *Phys. Chem. Chem. Phys.* **2020**, *22* (9), 5024–5032.

(10) Silva, W. G. D. P.; Poonia, T.; Wijngaarden, J. Targeting the Rich Conformational Landscape of N -Allylmethylamine Using Rotational Spectroscopy and Quantum Mechanical Calculations. *ChemPhysChem* **2020**, *21* (22), 2515–2522.

(11) Vitins, P.; Egger, K. W. The Thermochemical Kinetics of the Retro-'Ene' Reactions of Molecules with the General Structure (Allyl)XYH in the Gas Phase. Part IX. Unimolecular Thermal Decompostion of Allylmethylamine. *J. Chem. Soc., Perkin Trans. 2* **1974**, No. 11,

1289–1291.

(12) Bader, R. F. W. Atoms in Molecules. *Acc. Chem. Res.* **1985**, *18* (1), 9–15.

(13) Johnson, E. R.; Keinan, S.; Mori-Sánchez, P.; Contreras-García, J.; Cohen, A. J.; Yang, W. Revealing Noncovalent Interactions. *J. Am. Chem. Soc.* **2010**, *132* (18), 6498–6506.

(14) Weinhold, F.; Landis, C. R.; Glendening, E. D. What Is NBO Analysis and How Is It Useful? *Int. Rev. Phys. Chem.* **2016**, *35* (3), 399–440.

(15) Jeziorski, B.; Moszynski, R.; Szalewicz, K. Perturbation Theory Approach to Intermolecular Potential Energy Surfaces of van Der Waals Complexes. *Chem. Rev.* **1994**, *94* (7), 1887–1930.

(16) Evangelisti, L.; Sedo, G.; van Wijngaarden, J. Rotational Spectrum of 1,1,1-Trifluoro-2-Butanone Using Chirped-Pulse Fourier Transform Microwave Spectroscopy. *J. Phys. Chem. A* **2011**, *115* (5), 685–690.

(17) Sedo, G.; van Wijngaarden, J. Fourier Transform Microwave Spectra of a "New" Isomer of OCS-CO_2. *J. Chem. Phys.* **2009**, *131* (4), 044303.

(18) Bannwarth, C.; Ehlert, S.; Grimme, S. GFN2-XTB - An Accurate and Broadly Parametrized Self-Consistent Tight-Binding Quantum Chemical Method with Multipole Electrostatics and Density-Dependent Dispersion Contributions. *J. Chem. Theory Comput.* **2019**, *15* (3), 1652–1671.

(19) Grimme, S. Exploration of Chemical Compound, Conformer, and Reaction Space with Meta-Dynamics Simulations Based on Tight-Binding Quantum Chemical Calculations. *J. Chem. Theory Comput.* **2019**, *15* (5), 2847–2862.

(20) Pracht, P.; Bohle, F.; Grimme, S. Automated Exploration of the Low-Energy Chemical Space with Fast Quantum Chemical Methods. *Phys. Chem. Chem. Phys.* **2020**, *22* (14),

7169–7192.

(21) Becke, A. D. Density-functional Thermochemistry. III. The Role of Exact Exchange. *J. Chem. Phys.* **1993**, *98* (7), 5648–5652.

(22) Grimme, S.; Ehrlich, S.; Goerigk, L. Effect of the Damping Function in Dispersion Corrected Density Functional Theory. *J. Comput. Chem.* **2011**, *32* (7), 1456–1465.

(23) Grimme, S.; Antony, J.; Ehrlich, S.; Krieg, H. A Consistent and Accurate Ab Initio Parametrization of Density Functional Dispersion Correction (DFT-D) for the 94 Elements H-Pu. *J. Chem. Phys.* **2010**, *132* (15), 154104.

(24) Dunning, T. H. Gaussian Basis Sets for Use in Correlated Molecular Calculations. I. The Atoms Boron through Neon and Hydrogen. *J. Chem. Phys.* **1989**, *90* (2), 1007–1023.

(25) Grimme, S. Semiempirical Hybrid Density Functional with Perturbative Second-Order Correlation. *J. Chem. Phys.* **2006**, *124* (3), 034108.

(26) Møller, C.; Plesset, M. S. Note on an Approximation Treatment for Many-Electron Systems. *Phys. Rev.* **1934**, *46* (7), 618–622.

(27) Boys, S. F.; Bernardi, F. The Calculation of Small Molecular Interactions by the Differences of Separate Total Energies. Some Procedures with Reduced Errors. *Mol. Phys.* **1970**, *19* (4), 553–566.

(28) Frisch, M. J.; Trucks, G. W.; Schlegel, H. B.; Scuseria, G. E.; Robb, M. A.; Cheeseman, J. R.; Scalmani, G.; Barone, V.; Petersson, G. A.; Nakatsuji, H., et al. *Gaussian 16*, Revision C.01; Gaussian, Inc.: Wallingford, CT, 2016.

(29) Contreras-García, J.; Johnson, E. R.; Keinan, S.; Chaudret, R.; Piquemal, J.-P.; Beratan, D. N.; Yang, W. NCIPLOT: A Program for Plotting Noncovalent Interaction Regions. *J. Chem. Theory Comput.* **2011**, *7* (3), 625–632.

(30) Keith, T. A. *AIMALL*, version 17.11.14; TK Gristmill Software: Overland Park, KS, 2016.

(31) Glendening, E. D.; Badenhoop, J. K.; Reed, A. E.; Carpenter, J. E.; Bohmann, J. A.; Morales, C. M.; Karafiloglou, P.; Landis C. R.; Weinhold, F. *NBO 7.0*, Theoretical Chemistry Institute, University of Wisconsin: Madison, 2018.

(32) Hohenstein, E. G.; Sherrill, C. D. Density Fitting of Intramonomer Correlation Effects in Symmetry-Adapted Perturbation Theory. *J. Chem. Phys.* **2010**, *133* (1), 014101.

(33) Parrish, R. M.; Burns, L. A.; Smith, D. G. A.; Simmonett, A. C.; DePrince, A. E.; Hohenstein, E. G.; Bozkaya, U.; Sokolov, A. Y.; Di Remigio, R.; Richard, R. M.; et al. Psi4 1.1: An Open-Source Electronic Structure Program Emphasizing Automation, Advanced Libraries, and Interoperability. *J. Chem. Theory Comput.* **2017**, *13* (7), 3185–3197.

(34) Fonseca Guerra, C.; Handgraaf, J. W.; Baerends, E. J.; Bickelhaupt, F. M. Voronoi Deformation Density (VDD) Charges: Assessment of the Mulliken, Bader, Hirshfeld, Weinhold, and VDD Methods for Charge Analysis. *J. Comput. Chem.* **2004**, *25* (2), 189–210.

(35) Lu, T.; Chen, F. Multiwfn: A Multifunctional Wavefunction Analyzer. *J. Comput. Chem.* **2012**, *33* (5), 580–592.

(36) Pickett, H. M. The Fitting and Prediction of Vibration-Rotation Spectra with Spin Interactions. *J. Mol. Spectrosc.* **1991**, *148* (2), 371–377.

(37) Watson, J. K. G. *In Vibrational Spectra and Structure: A Series of Advances*; Durig, J. R., Ed.; Elsevier: New York, 1977, Vol. 6, pp. 1–89.

(38) Espinosa, E.; Molins, E.; Lecomte, C. Hydrogen Bond Strengths Revealed by Topological Analyses of Experimentally Observed Electron Densities. *Chem. Phys. Lett.* **1998**, *285* (3–4), 170–173.

(39) Lane, J. R.; Contreras-García, J.; Piquemal, J. P.; Miller, B. J.; Kjaergaard, H. G. Are Bond Critical Points Really Critical for Hydrogen Bonding? *J. Chem. Theory Comput.* **2013**, *9* (8), 3263–3266.

(40) Emamian, S.; Lu, T.; Kruse, H.; Emamian, H. Exploring Nature and Predicting Strength of Hydrogen Bonds: A Correlation Analysis Between Atoms-in-Molecules Descriptors, Binding Energies, and Energy Components of Symmetry-Adapted Perturbation Theory. *J. Comput. Chem.* **2019**, *40* (32), 2868–2881.

Chapter 10. Summary and Outlook

10.1 Summary

In this thesis, the non-covalent interactions governing the conformational landscape of selected molecular systems were successfully unveiled using high-level quantum chemical methods and Fourier transform microwave spectroscopy. The combination of the broadband chirped-pulse for initial surveys and the cavity-based Balle-Flygare FTMW to collect transitions with higher resolution and sensitivity was shown important for conformational analysis studies. Probing these systems in a collision-free environment by their rotational fingerprints allowed insights on molecular geometries, e.g. the determination of accurate spectroscopic parameters, and non-covalent interactions responsible for the conformational preferences to be obtained. These novel experimental data serve as the basis for the development and improvement of theoretical models about the forces that held molecules together. As molecular design is at the core of chemistry and as there is not always time and resources for trial-and-error benchtop experiments, chemical modelling and intuition, built on fundamental concepts like those presented in this thesis, have become crucial to advancements in many areas of chemistry including supramolecular catalysis, assembly, and recognition.

At first, by studying the conformers of 3-mercaptopropionic acid (MPA, Chapter 4) and methyl 3-mercaptopropionate (MP, Chapter 5), we learned that although weaker than its oxygen counterpart, the biologically relevant S–H···O=C interaction is the effect responsible for the greater stability of the global minimum geometry of both compounds as proven experimentally by their dominant patterns in the rotational spectrum. While no experimental structural information could

be extracted in Chapter 4 because of the low intensity of the MPA spectrum, in Chapter 5, the observation of transitions for the minor ^{13}C and ^{34}S isotopologues of MP allowed a ground state effective structure to be determined. This revealed that the S–H···O=C HB distance is about 2.5 Å while its oxygen counterpart is much shorter (2.1 Å). The bond length found for the S interaction in isolation is within the range of those involving the amino acid cysteine[1] (2.5 Å to 2.9 Å) and offered confirmation of benchmark methods used for prediction of those interactions in proteins. For MP, the observation of splittings related to the methyl internal rotation enabled the determination of the barrier to this motion which was then compared to those of other esters in the literature. It was shown that although the aforementioned HB interaction is dominant, it does not significantly affect the rotation of the methyl group.

In moving to the understanding of the intermolecular interactions occurring in the microsolvation of heterocycles, several important observations for the preferred binding site and internal dynamics of water were made. The four-membered rings trimethylene oxide (TMO) and sulfide (TMS), given in Chapter 6, are primarily bound to water through the site of the heteroatom that serves as a HB acceptor via X···H–O (X= O, S) HB. In contrast, the presence of a π-system in the heteroaromatic ring thiophene in Chapter 7 completely altered the binding preference of water in this S containing molecule. While the O heteroaromatic ring (furan)[2] still interacts with water at the site of the heteroatom, which is also valid for the nitrogen analog[3,4] (both based on previously reported results), thiophene has a strong preference for the π···H–O HB. As the binding between water and thiophene was weak, splittings related to internal motions of water were observed in the rotational spectrum. These large amplitude motions revealed how dynamic water is and how flexible its weakly bound complexes with partner molecules can be.

In the last part of the thesis, the geometries of *N*-allylmethylamine (AMA) and of its monohydrated complex (AMA–w) were reported. Although the study of AMA (Chapter 8) was first necessary to facilitate the assignment of the lines from its monohydrated complex, the results of this study provided interesting information about the complex conformational landscape of a compound featuring the amine and allyl groups which are of astrochemical and atmospheric interest.[5] While in the S containing monomers MPA and MP the S–H···O=C interaction is dominant making the global minimum geometry much lower in energy than the other conformers, in AMA, the absence of strong donor and acceptor groups results in a much more competitive equilibrium. This is highlighted by the four conformers of AMA observed experimentally and by their very close relative energies which are explained by a subtle balance between the attractive orbital and repulsive interactions. In the presence of a water molecule (Chapter 9), the two most stable conformers of AMA were favoured to form water complexes through primary N···H–O and secondary C–H···O interactions with the N atom serving as a HB acceptor while the C–H group acts as a HB donor. Although water did not alter the geometry of the AMA conformers significantly, changes in the relative energy and in the intramolecular interactions of some higher energy conformers of AMA were observed. Among a small family of primary, secondary and tertiary amines, AMA–w was shown to be the strongest bound complex.

By decomposing the interaction energy of the intermolecular complexes studied in this thesis, the nature behind the formation of each cluster was revealed. For all hydrogen bound complexes, the interaction was proven to be mainly electrostatic and stronger for the O and N containing complexes due to the larger donor characters of these atoms in comparison to those of S, Se and of the π-system. It is evident, however, that the complexes featuring interactions with the latter showed larger contributions from dispersion to the stabilization energies which are

mainly explained by the weaker and longer-range character of these interactions and the common presence of additional secondary contacts. The increase in the percentage of dispersion varied from about 10% – 20% depending on the chemical system.

10.2 Outlook

The work of this thesis can be further extended in several aspects including:

i) The conformational landscape of the monomers can be investigated in other regions of the electromagnetic spectrum, especially in higher frequency regions, to probe transitions with higher rotational quantum number. As centrifugal distortion effects are greater at higher frequencies, higher order centrifugal distortion constants (e.g. sextic and beyond) can be determined which in turn allow rotational energy levels to be derived with greater accuracy. This provides even more precise information about the geometries governing the molecule's potential energy surface. It may also allow the observation of transitions corresponding to vibrationally excited states that are also intimately related to the vibrational potential function offering details about the spacing between vibrational energy levels, the nature of vibrational modes, and effective molecular geometry in these excited levels. Additionally, conformational studies of the monomers in the absence of a supersonic jet (at room temperature) will provide extra information as at room temperature, relaxation phenomena may not occur, facilitating the observation of additional conformers in the rotational spectrum.

As AMA is of astrochemical interest, its study in the millimeterwave and sub-millimeterwave regions may be particularly interesting to support its astrochemical

observation as they overlap with the operating frequency of many ground-based radio telescopes. Discovery of novel molecular species in the remote environments of the interstellar medium constitutes the basis to improve our knowledge about chemical complexity in space which may be related to questions as profound as the origins of life in the Universe and is still an open scientific pursuit.[6]

ii) Studies on similar compounds varying the type of substituents are of interest to evaluate the effect of different side chains on the conformational landscape. For example, taking the results reported for AMA and its surprisingly competitive equilibrium as a motivation, projects in the van Wijngaarden group have already started to investigate the effects of functional group substitution on the conformational landscape by studying analogues not only of diallyl compounds such as diallylamine,[7] triallylamine, diallyl sulfide and diallyl ether, but also with propargyl and ethyl groups, such as dipropargyl amine, among others. The study of these molecules will not only provide sufficient data for observational astronomy as the amine, allyl and propargyl groups are particularly promising astrochemical targets, but will also offer details on the subtle attractive and repulsive forces governing the folding topologies of the bridged-like compounds by identifying their donor and acceptor groups in a chemically intuitive way. This is key to model their reactivity with partner molecules and self-assembly as for the disulfide bridges present in globular proteins, for example.[8]

iii) The studies on the S compounds and their molecular complexes can be extended to elucidate the characteristics of other sulfur HBs, such as the S–H···O instead of S–H···O=C by replacing the acid and ester groups of MPA and MP by a hydroxyl (O–H) moiety and by investigating molecular aggregates formed with larger cycles such as 5- and 6-membered rings including tetrahydro and hexahydro thiophene. Comparison with their O and especially Se

counterparts (even if only theoretically) would also be of interest to extend the knowledge about the nature of the HBs when going from O to S and Se. As there is now general agreement about the importance of S and Se HBs,[9] molecular studies need to keep evolving to provide insights on these non-covalent forces that are intimately linked to multifaceted applications. These include understanding of supramolecular architectures, interactions between a drug and a molecule and the biological structure–function relationship, among others, to thus will promote novel perspectives into reaction mechanisms and bio- and crystal engineering of S and Se containing compounds.[9]

iv) The studies of the hydrates could also be extended to include larger solvation shells as knowledge about the first steps of solvation was now obtained. Investigating larger clusters at the molecular level is essential to understand the chemical properties of condensed phases which bridges the microscopic (isolation) and the macroscopic (bulk) world.[10] Additionally, as spectroscopic, and geometric parameters for each complex can be determined via rotational spectroscopy (as shown throughout this thesis), information about changes in geometry in the presence of multiple molecules of the solvent can be achieved in a step-wise fashion. This is extremely relevant to rationalize the impact of external effects in shaping molecular geometries through alteration of their stabilizing interactions which is also essential for tuning molecular design principles.

Extensions of the results presented in this thesis are not limited by the examples listed above. Studies combining high resolution spectroscopic experiments and theory such as those reported here are powerful methods to obtain insights on the fundamental chemical and physical properties of increasingly complicated molecules. The foundation established in this thesis forms

the basis for the further advances in our understanding of the critical role of non-covalent interactions in many fields of science.

10.3 References

(1) van Bergen, L. A. H.; Alonso, M.; Palló, A.; Nilsson, L.; De Proft, F.; Messens, J. Revisiting Sulfur H-Bonds in Proteins: The Example of Peroxiredoxin AhpE. *Sci. Rep.* **2016**, *6* (1), 30369.

(2) Lockwood, S. P.; Fuller, T. G.; Newby, J. J. Structure and Spectroscopy of Furan:H_2O Complexes. *J. Phys. Chem. A* **2018**, *122* (36), 7160–7170.

(3) Wu, B.; Xie, F.; Xu, Y. The Pyrrole-Water Complex: Multidimensional Large Amplitude Dynamics and Rotational Spectra of Its ^{13}C Isotopologues. *J. Mol. Spectrosc.* **2020**, *374*, 111381.

(4) Tubergen, M. J.; Andrews, A. M.; Kuczkowski, R. L. Microwave Spectrum and Structure of a Hydrogen-Bonded Pyrrole-Water Complex. *J. Phys. Chem.* **1993**, *97* (29), 7451–7457.

(5) Silva, W. G. D. P.; Poonia, T.; Wijngaarden, J. Targeting the Rich Conformational Landscape of N -Allylmethylamine Using Rotational Spectroscopy and Quantum Mechanical Calculations. *ChemPhysChem* **2020**, *21* (22), 2515–2522.

(6) Puzzarini, C.; Barone, V. The Challenging Playground of Astrochemistry: An Integrated Rotational Spectroscopy – Quantum Chemistry Strategy. *Phys. Chem. Chem. Phys.* **2020**, *22* (12), 6507–6523.

(7) Silva, W. G. D. P.; Daudet, G.; Perez, S.; Thorwirth, S.; van Wijngaarden, J. Conformational Preferences of Diallylamine: A Rotational Spectroscopic and Theoretical Study. *J. Chem.*

Phys. **2021**, *154* (16), 164303.

(8) Thornton, J. M. Disulphide Bridges in Globular Proteins. *J. Mol. Biol.* **1981**, *151* (2), 261–287.

(9) Chand, A.; Sahoo, D. K.; Rana, A.; Jena, S.; Biswal, H. S. The Prodigious Hydrogen Bonds with Sulfur and Selenium in Molecular Assemblies, Structural Biology, and Functional Materials. *Acc. Chem. Res.* **2020**, *53* (8), 1580–1592.

(10) Tang, J.; Xu, Y.; Mckellar, A. R. W.; Ja, W. Quantum Solvation of Carbonyl Sulfide with Helium Atoms. *Science* **2002**, *297* (September), 2030–2034.